Silicon nitride waveguides and micro-ring resonators for photonic integrated circuits

Martin Sinclair

Submitted in fulfilment of the requirements for the
Degree of Doctor of Philosophy

School of Engineering
College of Science and Engineering
University of Glasgow

June, 2020

Abstract

This work represents significant progress in the development of a Si_3N_4 waveguide platform for near infra-red wavelengths as required for ^{87}Rb chip-scale atomic systems. The theoretical framework provided by ray optic and electromagnetic theory have formed a basis for understanding waveguide phenomena. Coupled mode theory has been used to determine the micro-ring resonator coupling coefficient. An analytical model of a micro-ring resonator has been used to show that Q factor can be optimised by the decreasing the coupling coefficient. The Lacey-Payne scattering model suggests that increased waveguide width and reduced index contrast results in decreased loss due to sidewall scattering. Q factor has therefore been optimised by increasing waveguide width, developing a top cladding process, and operating in the under-coupled regime. By this approach, a record high Q factor value of $(1.38 \pm 0.04) \times 10^6$ has been demonstrated for buried waveguide micro-ring resonators operating around 780 nm corresponding to a propagation loss of 0.261 ± 0.009 dB cm^{-1}. This high-Q micro-ring resonator could serve as a frequency reference for laser frequency stabilisation but a temperature dependent resonance wavelength shift of 7.34 pm K^{-1} is expected and would require active temperature stabilisation to within ± 25 mK. Passive athermalisation of a micro-ring resonator by optimising the thickness of polymer top cladding materials with a negative thermo-optic coeffcient has been investigated by simulation. A significant reduction of the temperature dependent wavelength shift of a micro-ring resonance peak has been found for PMMA and SU8 top cladding layers, 1.20 pm K^{-1} and 0.14 pm K^{-1} respectively corresponding to a required temperature stability of ± 167 mK and ± 1.43 K.

Coupling of light from a Si_3N_4 waveguide to collimated free-space Gaussian beam has been considered within the context of developing an on-chip interferometer intended to measure the displacement of a MEMS gravimeter proof-mass. The divergence of a free-space coupled Gaussian beam has been determined. Taking into account the use of an SU8 spot-size converter, the Fresnel reflectance of the SU8 waveguide, and the measured reflectance of the silicon proof mass, the beam divergence is still found to be the dominant loss mechanism for the propagation distances involved in this application. Use of a micro-ball lens to collimate the beam was considered using various simulation techniques, determining that the vertical positioning of the lens would pose the greatest fabrication challenge. Processes were developed to produce SU8 waveguides, registration blocks, and micro-ball lens receptacles.

Publications

Journal Publications

Sinclair, M., K. Gallacher, M. Sorel, J. C. Bayley, E. McBrearty, R. W. Millar, S. Hild, and D. J. Paul. "1.4 million Q factor Si_3N_4 micro-ring resonator at 780 nm wavelength for chip-scale atomic systems." Optics Express 28, no. 3 (2020): 4010-4020.

Gallacher, K., R. W. Millar, U. Griškevičiūtė, **M. Sinclair**, M. Sorel, L. Baldassarre, M. Ortolani, R. Soref, and D. J. Paul. "Ultra-broadband mid-infrared Ge-on-Si waveguide polarization rotator" APL Photonics 5, no. 2 (2020): 026102.

Conference Proceedings

Sinclair, M., K. Gallacher, M. Sorel, J. C. Bayley, E. McBrearty, R. W. Millar, S. Hild, and D. J. Paul. "1.4 Million Q-Factor 780 nm Wavelength Si_3N_4 Micro-rings for Chip-Scale Atomic Systems." In 2020 Conference on Lasers and Electro-Optics (CLEO), In-press.

Sinclair, M., K. Gallacher, R. W. Millar, J. C. Bayley, O. Sharp, F. Mirando, G. Ternent et al. "High-Q Si3N4 ring resonators for locking 780 nm GaAs-based distributed feedback laser." In The European Conference on Lasers and Electro-Optics, p. cb_p_5. Optical Society of America, 2019.

Gallacher, K., **M. Sinclair**, R. W. Millar, O. Sharp, F. Mirando, G. Ternent, G. Mills, B. Casey, and D. J. Paul. "Integrated DFB Lasers on Si_3N_4 Photonic Platform for Chip-Scale Atomic Systems." In 2019 Conference on Lasers and Electro-Optics (CLEO), pp. 1-2. IEEE, 2019.

Contents

Acknowledgements

I would like to thank my supervisors Douglas Paul for all of his guidance and support in helping me to reach this point and Stefan Hild for giving me the opportunity. The experimental work completed in this thesis would not have been possible without the support of Kevin Gallacher who kindly shared the wealth of his experience in nano-fabrication and continued to help in the most difficult of times. The data analysis presented in this thesis was made possible by Joseph Bayley who took the time to help me get to grips with python and patiently explained parameter estimation, thank you for everything. Bryan Barr continued to provide support long after the completion of my masters project so thanks for all the help and for making this career seem like an alright choice, I think it's going ok so far. My thanks go to Jennie Wright for being so kind as to help me get into a PhD when I was figuring out what I wanted to do. I would like to thank everyone else that contributed to the work along the way, my examiners for the helpful feedback, and my fellow members of the Piledriver for the years of camaraderie. Finally, I want express my gratitude for the love and support shown by those nearest and dearest to me when it was needed it most.

List of Tables

List of Figures

Declaration

I hereby declare that all work presented in this thesis was carried out by the author unless otherwise explicitly stated. This work has not been presented in any previous application for a degree at this or any other institution.

The work presented in Chapters 5, 6, and 7 has previously been published in *Optics Express* [1].

Acronyms

AWG Arrayed waveguide grating 4

BSS Beam step size 70, 71

CMOS Complementary metal-oxide-semiconductor 1, 3

CMP Chemical Mechanical Polishing 75, 76

CVD Chemical Vapour Deposition 59

DARPA Defence Advanced Research Project 3

DFB Distributed Feedback 7, 131

EME Eigenmode expansion 104

FDE Finite difference eigenmode 30, 31, 33–35, 38, 89, 93, 96, 125

FSR Free spectral range 46, 93

FWHM Full width at half maximum 57, 87

GDSII Graphic Design System II is a database file used for integrated circuit layout 59, 60, 70, 71

HSQ Hydrogen silsequioxane 61, 65, 67–72, 76, 90, 99

JWNC James Watt Nanofabrication Centre 59, 61, 62, 68, 76, 104, 131

LIDAR Light detection and ranging 1, 127

LPCVD Low Pressure Chemical Vapour Deposition 3, 4, 63, 75, 76, 88

MEMS Micro-electro-mechanical Systems i, xii, 7–9, 101, 102, 106, 108, 113, 122, 124, 126

MMI Multi-mode interference 4, 5

PDH Pound-Drever-Hall laser frequency stabilisation 127

PECVD Plasma Enhanced Chemical Vapour Deposition 3, 59, 61, 64–66, 75, 76, 95

PGMEA Propylene glycol methyl ether acetate 116, 118, 120

PMMA Poly(methyl methacrylate) i, 65, 90, 97–100, 124, 126

RF Radio frequencies 6, 64, 72

RIE Reactive Ion Etching 59

RMOG Resonant micro-optic gyroscope 128, 131

SEM Scanning electron microscope 73

SOI Silicon-on-insulator 2

SolsTiS Ultra narrow linewidth continuos wave Ti:Sapphire laser manufactured by M Squared 80, 83

SU8 A high contrast, epoxy-based photoresist designed for micro-machining and other micro-electronic applications where a thick chemically and thermally stable image is desired i, 97–101, 103–108, 113–122, 124, 126, 127

TDWS Temperature dependent wavelength shift 96, 99, 100

TE Transverse electric 12, 13, 15, 17, 21, 26, 28, 30, 31, 35, 37, 38, 40, 42, 43, 95, 125

TEM Transverse electromagnetic 12, 17

TM Transverse magnetic 12, 13, 30, 31, 35, 37, 42, 125

TMAH Tetramethylammonium hydroxide 68, 71

TOC Thermo-optic coefficient. The change in refractive index for a change in temperature 96–99

VRU Variable resolution unit 70

Symbols

n The refractive index of a bulk material 11, 18, 28

c The velocity of light in a vacuum ($\mathrm{m\,s^{-1}}$) 11

v The velocity of light in a medium ($\mathrm{m\,s^{-1}}$) 11

E Electric field amplitude 11, 13, 44

r Complex reflection coefficient 12, 13

x Coordinate position in the plane of the substrate oriented in the direction of propagation (m) 14, 17

ω Angular frequency ($\mathrm{rad\,s^{-1}}$) 14

ν Frequency (Hz) 14

k Wave-vector 14, 28, 32

y Coordinate position in the plane of the substrate orthogonal to the direction of propagation (m) 15, 17, 21, 104, 107, 110, 114

b Half the height of a waveguide (m) 15, 18

l Integer designating mode number in the z-direction 15, 19, 21

θ_i Angle formed with normal incidence within a material of index i 15

z Coordinate position normal to the plane of the substrate (m) 17, 21, 104, 107, 110, 114, 122, 126

L_c The crossover length is the length which results in light coupling completely from one optical waveguide to another parallel waveguide 21, 28

m Integer designating mode number in the y-direction 21

h Transverse component of the wave-vector within the waveguide core 22

a Half the width of a waveguide (m) 28

$t_{a,b}$ The transmission coefficient of a bus waveguide of a micro-ring resonator corresponding to evanescent coupler a or b in the general case 44

$\kappa_{a,b}$ The coupling coefficient from a bus waveguide to a micro-ring resonator corresponding to evanescent coupler a or b in the general case 44

$\gamma_{a,b}$ The loss coefficient of evanescent coupler a or b in the general case 44

τ Normalised round-trip field attenuation of a ring resonator 46

Chapter 1

Introduction

Photonics is the scientific field concerned with the generation, manipulation, transmission, and detection of light and is generally used to refer to instances in which light is used to fulfil a purpose which has traditionally been served by electronics such as computation, data storage, and telecommunications. Photonic transceivers are already in common usage in data centres around the world due to the rapid development of silicon photonics in the past decade [2]. This has been possible because silicon photonics takes advantage of the pre-existing infrastructure established by the microelectronics industry and can be fabricated using the same tool-set. Platforms consisting of materials which are commonplace in complementary metal-oxide semiconductor (CMOS) fabrication techniques present less of a financial risk than a foundry dedicated to optical integrated circuits so have received much more research interest than more exotic materials such as lithium niobate and III-V compounds like indium phosphide [3,4]. Early work on silicon photonics for data communication was focused on the familiar telecommunication bands around 1.3 μm and 1.5 μm [5] but the successful deployment of silicon photonics in data communication has prompted interest in miniaturised optical systems for a wide range of applications some of which require different wavelengths to be used. The potential application of silicon photonics beyond data communication include biosensing [6], light detection and ranging (LIDAR) [7], optical gyroscopes [8], external laser cavities [9], and chip-scale atomic systems [10].

1.1 Optical Waveguide Platforms

There are a wide array of existing optical waveguide platforms which have been developed in order to harness the particular properties offered by each platform. Advantageous proprieties include low propagation loss which can allow for efficient data transmission [3], low confinement enables evanescent chemical sensing [11] while high confinement is more suitable for non-linear applications [12], and the wavelength transparency window often determines the possible applications. Silicon-on-insulator is cheap to manufacture and the most mature platform available but while the high index contrast allows for small bend radii it also results in relatively high

scattering loss. Silicon dioxide (glass) waveguides typically utilise thin film deposition of doped silicon dioxide or index modification methods including direct laser writing and ion implantation/exchange to define a waveguide core with low index contrast waveguide and potentially very low propagation loss. Glass waveguides have been commercially viable but as a result of the low index contrast, large bend radii are often required to keep losses low. As demand for smaller transceivers in data communications increases, smaller bend radii are required and so a waveguide platform with low propagation losses but with a high enough refractive index contrast to produce small footprint optical devices is sought after. Silicon nitride and silicon oxynitride waveguide platforms are poised to fulfil this requirement. There have been demonstrations of hybrid platforms with monolithic integration of SOI, silicon nitride, and even silicon dioxide waveguides in the same device. This approach takes full advantage of the active functionalities and mature infrastructure of silicon waveguides, the low propagation losses and relatively forgiving fabrication tolerances of silicon nitride waveguides, and the easy fibre coupling that comes with silicon dioxide waveguides [13–16].

1.1.1 Silicon-on-insulator

Silicon-on-insulator (SOI) is considered to be the mainstream of silicon photonics [4]. This platform consists of a crystalline silicon layer typically hundreds on nanometres thick on a layer of buried silicon dioxide on a silicon substrate. Research on this platform has been focused on the development of high speed transceivers for telecommunications but includes the development of components such as micro-ring resonators, multi-mode interference couplers, arrayed waveguide grating (de)multiplexers, and broadband grating couplers for fibre coupling [17, 18]. SOI is typically manufactured by bringing the oxidised surfaces of two silicon wafers into close proximity, bonding these surfaces together at high temperatures, and then etching away the excess silicon from one wafer to form a waveguide core layer [19]. The compatibility of SOI with other photonic and electronic structures is limited because SOI is manufactured at the wafer scale from bare silicon wafers whereas waveguide platforms that utilise chemical vapour deposition to produce the waveguide layers exhibit greater versatility in terms of the order in which components can be fabricated [4]. The high index contrast between the silicon core and the silicon dioxide cladding means that the waveguides can feature very small bend radii without suffering from significant bending loss allowing for devices with a small footprint. The high index contrast also means that loss due to scattering at the material interface is high, $\sim 1\,\mathrm{dB\,cm^{-1}}$ is considered low propagation loss for SOI waveguides [20–22]. SOI offers a transparency window from around 1.1 µm (due to absorption of silicon) to around 3.7 µm (due to absorption of the silicon dioxide) [4]. Therefore SOI cannot be used as a waveguide platform for some near infra-red or for any visible wavelengths.

1.1.2 Silicon Dioxide

Silicon dioxide (glass) waveguides are simple to manufacture, exhibit low propagation losses, and can be easily index-matched with optical fibre [23]. Standard glass compositions can offer a transparency range from ultra-violet to the mid-infrared [24] and waveguide propagation loss of about 0.06 dB cm^{-1} has been demonstrated at 777 nm [25] and at 1.5 µm wavelength [26]. The high index core layer can be deposited using physical methods including evaporation, sputtering, and pulsed vapour deposition and chemical methods such as chemical vapour deposition, flame hydrolysis, and spray pyrolysis [23]. Channel waveguides can subsequently be defined using lithography and etching techniques similar to the other waveguide platforms discussed here. Etching of waveguide channels inevitably introduces sidewall roughness to waveguides but the low index contrast inherent to this platform means that the resulting scattering loss is relatively low. Glass waveguides also offer the possibility of defining the waveguide core instead by modifying the index of a glass by selective irradiation (ultraviolet or femto-second lasers) or by ion diffusion (ion exchange at low energies and ion implantation at high energies) [23]. Index modification methods avoid the issue of sidewall scattering altogether but these can be quite specialised process generally not considered to be CMOS compatible. The major limitation of glass waveguides is the radiative bend losses resulting from the low index contrast which lead to large minimum bend radii.

1.1.3 Silicon Nitride On Silicon Dioxide

Silicon nitride exhibits low absorption down to wavelengths of ~ 400 nm and is commonly used in CMOS fabrication as an insulation layer [27]. Low pressure chemical vapour deposition (LPCVD) performed at high temperature ($> 700\,^{\circ}$C) and plasma enhanced chemical vapour deposition (PECVD) at low temperatures ($< 400\,^{\circ}$C) are used to form silicon nitride films. LPCVD typically results in films close to stoichiometric Si_3N_4 and offers precise control of film thickness and refractive index [4]. Early adoption of the platform came in 1993 in the form of bio-photonics research with one of the earliest silicon nitride waveguide devices being a Mach-Zehnder interferometer immunosensor operating at a wavelength of 632.8 nm [28]. The silicon dioxide top cladding was etched away to provide recesses for the application of the analyte direction to the silicon nitride waveguide cores, the optical mode then interacts evanescently with the analyte resulting in a detectable phase change. In 2005 there were papers published [29] detailing the development of low loss (~ 0.1 dB cm^{-1}) silicon nitride waveguides operating in the near infra-red C-band ($\sim$1550 nm). This was the beginning of an era in which a lot of research was conducted in order to reduce waveguide loss at around 1500 nm wavelength for moderately confined (film thickness > 100 nm) silicon nitride waveguides [30]. The Defense Advanced Research Project Agency (DARPA) funded research at the University Of Santa Barbara which, in collaboration with LioniX, led to the demonstration of record low propagation

losses of 0.045 dB m^{-1} for low confinement waveguides (films $<$ 100 nm) at 1580 nm in 2011. High confinement waveguides (films $>$ 400 nm) offer an alternative route for achieving low loss (0.13 dB m^{-1}) by reducing the interfacial scattering and are of particular interest for non-linear optics applications because silicon nitride exhibits a high Kerr non-linearity and anomalous group velocity dispersion can be realised for thick films [12, 31]. Due to the high tensile stress of LPCVD Si_3N_4, deposition thickness is typically limited to around 250 nm without cracks forming in the film, this limitation has been overcome utilising temperature cycling and annealing to fabricate films up to 744 nm thick without cracks forming [32]. The photonic Damascene process has also been used to fabricate silicon nitride waveguide cores up to 1.35 µm thick by depositing silicon nitride into trenches etched in silicon dioxide [33].

1.2 Passive Components

An optical waveguide can be formed simply by depositing a transparent material with a higher refractive index than glass on a oxidised silicon substrate. There are several waveguide geometries which have proved to be popular, these geometries are shown in Figure 1.1 [34]. This work is focused on ridge/wire waveguides and buried waveguides. With these simple geometries, numerous passive optical components have been developed to serve a wide array of functions. Perhaps the simplest of these is a curved waveguide. Waveguides with curves are required to direct light where it is required without abrupt junctions or discontinuities. Bends which are too tight can result in high radiative losses or significantly increased sidewall scattering [3]. A Y-branch can be used as either a splitter (with one input and two outputs) or combiner (with two inputs and one output) and if it designed to be symmetric, can reliably split light 50/50% (excluding excess loss) [35]. By attaching the outputs of a splitter to the inputs of a combiner, a simple Mach-Zehnder interferometer can be formed. By altering the phase of one of the two paths between the splitter and combiner, either by active phase modulation or by altering the length of one of the paths, the intensity of the interferometer output can be determined. The difference in path length can be predetermined by design or changed dynamically by thermal tuning.

Multi-mode interference (MMI) couplers and arrayed waveguide gratings (AWG) are commonly used components in data communications. MMIs present a versatile way of splitting or combining a potentially large number of inputs or outputs by determining how eigenmodes of the injected mode will interfere in a large multi-mode section of waveguide and positioning the desired number of single mode waveguides such that they collect light from the resulting interference pattern [36]. AWGs are used as (de)multiplexers to combine (or separate) different wavelengths which are to be (or have been) transmitted in one waveguide or optical fibre [37]. These operate similarly to MMIs but take advantage of the principle that dissimilar wavelengths will not interfere in order to separate out wavelengths. This work is focused on micro-ring

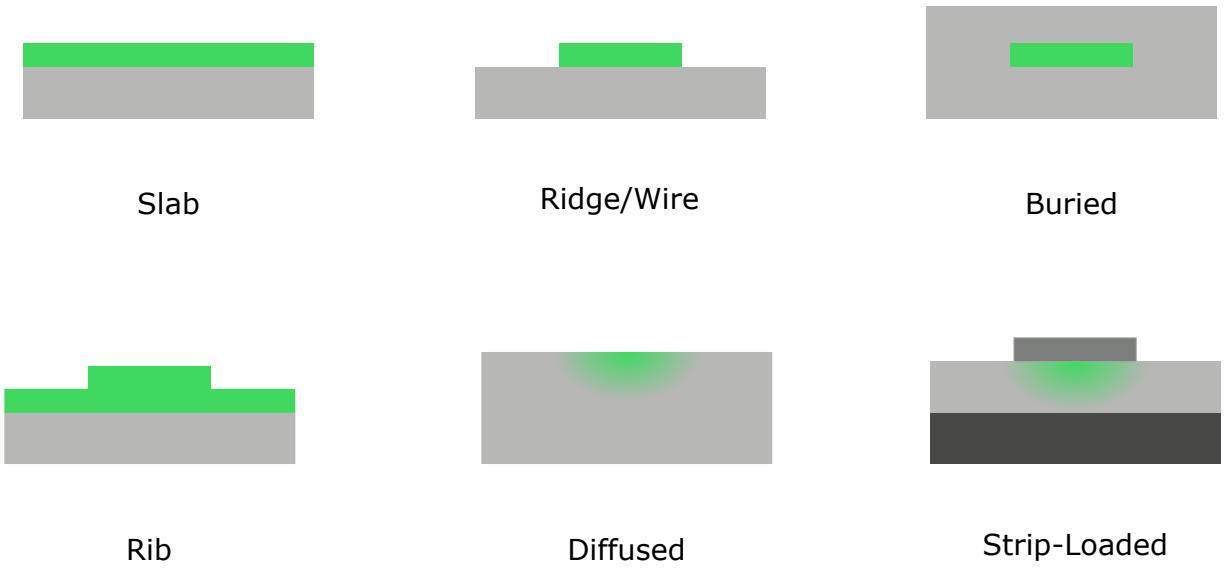

Figure 1.1: Schematic representation of common waveguide cross-section geometries. The waveguide is formed in the green region while the surrounding material acts as a cladding or substrate.

resonators and evanescent couplers and so only these components will be discussed in depth here.

1.2.1 Evanescent Couplers

Evanescent (or directional) couplers consist of two adjacent parallel waveguides close enough together that the evanescent field of a mode propagating in one waveguide interacts with the other waveguide allowing light to couple between the two. The extent of this power coupling is periodic and a function of the length of the coupler, the wavelength, polarisation state, and the difference in the effective indices of the coupled modes (this is explained further in Section 2.3). For highly confined waveguides, the required gap spacing can be very small and so y-splitters and MMIs would often be used instead because they can be more fabrication tolerant. Evanescent couplers can however be designed in order to take advantage of their wavelength and polarisation dependence allowing for light to be separated accordingly based on wavelength or polarisation [38, 39], couplers can even cascaded in order to achieve the desired effect. Evanescent couplers are used in this work to couple light into and out of micro-ring resonators via bus waveguides.

1.2.2 Micro-ring Resonators

A micro-ring resonator is an optical waveguide that forms a closed loop allowing light to circulate and resonate if the optical path length is equal to a integer number of wavelengths. They are commonly used as filters, delay lines, and switches [40] and have been demonstrated to serve as

an integrated laser cavity coupled to a gain medium [41] and an external cavity frequency reference for a diode laser [42]. Silicon-on-insulator micro-ring resonators with Q factors as high as 1.1×10^6 have been demonstrated [43]. High Q factors have been demonstrated with high confinement and low confinement silicon nitride waveguides with published Q factor values of 6.7×10^7 [12] and 8.1×10^7 [44] respectively. These high-Q factors are found using micro-ring resonators designed to operate at wavelengths around 1.5 µm. Higher Q factors are expected at higher wavelengths because of the dependence of scattering loss on wavelength, this is discussed in detail in Section 2.4.

Micro-ring resonators can be a useful tool for characterising the performance of a waveguide platform. By measuring the transmission spectrum and determining the resulting free spectral range of a series of micro-ring resonators with different lengths, the waveguide group index can be found [40]. Waveguide propagation loss can be determined from a single measurement of a micro-ring resonator transmission spectrum by fitting the appropriate transmission equation (see Chapter 4) to the transmission spectrum if the coupling coefficient value(s) are known explicitly or can be inferred to have a particular value [45]. Another approach is to take advantage of the wavelength dependence of an evanescent coupler. A broadband transmission spectrum including many resonance peaks is recorded and the transmission equation is fit to each resonance peak returning coupling and loss coefficients. The coupling coefficient is sinusoidal with wavelength while the loss coefficient should vary only slightly and so by examining the fits of multiple resonance peaks across a range of wavelengths, the two parameters can be distinguished [46].

The majority of research into silicon nitride micro-ring resonators has been concerned with applications in telecoms and so has been focused on operation around 1.3 µm and 1.5 µm. There are however many potential applications for micro-ring resonators which would require operation at shorter wavelengths, these include label-free biosensors [47], frequency comb generation [48], generation of entangled photon pairs [49], and chip-scale atomic systems utilising atomic transitions to realise devices such as atomic clocks [10, 50, 51] and quantum effects metrology references [52].

1.3 Chip-scale Atomic Systems

Atomic spectroscopy presents a method of providing a high precision frequency reference. Trapped atoms are well defined quantum systems quantified by fundamental natural constants. Alkali atoms with only one valence electron are typically used for three main reasons: the first is that the high vapour pressure results in strong spectroscopic signals; the second is the GHz range hyper-fine ground state transitions can be characterised with standard RF electronics; the third is that they have electronic band structures and optical absorption cross-sections which allows for efficient optical pumping and absorption spectrum characterisation using lasers [10]. Rubidium vapour is well suited for an optically probed atomic system because the energy band structure

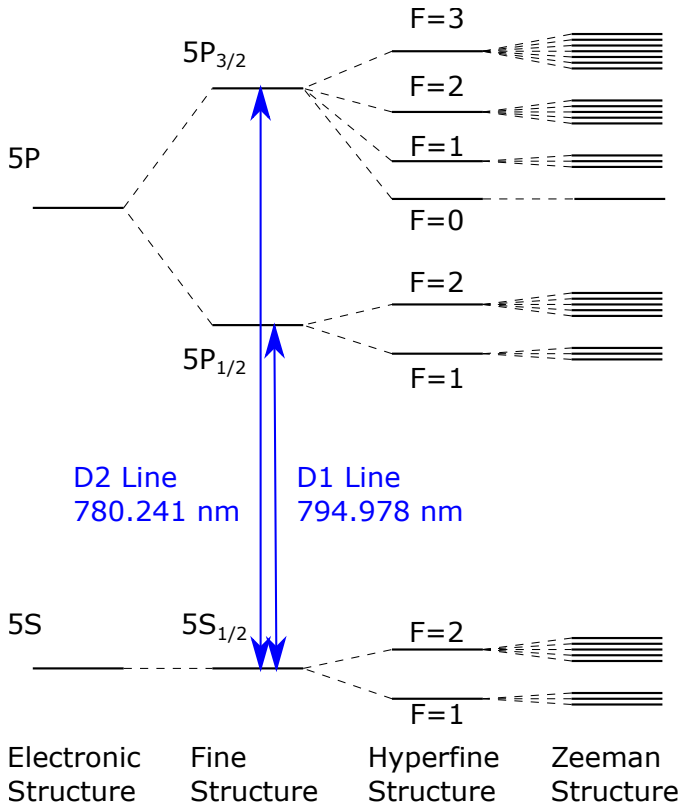

Figure 1.2: The energy level structure of ^{87}Rb. The D1 and D2 electron transitions are of particular interest for optically probed atomic systems.

of ^{87}Rb includes an electron transition from the $S_{1/2}$ ground state to the $P_{3/2}$ excited state which can be excited by a 780.241 nm light source and an electron transition from the $S_{1/2}$ to $P_{1/2}$ state which can be excited by a 794.978 nm light source [10, 53] (see Figure 1.2).

Traditional atomic systems rely upon free space beams and bulk optical components. Replacing these optical systems with an integrated photonics platform such as silicon nitride waveguides can result in increased manufacturability and reduced overall size, leading to chip-scale atomic systems [10]. The evolution of micro-electro-mechanical systems (MEMS) processing techniques has allowed for the realisation MEMS ^{87}Rb vapour cells which can be integrated on chip [54]. These cells typically consist of glass-silicon-glass assembled by anodic bonding. A "pill" of an alkali metal is placed within an etched through chamber in silicon bonded to the bottom layer of glass, the top glass layer is put in place and the assembly is either evacuated or filled with a buffer as the top layer is anodic bonded. The ^{87}Rb is then vaporised by laser ablation. The vaporised ^{87}Rb can then be excited using a diode laser on chip such as a distributed feedback DFB diode laser [55]. The diode laser could be frequency stabilised using a high Q factor micro-ring as the frequency discriminator [42].

1.4 Aims Of This Thesis

The goal of the work detailed in this thesis was to develop a waveguide platform consisting of a silicon nitride waveguide core, a silicon dioxide bottom cladding, and a silicon dioxide top cladding that would be compatible with a wavelength of 780.241 nm and thereby further the development of a chip-scale atomic system based upon the D2 transition of ^{87}Rb atoms. In the course of developing this platform, the main focus has been on optimisation of two figures of merit, the micro-ring Q factor and the waveguide propagation loss (dB cm^{-1}). This optimisation has been achieved by reducing the sidewall scattering induced propagation loss and increasing the coupling gap spacing so as to operate in the under-coupled regime of the micro-ring resonators. Potential application of a micro-ring resonator as a frequency reference has been explored by investigating the thermal dependence of the micro-ring resonance and the possibility of reducing this dependence by thermo-optic coefficient engineering. Applications of this waveguide platform have been explored further with some progress towards the development of a free-space coupled interferometer for displacement sensing of a MEMS gravimeter.

A brief outline of the remaining chapters in this thesis is as follows:

Chapter 2: Waveguide Theory

Ray optic and electromagnetic theory are used to explain waveguide behaviour and provide the required background knowledge for a discussion of coupled mode theory. An analytical solution for the coupling coefficient of the micro-ring resonators characterised in this work is derived from coupled mode theory. The Lacey-Payne scattering model is also introduced as a means of predicting the sidewall scattering induced propagation loss.

Chapter 3: Waveguide Simulation

The waveguide dimensions and material properties are simulated using a finite difference eigenmode solver in order to determine appropriate thicknesses for the material layers and appropriate widths for the waveguide core such that the fundamental waveguide mode is supported. The radiative bend loss is found to be a negligible factor, the Lacey-Payne model is used to predict scattering loss, and the eignemode expansion simulation tool is also introduced.

Chapter 4: Ring Resonator Analytical Modelling

The performance of micro-ring resonators is modelled analytically. This results in the derivation an equation representing the normalised power transmission of an all-pass micro-ring resonator to which the micro-ring resonator transmission spectra can be fit in order to determine the waveguide propagation loss. The Q factor, peak amplitude, and slope gradient of the resonance peak

are examined in the under, over, and critically coupled regimes leading to the conclusion that the Q factor can be optimised by operating in the under-coupled regime.

Chapter 5: Waveguide Process Development And Fabrication

The design, material deposition, and processing of sample devices is explained in detail. The design is created using Python-3 based Nazca Design™ and prepared for electron beam lithography using a series of software tools. The bottom cladding is grown by wet thermal oxidation, the core layer is deposited by low pressure chemical vapour deposition, and the top cladding is deposited by plasma enhanced chemical vapour deposition. Hydrogen silsequioxane is used as the electron beam lithography resist and as an etch mask. The waveguide pattern is then ecthed using trifluoromethane reactive ion etching. Waveguide facets are prepared either by cleaving the sample or by diamond saw and polishing prior to device characterisation.

Chapter 6: Ring Resonator Characterisation

Micro-ring resonators are characterised by recording their transmission spectra using a tunable Ti:sapphire laser. A least squares fit of a Lorentzian distribution and of the normalised power transmission is used to determine the Q factor and waveguide propagation loss respectively. A record high Q factor is found for buried silicon nitride waveguides at near infra-red wavelengths. Utilisation of this high Q micro-ring resonator as a frequency reference for laser frequency stabilisation is discussed.

Chapter 7: Athermalisation Of Micro-ring Resonators

The temperature dependence of the micro-ring resonance peak position is investigated by simulation. A top cladding material with a negative thermo-optic coefficient can be used to counteract the positive coefficients of the core and bottom cladding layers. The thermo-optic coefficients of candidate polymer top-cladding layers are found experimentally. The optimum temperature stability that could be realised using these top cladding layers is found by simulation.

Chapter 8: Free-space Coupled Interferometer Development

A means of coupling light from the silicon nitride waveguide to free-space is investigated in the course of developing an interferometer to be used to measure the displacement of a MEMS gravimeter proof-mass. An inverse taper spot-size spot-size converter is designed using the eigenmode expansion solver. Divergence of the free-space Gaussian beam is modelled analytically leading to the conclusion that a collimating lens is required. The alignment tolerance of a micro-ball lens is determined using ray transfer matrix analysis and the finite difference eigen-

mode solver. The development of fabrication processes required for the spot-size converter and lens alignment is detailed and their future development is discussed.

Chapter 9: Conclusions And Future Work

The main conclusions of the thesis are summarised and the conclusions of each chapter are given in detail. Future development of the silicon nitride waveguide platform is discussed. Specific work that had be planned out but could not be completed within the scope of this work are addressed in detail, in particular Pound-Drever-Hall laser frequency stabilisation and the development of a Sagnac effect resonant micro-optic gyroscope have been considered.

Chapter 2

Waveguide Theory

This chapter explains the underlying theory and background knowledge required to design planar optical waveguides. The transcendental equations describing the behaviour of light at the material boundaries of the planar waveguides are derived using ray optics in Section 2.1 and electromagnetic theory in Section 2.2. This provides the foundation for the derivation of the coupling coefficient of a directional coupler by means of coupled mode theory which is then adapted to the geometry of a circular micro-ring resonator in Section 2.3. Radiation loss due to scattering at the material boundaries is expected to be a dominant loss mechanism in this work and so the well established Lacey-Payne scattering model is introduced in Section 2.4.

2.1 Ray Optics

The refractive index of a material n quantifies how much light is slowed when it propagates in that material and is defined by

$$n = \frac{c}{v} \tag{2.1}$$

where c is the velocity of light in a vacuum $\left(\mathrm{m\,s^{-1}}\right)$ and v is the velocity of light in the corresponding material $\left(\mathrm{m\,s^{-1}}\right)$. The behaviour of a ray of light propagating in a medium with refractive index n_1 as it is incident, at an angle θ_1 from normal incidence, upon the boundary between that material and another with a refractive index n_2 can be described using Snell's law [56], see Figure 2.1,

$$n_1 \sin\theta_1 = n_2 \sin\theta_2, \tag{2.2}$$

where θ_2 is the angle of refraction of the transmitted light. If n_1 is higher than n_2 then there is an angle θ_1 such that θ_2 is 90°. This angle is called the critical angle [3, 56], θ_c, and is defined as

$$\sin\theta_c = \frac{n_2}{n_1}. \tag{2.3}$$

For $\theta_1 > \theta_c$, all of the light is reflected from the interface, this is called total internal reflec-

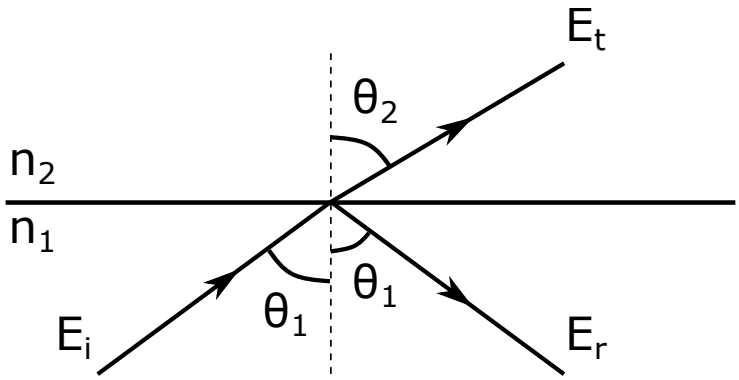

Figure 2.1: A beam of light, E_i, is incident upon a boundary between a material 1 with a refractive of n_1 and a material 2 with refractive index n_2. If the light is incident at an angle θ_1 relative in normal incidence then a reflected beam, E_r, would also form an angle of θ_1 from normal. A beam which is transmitted into material 2 would form an angle θ_2 from normal to material 2. The relationship between n_1, n_2, θ_1, and θ_2 is given by Snell's law in Equation 2.2

tion. If we introduce a second interface below the first, between the material with index n_1 and a new material with index $n_3 > n_1$, typically $n_3 \approx n_2$, then light will be continuously reflected within the material with refractive index n_1 (see Figure 2.2) and this is a simple example of a waveguide. Some fraction of the incident light field amplitude E_i is reflected E_r at the boundary while some is transmitted E_t. The fraction of the light amplitude reflected is the reflection coefficient given by

$$E_r = rE_i \tag{2.4}$$

where r is the complex reflection coefficient. This depends on the polarisation of the light as well as the angle of incidence. A propagating electromagnetic wave is described as a transverse electromagnetic wave (TEM). The transverse electric (TE) polarisation is the case in which the electric field is perpendicular to the plane of incidence, i.e. parallel with the material boundary, while for the transverse magnetic (TM) polarisation, the magnetic field is perpendicular to the plane of incidence. The reflection coefficients are given by the Fresnel formulae. The TE reflection coefficient is given by [3, 57]

$$r_{\mathrm{TE}} = \frac{n_1 \cos\theta_1 - n_2 \cos\theta_2}{n_1 \cos\theta_1 + n_2 \cos\theta_2} \tag{2.5}$$

and by substituting Snell's law, this becomes

$$r_{\mathrm{TE}} = \frac{n_1 \cos\theta_1 - \sqrt{n_2^2 - n_1^2 \sin\theta_1{}^2}}{n_1 \cos\theta_1 + \sqrt{n_2^2 - n_1^2 \sin\theta_1{}^2}}. \tag{2.6}$$

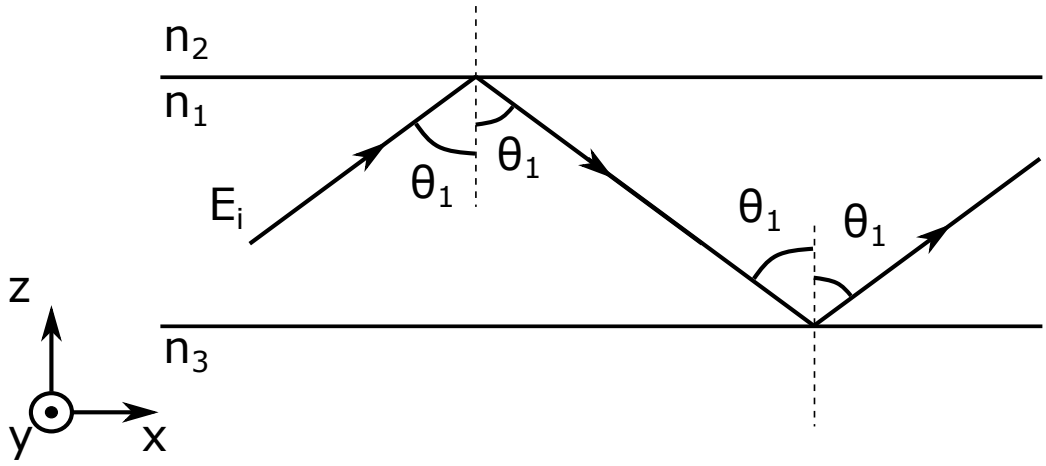

Figure 2.2: Total internal reflection within a waveguide. The waveguide is formed by a core, material 1, with refractive index n_1 with top cladding layer, material 2, with refractive index n_2, and bottom cladding layer, material 3, with refractive index n_3. The refractive index n_1 must be lower the refractive indices n_2 and n_3.

The TM reflection coefficient is given by

$$r_{\mathrm{TM}} = \frac{n_2 \cos\theta_1 - n_1 \cos\theta_2}{n_2 \cos\theta_1 + n_1 \cos\theta_2} \tag{2.7}$$

and by substituting Snell's law, this becomes

$$r_{\mathrm{TM}} = \frac{n_2^2 \cos\theta_1 - n_1 \sqrt{n_2^2 - n_1^2 \sin\theta_1{}^2}}{n_2^2 \cos\theta_1 + n_1 \sqrt{n_2^2 - n_1^2 \sin\theta_1{}^2}}. \tag{2.8}$$

For angles of incidence greater than the critical angle, r is complex and for both the TE and TM cases takes the form [3, 57]

$$r = \frac{a - ib}{a + ib} = \frac{\cos\alpha - i\sin\alpha}{\cos\alpha + i\sin\alpha} = \frac{e^{-i\alpha}}{e^{i\alpha}} = e^{-i2\alpha} = e^{i\phi}. \tag{2.9}$$

where a is the real part and b is the imaginary part of complex numbers with the argument (polar angle) $\pm\alpha$. The reflection coefficient is expressed as an exponential function where $\phi = -2\alpha$ represents the phase shift of E_r relative to E_i. Considering that

$$\tan\alpha = \frac{\sin\alpha}{\cos\alpha} = \frac{b}{a}, \tag{2.10}$$

the phase change upon reflection of the TE and TM fields can be expressed as

$$\phi_{\mathrm{TE}} = 2\tan^{-1} \frac{\sqrt{\sin\theta_1{}^2 - \left(\frac{n_1}{n_2}\right)^2}}{\cos\theta_1} \tag{2.11}$$

and

$$\phi_{\mathrm{TM}} = 2\tan^{-1}\frac{\sqrt{\frac{n_1^2}{n_2^2}\sin\theta_1{}^2 - 1}}{\frac{n_2}{n_1}\cos\theta_1}. \tag{2.12}$$

Up until this point the light has been considered simply as a ray indicating the direction of propagation. However, this light is comprised of electric E and magnetic H fields that can be represented by

$$E = E_0 \exp\left[i(kx \pm \omega t)\right] \tag{2.13}$$

and

$$H = H_0 \exp\left[i(kx \pm \omega t)\right] \tag{2.14}$$

respectively. Here, x is the direction of propagation, and the phase of the wave is given by, $\phi = kx \pm \omega t$. The phase of the wave is a function of both time and distance. The derivative of phase with respect to time is

$$\left|\frac{\partial \phi}{\partial t}\right| = \omega = 2\pi\nu \tag{2.15}$$

where ω is the angular frequency (rad s^{-1}) and ν is the frequency (Hz) of the light wave. The derivative of phase with respect to the direction of propagation is

$$\frac{\partial \phi}{\partial x} = k \tag{2.16}$$

where k is the wave-vector [3]. This is also known as the propagation constant and is defined as

$$k = \frac{2\pi}{\lambda}. \tag{2.17}$$

If the propagation constant of a free space light wave is designated as k_0, then the propagation constant for light travelling in a medium is given by

$$k = n_1 k_0 \tag{2.18}$$

and so the free space propagation constant is

$$k_0 = \frac{2\pi}{\lambda_0}. \tag{2.19}$$

The orthogonal components of the wave-vector can be found simply using trigonometry, see Figure 2.3, to be

$$h = n_1 k_0 \cos\theta_1. \tag{2.20}$$

and

$$\beta = n_1 k_0 \sin\theta_1 = n_{\mathrm{eff}} k_0 \tag{2.21}$$

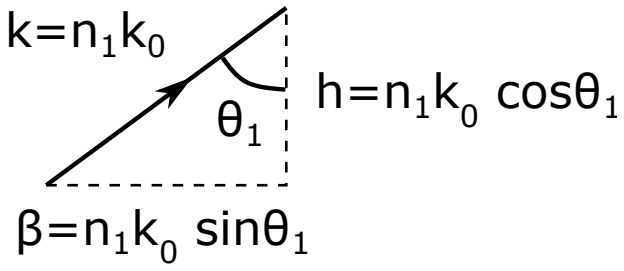

Figure 2.3: Orthogonal components, h and β, of the wave-vector, k, can be found using trigonometry.

where

$$n_{\text{eff}} = n_1 \sin\theta_1 = \frac{\beta}{k_0} \tag{2.22}$$

is the effective index of the waveguide. This parameter is often a very useful waveguide characteristic to consider.

The wave component travelling in the y direction, see Figure 2.2, reflects from each interface and forms a standing wave under certain conditions. The total phase shift of the wave component in the y direction upon completing one round trip in a waveguide of height $2b$, is given as

$$\phi_{\text{RT}} = 4k_0 n_1 b\cos\theta_1 - \phi_t - \phi_b = 4hb - \phi_t - \phi_b \tag{2.23}$$

where ϕ_t and ϕ_b are the phase shifts resulting from the reflections from the top and bottom interfaces respectively [3]. The standing wave condition is satisfied when the total phase shift upon completing the round is equal to an integer multiple of 2π, i.e.,

$$4hb + 2l\pi = \phi_t + \phi_b \tag{2.24}$$

where l is an integer. Because of this, there are discrete angles θ_i for which this condition can be satisfied. These solutions are the modes of propagation and the integer l is the mode number. For a TE mode, the phase change upon reflection, $\phi_{t,b}$, is given by Equation 2.11 and so this becomes

$$2hb + l\pi = \arctan\left(\frac{\sqrt{\sin^2\theta_1 - \left(\frac{n_2}{n_1}\right)^2}}{\cos\theta_1}\right) + \arctan\left(\frac{\sqrt{\sin^2\theta_1 - \left(\frac{n_3}{n_1}\right)^2}}{\cos\theta_1}\right) \tag{2.25}$$

which is a transcendental equation known as the eigenvalue equation.

2.2 Electromagnetic Theory

The behaviour of light waves are described by the electromagnetic model underpinned by the Maxwell equations which relate the electric E ($\mathrm{V\,m^{-1}}$) and magnetic H fields ($\mathrm{A\,m^{-1}}$) with the charge ($\mathrm{C\,m^{-2}}$) and current densities ($\mathrm{A\,m^{-2}}$), ρ and $\vec{J}$ respectively. These can be expressed as

$$\vec{\nabla} \cdot \vec{D} = \rho \tag{2.26}$$

$$\vec{\nabla} \cdot \vec{B} = 0 \tag{2.27}$$

$$\vec{\nabla} \times \vec{E} = -\frac{\partial B}{\partial t} \tag{2.28}$$

$$\vec{\nabla} \times \vec{H} = \vec{J} + \frac{\partial D}{\partial t} \tag{2.29}$$

where $\vec{D} = \varepsilon_m \vec{E}$ is the electric flux density, $\vec{B} = \mu_m \vec{H}$ is the magnetic flux density, and $\vec{J} = \sigma \vec{E}$ is the current density with ε_m, μ_m, and σ as the permittivity $\left(\mathrm{F\,m^{-1}}\right)$, permeability $\left(\mathrm{H\,m^{-1}}\right)$, and conductivity $\left(\Omega^{-1}\,\mathrm{m}\right)$ of the medium respectively [3]. The del operator ∇ is defined as

$$\nabla \equiv \left(\frac{\partial \vec{i}}{\partial x}, \frac{\partial \vec{j}}{\partial y}, \frac{\partial \vec{k}}{\partial z} \right). \tag{2.30}$$

Taking the curl of Equation 2.28 leads to

$$\nabla \times \nabla \times \vec{E} = -\frac{\partial}{\partial t} \left(\nabla \times \vec{B} \right), \tag{2.31}$$

by substituting the definition of magnetic flux density this becomes

$$\nabla \times \nabla \times \vec{E} = -\mu_m \frac{\partial}{\partial t} \left(\nabla \times \vec{H} \right) \tag{2.32}$$

into which $\nabla \times \vec{H}$, Equation 2.29, can be substituted to give

$$\nabla \times \nabla \times \vec{E} = -\mu_m \left[\frac{\partial \vec{J}}{\partial t} + \frac{\partial^2 \vec{D}}{\partial t^2} \right] \tag{2.33}$$

and upon substituting the definitions of electric flux and current densities, this becomes

$$\nabla \times \nabla \times \vec{E} = -\mu_m \left[\sigma \frac{\partial \vec{E}}{\partial t} + \varepsilon_m \frac{\partial^2 \vec{E}}{\partial t^2} \right]. \tag{2.34}$$

Now we have an expression of the spatio-temporal evolution of an electric field. This can be simplified by substituting the vector field identity

$$\nabla \times \nabla \times \vec{E} = \nabla \left(\nabla \cdot \vec{E} \right) - \nabla^2 \vec{E} \tag{2.35}$$

and by assuming that the resistivity and conductivity are equal to zero ($\rho = \sigma = 0$) and so $\nabla \cdot \vec{E} = 0$. This leaves

$$\begin{gathered} \nabla \cancelto{0}{\left(\nabla \cdot \vec{E} \right)} - \nabla^2 \vec{E} = -\mu_m \left[\cancelto{0}{\sigma \frac{\partial \vec{E}}{\partial t}} + \varepsilon_m \frac{\partial^2 \vec{E}}{\partial t^2} \right] \\ \nabla^2 \vec{E} = \mu_m \varepsilon_m \frac{\partial^2 \vec{E}}{\partial t^2} \end{gathered} \tag{2.36}$$

which is know as the electromagnetic wave equation. The velocity of the wave v is given by

$$v^2 = \frac{1}{\mu_m \varepsilon_m}. \tag{2.37}$$

The left hand side of the wave equation can be expressed in terms of its vector components as

$$\begin{aligned} \nabla^2 \vec{E} &= \frac{\partial^2 \vec{E}}{\partial x^2} + \frac{\partial^2 \vec{E}}{\partial y^2} + \frac{\partial^2 \vec{E}}{\partial z^2} \\ &= \left(\frac{\partial^2 E_x}{\partial x^2} + \frac{\partial^2 E_x}{\partial y^2} + \frac{\partial^2 E_x}{\partial z^2} \right) \vec{i} + \left(\frac{\partial^2 E_y}{\partial x^2} + \frac{\partial^2 E_y}{\partial y^2} + \frac{\partial^2 E_y}{\partial z^2} \right) \vec{j} + \left(\frac{\partial^2 E_z}{\partial x^2} + \frac{\partial^2 E_z}{\partial y^2} + \frac{\partial^2 E_z}{\partial z^2} \right) \vec{k}. \end{aligned} \tag{2.38}$$

However, this is a general solution which can describe a transverse electromagnetic (TEM) field propagating in any direction. For the case of a TE polarised wave oriented in the y direction propagating in the x direction this simplifies to

$$\frac{\partial^2 E_y}{\partial x^2} + \frac{\partial^2 E_y}{\partial z^2} = \mu_m \varepsilon_m \frac{\partial^2 \vec{E}_y}{\partial t^2} \tag{2.39}$$

which has the solution

$$E_y = E_y(z) e^{-i\beta x} e^{i\omega t}. \tag{2.40}$$

This describes the waves polarised in the y-direction propagating in the x-direction sinusoidally with time but does not describe the behaviour of the waves behaviour in the z-direction. To do this, the second derivative of Equation 2.40 with respect to time and the x-direction are found,

$$\frac{\partial^2 E_y}{\partial x^2} = \frac{\partial}{\partial x} \frac{\partial E_y}{\partial x} = -i\beta \frac{\partial E_y}{\partial x} = -\beta^2 E_y \tag{2.41}$$

$$\frac{\partial^2 E_y}{\partial t^2} = \frac{\partial}{\partial t}\frac{\partial E_y}{\partial t} = -i\omega\frac{\partial E_y}{\partial t} = -\omega^2 E_y, \tag{2.42}$$

and then substituted into Equation 2.39. This is then rearranged to give

$$\frac{\partial^2 E_y}{\partial z^2} = \left(\beta^2 - \omega^2 \mu_m \varepsilon_m\right) E_y \tag{2.43}$$

Considering the Equations 2.36, 2.37, and 2.1, this can be expressed as

$$\frac{\partial^2 E_y}{\partial z^2} = \left(\beta^2 - k_0^2 n_i^2 E_y\right) \tag{2.44}$$

where n_i has a subscript referring to the particular material that it corresponds to, i.e. $i = 1,2,3$ with reference to Figure 2.2. So there is a particular form of Equation 2.40 for each material. For a waveguide core of height $2b$, as in Section 2.1, with boundary conditions $-b \leq z \leq b$, the y component of the electric field in the core can be represented as

$$E_y(z) = E_1 e^{[-ihz]} \qquad \text{for} \quad -b \leq z \leq b, \tag{2.45}$$

in the top cladding as

$$E_y(z) = E_2 e^{[-p_2(z-b)]} \qquad \text{for} \quad z \geq b, \tag{2.46}$$

and in the bottom cladding as

$$E_y(z) = E_3 e^{[p_3(z+b)]} \qquad \text{for} \quad z \leq -b \tag{2.47}$$

where the propagation constant, h, and decay constants, p, are defined by [58–60]

$$h = \sqrt{k^2 n_1^2 - \beta^2} \tag{2.48}$$

$$p_2 = \sqrt{\beta^2 - k^2 n_2^2} \tag{2.49}$$

$$p_3 = \sqrt{\beta^2 - k^2 n_3^2}. \tag{2.50}$$

The boundary conditions require that E_y and $\frac{\partial E_y}{\partial z}$ are continuous, which is satisfied by these equations. This general solution is expressed as an exponential function. The even mode solutions take the form of cosine functions while the odd mode solutions take the form of sine functions. Upon inspection of Equations 2.46 and 2.47, it is clear the these solutions of the wave equation require the argument of the exponential function to be real and negative, taking the form of exponential decay known as the Beer-Lambert law, hence the definition of decay constants p_2 and p_3. However, the solution to the wave equation for the waveguide core (Equation 2.45) requires the argument of the exponential function to be imaginary and negative, taking the form of complex exponential function which can be decomposed into cosine and sine functions

by use of Euler's formula. This seems to contradict the ray optics model of waveguides because the fields propagate in the cladding to some extent, determined by their exponential decay, instead of being reflected at the material boundary. This decaying field is known as the evanescent field.

Considering the boundary conditions, the E_y fields given by Equations 2.45, 2.46, and 2.47 are equal at the boundaries $z = \pm b$. Therefore at $z = b$,

$$E_2 = E_1 \exp[-(ihb)], \tag{2.51}$$

where h is once again the propagation constant of the waveguide core. The fundamental mode is an even function and so is represented by the cosine function. In the case of the fundamental mode, Equation 2.51 can be rewritten as

$$E_2 = E_1 \cos(-hb + \phi). \tag{2.52}$$

Similarly, at $z = -b$

$$E_3 = E_1 \cos(hb + \phi) \tag{2.53}$$

Similarly, for the derivatives of Equations 2.45, 2.46, and 2.47, the boundary conditions dictate that

$$\left.\frac{\partial E_y}{\partial z}\right|_{|z|<|b|} = \left.\frac{\partial E_y}{\partial z}\right|_{z=b} = \left.\frac{\partial E_y}{\partial z}\right|_{z=-b}$$

and so this leads to

$$E_2 = \frac{h}{p_2} E_1 \sin(hb + \phi) \tag{2.54}$$

and

$$E_3 = \frac{h}{p_3} E_1 \sin(hb - \phi) \tag{2.55}$$

which means there are now two expressions for both E_2 and E_3. Equating these expressions gives

$$E_2 = E_1 \cos(hb + \phi) = \frac{h}{p_2} E_1 \sin(hb + \phi) \tag{2.56}$$

and

$$E_3 = E_1 \cos(hb + \phi) = \frac{h}{p_3} E_1 \sin(hb - \phi) \tag{2.57}$$

which can be rearranged to give

$$hb + \phi + l\pi = \arctan\left[\frac{p_2}{h}\right] \tag{2.58}$$

and

$$hb - \phi + l\pi = \arctan\left[\frac{p_3}{h}\right] \tag{2.59}$$

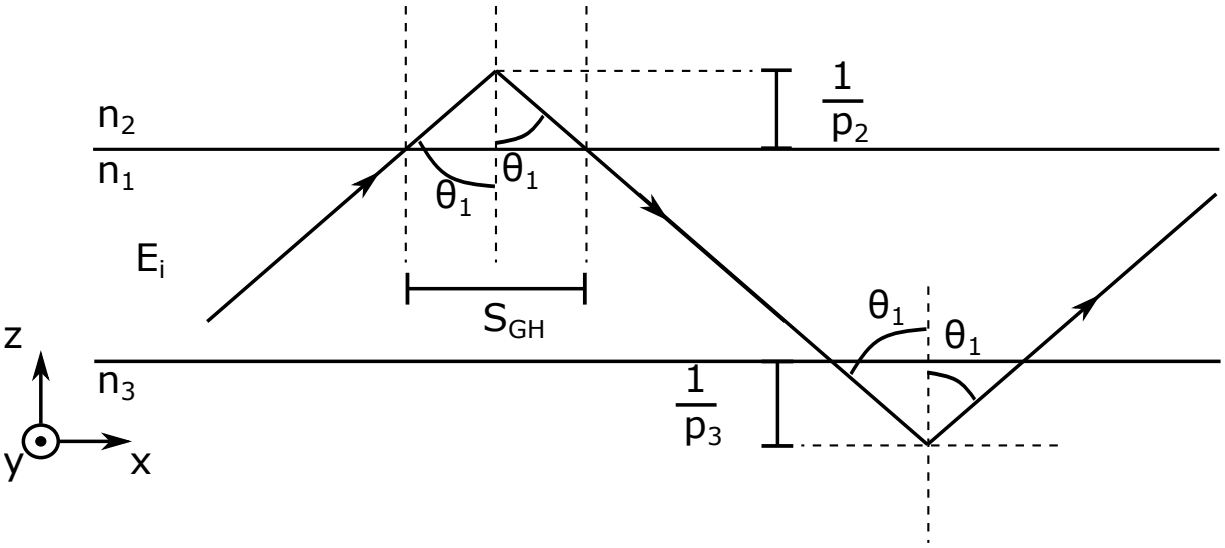

Figure 2.4: The point of reflection at the boundaries between material 1 and materials 2 and 3 appears to shift by a quantity $S_{2,3}^{\mathrm{GH}}$. The penetration depth is determined using the Beer-Lambert law and this allows the shift to be determined using trigonometry. The orthogonal propagation constants for the core, β and h, can then be substituted for $\tan\theta_1$.

respectively, where l is again an integer representing the mode number. Adding Equations 2.58 and 2.59 together gives

$$2hb + l\pi = \arctan\left[\frac{p_2}{h}\right] + \arctan\left[\frac{p_3}{h_1}\right] \tag{2.60}$$

where $l\pi$ is left instead of $2l\pi$ because the tangent function is periodic in π. This provides another form of the eigenvalue equation found in Equation 2.25.

The electromagnetic and ray optics approaches are used concurrently by considering the effect of the fields penetration depth upon the point of reflection of a ray. According to the Beer-Lambert law, the penetration depth of an electromagnetic field in a material is the inverse of its decay constant. This results in a lateral shift of the point of reflection know as the Goos-Hänchen shift. Simple trigonometry is used to determine the extent of this shift (see Figure 2.4)

$$S_{2,3}^{\mathrm{GH}} = \frac{2\tan\theta_1}{p_{2,3}} = \frac{2}{p_{2,3}}\frac{\beta}{h} \tag{2.61}$$

where subscripts, 2 and 3, correspond to the material in which the point of reflection occurs.

2.3 Coupled Mode Theory

The mode-coupling between pair of straight waveguides 1 and 2, see Figure 2.5, can be described by the mode interference between the even mode (the first order mode of the coupled system shown by the dotted line) and the odd mode (the second order mode of the coupled system

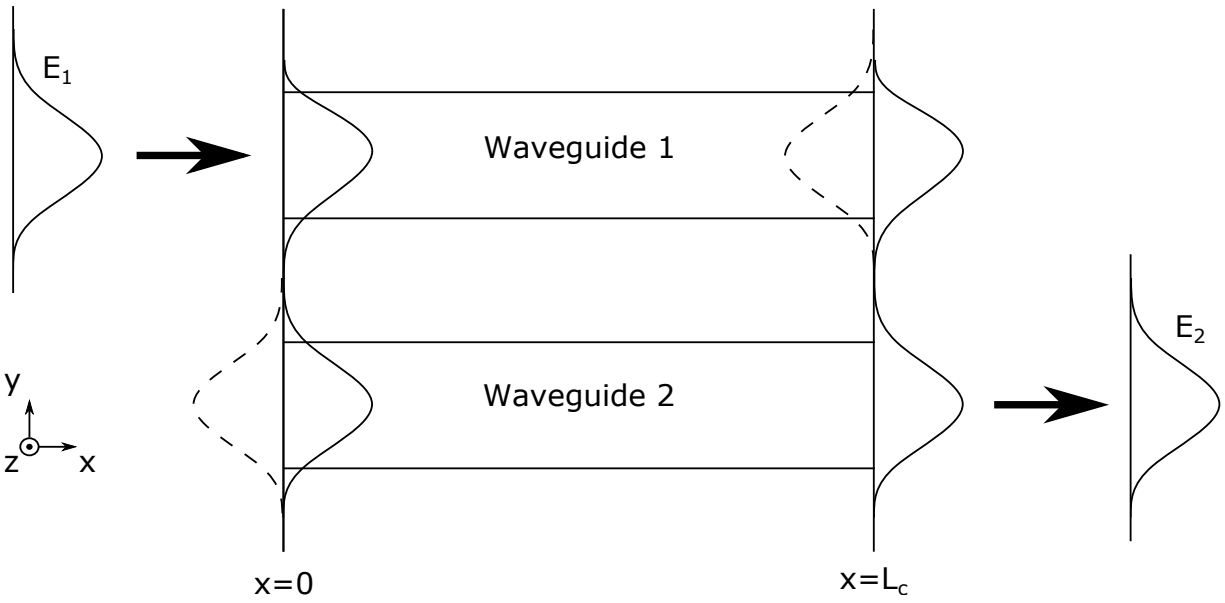

Figure 2.5: The coupled super-mode of two nearby and parallel waveguides. The even mode is represented by the solid line and the odd mode by the dashed line. As the odd mode falls out of phase with the even mode, light couples from the fundamental mode of waveguide 1 to the fundamental mode of waveguide 2. At the cross-over length, L_c, the light has completely coupled from the waveguide 1 TE_0 mode to the waveguide 2 TE_0 mode.

shown by the solid line) [58, 61]. This is represented by

$$E_y(x,z) = E_e(z)\exp(-i\beta_e x) + E_o(z)\exp(-i\beta_o x). \tag{2.62}$$

Light inject into waveguide 1 excites the even and odd coupled modes. As light couples from waveguide 1 to waveguide 2 this can be considered as a phase shift of the odd mode expressed as [58]

$$|E_y(x,z)| = |E_e(z) + E_o(z)\exp[i(\beta_e - \beta_o)x]| \tag{2.63}$$

where the phase shift of the odd mode is given by $\beta_e - \beta_o$. By definition, complete crossover occurs for $x = \frac{\pi}{(\beta_e - \beta_o)}$ [58]. The coupling coefficient between these coupled modes is given by [58, 59]

$$\kappa_{\|} = \frac{\pi}{2L_c} = \frac{\beta_e - \beta_o}{2} \approx \frac{h}{\beta}|h_{e,o} - h| \tag{2.64}$$

where L_c is the crossover length, h is the perpendicular propagation constant and β is the parallel propagation constant of an isolated waveguide, and $h_{e,o}$ is the perpendicular propagation constant of the even mode in the case of light coupling from the even mode into the odd mode or the propagation constant of odd mode in the case of light coupling into the even mode.

Another way to express the coupling coefficient of two coupled waveguides to use the Marcatili method [58, 62] and subsequent improvements that have been made to this approach [61].

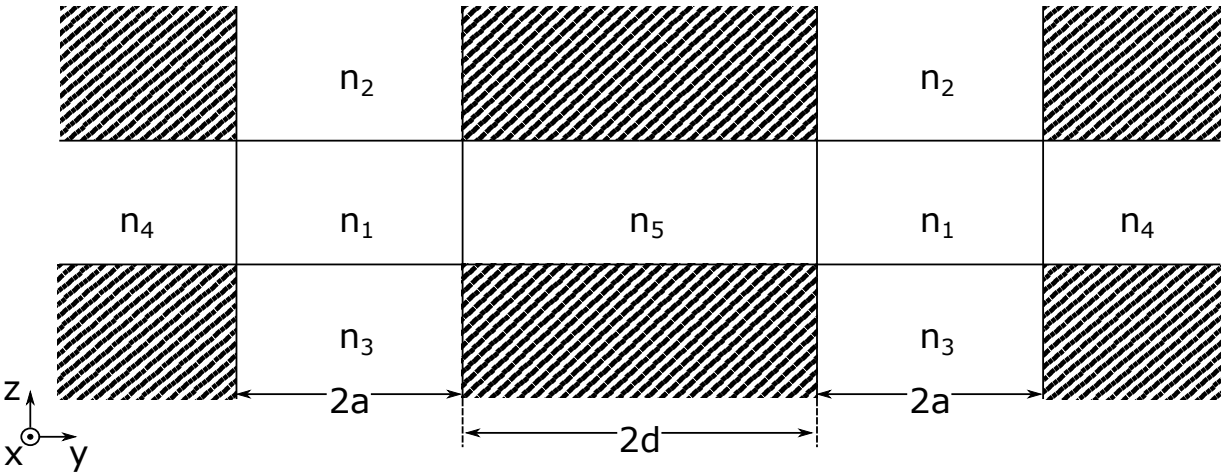

Figure 2.6: In the Marcatili method, a coupled pair of three dimensional rectangular waveguides with refractive index n_1 are represented as two orthogonal slab modes. The y oriented slab mode has width 2d and the z oriented slab mode

A pair of rectangular waveguides are each approximated as a two overlaid slab waveguides, one oriented in the y-direction and the other in the z-direction. The assumption made when using this approach is that any electromagnetic fields in the shaded area can be neglected. Referring to the waveguide geometry in Figure 2.6, for the E_z^{ml} mode (the electric field is oriented in the z-direction and m, l are the y, z mode numbers), the eigenvalue equation for the variation in the y-direction is [61, 62]

$$2ha = m\pi - \arctan\left(\frac{h}{p_4}\right) - \arctan\left(\frac{h}{p_5}\tanh\left(p_5 d + \gamma\right)\right) \tag{2.65}$$

where $\gamma = \frac{i\pi}{2}$ for the even mode and $\gamma = 0$ for the odd mode. For the E_z^{ml} mode, reflection from the waveguide sidewall at $y = \pm a$ is "TE-like" because the electric field is parallel with the sidewalls. For the E_y^{ml} mode, reflection from the sidewalls is "TM-like" because the electric field is no longer parallel with sidewalls but instead with the top and bottom of the waveguide and the H_z^{ml} mode is now parallel with the sidewalls. The resulting eigenvalue equation for the E_y^{ml} in the y direction is [61, 62]

$$2ha = m\pi - \arctan\left[\left(\frac{n_4}{n_1}\right)^2 \frac{h}{p_4}\right] - \arctan\left[\left(\frac{n_5}{n_1}\right)^2 \frac{h}{p_5}\tanh(p_5 d + \gamma)\right] \tag{2.66}$$

where $\gamma = \frac{i\pi}{2}$ for the even mode and $\gamma = 0$ for the odd mode. To solve this equation to first order in

$$u = \exp\left(-2p_5 d\right), \tag{2.67}$$

h can be expended to give

$$h = h(u=0) + \left.\frac{dh}{du}\right|_{u=0} u = h_0 + h'u \tag{2.68}$$

where h_0 is introduced for the time being as the perpendicular propagation constant of an isolated waveguide, $u = 0$ indicates an isolated waveguide. Lagrange notation is also introduced to represent a derivative with respect to u, this will make the following equations less unwieldy. To find h', the derivative of Equation 2.66 with respect to u is taken and evaluated at $u = 0$ [61].

$$\begin{aligned} 2h'a &= -\frac{\left[\left(\frac{n_4}{n_1}\right)^2 \frac{h}{p_4}\right]'}{1+\left(\frac{n_4}{n_1}\right)^4\left(\frac{h_0}{p_{4,0}}\right)^2} - \frac{\left[\left(\frac{n_5}{n_1}\right)^2 \frac{h}{p_5}\right]' \pm 2\left(\frac{n_5}{n_1}\right)^2 \frac{h_0}{p_{5,0}}}{1+\left(\frac{n_5}{n_1}\right)^4\left(\frac{h_0}{p_{5,0}}\right)^2} \\ &= -\left(\frac{n_4}{n_1}\right)^2 \frac{1}{1+\left(\frac{n_4}{n_1}\right)^4\left(\frac{h_0}{p_{4,0}}\right)^2}\left(\frac{h}{p_4}\right)' - \left(\frac{n_5}{n_1}\right)^2 \frac{1}{1+\left(\frac{n_5}{n_1}\right)^4\left(\frac{h_0}{p_{5,0}}\right)^2}\left[\left(\frac{h}{p_4}\right)' \pm 2\frac{h_0}{p_{5,0}}\right] \end{aligned} \tag{2.69}$$

Considering Equations 2.48, 2.49, and 2.50, the following relationship is found

$$h^2 + p^2 = \left(n_1^2 - n_i^2\right) k_0^2 \qquad \text{for} \quad i = 4,5 \quad \forall u \tag{2.70}$$

from which it can be found that

$$p_i' = -\frac{h}{p_i} h' \qquad \text{for} \quad i = 4,5 \quad \forall u. \tag{2.71}$$

This allows Equation 2.69 to be rewritten using the quotient rule as

$$\begin{aligned} 2h'a = &-\left(\frac{n_4}{n_1}\right)^2 \frac{1}{1+\left(\frac{n_4}{n_1}\right)^4\left(\frac{h_0}{p_{4,0}}\right)^2} \frac{p_{4,0}h' - h_0 p_4'}{p_{4,0}^2} \\ &-\left(\frac{n_5}{n_1}\right)^2 \frac{1}{1+\left(\frac{n_5}{n_1}\right)^4\left(\frac{h_0}{p_{5,0}}\right)^2}\left(\frac{p_{4,0}h' - h_0 p_4'}{p_{4,0}^2} \pm 2\frac{h_0}{p_{5,0}}\right) \end{aligned} \tag{2.72}$$

which can then be solved for h' using Equation 2.71 to give

$$\begin{aligned} h' = &\mp \frac{h_0 p_{5,0}}{a}\left(\frac{n_1}{n_5}\right)^2 \frac{1}{h_0^2 + \left(\frac{n_1}{n_5}\right)^4 p_{5,0}^2} \\ &\times \left[1 + \frac{1}{2p_{4,0}a}\left(\frac{n_1}{n_4}\right)^2 \frac{h_0^2 + p_{4,0}^2}{h_0^2 + \left(\frac{n_1}{n_4}\right)^4 p_{4,0}^2} + \frac{1}{2p_{5,0}a}\left(\frac{n_1}{n_5}\right)^2 \frac{h_0^2 + p_{5,0}^2}{h_0^2 + \left(\frac{n_1}{n_5}\right)^4 p_{5,0}^2}\right]^{-1} \end{aligned} \tag{2.73}$$

for the even (-) and odd modes (+). All the propagation constants in this equation have a subscript 0 to indicate they are for an isolated waveguide, henceforth this will be assumed and the subscripts will be neglected. Considering Equation 2.64 to first order in $\exp(-2p_5 d)$, the coupling coefficient for a pair of parallel waveguides is found to be

$$\begin{aligned}\kappa_{\parallel} \approx & \frac{h}{\beta}|h_{e,o}-h| = \frac{h}{\beta}|(h+h'\exp(-2p_5 d))-h| \\ = & \mp \frac{h^2 p_5}{a\beta}\left(\frac{n_1}{n_5}\right)^2 \frac{\exp(-2p_5 d)}{h^2+\left(\frac{n_1}{n_5}\right)^4 p_5^2} \\ & \times \left[1+\frac{1}{2p_4 a}\left(\frac{n_1}{n_4}\right)^2 \frac{h^2+p_4^2}{h^2+\left(\frac{n_1}{n_4}\right)^4 p_4^2}+\frac{1}{2p_5 a}\left(\frac{n_1}{n_5}\right)^2 \frac{h^2+p_5^2}{h^2+\left(\frac{n_1}{n_5}\right)^4 p_5^2}\right]^{-1}\end{aligned} \tag{2.74}$$

for an E_y^{ml} TE mode. The coupling coefficient for an E_z^{ml} TE mode would be derived from Equation 2.65 instead of Equation 2.66 and the result would be the same as Equation 2.74 but without the refractive index terms resulting in a simpler expression. This is one of the many solutions for the coupling coefficient between two straight and a parallel waveguides found either by the overlap integral method [58, 59, 63, 64], by calculation from the propagation of the even and odd coupled modes of a waveguide pair [61, 62], or even by a ray optics approach [65]. A common feature in these solutions is the exponential decay as a function of the gap spacing, $\exp(-2p_5 d)$, which is crucial for applying this to the particular case wherein the second waveguide is a completely circular micro-ring.

Following the approach outlined in [59, 64], the coupling between a straight bus waveguide and a circular ring resonator can be given by integrating the coupling as a function of waveguide separation weighted by the phase mismatch of those two separated sections of waveguide.

$$\kappa = \int_{-\infty}^{\infty} \kappa_{\parallel}[s(x)]\exp(-i\Delta\beta x)dx \tag{2.75}$$

where $s(x)$ is the separation between a straight bus waveguide and a circular micro-ring, and $\Delta\beta$ is the difference between the propagation constants of the coupled modes. The separation between a bus waveguide and a micro-ring resonator of radius r is given the separation at the closest point, $s(x=0)=2d$, and the additional separation caused by the curve of the micro-ring for $x \neq 0$. [59, 64]

$$s(x) = 2d + \left(r - \sqrt{r^2 - x^2}\right) \simeq 2d + \frac{x^2}{2r}. \tag{2.76}$$

Substituting this into the exponential dependence of the coupling coefficient gives

$$\kappa_{\parallel} \propto \exp(-p_5 s) = \exp(-2p_5 d)\exp\left(\frac{-p_5 x^2}{2r}\right) \tag{2.77}$$

and this means that the coupling coefficient as a function of x is now given by

$$\kappa = \kappa_{\|}[s(x=0)] \int_{-\infty}^{\infty} \exp\left(\frac{-p_5 x^2}{2r}\right) \exp\left(-i\Delta\beta x\right) dx. \tag{2.78}$$

The phase mismatch, $\Delta\beta = \beta_1 - \beta_2'(x)$, is the given by the difference between the propagation constants of the bus waveguide propagation constant, β_1, and the parallel component of the micro-ring propagation constant, $\beta_2'(x)$. The parallel component of micro-ring propagation constant is given by [59]

$$\beta_2'(x) = \cos(\arcsin\theta) \cdot \beta_2 \simeq \left(1 - \frac{x^2}{2r^2}\right)\beta_2 \tag{2.79}$$

and so this allows Equation 2.78 to be re-written to include the effect of the phase mismatch from the curved waveguide of the micro-ring

$$\kappa = \kappa_{\|}[s(x=0)] \int_{-\infty}^{\infty} \exp\left[\frac{-p_5 x^2}{2r} - i\left(\beta_1 x - \beta_2 x + \frac{x^3}{2r^2}\beta_2\right)\right] dx. \tag{2.80}$$

This coupling coefficient between two parallel waveguides is taken as $\kappa_{\|}$ from Equation 2.64 and $\beta_{1,2}$ is taken to be the even and odd coupled modes, $\beta_{e,o}$, of a coupled pair of parallel waveguides. Recalling that $p_5 = \sqrt{\beta^2 - n_5^2 k^2}$, the final expression is found for the coupling coefficient from a bus waveguide to a micro-ring resonator, expressed in terms of the propagation constants of an isolated waveguide and the even and odd coupled modes.

$$\kappa = \frac{\beta_e - \beta_o}{2} \int_{-\infty}^{\infty} \exp\left[\frac{-\sqrt{\beta^2 - n_5^2 k^2}}{2r} x^2 - i\left(\beta_e x - \beta_o x + \frac{x^3}{2r^2}\beta_o\right)\right] dx \tag{2.81}$$

This solution maintains generality by virtue of the exponential form. Even modes such as the fundamental TE mode can be presented in the cosine form by

$$\kappa = \frac{\beta_e - \beta_o}{2} \int_{-\infty}^{\infty} \exp\left(\frac{-\sqrt{\beta^2 - n_5^2 k^2}}{2r} x^2\right) \cos\left(\beta_e x - \beta_o x + \frac{x^3}{2r^2}\beta_o\right) dx. \tag{2.82}$$

2.4 Scattering Loss

There has been extensive work conducted to derive an analytical model of waveguide scattering loss due to surface roughness [66–70]. In that work it has been shown that the radiation loss of a planar waveguide such as is shown in Figure 2.7, can be expressed in the form

$$\alpha = E_{\mathrm{TE0}}^2(a)(n_1^2 - n_2^2)^2 \frac{k_0^3}{4\pi n_1} \int_0^{\pi} \tilde{R}(\beta - n_2 k_0 \cos\theta) d\theta \tag{2.83}$$

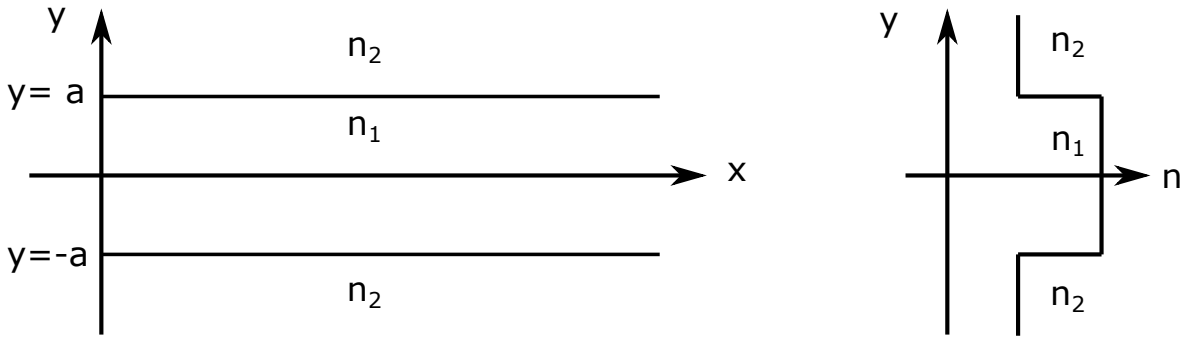

Figure 2.7: The geometry and index profile of a simple two-dimensional waveguide used to derive a model for scattering loss. The waveguide core has width of $2a$ with material boundaries at $y = a$ and $y = -a$.

where $E^2_{\mathrm{TE}0}(a)$ is the normalised power of light propagating in the TE_0 mode between the material boundaries at $y = a$ and $y = -a$ such that $\int_{-\infty}^{\infty} E(y)\, dy = 1$, $\tilde{R}(\beta - n_2 k_0 \cos\theta)$ is the spectral density function describing the roughness of the waveguide walls, and $\theta_s = \arccos\frac{\beta}{n_2 k_0}$ is the scattering angle between the wave-vector of light propagating in the cladding and its x-component, β [66–68, 70]. The spectral density function can be expressed in terms of an auto-correlation function by application of the Wiener-Khinchin theorem [71, 72],

$$\tilde{R}(\Omega) = \int_{-\infty}^{\infty} R(u) e^{i\Omega u}\, du \tag{2.84}$$

where $R(u)$ is the auto-correlation function of the roughness function $f(x)$ defined by the correlation length, L_c, and mean square deviation, σ^2, such that

$$R(0) = \sigma^2. \tag{2.85}$$

Auto-correlation functions of a Gaussian and exponential form are commonly used [66, 68] to describe the surface roughness. The Gaussian form is given by

$$R(u) = \sigma^2 e^{-\frac{u^2}{L_c^2}} \tag{2.86}$$

and the exponential form is given by

$$R(u) = \sigma^2 e^{-\frac{|u|}{L_c}}. \tag{2.87}$$

However, it has been shown [68, 70] that sidewall roughness of waveguide features in etch masks written by electron beam (and by laser) can be best described by an exponential auto-correlation function. Lorentzian and Gaussian distributions were fit to the spectral density function and the Lorentzian provided the better fit and so this means that the exponential form of the auto-correlation function provides the better model of the surface roughness [66]. The integral

from Equation 2.83 is now solved using the exponential form [66] (this is detailed in Appendix A).

$$\begin{aligned} S &= \int_0^{\pi} \tilde{R}(\beta - n_2 k_0 \cos\theta) d\theta \\ &= \sqrt{2}\sigma^2 L_c \pi \frac{\left[\left\{4\beta^2 L_c^2 + \left[1 - L_c^2(\beta^2 - n_2^2 k_0^2)\right]^2\right\}^{\frac{1}{2}} + 1 - L_c^2(\beta^2 - n_2^2 k_0^2)\right]^{\frac{1}{2}}}{\left\{4\beta^2 L_c^2 + \left[1 - L_c^2(\beta^2 - n_2^2 k_0^2)\right]^2\right\}^{\frac{1}{2}}} \end{aligned} \tag{2.88}$$

Equation 2.83 was deemed by the original authors [66] to provide insufficient insight for the waveguide designer and so an alternate form was sought after, one which could be expressed in terms over which the designer has control such as n_1, n_2, a, k_0, σ, and L_c. Normalised waveguide parameters U, V and W are defined in terms of parameters determined by the waveguide geometry [66, 68], V in particular is known as the normalised frequency [58, 66, 73].

$$U = a\sqrt{n_1^2 k_0^2 - \beta^2} \tag{2.89}$$

$$V = k_0 a\sqrt{n_1^2 - n_2^2} \tag{2.90}$$

$$W = a\sqrt{\beta^2 - n_2^2 k_0^2} \tag{2.91}$$

Dimensionless parameters are also introduced to simplify Equation 2.83 and express it in a form where the function $g(V)$ describes the behaviour due to the waveguide geometry and $f(\chi, \gamma)$ describes the integral over the spectral density function [66]. These dimensionless parameters are the index contrast

$$\Delta = \frac{n_1^2 - n_2^2}{2n_1^2}, \tag{2.92}$$

the normalised correlation length

$$\chi = W\frac{L_c}{a} \tag{2.93}$$

and a parameter, η, which quantifies the confinement of the mode ($\eta \approx 1$ indicates high confinement while $\eta \gg 1$ indicates weak confinement),

$$\eta = \frac{n_2 V}{n_1 W\sqrt{\Delta}}. \tag{2.94}$$

These functions, $g(V)$ and $f(\chi, \eta)$, are given [66] by

$$g(V) = \frac{U^2 V^2}{1 + W} \tag{2.95}$$

and

$$f(\chi,\eta)=\frac{\chi\left\{\left[(1+\chi^2)^2+2\chi^2\eta^2\right]^{\frac{1}{2}}+1-\chi^2\right\}^{\frac{1}{2}}}{\left[(1+\chi^2)^2+2\chi^2\eta^2\right]^{\frac{1}{2}}}. \tag{2.96}$$

The fundamental TE mode can be represented in terms of the normalised frequency, V, from Equation 2.90,

$$E^2_{\mathrm{TE0}}(a)=\frac{2V(1-b)}{a\left[V+\frac{1}{\sqrt{b}}\right]} \tag{2.97}$$

where

$$b=\frac{\beta^2-n_2^2k_0^2}{\left(n_1^2-n_2^2\right)k_0^2} \tag{2.98}$$

is the normalised propagation constant [66].

Substituting Equations 2.88 and 2.97 into Equation 2.83 and rearranging this into terms of $g(V)$ and $f(\chi,\eta)$ gives a new expression for scattering loss due to surface roughness,

$$\alpha=\frac{\sigma^2}{\sqrt{2}k_0a^4n_1}g(V)f(\chi,\eta), \tag{2.99}$$

which is dependent only upon n_1, n_2, a, k_0, σ, and L_c as desired [66]. This complete form is known as the Lacey-Payne scattering model; this is generally accepted with the field [74, 75] and shows good agreement with experiment [76].

2.5 Summary

The theoretical framework laid out in this chapter provides a number key insights which have informed the design, simulation, and characterisation of micro-ring resonators. Ray optic and electromagnetic theory have been used concurrently to arrive at the eigenvalue equation of a waveguide as found in Equations 2.25 and 2.60. The understanding gained in the course of deriving the eigenvalue equations is put into practice in Chapter 3 in which software tools are used to find solutions to the electromagnetic wave equation (Equation 2.36) for the particular waveguide geometry and material properties of interest. The effective indices and therefore the waveguide propagation constants can be found in this way. From the eigenvalue equation of two nearby and parallel waveguides (Equations 2.66 and 2.65), an analytical solution has been found (Equations 2.81 and 2.82) for the coupling coefficient κ between a straight bus waveguide and a circular micro-ring resonator using coupled mode theory. This solution allows for the coupling coefficient of a circular micro-ring resonator to be calculated from the propagation constants of the even and odd coupled modes of a parallel pair of similar waveguides, the propagation constant a similar isolated waveguide, the top cladding refractive index, the operational wavelength,

and the radius of the micro-ring resonator. The scattering loss of a rectangular waveguide has been considered using the Lacey-Payne scattering model (Equation 2.99), this model has informed the design decision to try an reduce waveguide loss (and increase micro-ring Q factor) by increasing waveguide width in order to reduce the loss due to sidewall scattering.

Chapter 3

Waveguide Simulation

The waveguide platform of interest in this work consists of a silicon nitride waveguide core, a silicon dioxide bottom cladding, and in the case of buried waveguides, a silicon dioxide top cladding. A chip-scale atomic system probing the D2 transition of ^{87}Rb atoms at 780.241 nm requires photonics component compatible with this wavelength and so all simulation and subsequent characterisation is performed assuming an operational wavelength of ~ 780 nm. A good design procedure is presented in [35]. First it is suggested to perform a one dimensional calculation to determine the vertical modes supported by the layer stack. Once the thicknesses of the materials has been decided, two dimensional simulations can be performed to determine which modes are supported horizontally, usually single mode operation would be desired.

The width of the waveguides also determines the intensity of the light field interacting with the waveguide sidewalls and the polarisation state that can be supported (i.e. TE or TM). Scattering of light interacting with the etched sidewalls of a waveguide is expected to be the dominant loss mechanism in this work [66, 77, 78]. Scattering loss is investigated using the Lacey-Payne scattering model discussed in Section 2.4. The radiation loss due to scattering is found to be significantly reduced for wider silicon nitride waveguides and for buried waveguides with a silicon dioxide top cladding as opposed to ridge waveguides with no top cladding. Eigenmode expansion simulations also explained in this chapter and are used the determine the scattering matrix, and therefore the reflection and transmission coefficients, for long waveguide structures such as the inverse taper spot-size converter discussed in Chapter 8.

3.1 Finite Difference Eigenmode Solver

The Lumerical finite difference eigenmode (FDE) solver is used to solve the electromagnetic wave equation for a given set of boundary conditions and material properties. The FDE solver is the predominant simulation tool used to determine the appropriate waveguide geometry such that the desired modes are supported. There are inherent limitations imposed upon material thickness that are discussed in Chapter 5 but it is essential to find a bottom cladding thickness that reduces

coupling from the desired optical mode into the silicon substrate. This is of particular importance in this platform at 780 nm. One reason for this is that the refractive index of silicon is much higher than that of silicon nitride and the mode will couple into the silicon readily. Silicon is also strongly absorbing at 780 nm and thus light that is allowed to couple into the substrate will be absorbed [79]. The FDE solver is a fully-vectorial frequency domain mode solver [80]. This approach considers the following form of the wave equation for a TE mode,

$$\nabla^2 E_y + k^2 E_y = \beta^2 E_y, \tag{3.1}$$

and for a TM mode,

$$\nabla^2 E_z + k^2 E_z = \beta^2 E_z. \tag{3.2}$$

These are converted into the algebraic eigenvalue problems

$$\mathbf{A}_{\mathrm{TE}} \mathbf{E}_{\mathrm{TE}} = \beta_{\mathrm{TE}}^2 \mathbf{E}_{\mathrm{TE}} \tag{3.3}$$

and

$$\mathbf{A}_{\mathrm{TM}} \mathbf{E}_{\mathrm{TM}} = \beta_{\mathrm{TE}}^2 \mathbf{E}_{\mathrm{TM}} \tag{3.4}$$

respectively, where $\mathbf{A}_{\mathrm{TE,TM}}$ are real non-symmetric band matrices such that $\mathbf{A}_{\mathrm{TE}} \neq \mathbf{A}_{\mathrm{TM}}$, $\mathbf{E}_{\mathrm{TE,TM}}$ are the normalised eigenvectors for the field profiles $E_y(y,z)$ and $E_z(y,z)$, and $\beta_{\mathrm{TE,TM}}^2$ is the mode propagation eigenvalue of the corresponding mode [80, 81]. These sparse matrices $\mathbf{A}_{\mathrm{TE,TM}}$ can be efficiently stored and operated upon [80]. The user enters the wavelength of interest, the number of trial modes, and an effective index value close to that of the mode they are interested in. The mode solver converts the effective index into a propagation eigenvalue β^2 using Equation 2.22 and uses proprietary numerical routines to find solutions to the eigenvalue problems.

3.1.1 One Dimensional Simulation

The one dimensional FDE solver is used to solve the electromagnetic wave equation in the frequency domain for a line through a material stack. The unit step size is the length between points at which the equation is to be solved and must be chosen such that the simulation results converge i.e. the results do not change significantly by further decreasing the unit step size. The results from the 1D FDE solver for a silicon substrate, silicon dioxide bottom cladding, and silicon nitride core layer are shown in Figures 3.1 and 3.2. The intensity of the electric field propagating in the fundamental mode of the silicon nitride waveguide is plotted in each case both with and without a 1 µm thick silicon dioxide top cladding layer. For a 4 µm bottom cladding and 100 nm waveguide layer, there is significant interaction with the silicon substrate. This is reduced by 5 orders of magnitude with the addition of the top cladding because the mode is more confined to the waveguide layer. Substrate leakage can be reduced by using a thicker bottom cladding [77,78,82] but 4 µm is the upper limit of wet SiO_2 which can be grown using the

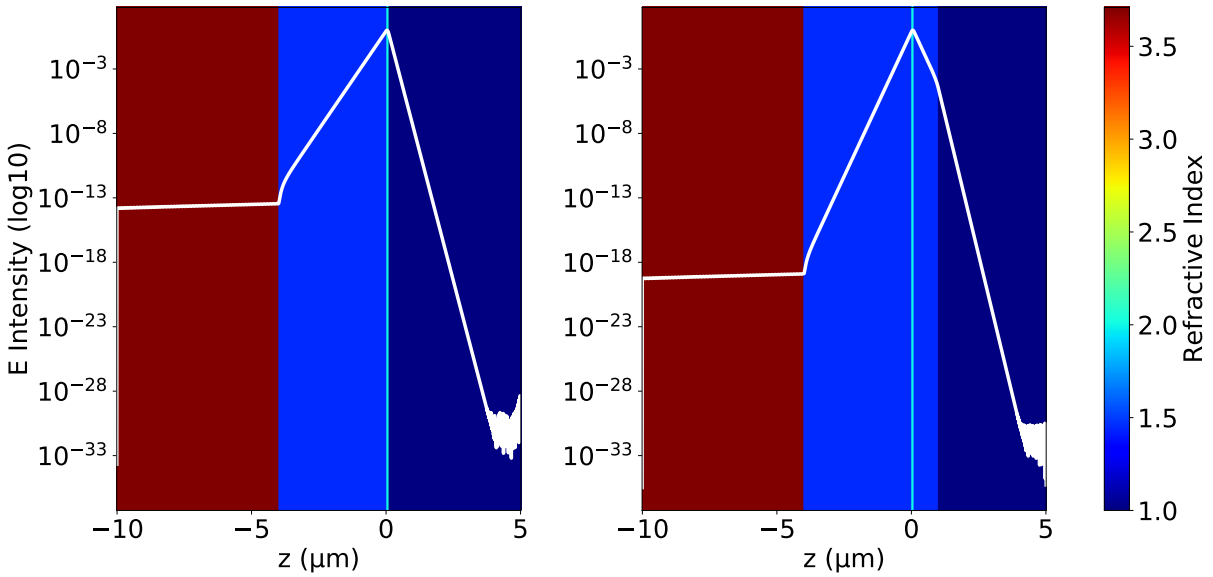

Figure 3.1: The refractive index of the material stack is represented by the colour-map and consists of a silicon substrate, a silicon dioxide bottom cladding 4 µm thick, a silicon nitride waveguide layer 100 nm thick, and on the left simply air above while on the right there is a top cladding layer of silicon dioxide 1 µm thick. The intensity of the electric field propagating in the fundamental TE mode of the silicon nitride waveguide is plotted for each.

facilities available within the James Watt Nanofabrication Centre at the University Of Glasgow, this is discussed further in Chapter 5.

For the same bottom cladding thickness, a silicon nitride waveguide layer 200 nm thick, results in greatly reduced interaction with the silicon substrate (see Figure 3.2). For the thickness present in this stack there is still some interaction with the silicon substrate but the addition of a top layer has comparatively little effect on the substrate leakage. This reduction in substrate leakage for the 200 nm thick silicon nitride will be referred to in Chapter 6 to explain low Q-factor values for micro-ring resonators fabricated with 100 nm thick silicon nitride cores.

The field attenuation of light with wavelength λ_0 propagating in a bulk material is expressed in dB m^{-1} and given by [83],

$$\alpha_{\text{att}}^{dB} = -20\log_{10}\left(\exp -\frac{2\pi k}{\lambda_0}\right) \tag{3.5}$$

where k is absorption of the material at the wavelength of interest and is expressed as the imaginary component of the complex refractive index given by

$$\underline{n} = n + ik. \tag{3.6}$$

In the case of a guided mode it is no longer the bulk material refractive index that needs to be considered but instead the effective index of the guided mode. If the complex refractive index of a bulk material is defined by Equation 3.6 then it follows from Equation 2.22 that the complex

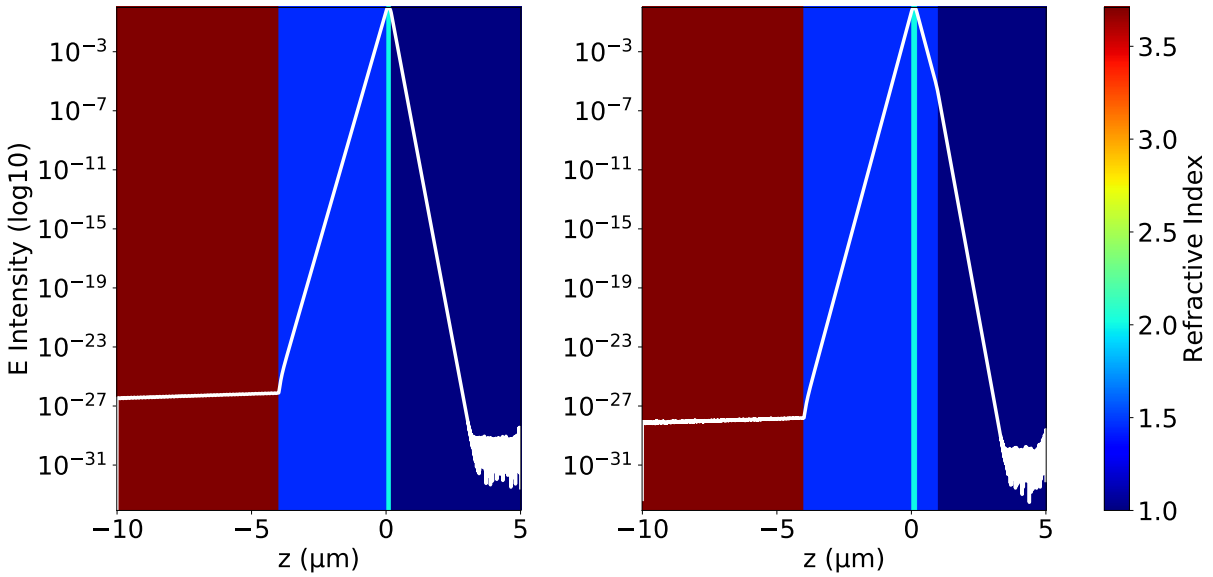

Figure 3.2: The refractive index of the material stack is again represented by the colour-map and consists of a silicon substrate, a silicon dioxide bottom cladding 4 μm thick, a silicon nitride waveguide layer 200 nm thick, and on the left simply air above while on the right there is a top cladding layer of silicon dioxide 1 μm thick. The intensity of the electric field propagating in the fundamental TE mode of the silicon nitride waveguide is plotted for each.

effective index of a guided mode is defined as

$$\underline{n}_{\text{eff}} = n_{\text{eff}} + ik_{\text{eff}} \tag{3.7}$$

and indeed this is the form of solutions found for the effective index of modes using Lumerical's FDE solver [83]. This allows the solver to determine the field modal loss using the formula

$$\alpha^{dB}_{\text{modal loss}} = -20\log_{10}\left(\exp\left[-\frac{2\pi k_{\text{eff}}}{\lambda_0}\right]\right) \tag{3.8}$$

similarly as before. The attenuation coefficients of silicon dioxide and silicon nitride are so low that they cannot be effectively measured by surface-normal measurements such as ellipsometry. Therefore the only material absorption that will be considered in modelling is that of silicon. This is not very useful when considering the total propagation loss of Si_3N_4 waveguides as the sidewall scattering is expected to dominate the modal loss but it is helpful in determining the loss of any slab mode that might form in the SiO_2 cladding as a result of improper laser coupling. The tolerance of the refractive index of the top cladding material must be considered to ensure that the top cladding is not of a sufficiently high index and thickness to support a strongly guided optical mode. This proved to be an issue when developing a process for the top cladding layer, see Section 5.2.3. The effect of having a 1 μm thick SiO_2 top cladding with a refractive index only 0.01 higher than that of the 4 μm SiO_2 bottom cladding is shown in Figure 3.3. The peak of the slab mode formed in the SiO_2 cladding is shown to drift towards the top cladding for higher

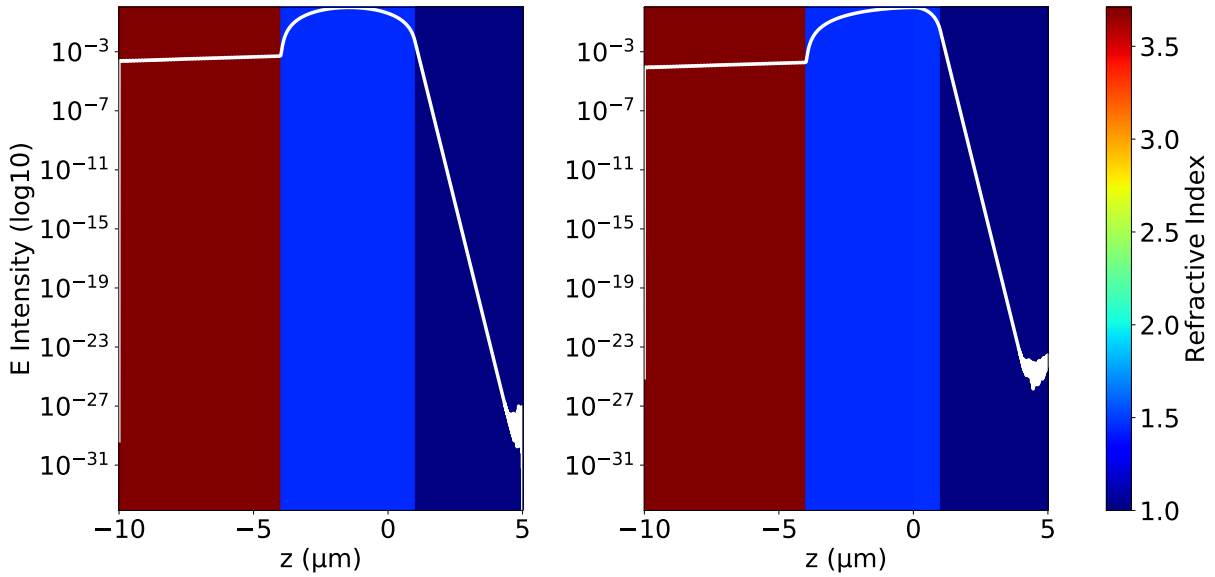

Figure 3.3: The refractive index of the material stack is again represented by the colour-map and consists of a silicon substrate, a silicon dioxide bottom cladding 4 µm thick and a top cladding layer of silicon dioxide 1 µm thick. On the left there is no difference in the refractive index of the top and bottom cladding whereas on the right the top cladding refractive index is 0.01 higher than the bottom cladding. The intensity of the electric field propagating in the fundamental TE mode of the silicon dioxide cladding is plotted for each.

top cladding index values and the end result of this is that during device characterisation (see Chapter 6) the slab mode obscures the fundamental mode propagating in the Si_3N_4 core.

The modal loss of each slab mode is found by the FDE solver using Equation 3.8 and for the perfectly matched indices the modal loss is 2000 dB m^{-1}, while for a top cladding with an index 0.01 higher than the bottom cladding the modal loss is 800 dB m^{-1}. This was investigated further by finding the simulated modal loss of the fundamental TE slab mode for various SiO_2 top cladding thicknesses (1, 1.5, and 2µm) as a function of the refractive index difference between the top and bottom cladding; this is shown is Figure 3.4. Thinner top cladding layers provide greater slab mode suppression but result in increased electric field intensity at the surface of the top cladding, which could increases losses if any absorbing material such as metal were placed on the top cladding surface in the vicinity of the waveguides. This would also increase scattering losses at the boundary between SiO_2 and air. A thicker top cladding is also desirable for certain fabrication processes outlined in Chapter 5 and so these requirements must be weighed and a compromise reached. A top cladding layer 1 µm thick was used for samples fabricated in this work.

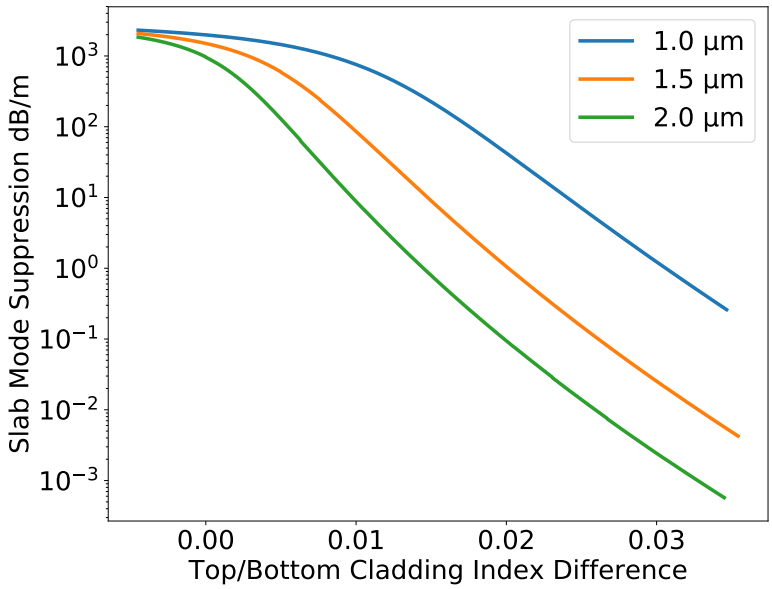

Figure 3.4: A bottom cladding thickness of 4 µm was chosen and for top cladding thicknesses of 1, 1.5, and 2 µm the modal loss of the fundamental slab mode was found as a function of the difference between top cladding and bottom refractive index ($n_{\text{top}} - n_{\text{bottom}}$).

3.1.2 Two Dimensional Simulation

Once it was determined that a 4 µm bottom cladding was sufficient to reduce the substrate leakage loss of a 200 nm thick waveguide core to the silicon substrate, the lower bound of the simulation region can be set such that the silicon substrate is no longer included. Two dimensional FDE simulations are used to determine the effect of waveguide width upon the parameters like the modal field distribution, mode number, effective index, modal loss, and polarisation (TE or TM) by again solving the electromagnetic wave equation but now on a 2D mesh grid. Figure 3.5 shows the electric field distribution found for a TE_0 mode propagating in a 1100 nm wide, 200 nm thick Si_3N_4 waveguide core on top of a 4 µm SiO_2 bottom cladding with a 1 µm top cladding, the refractive index distribution was passed through an edge detection filter to provide the outline of the refractive index boundaries. Similar to the 1D FDE solver the unit step size must be sufficient such that the simulation results are not dominated by artefacts imposed by the meshing grid used to define the spatial region. Optimisation of this is more crucial for the 2D solver because the time taken to run a simple simulation can be excessive if it has not been optimised. To make this easier, a region of higher density mesh can be placed surrounding the waveguide core providing sufficient spatial resolution surrounding the core while allowing for much lower but still sufficiently dense mesh at the outer extents of the mode of interest. Fundamental mode operation is desirable because it simplifies the resonance behaviour (see Chapter 4) and is necessary for many potential applications for waveguides.

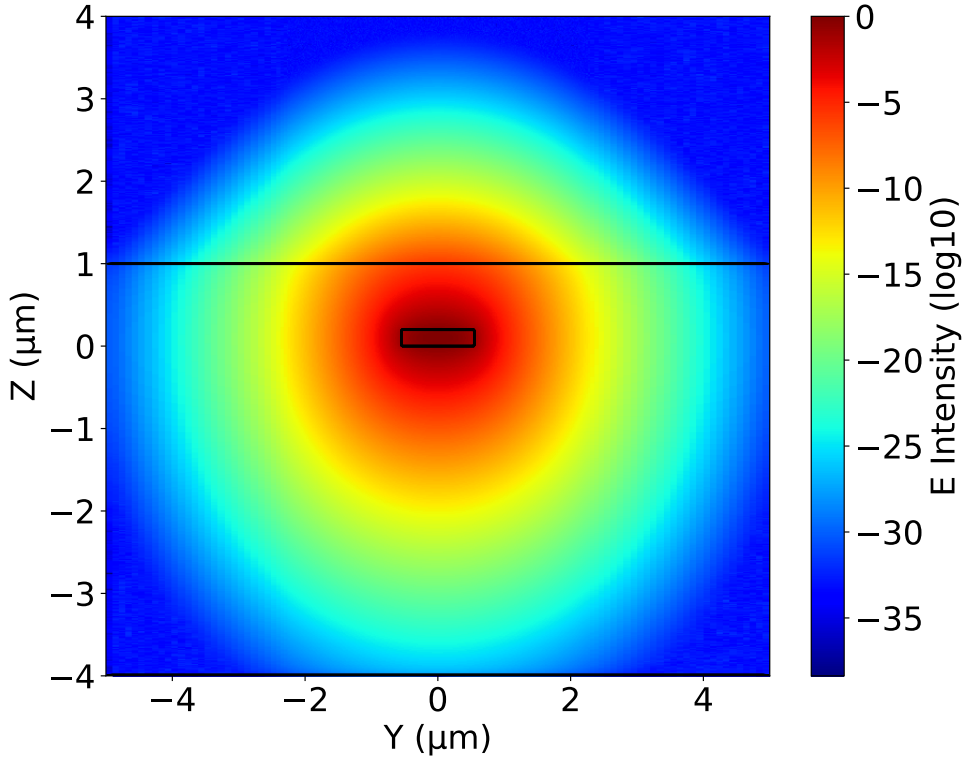

Figure 3.5: The base 10 logarithm of the electric field intensity distribution of a TE_0 mode plotted in a region of space 10 µm wide in the y-direction and 8 µm high in the z-direction. A 4 µm thick SiO_2 bottom cladding extends from $z = 0$ to $z = -4$ µm, a 1 µm thick top cladding extends from $z = 0$ to $z = 1$ µm, and a Si_3N_4 waveguide core extends from $z = 0$ to $z = 200$ nm and from $y = -550$ nm to $y = 550$ nm. Black lines indicate refractive index boundaries such as the outline of the Si_3N_4 waveguide core and the boundary between the SiO_2 top cladding and air.

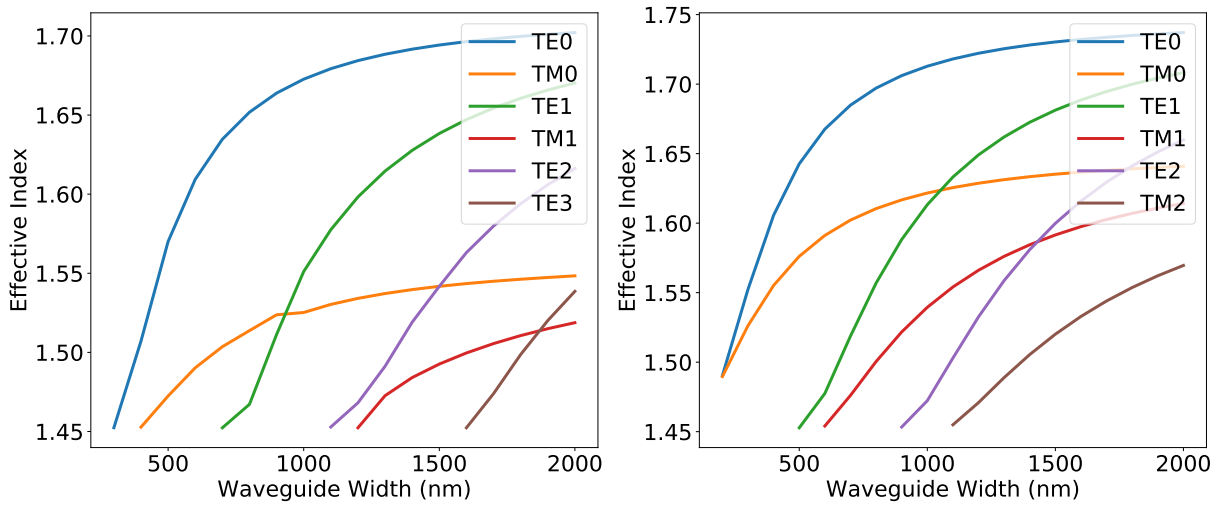

Figure 3.6: The simulated effective index of the transverse electric (TE) and transverse magnetic (TM) modes against the width of 200 nm Si_3N_4 thick waveguide cores with a 4 µm bottom cladding. Left: there is no top cladding; Right: there is a 1 µm SiO_2 top cladding.

Waveguide cross-sectional dimensions were modelled to determine the effective index of the guided modes for different waveguide widths both with and without the 1 µm SiO_2 top cladding, see Figure 3.6. A width of 500 nm was chosen initially to be certain that only the fundamental mode was supported. However, during the characterisation detailed in Chapter 6, there was no experimentally observed coupling into higher order modes for 200 nm thick waveguides of widths up to 1100 nm either with or without the top cladding.

Ring-resonators require the design of curved waveguides in order to form the ring. This is non-trivial because the optical path length on the outside of a curve is greater than it is on the inside of the curve and so in order for light in the outer cladding to remain in phase with the mode, this light must propagate at greater velocity than light in the cladding on the inside of the curve. The further out from the waveguide, the more exaggerated this difference in propagation velocity between the inner and outer cladding becomes. There exists an extent at which the light in the outer cladding would have to propagate faster than unguided light can travel in the cladding material, this is not possible and so this light is radiated away from the waveguide contributing to the total propagation loss of the waveguide [3]. For smaller bend radii, the mode distribution shifts more towards the outer wall of the waveguide resulting in greater radiative loss. Another potential source of loss is the coupling from curved waveguides to straight waveguides. The mode profile of a curved waveguide is decentered from the waveguide cross-section and so a continuous waveguide could result in significant modal mismatch at the interface between straight and curved waveguides sections and so it is common practice to impose a physical lateral offset of curved sections of waveguide in order to reduce the modal mismatch. The decentering of the mode also exacerbates the sidewall scattering as the resulting intensity at the sidewall is greater than it is for a similar straight waveguide. Radiation loss, the addition scat-

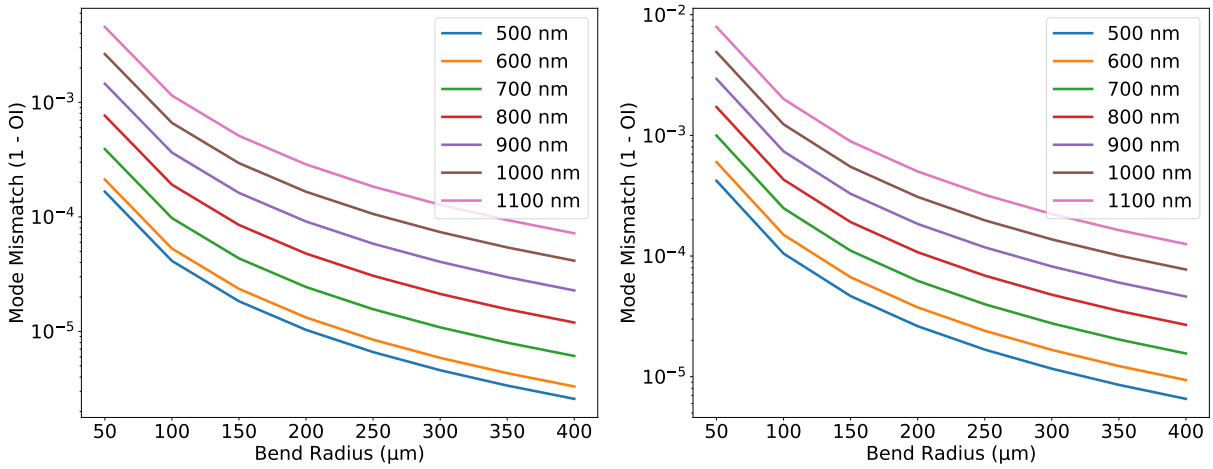

Figure 3.7: The mode mismatch (1 minus the overlap integral) of a straight and a curved waveguide of varying bend radii is found for the TE_0 mode in waveguides 200 nm thick, 500-1100 nm wide, and (in the case of the curved waveguide) curve radii of 50-400 µm. This is found without a top cladding (left) a with a 1 µm SiO_2 top cladding (right). By considering these results, a waveguide bend radius can be chosen such that the effects due to the waveguide bend are negligible.

tering loss due to a bend, and loss due to modal mismatch can be reduced by simply choosing a sufficiently large bend radius such that these factors are negligible. This is the approach taken in this work as the only limit imposed on the micro-ring radius was the main field size of the electron beam lithography tool which at 1.2 mm means that the micro-ring radius needs to be less than 600 µm to avoid stitching errors (this is discussed in Section 5.3.4).

To find a radius which is sufficiently large, the mode overlap integral of a curved and straight waveguide is found for series of bend radii. The mode overlap integral is given by

$$S = \frac{|\int E_{\text{straight}} E_{\text{curved}} dA|^2}{\int |E_{\text{straight}}|^2 dA \int |E_{\text{curved}}|^2 dA} \tag{3.9}$$

and can be found using the FDE solver [84]. The overlap integral of normalised electric fields should approach 1 as the radius is increased. To facilitate plotting on a logarithmic scale in Figure 3.7, the overlap integral is subtracted from 1 and the result is plotted against the bend radius for several waveguide cross-sections with varying widths and thickness fixed at 200 nm. This simulation has been performed for waveguides with no top cladding and for waveguides with a 1 µm SiO_2 top cladding. A radius of 300 µm was chosen for most of the micro-ring resonators produced in this work. At this radius the overlap integral with a straight waveguide is greater than 99.9 % and the waveguide bend can often safely be neglected. A simple circular design is used to avoid having to either increase the total path length on the resonator or use smaller bend radii for a racetrack style micro-ring resonator.

All-pass micro-ring resonators were designed and fabricated for a series of gap spacing and waveguide widths both with and without the top cladding. The gap spacing between the bus

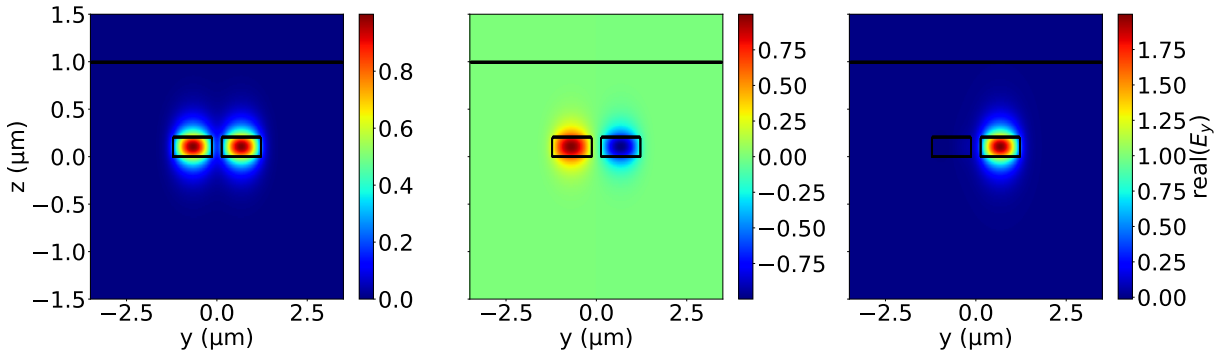

Figure 3.8: The E_y field amplitude in a coupled pair of Si_3N_4 waveguides each 200 nm thick and 1100 nm wide, separated by 250 nm, is shown for the even mode (left), the odd mode (middle), and the odd mode subtracted from the even mode (right). Black lines indicate refractive index boundaries such as the outline of the Si_3N_4 waveguide core and the boundary between the SiO_2 top cladding and air.

waveguide and the micro-ring resonator determines the power coupling into the micro-ring resonator. Coupled mode theory is used to determine the power coupling from the bus waveguide into the micro-ring resonator by finding the effective index, and therefore the propagation constant, of the even and odd coupled modes using the FDE solver, see Figure 3.8. This is simply a 2D case of the example given in Figure 2.5. For an array of input gap spacings, the even and odd mode effective indices are found (see Figure 3.9) for a pair of coupled waveguides with the same cross-section as the one shown in Figure 3.5. The propagation constants of the even and odd modes are input into Equation 2.81 to find the coupling coefficient. Using similar data for the different waveguide configurations that were designed, the coupling coefficient of any micro-ring resonator can be determined. The coupling coefficients for every micro-ring resonator with a 200 nm thick core that was designed and fabricated in this work are shown in Figure 3.10. Gap spacing values were chosen for each design iteration such that a similar span of Δn_{eff} values were tested for each waveguide cross section.

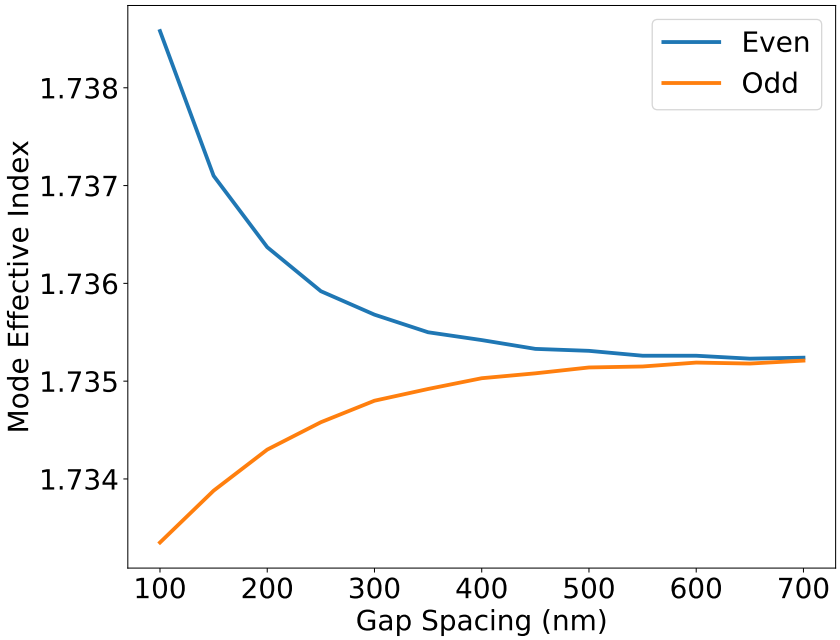

Figure 3.9: The simulated effective indices of the even and odd coupled TE_0 mode against the gap spacing. Each of the two adjacent parallel waveguides has a 4 µm thick SiO_2 bottom cladding, a 1 µm thick top cladding, and a 200 nm thick, 1100 nm wide Si_3N_4 waveguide core.

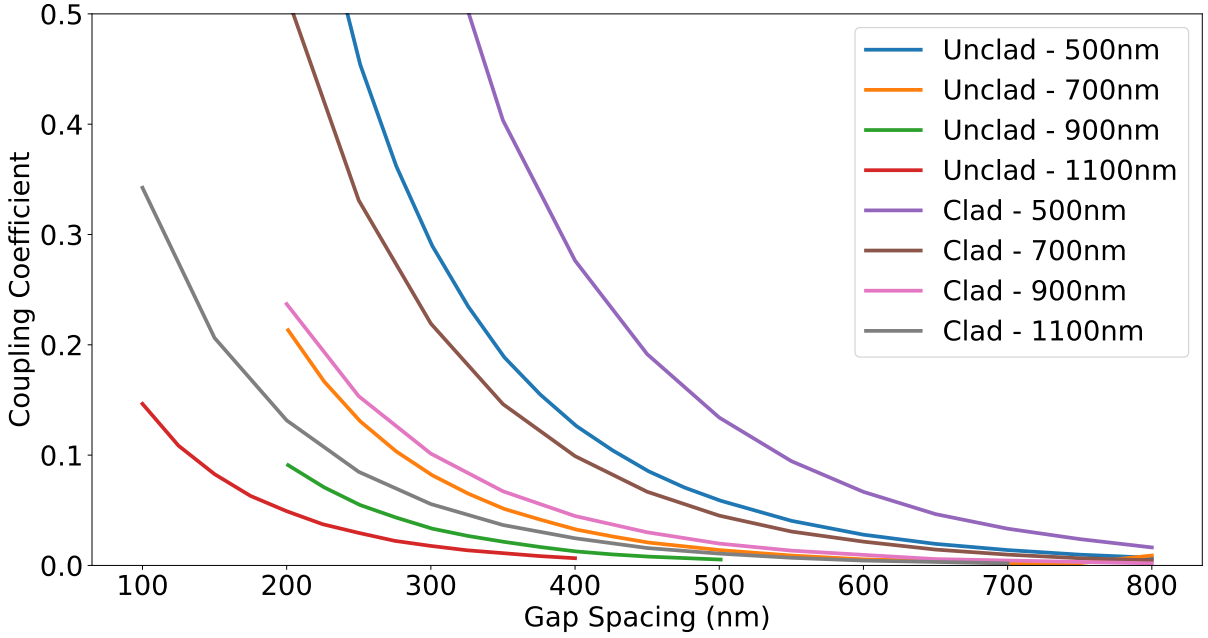

Figure 3.10: The calculated coupling coefficient of the TE_0 mode for each micro-ring resonator design with a 200 nm thick waveguide core against the gap spacing between the bus and micro-ring waveguides.

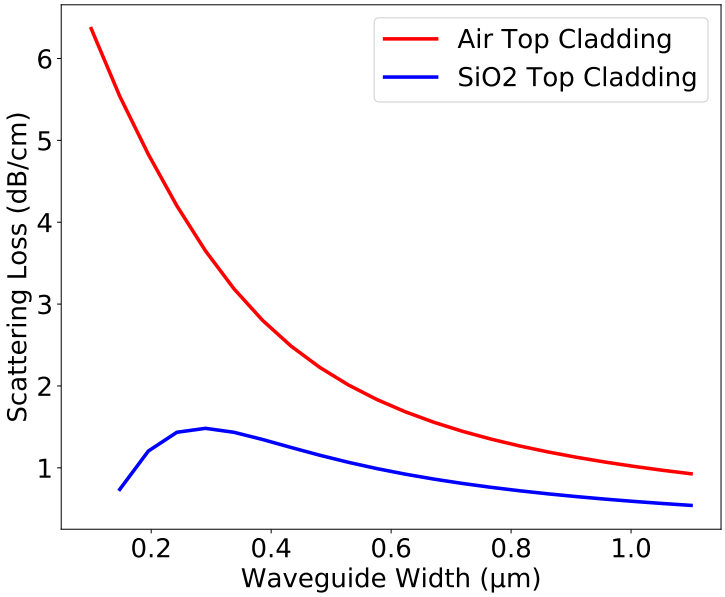

Figure 3.11: Modelled scattering loss (dB/cm) against the width of Si_3N_4 waveguides for only air as a top cladding and with an SiO_2 top cladding. This simple 2D model considers only the sidewall scattering and does not consider the scattering from the top and bottom interfaces of the waveguide.

3.2 Lacey-Payne Scattering Model

The Lacey-Payne scattering model introduced in Section 2.4 was used to estimate the scattering loss of Si_3N_4 waveguides of varying widths, with and without a SiO_2 top cladding. There are two main conclusions to be drawn from Figure 3.11. The first conclusion is that the scattering loss is reduced by about a factor of 2 by the addition of the SiO_2 top cladding for waveguides 500-1100 nm wide. This conclusion is borne out by the improvement in Q factor demonstrated in Chapter 6 for waveguides with the top cladding layer. The second conclusion is that scattering loss can be reduced by simply increasing the waveguide width thereby decreasing the modal interaction with sidewalls. Figure 3.11 shows that the propagation loss of SiO_2 clad waveguides peaks for waveguide widths around 300 nm, this is because the waveguide confinement peaks at this value and for smaller values of waveguide widths the mode would expand vertically becoming weakly confined in the simulation plane. In order to use the model, a line edge roughness of 1.3 nm RMS and a correlation length of 10 nm was assumed based upon values reported for similarly fabricated Germanium waveguides [85]. This is inherently a difficult measurement to perform and this difficulty would be accentuated by the inability to produce thick films of Si_3N_4.

3.3 Eigenmode Expansion Solver

Three dimensional structures can be also be simulated using finite difference methods but this can be computationally expensive and time consuming. Lumerical's Eigenmode Expansion (EME) solver is ideally suited for the simulation of light field propagation over long distances. Eigenmode expansion models do not rely upon the discretisation of space in the direction of propagation and so simulation time does not scale with structure size in the same way as more computationally expensive finite difference models [86]. The FDE solver is used to find the desired eigenmode and the propagation of that mode in the x direction can be expressed by the eigenfunction problem

$$E(x,y,z) = E_m(y,z)\exp(i\beta_m x) \tag{3.10}$$

where $E(x,y,z)$ is the three dimensional field, $E_m(y,z)$ is the transverse eigenfunction, and $\exp(i\beta_m x)$ is the eigenvalue of the solution which describes the x dependence of the mode [87]. The electromagnetic field within a structure can be decomposed into a basis set of eigenmodes by splitting the structure up into a series of sequential cells with an FDE solver in each cell. The reflection and transmission coefficients are found for each cell boundary forming a bidirectional scattering matrix. By cascading these scattering matrices, the scattering matrix (and therefore the reflection and transmission coefficients) for the complete structure can be found [88]. Historically, the staircase approximation would be used to account for structures variation between cells leading to artificial interfaces and reflections [87] but Lumerical's implementation of EME uses it's "Continuously Varying Cross-sectional Subcell" method to prevent this. This simulation tool is well suited for designing waveguide tapers and spot-size converters [89], see Chapter 8.

3.4 Summary

The theoretical framework established in Chapter 2 has provided a foundation for investigation in this chapter of the essential design parameters for silicon nitride waveguides and micro-ring resonators using a combination of software tools and analytical methods. The one dimensional finite difference eigenmode solver has been used to determine that 4 µm is an appropriate bottom cladding thickness to reduce loss due to substrate leakage and that a 1 µm top cladding thickness can suppress the formation of a slab mode (resulting from a index mismatch between the top and bottom cladding) which can cause issues during micro-ring resonator characterisation as discussed further in Chapter 5. The two dimensional finite difference eigenmode solver has been used to determine the effective indices of the supported (TE and TM) modes as a function of waveguide width (with and without the top cladding layer), to demonstrate that the ring radius used in this work is sufficiently large such that the curved waveguide can be considered to be equivalent to a straight waveguide (i.e. does not exhibit significant modal displacement due

to the waveguide bend), and to find the even and odd effective indices of a coupled pair of parallel waveguides. The even and odd effective indices can be used in Equation 2.82 to find the coupling coefficient between a straight waveguide and a circular micro-ring resonator for a TE_0 mode for each waveguide cross-section and gap spacing used in this work. The Lacey-Payne model detailed in Chapter 2 has been used with suitable input variables to provide an estimate of propagation loss which can be expected for the different waveguide cross-sections which have been tested. The eigenmode expansion solver which will be used in Chapter 8 to simulate inverse taper spot-size converters has also been explained here for completeness.

Chapter 4

Ring Resonator Analytical Modelling

Modelling the performance of a micro-ring resonator allows for a greater understanding of how the transmission spectra and resonator characteristics vary based upon the input parameters. With this understanding much greater insight can be gleamed from the experimental characterisation of the micro-ring resonators. The transmission equations derived in this chapter can be fitted to the experimental spectra and used to perform parameter estimation. In this chapter it is illustrated that the maximum Q-factor and peak slope gradient of micro-ring resonator transmission spectra can be found in the under-coupled regime while the maximum peak amplitude can be found at critical coupling.

4.1 Ring Resonator Equations

The four main ports of a general ring resonator are referred to as the input, through, add, and drop ports [90]. The amplitude of the electric field component of the electromagnetic wave amplitude present at these ports is labelled as E with a subscript to indicate the port and whether the field is in the bus waveguide (1) or the ring resonator (2), see Figure 4.1. The coupling coefficients between the bus waveguide and ring resonator are $t_{a,b}$ and $\kappa_{a,b}$, where $|\kappa^2|+|t^2|+|\gamma^2|=1$, and $\gamma_{a,b}$ represents any loss inherent to the evanescent coupler. The two coupling regions are simply labelled a and b, and * represents the complex conjugate. This means that these two coupling regions can be described by the matrix relations in equations (4.1) and (4.2).

$$\begin{pmatrix} E_{t1} \\ E_{t2} \end{pmatrix} = \begin{pmatrix} t_a & i\kappa_a \\ i\kappa_a^* & t_a^* \end{pmatrix} \begin{pmatrix} E_{i1} \\ E_{i2} \end{pmatrix} \tag{4.1}$$

$$\begin{pmatrix} E_{d1} \\ E_{d2} \end{pmatrix} = \begin{pmatrix} t_b & i\kappa_b \\ i\kappa_b^* & t_b^* \end{pmatrix} \begin{pmatrix} E_{a1} \\ E_{a2} \end{pmatrix} \tag{4.2}$$

Before the resulting electric fields can be derived, the losses involved need to be described mathematically. There is the insertion loss which will be described as a combination propagation

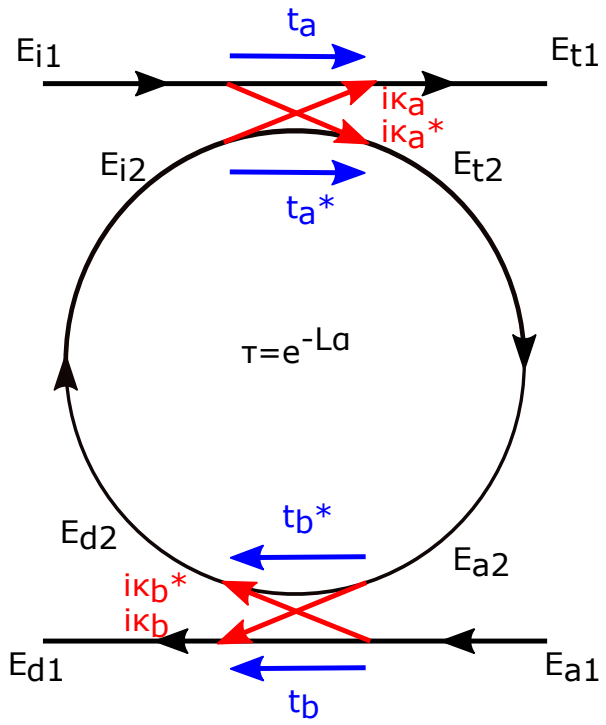

Figure 4.1: General add-drop ring resonator. E_i, E_t, E_a, and E_d are the electromagnetic fields at the input, through, add, and drop ports respectively. The coupling coefficients, t and κ, of coupling regions a and b are also shown as well as the loss coefficient of the ring resonator, τ

loss of the bus waveguide and the coupling loss between the light source and bus waveguide and there is loss inherent to the ring resonator. The ring resonator loss coefficient is determined by the waveguide propagation loss and circumference of the ring resonator, and is used to determine the field amplitude that is transmitted around the ring from one coupling region to the other.

The ring resonator loss coefficient is given by equation (4.3)

$$\tau = e^{-L\alpha} \tag{4.3}$$

where L is the length or circumference of the resonator (m) and α is the field amplitude propagation loss per unit length (m^{-1}) of the waveguide [90]. The insertion loss can be described by equation (4.4)

$$C_{IL} = 10^{\frac{IL_{dB}}{10}} e^{-L_{\text{bus}}\alpha} \tag{4.4}$$

where IL_{dB} is the insertion loss (dB) from coupling light from it's source into the bus waveguide, and L_{bus} is the length of the bus waveguide (m) [90].

The wave behaviour of the field must be considered so that that transmission of the resonator can be determined. The steady state approach is taken whereby the phase of the travelling wave is given by the product of the angular frequency and the resonator round-trip time [90, 91]

$$\theta = \omega t_{\text{RT}} = \omega \frac{n_{\text{eff}} L_{\text{ring}}}{c} = 2\pi\nu \frac{n_{\text{eff}} L_{\text{ring}}}{c} \tag{4.5}$$

where L_{ring} is the ring resonator length/circumference (meter), ω is the angular frequency (rad s^{-1}), c is the free-space velocity of light (m s^{-1}), ν is frequency (Hz), and λ is the wavelength (m). The resulting general expression for the travelling wave is given by [91, 92]

$$E(t) = Ae^{i\omega t_{\text{RT}}} = Ae^{i\theta}. \tag{4.6}$$

where A is the wave amplitude. The resonance condition is satisfied for every integer multiple of the source wavelength which is equal to the resonator optical path length. The spacing in the wavelength or frequency domain between resonance peaks in defined as the free-spectral range. This is equivalent to the phase being equal to 2π. Considering Equation 4.5, the free-spectral range in terms of frequency is given by [91]

$$\text{FSR}_\nu \approx \frac{c}{n_{\text{eff}} L_{\text{ring}}} \tag{4.7}$$

for a ring resonator of a certain length with a given effective index. The free spectral range in terms of wavelength is therefore found by a simple bandwidth conversion [93] to be

$$\text{FSR}_\lambda = \frac{c}{\nu^2}\text{FSR}_\nu \approx \frac{\lambda^2}{n_{\text{eff}} L_{\text{ring}}}. \tag{4.8}$$

The FSR found analytically in this way is directly compared to an experimental value in Section 6.3.

4.1.1 Through Port Power Transmission

The phase of the travelling wave is considered to be equal to zero upon coupling from the bus waveguide to the ring resonator and the field amplitudes are considered to be normalised with respect to the light source field amplitude. The field amplitude at the input port of a ring resonator bus waveguide is therefore given by [8, 90]

$$E_{i1} = 1 \cdot \frac{1}{\sqrt{C_{IL}}} \tag{4.9}$$

and so the amplitude of light coupled into the ring resonator is determined by Equations (4.1) and (4.9) such that

$$E_{t2} = i\kappa_a^* \frac{1}{\sqrt{C_{IL}}} + t_a^* E_{i2} \tag{4.10}$$

where E_{i2} is the light that has passed all the way around the ring resonator experiencing an attenuation defined by the ring resonator loss τ and is incident once again upon coupling region a [90]. It is now important to consider the wave like behaviour of the field and the accumulated

phase angle θ resulting from one round-trip around the ring. E_{i2} is therefore given by

$$E_{i2} = t_b^* \tau e^{-i\theta} E_{t2} \tag{4.11}$$

and so

$$\begin{aligned} E_{t2} &= i\kappa_a^* \frac{1}{\sqrt{C_{IL}}} + t_a^* t_b^* \tau e^{-i\theta} E_{t2} \\ E_{t2} &= \frac{i\kappa_a^*}{1 - t_a^* t_b^* \tau e^{-i\theta}} \frac{1}{\sqrt{C_{IL}}} \end{aligned} \tag{4.12}$$

is the final expression for E_{t2}. This feeds back into equation (4.11) to give the final expression for E_{i2}

$$E_{i2} = \frac{i\kappa_a^* t_b^* \tau e^{-i\theta}}{1 - t_a^* t_b^* \tau e^{-i\theta}} \frac{1}{\sqrt{C_{IL}}}. \tag{4.13}$$

The field at the through port is found using equations (4.1), (4.12), and (4.13).

$$\begin{aligned} E_{t1} &= t_a E_{i1} + i\kappa_a E_{i2} \\ &= \left[t_a + i\kappa_a \left(\frac{i\kappa_a^* t_b^* \tau e^{-i\theta}}{1 - t_a^* t_b^* \tau e^{-i\theta}} \right) \right] \frac{1}{\sqrt{C_{IL}}} \\ &= \left[\frac{t_a - t_a t_a^* t_b^* \tau e^{-i\theta} - \kappa_a \kappa_a^* t_b^* \tau e^{-i\theta}}{1 - t_a^* t_b^* \tau e^{-i\theta}} \right] \frac{1}{\sqrt{C_{IL}}} \\ &= \left[\frac{t_a - (|t_a^2| + |\kappa_a^2|) t_b^* \tau e^{-i\theta}}{1 - t_a^* t_b^* \tau e^{-i\theta}} \right] \frac{1}{\sqrt{C_{IL}}} \\ &= \frac{t_a - t_b^* \tau e^{-i\theta}(1 - |\gamma_a^2|)}{\sqrt{C_{IL}}(1 - t_a^* t_b^* \tau e^{-i\theta})} \end{aligned} \tag{4.14}$$

Until this point the field amplitude of light has been considered. This representation allows for calculation of the field interactions but the field amplitudes cannot be measured directly. It is the power of light that is measured using a photodetector. The power of light is found by integrating the time average of the Poynting vector over the mode area, the time average Poynting vector can be expressed as [92]

$$|\vec{S}| = \frac{c\varepsilon_0}{2} E E^* \tag{4.15}$$

and so

$$P \propto E E^*. \tag{4.16}$$

If the field amplitude is represented by equation (4.14) then its complex conjugate is represented

by

$$E_{t1}^{*} = \frac{t_a^{*} - t_b \tau^{*}(1-|\gamma_a^2|)^{*} e^{i\theta^{*}}}{\sqrt{C_{IL}}(1 - t_a t_b \tau^{*} e^{i\theta^{*}})} \tag{4.17}$$

and so the normalised power transmission can be considered to be

$$\begin{aligned} |E_{t1}|^2 &= E \cdot E^{*} \\ &= \frac{t_a - t_b^{*}\tau(1-|\gamma_a^2|)e^{-i\theta}}{\sqrt{C_{IL}}(1 - t_a^{*} t_b^{*} \tau e^{-i\theta})} \cdot \frac{t_a^{*} - t_b \tau^{*}(1-|\gamma_a^2|)e^{i\theta^{*}}}{\sqrt{C_{IL}}(1 - t_a t_b \tau^{*} e^{i\theta^{*}})} \\ &= \frac{|t_a^2| - t_a t_b \tau^{*}(1-|\gamma_a^2|)e^{i\theta} - t_a^{*} t_b^{*} \tau (1-|\gamma_a^2|)e^{-i\theta} + {t_b}^2 \tau^2 (1-|\gamma_a^2|)^2}{C_{IL}(1 - t_a^{*} t_b^{*} \tau e^{i\theta} - t_a t_b \tau^{*} e^{-i\theta} + |t_a|^2 |t_b|^2 |\tau|^2)} \end{aligned} \tag{4.18}$$

If t_a, t_b, τ, and γ_a are real, then the normalised transmitted power through the bus waveguide of a ring resonator is given by

$$\begin{aligned} |E_{t1}|^2 &= \frac{t_a^2 - t_a t_b \tau (1-|\gamma_a^2|)(e^{i\theta} + e^{-i\theta}) + {t_b}^2 \tau^2 (1-|\gamma_a^2|)^2}{C_{IL}[1 - t_a t_b \tau (e^{i\theta} + e^{-i\theta}) + t_a^2 t_b^2 \tau^2]} \\ &= \frac{t_a^2 - 2 t_a t_b \tau (1-|\gamma_a^2|)\cos\theta + {t_b}^2 \tau^2 (1-|\gamma_a^2|)^2}{C_{IL}[1 - 2 t_a t_b \tau \cos\theta + t_a^2 t_b^2 \tau^2]}. \end{aligned} \tag{4.19}$$

This is represented as a function of the phase in Figure 4.2 where $C_{\mathrm{IL}} = 1$, $\gamma_a = 0$, and $t_b = 1$. In this simple case, critical coupling is defined as the field transmission through the bus and not coupled into the ring, t_a, being equal the single round trip field transmission of the ring resonator, τ. Under-coupling is the case in which $t_a > \tau$, which means that there is more light passing straight through the bus waveguide without coupling into the resonator than there is completing a single round trip of the resonator. Over-coupling is the opposite case in which there is more light propagating round the ring than there is transmitted straight though the bus without interacting with the ring. In the more general case, considering an evanescent coupler with loss and a second bus waveguide, critical coupling occurs for $t_a = t_b \tau (1-|\gamma_a^2|)$; similarly, under-coupling is defined as $t_a > t_b \tau (1-|\gamma_a^2|)$ and over-coupling is defined as $t_a < t_b \tau (1-|\gamma_a^2|)$. The amplitude of a the resonance peak is maximum in the case of critical coupling for an all-pass ring resonator (see Figure 4.2). The normalised power transmission at the through port of an add-drop ring resonator is shown in Figure 4.3 for $C_{\mathrm{IL}} = 1$, $\gamma_a = 0$, and $t_b = 0.95$. For an add-drop ring resonator, the amplitude of a the resonance peak is also maximum in the case of critical coupling.

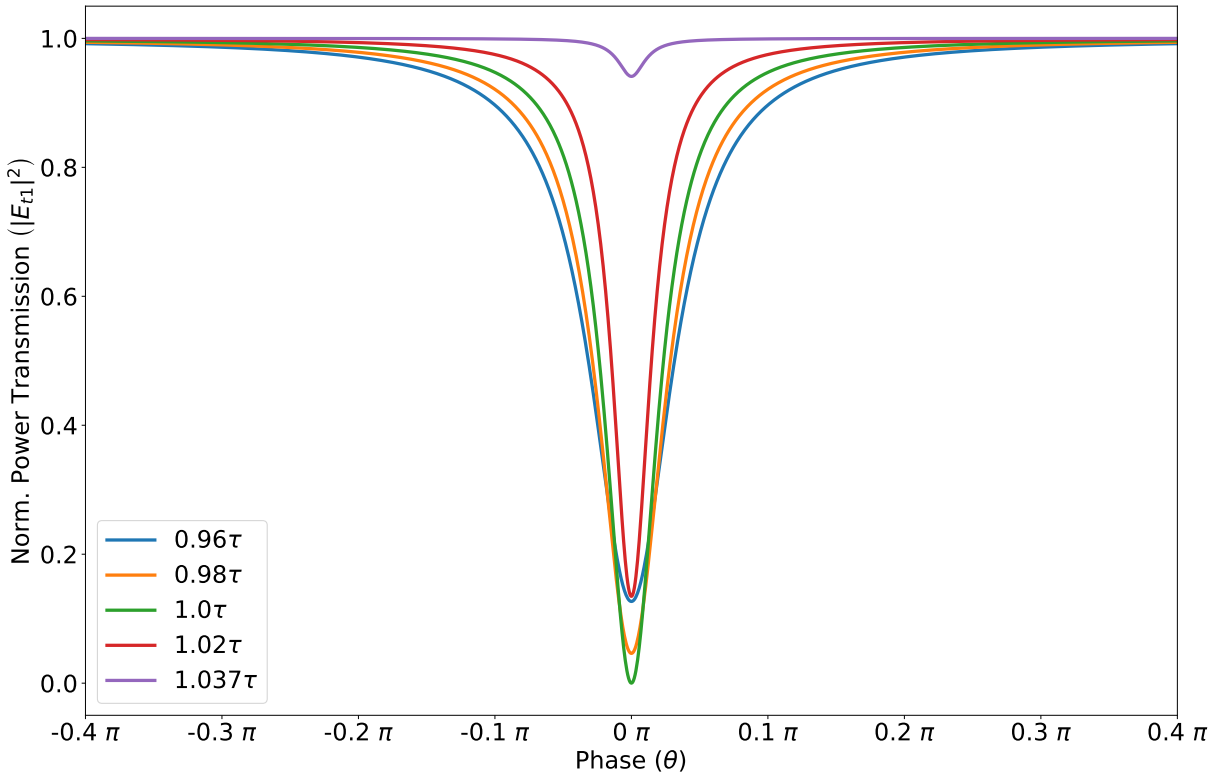

Figure 4.2: Normalised power transmission at the through port as a function of phase for an all-pass ring resonator with a normalised input power $P = 1$, propagation loss of 1 dB cm^{-1}, and a radius of 300 µm. This is shown for values of the coupling coefficient t_a expressed as a multiple of τ. Under, over, and critical coupling are defined such that $t_a > \tau$, $t_a < \tau$, and $t_a = \tau$ respectively.

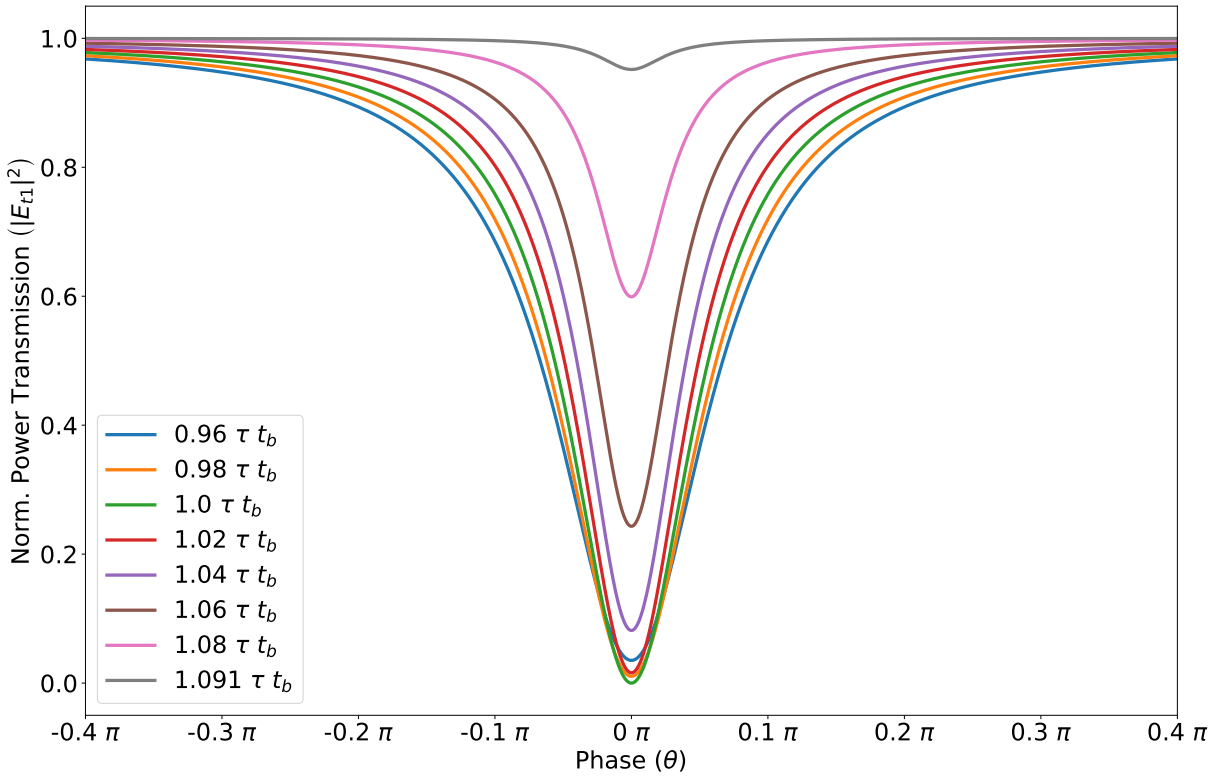

Figure 4.3: Normalised power transmission at the through port as a function of phase for an add-drop ring resonator with an input power $P = 1$, propagation loss of 1 dB cm^{-1}, a radius of 300 µm, and coupling parameter $t_b = 0.95$. This is shown for values of the coupling coefficient t_a expressed as a multiple of τt_b. Under, over, and critical coupling are defined such that $t_a > \tau t_b$, $t_a < \tau t_b$, and $t_a = \tau t_b$ respectively.

4.1.2 Derivatives Of Transmitted Power With Respect To Phase

The first derivative of the normalised transmitted power with respect to phase is found using the product rule,

$$\begin{aligned}\frac{\partial|E_{t1}|^2}{\partial\theta} &= \frac{1}{C_{IL}^2[1-2t_at_b\tau\cos\theta+t_a^2t_b^2\tau^2]^2}\\ &\quad\Big\{C_{IL}[1-2t_at_b\tau\cos\theta+t_a^2t_b^2\tau^2]\frac{\partial(-2t_at_b\tau(1-|\gamma_a^2|)\cos\theta)}{\partial\theta}\\ &\quad-[t_a^2-2t_at_b\tau(1-|\gamma_a^2|)\cos\theta+{t_b}^2\tau^2(1-|\gamma_a^2|)^2]\frac{\partial(-2C_{IL}t_at_b\tau\cos\theta)}{\partial\theta}\Big\}\\ &= \frac{C_{IL}}{C_{IL}^2[1-2t_at_b\tau\cos\theta+t_a^2t_b^2\tau^2]^2}\\ &\quad\big\{[1-2t_at_b\tau\cos\theta+t_a^2t_b^2\tau^2](2t_at_b\tau(1-|\gamma_a^2|)\sin\theta)\\ &\quad-[t_a^2-2t_at_b\tau(1-|\gamma_a^2|)\cos\theta+{t_b}^2\tau^2(1-|\gamma_a^2|)^2](2t_at_b\tau\sin\theta)\big\}.\end{aligned}$$

This can then be expanded,

$$\begin{aligned}\frac{\partial|E_{t1}|^2}{\partial\theta} &= \frac{1}{C_{IL}[1-2t_at_b\tau\cos\theta+t_a^2t_b^2\tau^2]^2}\\ &\quad\big[2t_at_b\tau(1-|\gamma_a^2|)\sin\theta-4t_a^2t_b^2\tau^2(1-|\gamma_a^2|)\sin\theta\cos\theta+2t_a^3t_b^3\tau^3(1-|\gamma_a^2|)\sin\theta\\ &\quad-2t_a^2t_at_b\tau\sin\theta+4t_a^2t_b^2\tau^2(1-|\gamma_a^2|)\sin\theta\cos\theta-2{t_b}^2\tau^2(1-|\gamma_a^2|)^2t_at_b\tau\sin\theta\big]\end{aligned}$$

simplified,

$$\frac{\partial|E_{t1}|^2}{\partial\theta} = \frac{2t_at_b\tau(1-|\gamma_a^2|)\sin\theta}{C_{IL}[1-2t_at_b\tau\cos\theta+t_a^2t_b^2\tau^2]^2}\left(1+t_a^2t_b^2\tau^2-\frac{t_a^2}{(1-|\gamma_a^2|)}-{t_b}^2\tau^2(1-|\gamma_a^2|)\right)$$

and factorised resulting in the form

$$\frac{\partial|E_{t1}|^2}{\partial\theta} = \frac{2t_at_b\tau(1-|\gamma_a^2|)\sin\theta}{C_{IL}[1-2t_at_b\tau\cos\theta+t_a^2t_b^2\tau^2]^2}\left(1-\frac{t_a^2}{(1-|\gamma_a^2|)}\right)\left(1-{t_b}^2\tau^2(1-|\gamma_a^2|)\right). \tag{4.20}$$

This is an important relationship for characterising a resonator as it determines the slope of the resonance peak. Since changes in frequency (or phase) are transduced to a change in transmitted power, this allows the resonator to serve as a frequency (or phase) discriminator. A larger value for this derivative term means that the resonator has greater responsivity and will act as a more sensitive discriminator. Figure 4.4 shows the derivative of the normalised power transmission at the through port of an all-pass ring resonator as a function of phase for an input power $P = 1$, propagation loss of $1\,\mathrm{dB\,cm^{-1}}$, and a radius of $300\,\mu\mathrm{m}$. The maximum response is found in under-coupled regime but this tails off quickly as t_a is increased further. The derivative of normalised power transmission at the through port of an add-drop ring resonator as a function

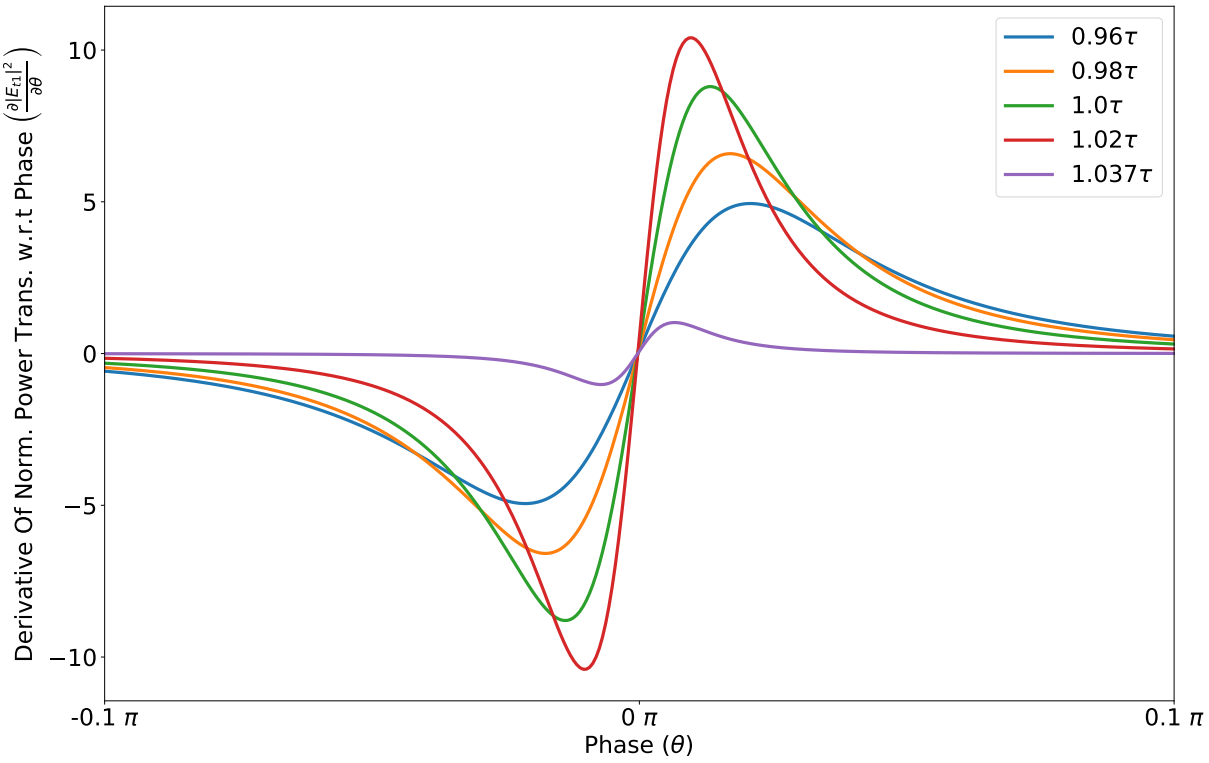

Figure 4.4: The derivative of the normalised power transmission with respect to phase for an all-pass ring resonator with a propagation loss of 1 dB cm^{-1} and a radius of 300 µm. This is shown for values of the coupling coefficient t_a expressed as a multiple of τ. Under, over, and critical coupling are defined such that $t_a > \tau$, $t_a < \tau$, and $t_a = \tau$ respectively.

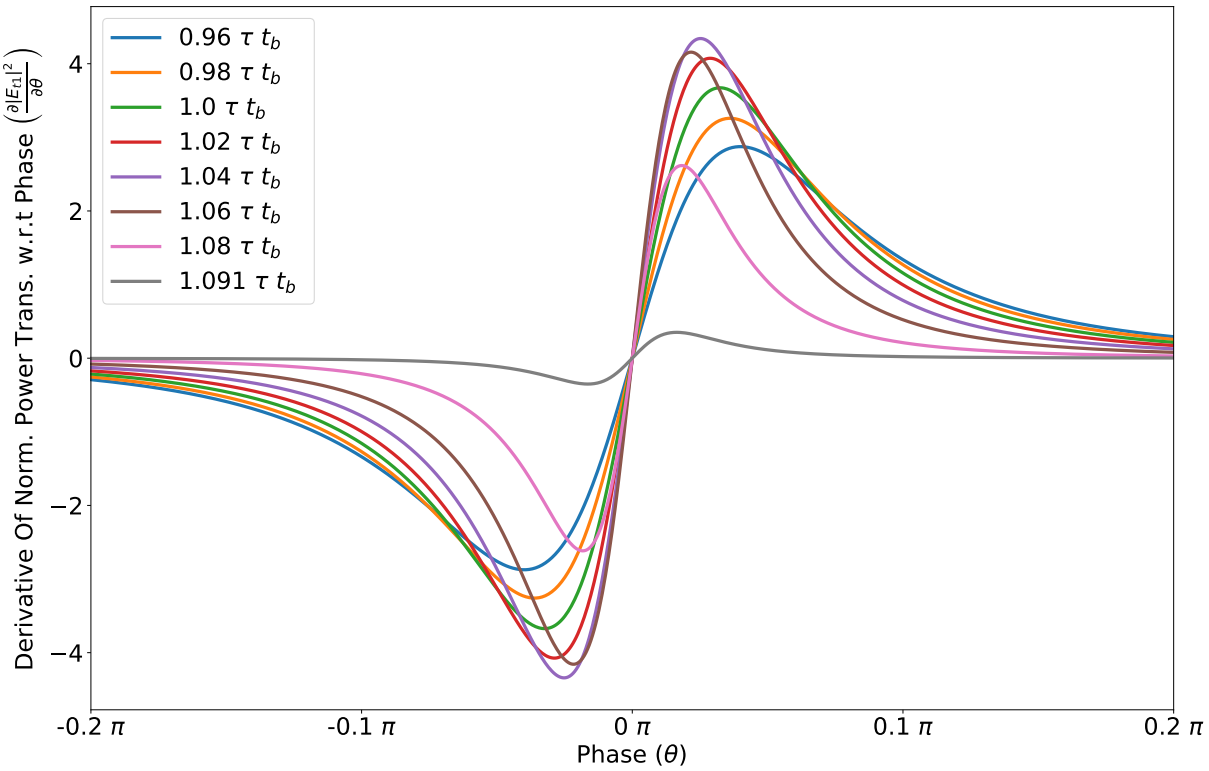

Figure 4.5: The derivative of the normalised power transmission at the through port with respect to phase for an add-drop ring resonator with a propagation loss of 1 dB cm^{-1} and a radius of 300 µm. This is shown for values of the coupling coefficient t_a expressed as a multiple of τt_b. Under, over, and critical coupling are defined such that $t_a > \tau t_b$, $t_a < \tau t_b$, and $t_a = \tau t_b$ respectively.

of phase for an input power $P = 1$, propagation loss of 1 dB cm^{-1}, a radius of 300 µm, and coupling parameter $t_b = 0.95$ is shown in Figure 4.5. Again, the maximum response is in the under-coupled regime and this tails off quickly as t_a is increased further.

4.1.3 Drop Port Power Transmission

The derivation of the drop port normalised power transmission is given here to prove the validity of the general model of a ring resonator by ensuring that it is self consistent. The field amplitude E_{t2} has been defined in equation (4.12) and is required to determined the field amplitude E_{a2} as marked in Figure 4.1. The field incident upon evanescent coupler b from within the resonator is [8, 90, 91]

$$\begin{aligned} E_{a2} &= \sqrt{\tau} e^{-i\frac{\theta}{2}} E_{t2} \\ E_{a2} &= \frac{i\kappa_a^* \sqrt{\tau} e^{-i\frac{\theta}{2}}}{1 - t_a^* t_b^* \tau e^{-i\theta}} \frac{1}{\sqrt{C_{IL}}} \end{aligned} \tag{4.21}$$

and assuming $E_{a1} = 0$

$$\begin{aligned} E_{d1} &= i\kappa_b E_{a2} + 0 t_b \\ &= \frac{-\kappa_a^* \kappa_b \sqrt{\tau} e^{-i\frac{\theta}{2}}}{1 - t_a^* t_b^* \tau e^{-i\theta}} \frac{1}{\sqrt{C_{IL}}} \end{aligned} \tag{4.22}$$

which is the result field amplitude of interest. To confirm that this matches up with the general through port derivation consider

$$E_{d2} = \frac{i\kappa_a^* t_b \sqrt{\tau} e^{-i\frac{\theta}{2}}}{1 - t_a^* t_b^* \tau e^{-i\theta}} \frac{1}{\sqrt{C_{IL}}} \tag{4.23}$$

Which after another half round trip gives

$$\begin{aligned} E_{i2} &= \sqrt{\tau} e^{-i\frac{\theta}{2}} E_{d2} \\ &= \frac{i\kappa_a^* t_b^* \tau e^{-i\theta}}{1 - t_a^* t_b^* \tau e^{-i\theta}} \frac{1}{\sqrt{C_{IL}}} \end{aligned}$$

as is seen in equation 4.13.

The normalised power at the drop is found, again by multiplying the field by its complex conjugate

$$\begin{aligned} |E_{d1}|^2 &= \frac{(-\kappa_a^* \kappa_b \sqrt{\tau} \cos\frac{\theta}{2})^2 + (\kappa_a^* \kappa_b \sqrt{\tau} \sin\frac{\theta}{2})^2}{(\sqrt{C_{IL}} - \sqrt{C_{IL}} t_a^* t_b^* \tau \cos\theta)^2 + (\sqrt{C_{IL}} t_a^* t_b^* \tau \sin\theta)^2} \\ &= \frac{\kappa_a^2 \kappa_b^2 \tau}{C_{IL}[1 - 2t_a^* t_b^* \tau \cos\theta + (t_a^* t_b^* \tau)^2]}. \end{aligned} \tag{4.24}$$

Once more assuming that t_a, t_b, τ, and γ_a are real, then normalised power transmitted at the drop port of a ring resonator is given by

$$|E_{d1}|^2 = \frac{\kappa_a^2 \kappa_b^2 \tau}{C_{IL}[1 - 2t_a t_b \tau \cos\theta + t_a^2 t_b^2 \tau^2]}. \tag{4.25}$$

The normalised power transmission at the drop port of an add-drop ring resonator is shown in Figure 4.6 for $C_{\mathrm{IL}} = 1$, $\gamma_a = 0$, and $t_b = 0.95$. This peak amplitude is also maximised in the case of critical coupling. The introduction of another coupling section introduces another loss mechanism for the ring resonator and so the resonance peak of the add-drop ring resonator is broader (lower Q) than that of the all-pass ring resonator with similar t_a values.

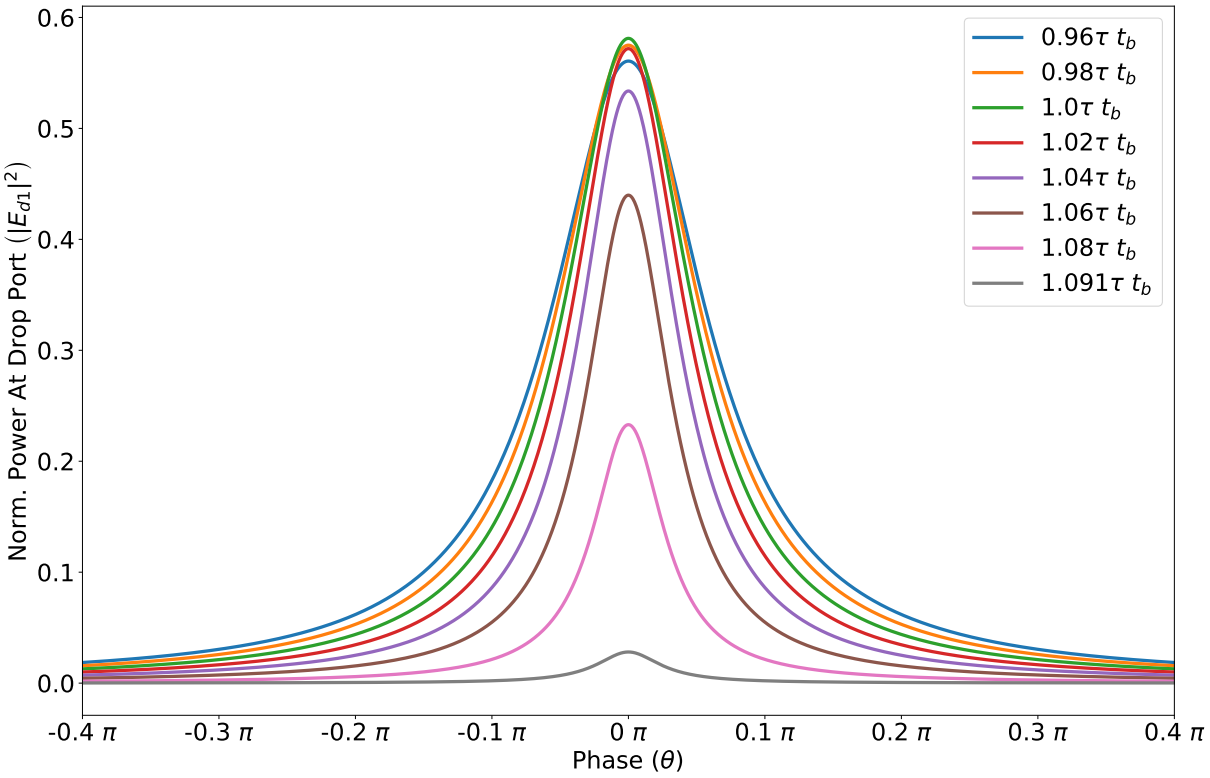

Figure 4.6: Normalised power transmission at the drop port as a function of phase for an add-drop ring resonator with an input power $P = 1$, propagation loss of 1 dB cm^{-1}, a radius of 300 µm, and coupling parameter $t_b = 0.95$. This is shown for values of the coupling coefficient t_a expressed as a multiple of τt_b. Under, over, and critical coupling are defined such that $t_a > \tau t_b$, $t_a < \tau t_b$, and $t_a = \tau t_b$ respectively.

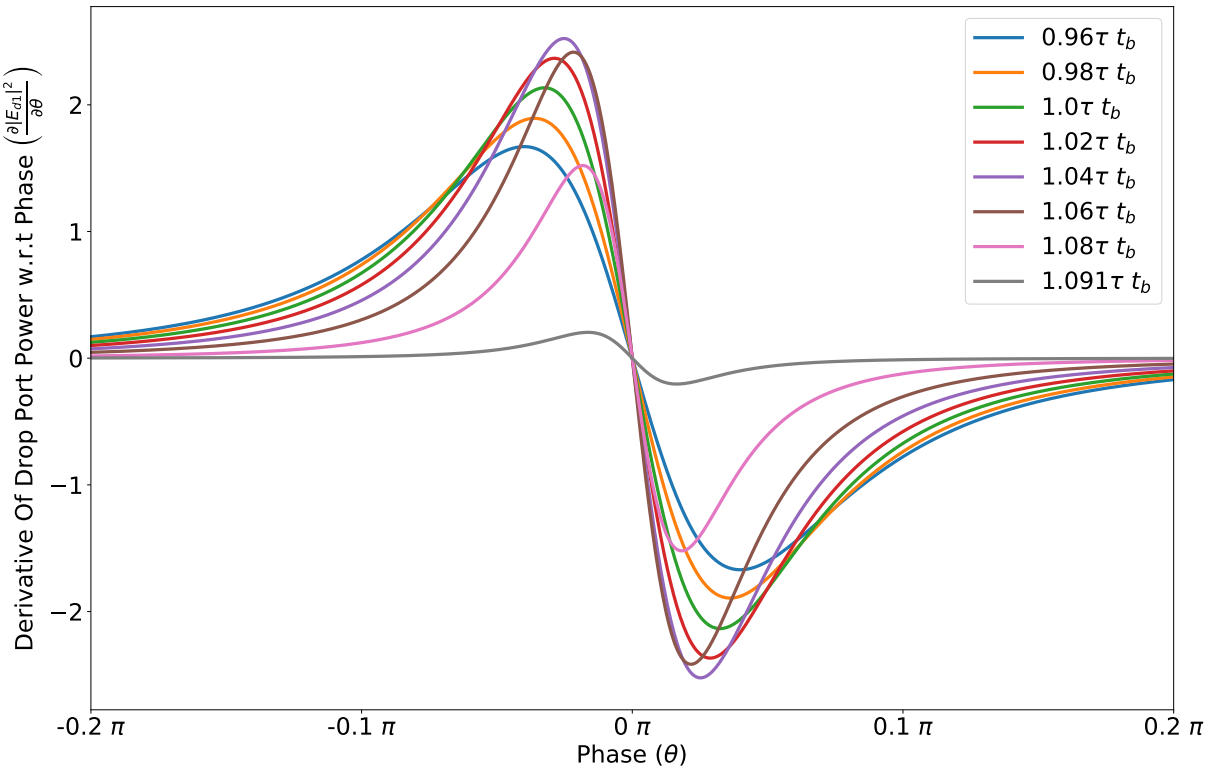

Figure 4.7: The derivative of the normalised power transmission at the drop port with respect to phase for an add-drop ring resonator with a propagation loss of 1 dB cm^{-1} and a radius of 300 µm. This is shown for values of the coupling coefficient t_a expressed as a multiple of τt_b. Under, over, and critical coupling are defined such that $t_a > \tau t_b$, $t_a < \tau t_b$, and $t_a = \tau t_b$ respectively.

4.1.4 Derivatives Of Power At Drop Port With Respect To Phase

The derivative of the normalised power found at the drop port is given by

$$\frac{\partial|E_{d1}|^2}{\partial\theta} = -\frac{2\kappa_a^2\kappa_b^2\tau^2 t_a t_b sin\theta}{C_{IL}[1-2t_a t_b\tau\cos\theta + t_a^2 t_b^2\tau^2]^2}. \tag{4.26}$$

The derivative of normalised power transmission at the drop port of an add-drop ring resonator as a function of phase for an input power $P = 1$, propagation loss of 1 dB cm^{-1}, a radius of 300 µm, and coupling parameter $t_b = 0.95$ is shown in Figure 4.7. The maximum response is once more in the under coupled regime and decreases as t_a is increased further.

4.2 Modelling Ring Resonator Parameters

Practically, it is much easier to characterise a resonator by measuring the power transmission at the through port because the critical coupling case is readily identified as transmitted power approaches zero. The maximum power transmission at the drop port is less well defined. To further simplify characterisation and optimise the footprint of sample devices, all of the micro-

ring resonators fabricated and characterised in this work were of the all-pass configuration. The goal was to achieve the highest possible Q factor value, Q factor is defined as the position of that resonance peak in either wavelength or frequency (these yield the same value) divided by the full width at half maximum (FWHM) of the resonance peak.

$$Q = \frac{\lambda_0}{\mathrm{FWHM}_\lambda} = \frac{\nu_0}{\mathrm{FWHM}_\nu} \tag{4.27}$$

Q factor is regarded as the figure of merit for micro-ring resonators [12, 32, 40, 77, 94] rather than finesse which is defined as the free spectral range divided by the the full width at half maximum and is more routinely used to characterised free space resonators [95]. In literature, a distinction is made between the loaded and unloaded Q factor of a micro-ring resonator, an unloaded Q factor is calculated for a micro-ring resonator which is not coupled to a waveguide, the bus waveguide introduces loss which lowers the Q factor, whereas a loaded Q factor is found in the case where there is a bus waveguide coupled to the micro-ring. All Q factor values stated as part of this work are loaded Q factor values. There are two variables which the designer can change to maximise the Q factor of an all-pass micro-ring resonator; these are the round-trip transmission given by the loss coefficient τ which is dependent on the waveguide loss, and the transmission coefficient of the bus waveguide (t_a) which depends on the confinement of the bus and micro-ring waveguides and the size of the gap between them. Here it is assumed that the centre wavelength and bulk material properties are fixed. For a given waveguide loss, $\alpha_{\mathrm{dB}} = 1\,\mathrm{dB\,cm^{-1}}$, the effect of varying the coupling parameters is shown in Figure 4.8, this is plotted in terms of κ_a to demonstrate the effect of t_a approaching 1 asymptotically.

The peak amplitude is maximum for the critical coupling condition as illustrated in Figure 4.2, the slope gradient is maximum for an under-coupled resonator as illustrated in 4.4, and the Q factor is increased as coupling is decreased but the peak becomes more difficult to resolve. This is because as κ_a is decreased beyond the critical coupling condition, the resonance peak amplitude will only decrease resulting in a shorter peak. Ideally, the ability to resolve this peak would be limited by the noise equivalent power of the detector which is used but laser intensity noise and noise due to scattered light are also limiting factors. The peak would also continue to get narrower as κ_a is decreased and so the ability to resolve the peak is also limited by the resolution of the frequency scan used to acquire the resonance spectra.

4.3 Summary

In this chapter, the general formalism of normalised power transmission at the through port of an all-pass and add-drop micro-ring resonator, and at the drop port of an add-drop micro-ring resonator have been found have been found to be self-consistent and maintain generality. The equation governing the normalised power transmission of an all-pass micro-ring resonator

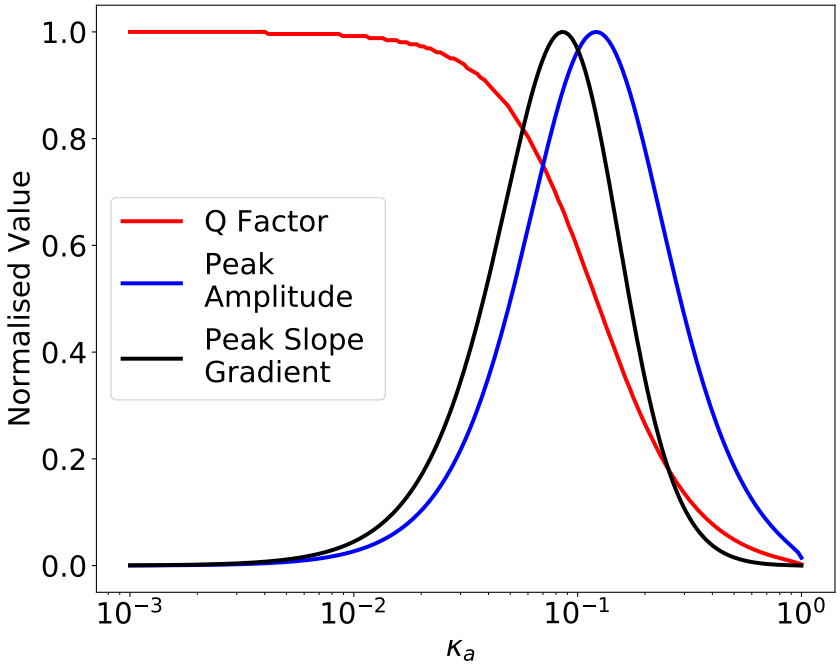

Figure 4.8: The normalised Q factor, peak amplitude, and slope gradient are plotted against the micro-ring resonator coupling coefficient. The peak amplitude is maximum for the critical coupling condition, the slope gradient is maximum for an under-coupled resonator, and the Q factor is increased as coupling is decreased but the peak becomes more difficult to resolve.

(Equation 4.19) is adapted for a frequency spectrum in Chapter 6 and used to determine the loss coefficient of micro-ring resonators. By considering the length of micro-ring resonator, the propagation loss of a given waveguide configuration can be determined from the loss coefficient of the micro-ring resonator. The coupling coefficient values found in Chapter 3 are used as an input variable in the curve fitting function thereby avoiding the issue of distinguishing between of the coupling and loss coefficients if they were both fit parameters [46]. The behaviour of the Q factor, resonance peak amplitude, and slope gradient of a micro-ring resonance peak as a function of the coupling parameter κ_a has been examined leading to the conclusion that high Q factors can be realised by operating in the under-coupled regime. This informed the design decision to try and achieve higher Q factors by increasing the gap spacing (and thereby decreasing the coupling coefficient) for each waveguide design iteration that was tested during the micro-ring resonator characterisation discussed in Chapter 6.

Chapter 5

Waveguide Process Development And Fabrication

The facilities available in the James Watt Nanofabrication Centre (JWNC) allow for every step of the design, fabrication, and characterisation of silicon nitride waveguide devices to be done on-site. The JWNC consists of class 10, 100, and 1000 clean-rooms where the class number denotes the allowable number of particles $\geq$0.5 µm in a cubic foot of air. Deposition tools include the SEMCO chemical vapour deposition (CVD) furnace with multiple furnace chambers capable of wet oxide growth of SiO_2 and low pressure chemical vapour deposition of Si_3N_4 (as required for bottom cladding and core layers respectively), and the SPTS Delta capable of plasma enhanced chemical vapour deposition (PECVD) of SiO_2 (as required for the top cladding layer). Lithography is performed using a Vistec VB6 electron beam lithography tool and reactive ion etching (RIE) of the waveguides is performed using an Oxford Instruments RIE80+. The material deposition, reactive ion etching, and electron beam lithography processes were performed by JWNC technicians.

5.1 Design

Designs were mostly created using the Nazca Design™, an open-source photonic integrated circuit design tool based on Python-3 [96]. This allows for a parametric approach where photonic components such as all-pass and add-drop ring resonators are created as discrete building blocks which can be easily joined together to create a complete photonic circuit. This allows important variables such as width, gap spacing, radius, and evanescent coupler length to be changed easily; for example, a narrower waveguide core would have a less confined mode and would therefore require greater gap spacing to achieve similar power coupling to the ring resonator as a wider waveguide core. Features can be drawn on separate layers allowing for easy distinction between materials or desired resolution of different features on a given device. Completed designs are saved as Graphic Design System II (GDSII) files, a standard format for mask design in pho-

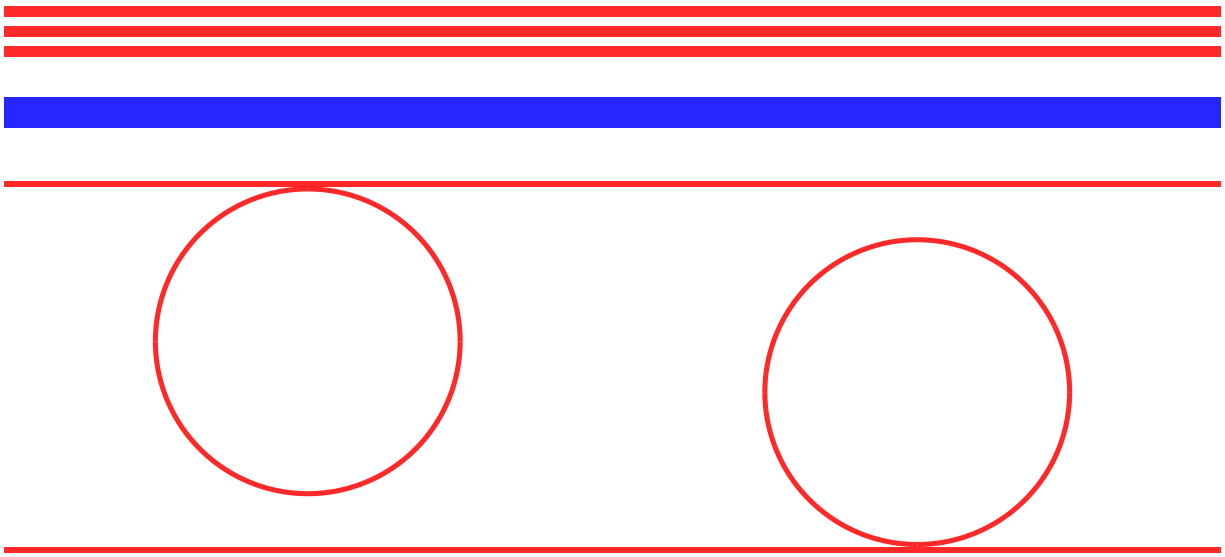

Figure 5.1: Essential features present on micro-ring resonator sample devices. The wide slab mode waveguide (blue) is used to find rough alignment of the lensed fibre input, sample chip, object lens, and camera during characterisation. The triplet of waveguides (red) is used to find the correct working distance of the lens fibre during. The all-pass micro-rings (red) are tessellated such that a pair of micro-ring resonators takes up little more space than a single micro-ring resonator. Features shown in red are on a layer within the GDSII file which will be written with a high resolution electron beam (12 nm) while features in blue are on a layer which will be written with a lower resolution (32 nm). Waveguide widths are exaggerated and lengths greatly reduced here for the purposes of illustration.

tolithography. Examples of when it would be advantageous to define different materials are if the design includes metallisation for electrical components, such as thermo-optic modulators, or another optical layer, such as a spot-size converter for port coupling.

The design changed and evolved over time but the essential features that were present on all samples that were fabricated and characterised are shown in Figure 5.1 (not to scale). Features shown in red are on a layer within the GDSII file which will be written with a high resolution electron beam (12 nm) while features in grey are on a layer which will be written with a lower resolution (33 nm). The waveguide triplet and wide slab mode waveguide are for alignment purposes and are discussed further in Section 6.1 and demonstrated in Figure 6.3. The all-pass micro-rings are tessellated such that a pair of micro-ring resonators takes up little more vertical space than a single micro-ring resonator. These features are treated as a repeating unit on the sample chip, the gap spacing between the bus waveguide and micro-rings of each micro-ring pairs is incremented in each unit and a macroscopic numeral is written in the lower resolution layer adjacent to the micro-ring pair to denote the unit number during characterisation. While creating this design care is taken to avoid features overlapping with the field boundaries of the electron beam lithography tool, resulting in "stitching" errors which are discussed further in Section 5.3.4 and demonstrated in Figure 5.8. To achieve this, a layer was created within the GDSII file which represented these field boundaries in the design but was not written at the

lithography stage. This made it easy to adjust the placement of the repeating unit such the field boundaries were avoided where possible by setting the spacing between the units to be equal to the field grid spacing and placing each micro-ring central within its own field boundary. The bus waveguides of each micro-ring inevitably cross many field boundaries but the loss incurred due to stitching errors is less significant than it would be if there was a stitching error within the resonators.

5.2 Material Deposition

Silicon nitride layers for the waveguide cores were deposited using a low-pressure chemical vapour deposition (LPCVD) furnace at 750 °C onto a 4 µm thick thermal SiO_2 layer grown by wet oxidation at 1000 °C. The waveguide pattern was written in hydrogen silsequioxane (HSQ) negative resist using electron beam lithography with a Vistec VB6 electron beam lithography tool and etched using a CHF_3/O_2 reactive ion etch. Typically HSQ is removed with hydroflouric acid which would damage the Si_3N_4 core and SiO_2 bottom cladding. In this work a sacrificial layer of poly-methyl-methacrylate (PMMA) ∼50 nm is used to perform lift-off of ∼330 nm HSQ, this technique has been previously established [97]. After etching, the HSQ etch mask is removed by lift-off and a SiO_2 top cladding layer can be added using plasma-enhanced chemical vapor deposition (PECVD) at 300 °C.

5.2.1 Thermal Oxidation Of Silicon

The bottom cladding layer of the waveguide is a thick film of SiO_2 that is grown by wet thermal oxidation of a silicon wafer. This can achieved by heating the silicon wafer to 700-1100°C in the presence of water vapour and is performed at 1000 °C in the SEMCO oxidation furnace tube in the JWNC. The benefit of using water vapour, producing wet thermal SiO_2, is that the solubility of water molecules ($3.0 \times 10^{19}\,cm^{-3}$) is greater than the that of diatomic oxygen molecules ($5.2 \times 10^{16}\,cm^{-3}$) and so thick films can be produced much faster [98]. The rate of oxide growth decays exponentially however because the water (or oxygen) needs to diffuse through an ever increasing thickness of SiO_2 and so to grow 4 µm film of wet thermal SiO_2 at 1000 °C requires about 60 h of continuous operation. A dry oxidation furnace (using oxygen instead of water) would be expected to take $>$ 1500 h to grow the same thickness [99]. The wet oxidation furnace can only be operated during working hours due to safety considerations and so this takes about two weeks of real time to grow. Fortunately, this can be done with 6 ” wafers in batches of up to 25 wafers and so this needs to be done relatively infrequently.

It is essential that the bottom cladding layer is thick enough to prevent the optical mode from coupling into the higher index silicon substrate and being absorbed resulting in catastrophic propagation losses [100]. This problem is of greater significance for optical modes with low to moderate confinement such as those presented in this work [1]. The optical properties of the wet

thermal SiO_2 were characterised using a JA Woollam M2000X spectroscopic ellipsometer and it was found to have a refractive index of 1.4544±0.0001 (see Figure 5.4). This low variance in refractive index can be attributed to the optical purity typically associated with this process.

5.2.2 Low Pressure Chemical Vapour Deposition Of Silicon Nitride

Silicon nitride is is deposited on top of the bottom cladding layer by low pressure chemical vapour deposition (LPCVD). Dichlorosilane ($SiCl_2$) and ammonia (NH_3) are typically introduced at a controlled rate into a vacuum furnace between 700-800 °C [101, 102] and specifically for the SEMCO furnace in the JWNC the operational temperatures are 765 °C at the chamber inlet, 790 °C in the middle of the chamber, and 810 °C at the chamber outlet. The chamber is maintained at 300 mTorr during deposition. The chemical reaction is given by

$$3SiCl_2 + 4NH_3 \rightarrow Si_3N_4 + 6HCl + 6H_2 \tag{5.1}$$

and precursor gases have flow rates of 40 sccm for $SiCl_2$ and 160 sccm for the NH_3. The resulting Si_3N_4 can be expected to exhibit high tensile stress as established in literature [32, 33], the greatest deposition thickness achieved in this work was 300 nm. It is possible to deposit thicker films using temperature cycling and annealing techniques, but the increased strain could result in cracks from during the etching process due to the stain on the backside of the wafer. This deposition can lead to hydrogen being incorporated into the film and forming bonds with nitrogen. The N-H bond has a stretching absorption at 3300-3400cm^{-1} which corresponds to about 3 µm which gives a first order harmonic at 1500 nm and a second order harmonic at 750 nm [103, 104]. This could cause significant absorption for a Si_3N_4 waveguide operating at 780 nm if the absorption peak is sufficiently broad. It is common practise to reduce the hydrogen content in silicon nitride by annealing at high temperatures (>1000°C) for several hours [102–105].

An experiment was conducted with three test samples and a control sample, all of which consisted of 200 nm of LPCVD Si_3N_4 on a silicon substrate, annealed in a small Carbolite tube furnace at 1000 °C with a nitrogen gas flow of $\sim 50\ l\,h^{-1}$. A silicon reference sample was prepared to be measured and so provide the background absorption of the substrate. The reference sample is taken from the same wafer as the test sample and so the Si_3N_4 is removed by wet etching in hydrofluoric acid, this sample preparation was carried out by Dr Kevin Gallacher. The absorption was seen to decrease at 3 µm and therefore the harmonics at 1500 and 780 nm (the detector is not sensitive to these wavelengths) but the results are very inconsistent for the three samples. This was attributed to inconsistent temperatures along the length of the tube furnace. It is clear that a larger furnace with greater uniformity is required; the wet oxidation furnace tube in the SEMCO furnace in the JWNC was considered but its maximum operating temperature is 1000°C. Work in the literature suggests that the process is greatly affected by varying temperature between 900-1150°C [104].

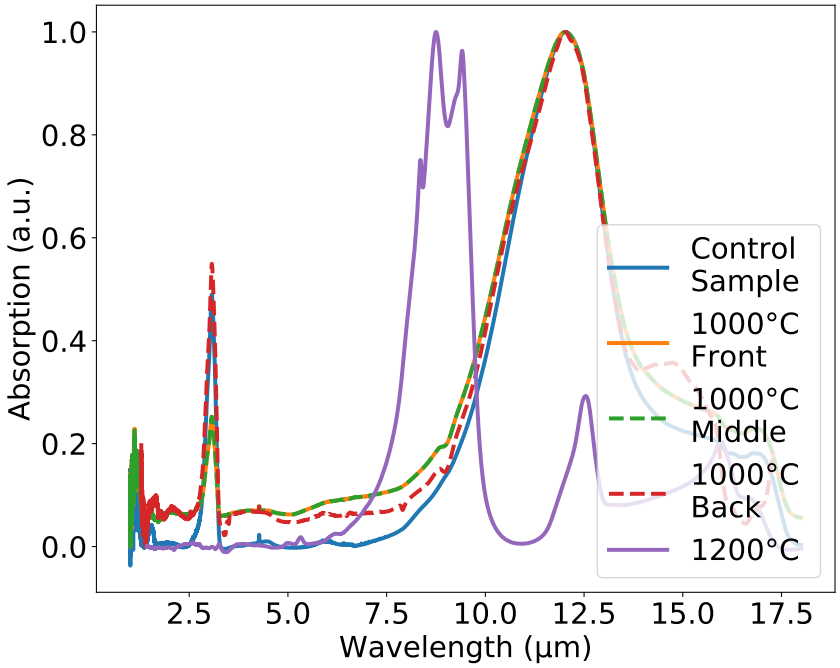

Figure 5.2: Fourier transform infra-red spectroscopy of Si_3N_4 annealed under various conditions and a control sample which was not annealed. The difference in absorption spectra between the samples annealed in a 1000 °C tube furnace indicates that the samples experienced a considerable temperature gradient depending upon their position in the tube. The sample annealed at 1200 °C shows that the N-H bonds have been eliminated as expected but that the Si_3N_4 has oxidised.

To demonstrate this, a wafer was annealed in the Carbolite RHF 1500 at 1200°C for 4 hours and another FTIR measurement was performed (see Figure 5.2). Unfortunately, this furnace operates at atmospheric conditions with no vacuum or gas flows. It is because the furnace operates in atmosphere that the silicon nitride has oxidised causing a substantial change in the absorption spectra at higher wavelengths. The large peak at 12.5 µm is indicative of Si-N bonds while the peaks around 9 µm are indicative of Si-O bonds [106]. Silicon oxynitride has a lower refractive index that silicon nitride [107] and so could result in reduced scattering loss if used as a waveguide core, this will be investigated in future work. This experiment has shown that annealing at 1200 °C can eliminate absorption as 3 µm but it has also shown that this oven is not suitable for annealing silicon nitride.

The Carbolite tube furnace was then modified by re-positioning the quartz tube which allowed for greater uniformity and for the furnace to be safely operated at its maximum temperature of 1100°C. The LPCVD Si_3N_4 was characterised by ellipsometery, finding the refractive index at 780 nm to be 1.987±0.001 as deposited, and 1.9973±0.0004 after annealing at 1100 °C (see Figure 5.3). The refractive index increases as a result of the annealing while the error associated with this measurement goes down. As film densification occurs, residual hydrogen trapped during deposition are allowed to escape resulting in a more consistent and higher refractive index film.

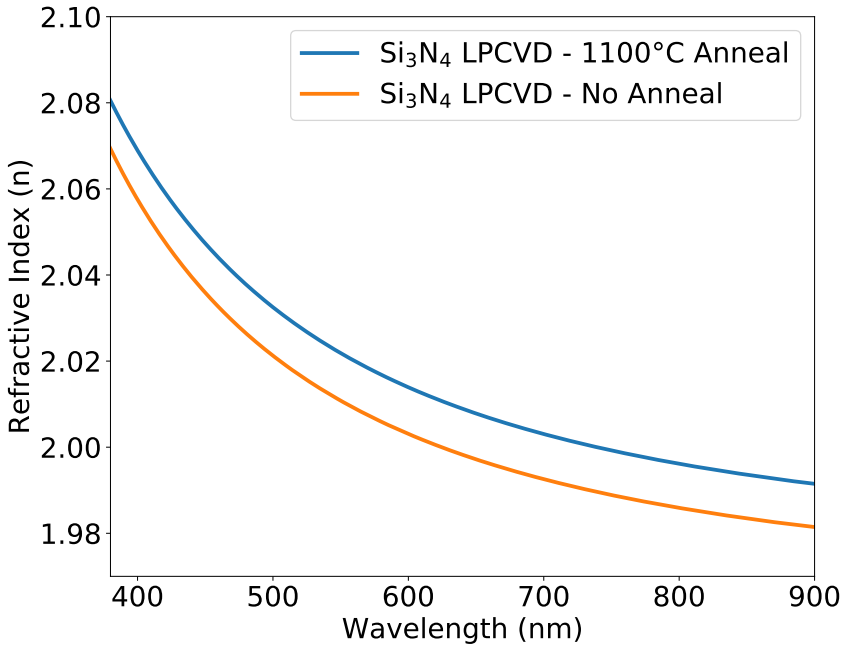

Figure 5.3: The refractive index of Si_3N_4 is found by fitting a Cauchy model to the ellipsometer data. The refractive index for Si_3N_4 LPCVD is shown to increase upon annealing at 1100 °C as film densification occurs.

5.2.3 Plasma Enhanced Chemical Vapour Deposition Of Silicon Dioxide

PECVD is used to deposit SiO_2 on top of samples with etched Si_4N_4 waveguides. Samples are loaded on to grounded bottom electrode in a vacuum chamber. The top electrode is excited with a radio frequency (RF) to produce a plasma within the chamber during deposition performed at 300 °C. The tool that is used is the SPTS PECVD from Orbotech. The initial recipe, which shall be referred to as PECVD 1, was performed at 300 °C and 900 mT with high frequency RF power of 40 W, and N_2 (392 sccm), N_2O (1420 sccm), and SiH_4 (20 sccm) gases. This process produced a SiO_2 film with a refractive index of 1.464, far from the desired 1.4544 required to match the index of the bottom cladding. This index mismatch results in a top cladding which supports a slab mode. Because this slab mode is perturbed by the Si_3N_4 waveguides, some combination of the higher order modes supported by the SiO_2 film are detected in the vicinity of the waveguides, thereby obscuring the desired mode by raising the noise floor. The effect of a top cladding mismatch is best modelled using the 1-D solver (see Figure 3.4). The refractive index of the SiO_2 film can be lowered by annealing the sample at 1100 °C (see Figure 5.4) but ultimately the refractive index could not be lowered enough in this way and the resulting slab mode caused insurmountable obfuscation of the waveguide fundamental mode.

A new process (PECVD 2) was developed which could, without annealing, provide a refractive index close enough to that of the bottom cladding to suppress the formation of any undesired slab mode. This new deposition process was again performed at 300 °C but at a pressure of 2150 mTorr with 550 W of high frequency RF power and only N_2O (3000 sccm), and

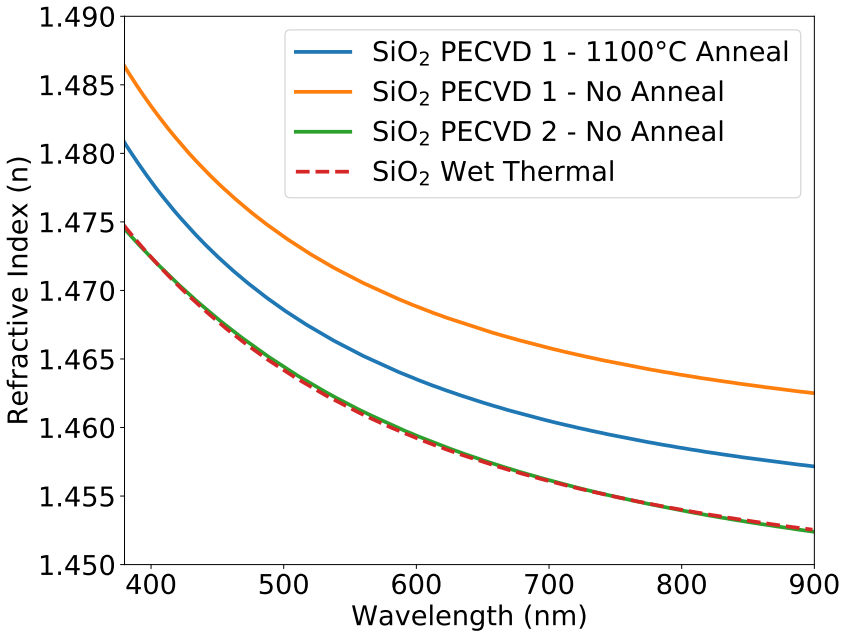

Figure 5.4: The refractive index of SiO_2 is found by fitting a Cauchy model to the ellipsometer data. The refractive index for SiO_2 PECVD 1 is shown to improve upon annealing at 1100 °C but still differ significantly from the refractive index of wet thermal SiO_2. The refractive index for SiO_2 PECVD 2 is shown to match the refractive index of wet thermal SiO_2 with requiring any further annealing.

SiH_4 (175 sccm) gases. Sample wafers were prepared with 1 µm of SiO_2 and measured using a JA Woollam M2000X spectroscopic ellipsometer, finding that the PECVD SiO_2 as deposited had a refractive index of 1.454 $\pm$ 0.003 at 780 nm whilst the SiO_2 bottom cladding grown by wet thermal oxidation has a refractive index of 1.4544 $\pm$ 0.0001, see Figure 5.4. The thermal oxide process is more consistent than the PECVD process as expected, with a refractive index error which is an order of magnitude less.

5.3 Sample Processing

Bottom cladding and core material deposition steps are carried out at the 6” wafer scale. This is much larger than the typical sample size and so the wafers must be cleaved into chips of the desired size. Each design iteration leads to the production of multiple test samples which can be processed individually or in batches depending on the test parameters. The process flow used to fabricate test devices is shown in Figure 5.5. Solvent cleaning and HSQ development followed standard procedures which were not modified. The resist spinning process was varied while the lift-off process was developed and the PMMA deposition was omitted while experimenting with a process in which the HSQ mask was left on top of the waveguide in the finished device. Electron beam lithography processing was routinely modified to reduce the electron beam write time while providing sufficient resolution and reactive ion etching processing times were modified for

Si_3N_4 films of different thicknesses. The SiO_2 PECVD process was developed in parallel as the work progressed and so was modified frequently; often samples within the same design batch would receive different top cladding layers. Waveguide facet preparation followed a standard process but inherently required that samples were polished individually.

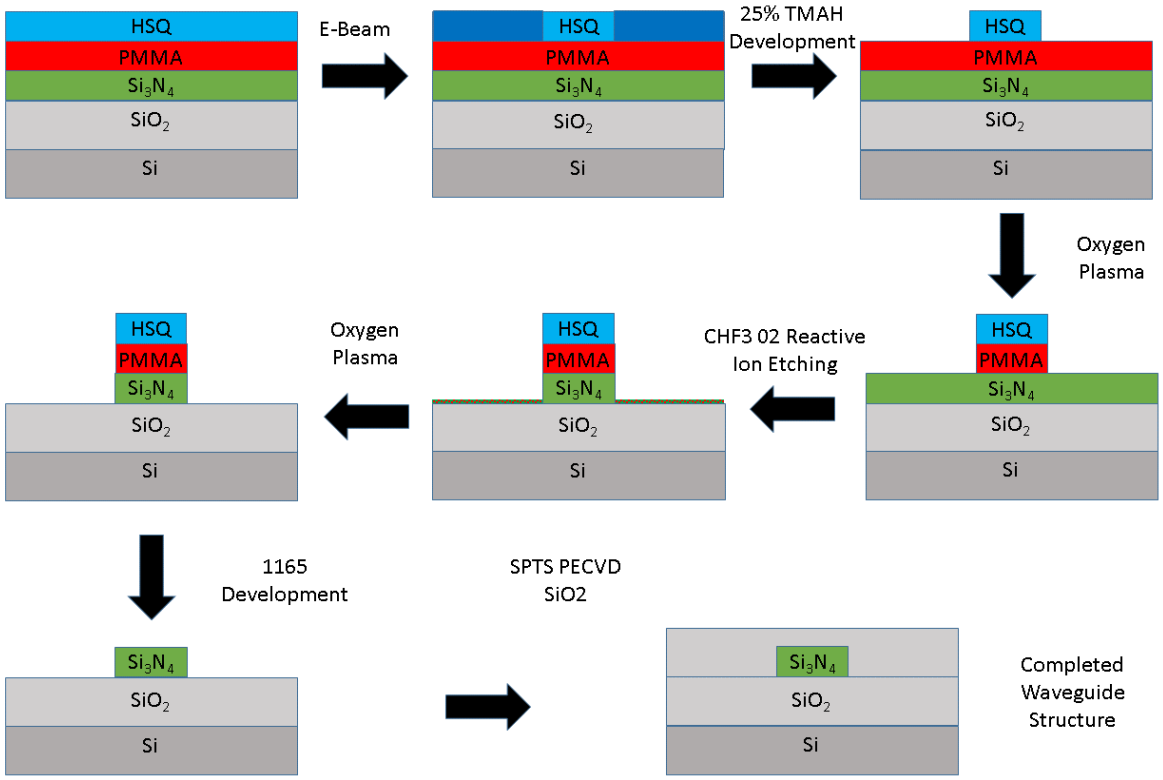

Figure 5.5: Si wafer is subjected to wet oxidation providing a SiO_2 substrate, a Si_3N_4 core layer is then deposited by low pressure chemical vapour deposition. PMMA resist and HSQ resist layers are then spun on. The HSQ is patterned with electron beam lithography, then developed with Tetramethylammonium Hydroxide. The exposed PMMA is removed with O_2 plasma. The Si_3N_4 is ecthed with CHF_3 reactive ion etching, and the remaining PMMA is removed with 1165 resist stripper leaving a ridge waveguide. A top cladding layer is then deposited by plasma-enhanced chemical vapour deposition to create a buried waveguide.

5.3.1 Wafer Cleaving

The silicon wafers are chosen such that they have (100) crystal orientation [108]. To ensure that any resulting shards of silicon or any particulates do not contaminate the wafer surface, the

wafer is first subjected to spin-coating of a photoresist. Typically MicroChem S1818 was used for this but the actual resist used is immaterial as long as in can be removed later in the solvent cleaning step. The coated wafer is secured to the work surface and a diamond tipped scribe tool is used to nick the edges of the silicon where it is to be cleaved and the crystal orientation typically ensures that cleaving is orthogonal.

5.3.2 Solvent Cleaning

Samples are cleaned in a laminar air flow cabinet. They are first submerged in acetone in a beaker and then placed into an ultrasonic bath which is then turned on for 2 minutes. This is repeated with a new beaker of acetone to minimise any residue. The sample should not be left to dry because acetone leaves a residue as it dries. Instead the samples are transferred to beakers with isopropyl alcohol (IPA). Samples are removed from the IPA and then held down on a clean room wipe and dried with a nitrogen gun. Cleaned samples are then subjected to O_2 plasma ashing which, as well as aiding in cleaning the samples, promotes adhesion of the resist because it results in an active surface [109].

5.3.3 Resist Spinning For Lift-off

Prior to resist spinning, samples are dried in an 180 °C oven for about 30 min to further promote resist adhesion. There are two stages of resist spinning in this process because lift-off is performed. The sacrificial layer of resist is spun on first, polymethyl methacrylate (PMMA) is spun on at 2,000 rpm resulting in approximately 50 nm of PMMA on the sample. The sample must then be baked either in an oven or on a hotplate at 180°C for 30 min or 90 s respectively. The thickness of the remaining PMMA film is measured using the Filmetrics thin film mapping tool which measures the reflectance of the sample, compares this to a baseline measurement of a calibration wafer of known reflectance, and then fits a model to the measured data which takes into consideration the refractive indices of the material stack and approximate thickness estimated by the user (see Figure 5.6).

The resist which is actually used for lithography is hydrogen silsequioxane (HSQ) which is a inorganic negative tone electron beam lithography resist, negative tone means that the areas of resist exposed to the electron beam will remain after development. This is especially desirable when writing very small features by electron beam, as writing the same features in a positive tone resist would take a far greater amount of time. HSQ was originally developed for the semiconductor industry to serve as an insulating layer and to be used in planarisation [110]. Early work using HSQ as an electron beam lithography resist demonstrated that a line edge roughness of < 2 nm was achievable [111], this agrees with the line edge roughness value used in the Lacey-Payne model in Section 3.2. Electron beam exposure causes the cubic structure of HSQ (see Figure 5.7) to break up and form a linear network structure by cross-linking. The

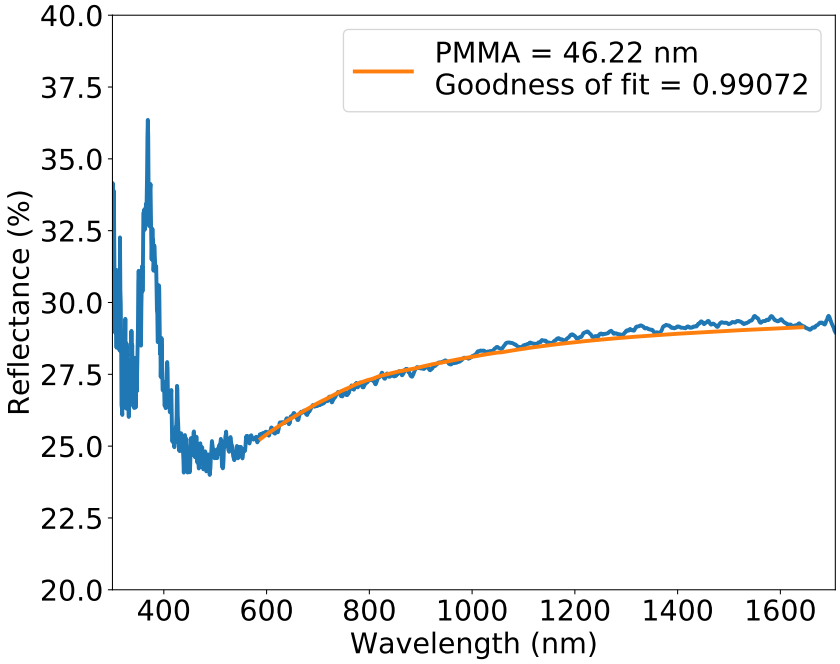

Figure 5.6: Reflectance measurement using the Filmetrics thin film mapping tool. The reflectance is modelled by taking into consideration the material refractive index and estimated thickness. The sample used was bare Silicon with PMMA spun on top. This allowed for a cleaner signal and a high "goodness of fit". A goodness of fit of 1 would be a perfect fit.

Si-H bonds are weaker than the Si-O and so these bonds break due to the electron beam expose resulting in the formation of silanols (with the Si-OH group) which form a linear network of Si-O-Si bonds. This final cross linked structure is silica like and when used as an etch mask, is often left in place as its absorption is very similar to silicon dioxide [112]. Alkaline developers are used to develop HSQ. The OH^- reacts the unexposed HSQ to from ionised silanol which is soluble in the developer and so the unexposed HSQ dissolves in the developer. Several alkaline developers can be used for developing HSQ such as sodium hydroxide (NaOH), lithium hydroxide (LiOH), and potassium hydroxide (KOH) however tetramethylammonium hydroxide (TMAH) is commonly used to develop HSQ in the JWNC [110]. HSQ is spun on at 5,000 rpm resulting in a film around 330 nm thick.

5.3.4 Electron Beam Lithography

The Vistec VB6 UHR EWF electron beam lithography tool is used to pattern device features. The main benefits of electron beam lithography are the possibility of writing sub-5 nm features and the ability to change designs without producing multiple photomasks (as would be required for photolithography). The VB6 has many electromagnetic coils to align, shift, focus, and scan the beam in the x and y directions; there is also an electrostatic blanker unit which uses an electric field to divert the beam such that it can be blocked, turning it on or off. The main-field coils direct the beam within the main field to select a sub-field and the sub-field coils

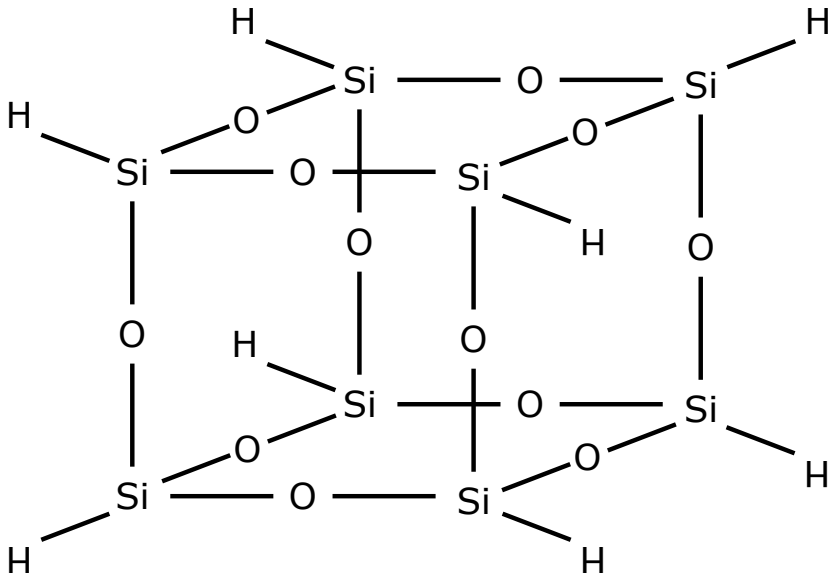

Figure 5.7: Hydrogen silsequioxane (HSQ) is commonly used resist for high resolution (< 2 nm) electron beam lithography, it has a cubic structure which is broken up by alkaline developers resulting in the formation of a liner network of silanols that is silica-like.

write a pattern within the sub-field. The tools pattern generator has a 20 bit digital to analogue converter (DAC) allowing $2^{20} = 1,048,576$ pixels while the maximum size of the writing field is 1.310 72 mm as determined by the design of the tool. The VB6 resolution is the writing field size divided by the number of pixels and so the maximum writing size gives a resolution of 1.25 nm; it is also calibrated for 1.0 nm and 0.5 nm resolution corresponding to a maximum field size of 1048.576 µm and 524.288 µm respectively but for this application it is generally beneficial to have the largest main field possible and a resolution of 1.25 nm is more than sufficient. For patterns larger than the main field the electron beam cannot be deflected enough to write the entire pattern and so the pattern is split into fields 1.2 mm $\times$ 1.2 mm; to move between these fields, the sample stage must be moved such the centre of the electron beam deflection range is centred on the next field. The calibration of the sample stage movement drifts over time and can introduce significant stitching errors in features crossing adjacent main fields (see Figure 5.8).

The main fields are then split into up to 64 $\times$ 64 sub-field squares for the 1.25 nm resolution. Within each sub-field, the beam moves between dose locations remaining at each one for a duration of time which will give the required dose. The minimum time is limited by the maximum clock frequency of the pattern generator which is 50 MHz, the time needs to be long enough that it can be sampled at 50 MHz. Dose is a measure of the number of electrons incident on an area and is affected by proximity to other areas of exposure; this is called the proximity error effect. The area dose is defined by [110]

$$\text{Area Dose} = \frac{I_{\text{Beam}}}{f_{\text{Clock}} \times \text{BSS}^2} \tag{5.2}$$

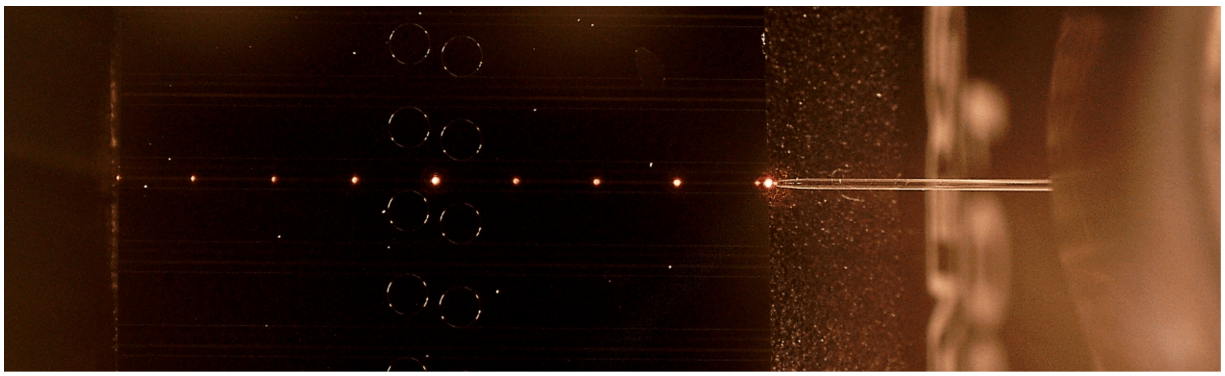

Figure 5.8: A sample fabricated during a period in which the electron beam sample stage was poorly calibrated. Light is coupled into the waveguide by lensed fibre and the effect of the waveguide stitching errors can be seen as there is significant light scattering at each main field boundary within the bus waveguide of the micro-ring resonator.

Table 5.1: VB6 Beam Current And Spot Size.

Beam Current (nA)	Spot Size (nm)
1.0	4
2.0	6
3.9	9
8.2	12
16.0	19
32.0	24
63.6	33
131	45

where I_{Beam} is the beam current (A), f_{Clock} is the clock frequency (Hz), and BSS is the beam step size (m). BSS is given by

$$\text{BSS} = \text{VRU} \times \text{Resolution (1.25nm)} \tag{5.3}$$

where the VRU is the variable resolution unit, an integer between 1 and 512 chosen by the user. When submitting a VB6 job, the user selects the dose, the beam current and VRU (thereby determining the BSS). If too small a VRU is chosen, then this will violate the maximum clock frequency of the pattern generator. The choice of beam current affects the spot size of the beam (see Table 5.1) [110]. A higher VRU results in a larger BSS which causes greater roughness in features, while a larger spot size results in a larger minimum feature size. A dose of $1300\,\mu\text{C}\,\text{cm}^{-2}$ was used to write the patterns using HSQ resist, high resolution feature like the waveguide were written using the 8 nA (12 nm) beam while larger, lower resolution features were written using a 64 nA (33 nm) beam. Vistec provide a software called Beamer which is used to extract layers from a GDSII file and create a VEP file which the VB6 can interpret and is used to direct the electron beam and write the pattern. The VEP file provides information like proximity error correction, fracturing method, and is used to merge overlapping layers.

Proximity error correction routines ensure that the edges and corners of features are sufficiently dosed, fracturing breaks down shapes in the design into smaller rectangles the VB6 can write, and healing layers eliminates regions of overlap ensuring that these regions are not accidentally overdosed. Beamer can be used to visualise the effects of spot size and beam step size. A novel use of Beamer is to reduce the job time by using the bulk and sleeve method which is used to split a layer into regions that written using the large and small spot sizes. The edge roughness of a waveguide greatly affects performance and so the edges are patterned with a smaller spot size. This is achieved by negatively biasing the original layout to reduce its size forming the bulk, subtracting the bulk from the original to form the sleeve and positively biasing the bulk by at least 1 BSS to ensure there is no gap between bulk and sleeve. Completed Beamer files are exported as separate VEP files and typically there is a Beamer file and VEP file for each layer in the GDSII file.

Belle is software created by Stephen Thoms at The University Of Glasgow. The software is necessary to gather all VEP files that are to be written in one VB6 job. Within Belle the user defines the substrate size and type, beam current and spot size, beam step size, dose, pattern locations, text to be written on the sample, layer to layer alignment, tilt correction, and other options. A Belle file is saved with a filename, comprised of the users initials followed by 4 digits, and transferred to the computer used to operate the VB6 tool. This filename is written on the sample box as well as a unique sample number and VB6 job number before samples are submitted for lithography. The naming convention is important because the VB6 tool is operated by technicians who are not expected to have intimate knowledge of the device that they are processing.

5.3.5 Hydrogen Silsequioxane (HSQ) Development

Typically, exposed HSQ is developed by holding the sample in a beaker of room temperature 25% tetramethylammonium hydroxide (TMAH) solution for 30 seconds, then a beaker of deionised water for 30 seconds, then a beaker of IPA. However, in this case the surface tension of water could cause features to collapse or delaminate and so IPA is used in place of de-ionised water. Appropriate safety measures must be taken when using 25% TMAH because it is a strong alkaline and can cause severe chemical burns, even death if inhaled, ingested or absorbed through the skin [113].

The next fabrication step (see Figure 5.5) is to remove the exposed PMMA using an oxygen plasma. The Plasmafab RF Barrel Asher has been calibrated to provide an etch rate of ~ 10 $\mathrm{nm\,min^{-1}}$ for organic polymers when the oxygen flow rate is set to 35 sccm and the RF power is set to 110 W. This process is dependent on temperature and so the chamber of the asher is water cooled, to ensure the process is consistent and the chamber is allowed to cool before the process is run. The success of this process was confirmed by measuring the step height of waveguide features using Dektak stylus profiler before and after lift-off. The result of this characterisation

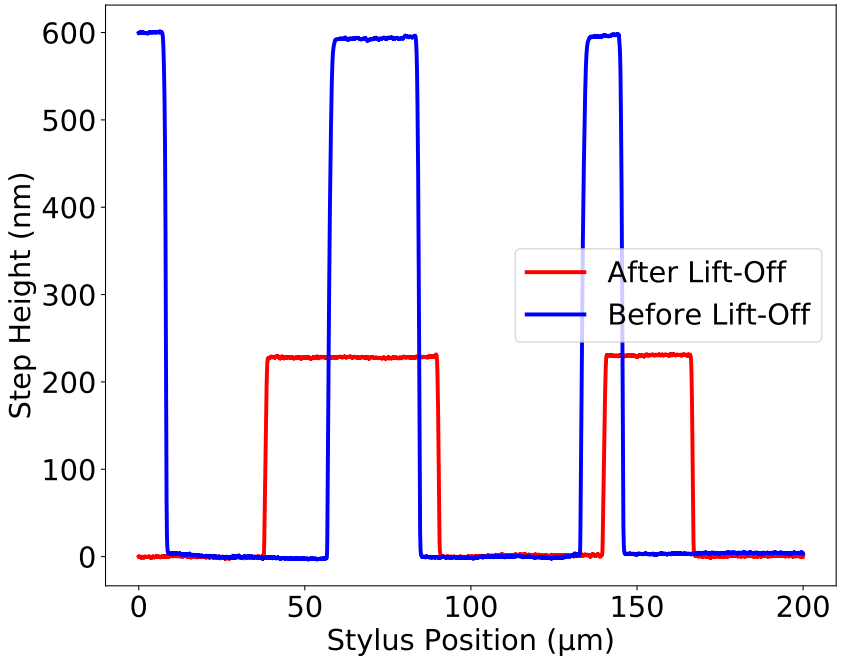

Figure 5.9: The Detak stylus profiler data for $\sim 200\,\text{nm}$ thick waveguide features before and after the HSQ etch mask is removed by lift-off. Before and after measurements were not performed in the exact same location. Lift-off is achieved using a sacrificial layer of PMMA which can be easily removed with acetone. The waveguide thickness may be exaggerated by over-etching into the SiO_2 cladding

is shown in Figure 5.9.

5.3.6 Reactive Ion Etching And Lift Off

The developed HSQ acts as an etch mask ensuring that the desired pattern is protected from an etching process that removes the rest of the silicon nitride. The etching process used for this work is a reactive ion etching process using trifluoromethane (CHF_3) as the principal etch gas with a flow rate of 50 sccm and oxygen (O_2) with a flow rate of and 5 sccm. The RF power was set to 150 W, the temperature to 20 °C, and the pressure to 55 mTorr. The RF field strips electrons from the CHF_3 causing the trifluoromethane to disassociate into fluorine atoms and $CHF_2{}^+$ ions. The ions are accelerated towards the sample placed on the negatively charged electrode. The chemical reactions that result in etching of the Si_3N_4 surface are [114, 115]

$$Si_3N_4 + 12CHF_2^+ \rightarrow 3SiF_4 + 2N_2 + 6H_2 + 12CF \tag{5.4}$$

and

$$Si_3N_4 + 12F \rightarrow 3SiF_4 + 2N_2. \tag{5.5}$$

The etch rate is expected to be around $50\,\text{nm}\,\text{min}^{-1}$ and this can be confirmed using an interferometer during the etching process (see Figure 5.10). The thin Si_3N_4 films used in this

work result in short etch times and so there is no need to be concerned about the formation of excess polymers of the sample surface [102]. As the silicon nitride is etched away, the interferogram moves through a few fringes and the there is a noticeable change in etch rate as the silicon dioxide bottom cladding is reached. Some over-etching is expected and it is possible that the roughness introduced by this over-etching is a contributing factor to the improved performance seen in devices with a top cladding. The reduced index contrast between the top and bottom cladding relative to the air and bottom cladding would result in reduced scattering with the addition of a top cladding layer.

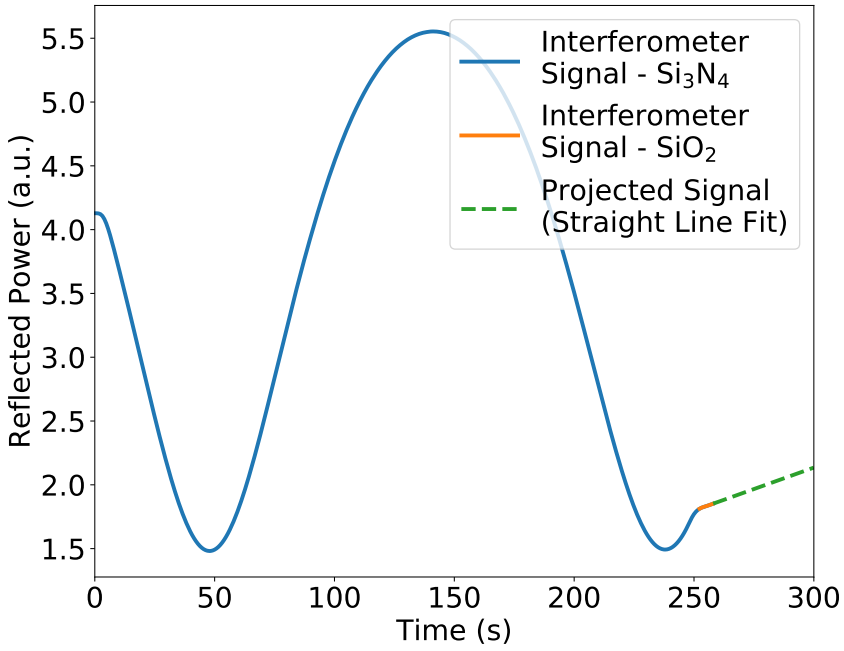

Figure 5.10: The sinusoidal interferogram is expected as the Si_3N_4 is etched away, this is similar to scanning a mirror on a Fabry Pérot interferometer. The SiO_2 has a different etch rate and so there is a noticeable deflection in the interferogram once the etch is complete and the SiO_2 has begun to be etched. This is emphasised here by a projected straight line fit of the deflected region, this would take a sinusoidal form if the etch were allowed to continue.

Once the etch is completed, the etch mask can be removed by lift-off. The lift-off is performed by submerging the sample in a beaker with Microposit Remover 1165 which is an organic solvent typically used to remove baked photoresist. The beaker is then placed in a 80 °C water bath for a period of 10 min. Due to the flammable nature of Microposit Remover 1165, this is not done at higher temperatures. The success of this process is illustrated in Figure 5.9. At this stage the sample is ready for the top cladding deposition as outlined in Section 5.2.3. Before this step the sample can be inspected by scanning electron microscope (SEM) to ensure that there are no etch defects, this is of particular importance in the coupling region, an example SEM image of a Si_3N_4 micro-ring resonator is shown in Figure 5.11.

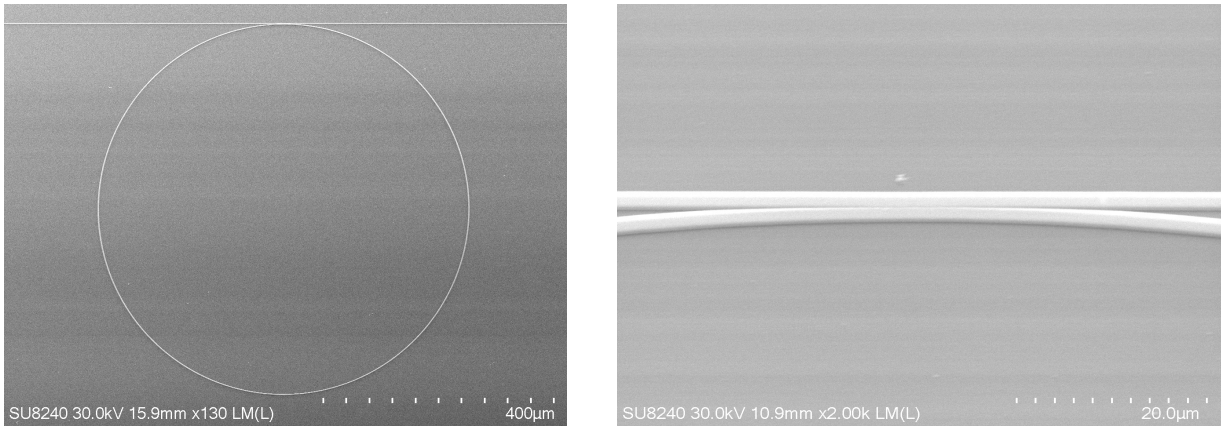

Figure 5.11: Scanning electron microscope images were taken of a micro-ring resonator (left) and a close up image of the coupler region (right).

5.3.7 Waveguide Facet Preparation

Completed waveguide samples must be diced or cleaved to expose the waveguide facets for testing. Cleaving is a simple method of sample preparation but the optical quality of the resulting facets is not guaranteed. Before cleaving or dicing, the sample is coated in a protective layer of photoresist which protects the waveguide features from the resulting silicon debris would could potentially scratch or otherwise contaminate the waveguides. In order to cleave samples, a scribing tool is used to nick the edge of the samples at precise locations parallel to the sample cleavage planes, the samples are then placed over a securely held razor blade aligned to the scribe marks, this allows the samples to be cleaved manually in a controlled manner. Dicing and polishing is a more involved but more repeatable process. Samples are cut perpendicular to the waveguides using a DISCO DAD3350 diamond dicing saw. This results is a flat edge which can be easily polished but does not produce optical quality facets initially because of saw marks in the facet. Diced samples are then securely clamped in the waveguide polishing gig and mounted in the Allied High Tech Products Multi-prep Polishing System. The polishing system consists of a rotating platen with an abrasive pad and an oscillating head which moves samples across the rotating platen and then water is flowed across the platen surface to act as a cutting fluid and remove debris (see Figure 5.12). The force applied by the oscillating head is controlled by varying the counter weight from 400-200 g and abrasive pads with particles sizes of 9 µm down to 10 nm are used. The rotational speed of the platen and the sample oscillation rate can be controlled and slower speeds result in a less aggressive rate of material removal. A slower rate of removal can be sought after in order to minimise the heat build-up due to friction as a excessive heat build-up can lead to carbonisation of the protective layer of photoresist. By decreasing the force applied and decreasing the particle size of the abrasive pads, a smooth, optical quality waveguide facet can be achieved. Polished or cleaved samples are then subject to another solvent clean (as detailed in section 5.3.2) to remove any leftover debris from the polishing/cleaving process and the protective resist layer.

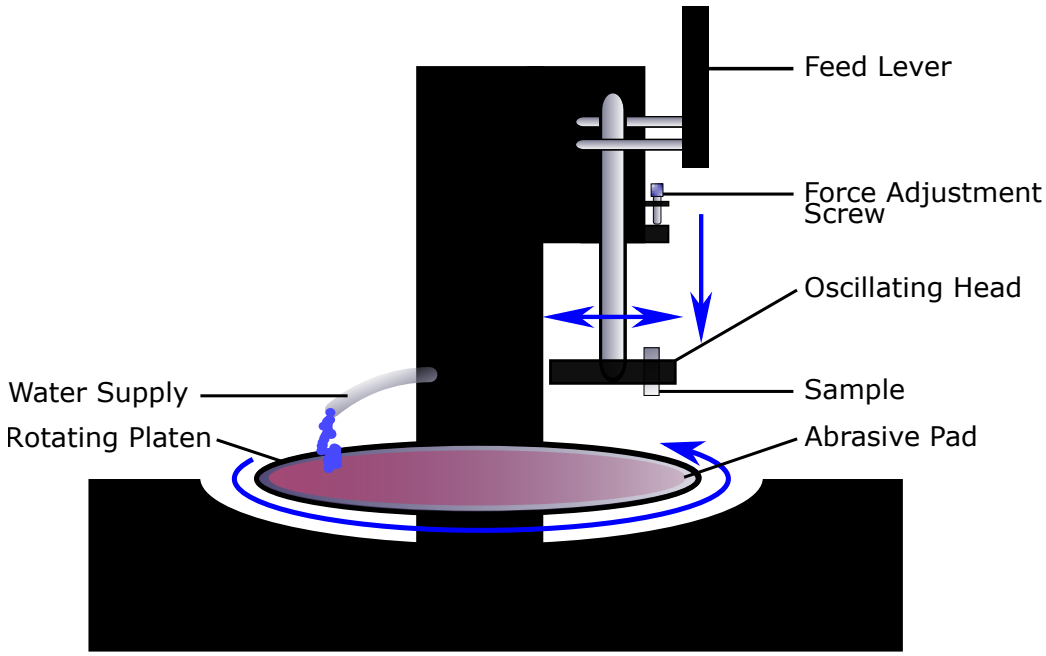

Figure 5.12: Allied High Tech Products Multi-prep Polishing System consists of a rotating platen with interchangeable abrasive pads and an oscillating head which moves samples across the rotating platen. Water is flowed across the platen surface to act as a cutting fluid and remove debris. Force applied to the oscillation head, the rate of oscillation, and the rotational speed of the platen can be controlled. Together these determine the rate of material removal.

5.4 Discussion

A process has been developed for the fabrication of LPCVD silicon nitride core waveguides with a thermal oxide bottom cladding and PECVD silicon dioxide top cladding on a silicon substrate. There remain many possible avenues of process development for future work. These include the development of thicker top and bottom cladding layers, a reactive ion etching process resulting in lower damage and smoother sidewalls, a comparison of photo-lithography and electron beam lithography methods, the development of thicker silicon nitride (requiring stress relaxation of the Si_3N_4 film) or thinner silicon nitride (requiring a thicker bottom cladding to avoid substrate loss), and smoothing of the material interfaces by chemical mechanical polishing (CMP) in order to reduced scattering at top and bottom faces of the silicon nitride core. Thicker bottom cladding could be achieved simply by increasing the growth time but as required deposition time goes exponentially with film thickness this was not deemed to be a practical solution. Thermal silicon dioxide films up to 15 µm are commercially available and have been procured for future development. Another possible method of producing thicker bottom cladding is to use PECVD to supplement the thermal oxide bottom cladding or simply use PECVD for the entire bottom cladding. Using PECVD to supplement a thermal oxide bottom cladding could introduce another material interface resulting in increased scattering at that interface. A PECVD bottom cladding could potentially improve the index matching between the top and bottom cladding if the same

process was used for both films but at present the refractive index resulting from the PECVD process has a refractive index error an order of magnitude greater the refractive index of films produced by thermal oxidation and so a PECVD bottom cladding is expected to only exacerbate modal mismatch and the resulting issues caused by slab mode formation. A reactive ion etching process using sulphur hexafluoride and nitrogen gas flows has been shown [116] to produce vertical, low damage sidewalls and shows promise for development of an etch process resulting in smoother sidewalls. Micro-rings were fabricated using this process and subsequently characterised but the results were inconclusive and this avenue of process development was deemed too time consuming to be completed within this body of work. Electron beam lithography was used in this work because it allows for rapid prototyping and very small feature sizes ($< 10\,\text{nm}$). It is possible however that the line edge roughness of the waveguides is limited by the electron beam lithography rather the etch process and so it is desirable to directly compare the results of a micro-ring fabricated using electron beam lithography with a micro-ring fabricated using photo-lithography [117]. It has been found that propagation loss of waveguides is expected to be reduced for wider waveguides and so for micro-rings with wider waveguides ($> 1\,\mu\text{m}$), the small feature size was only required to realise the gap spacing between the bus waveguide and the micro-ring which was typically $\sim 200 - 300\,\text{nm}$. Larger gap spacing with similar coupling coefficient could be realised utilising a racetrack ring-resonator design. It would be possible to design micro-rings with minimum features size ($> 1\,\mu\text{m}$) which could be fabricated by photo-lithography and by electron beam lithography to allow a direct comparison of micro-ring Q factors resulting from the two fabrication methods which would determine whether or not the line edge roughness of the waveguides was limited by the electron beam lithography.

The fabrication of low confinement nitride waveguide cores ($< 100\,\text{nm}$ thick) was hindered only by the unavailability of material with a suitably thick bottom cladding layer, these wafers are now available and this will be pursued in future work. Thicker silicon nitride layers require temperature cycling and potentially some form of strain relaxation. Strain relaxation of silicon nitride films can be achieved by the Damascene photonic process [33] whereby waveguide features are etched into the silicon dioxide bottom cladding and the resulting trenches are over filled with LPCVD silicon nitride and then planarized by CMP. This would require development of many new processes. Thicker silicon dioxide bottom cladding could be required to provide the same isolation from the silicon substrate for silicon nitride waveguides fabricated by the Damascene process although this could be mitigated if thicker (and higher confinement) silicon nitride waveguide cores could be fabricated. The lithography could require a positive tone resist as it would be the features that would need to be etched rather than the surrounding material but a suitable resist might not be able to function as an etch mask (such as HSQ does during the Si_3N_4 etch process used in this work). Amorphous silicon is used as an etch mask for etching the SiO_2 in the process detailed in [33] which would required some development before it could be used in the JWNC. Polishing by CMP would require characterisation of the surface roughness

by atomic force microscopy to check if polishing can be used to reduce the surface roughness and to quantify the resulting change.

Chapter 6

Ring Resonator Characterisation

Micro-ring resonators fabricated using the methods detailed in Chapter 5 were subjected to optical characterisation in order to determine their Q factor, considering the Q-factor to be the figure of merit for micro-ring resonators. Transmission spectra of the micro-rings were recorded by sweeping the input frequency of a 780 nm titanium sapphire laser and detecting the transmitted power on a silicon photodetector. The recorded spectra were analysed using regression analysis by the method of least squares to fit both a Lorentzian distribution and the equation describing the normalised power transmission of an all-pass micro-ring resonator (Equation 4.19) to the raw data in order to perform parameter estimation. The coupling coefficient was found using the method detailed in Chapters 2 and 3 and conclusions regarding micro-ring resonator performance are drawn with the assistance of insight gained from Chapter 4. The highest Q-factor value found in this work was $(1.38 \pm 0.04) \times 10^6$ for a 200 nm thick and 1100 nm wide silicon nitride waveguide core with a 1 µm silicon dioxide top cladding corresponding to a propagation loss of 0.261 ± 0.009 dB cm^{-1}. Comparisons are drawn between the micro-ring resonators in this work and those found in literature, finding that this work represents the highest Q-factor demonstrated for buried waveguides at such short wavelengths. The potential utilisation of the 1.4 million Q factor micro-ring resonator as a frequency discriminator is also discussed.

6.1 Method

A SolsTiS laser manufactured by M Squared Lasers was used to characterise micro-ring resonators designed and fabricated using the techniques outlined in Chapter 5. It has a titanium sapphire gain crystal and continuous tuning range of 670-1050 nm outputting TEM_{00} light with linewidth specification of $<$50 kHz (100 am). The laser linewidth was measured by beating it with a 200 Hz linewidth Koheras HARMONIK fiber laser system and fitting Lorentzian, Gaussian, and pseudo-Voigt distributions to the beat spectra in a process similar to that outlined in Section 6.2. From the fit parameters of these distributions, the linewidth was found to be 45, 56, and 51 kHz respectively (see Figure 6.1). The laser has three internal cavities which can

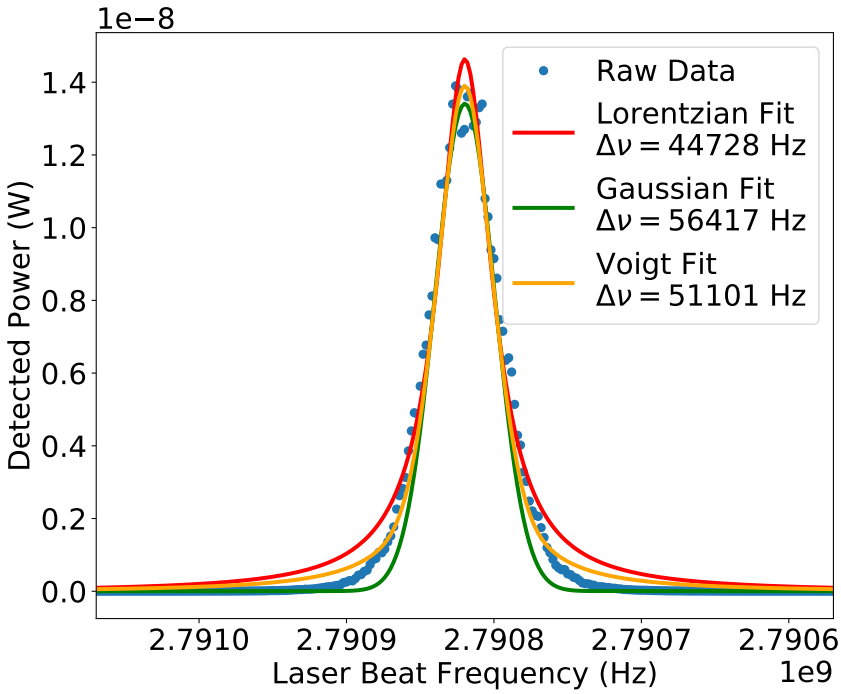

Figure 6.1: Linewidth of the SolsTiS laser measured by beating it with a 200 Hz secondary laser. A Lorentzian, Gaussian, and pseudo-Voigt distribution are fitted to the raw spectral data to determine linewidths of 45, 56, and 51 kHz respectively. Measurement was performed by Dr Euan McBrearty and Dr. Scott Watson.

provide three different frequency sweeps. These have a maximum scanning range of 250 GHz (500 pm), 66 GHz (130 pm), and 30 GHz (60 pm). The 30 GHz (60 pm) and 250 GHz (500 pm) scans were used exclusively in this work, these have a scanning resolution of 60 fm and 370 fm respectively. The laser output passes through an optical isolator to prevent reflected beams from entering the laser and an array of neutral density filters are in place to provide coarse control over the transmitted laser power. A optical chopper is in the free space path and the controller for the chopper provides a reference frequency for the lock-in amplifier that the photo-detector is connected to. This prevents stray light sources from introducing spurious signals.

Light is focused onto the tip of an optical fibre using an aspheric lens achieving typical output of 300 mW from the initial optical fibre which is then connected to a fibre attenuator which can provide fine adjustment. The complete fibre coupling layout is shown in Figure 6.2. A fibre based polarisation controller is used to ensure the correct polarisation is inject into the waveguides. The polarisation controller is connected to a lensed fibre constituting the last of 4 fibre-fibre connections in the optical path. Each of these connections is specified to have a loss of < 0.5 dB for 635 nm light when using single mode fibre such as was used in this setup. The fibre shielding is stripped back and the fibre is held in a V-groove fibre holder secured to a 4-axis stage (2 linear, 2 rotation) on a 1-axis stage which provides additional travel in the direction in which light is injected and raises the fibre to approximately the desired height. The lensed fibre has a spot-size of (5 ± 1) µm and a working distance of (25 ± 3) µm allowing for light to be

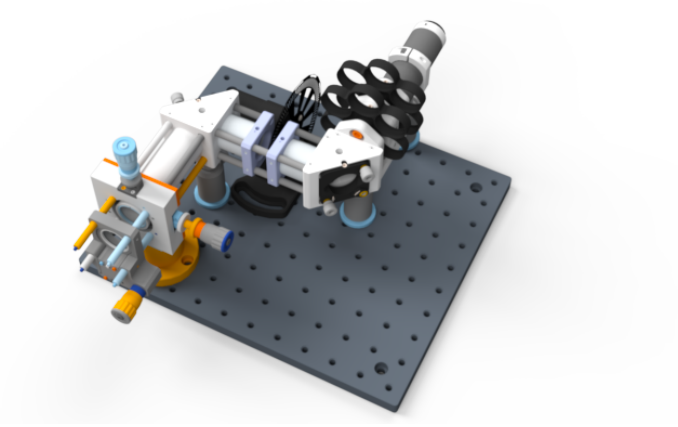

Figure 6.2: Fibre coupling setup is shown. Laser enters through the optical isolator (top right) and passes through the neutral density (ND) filter before hitting the first mirror. The beam then passes through the optical chopper before reflecting of the second mirror. The beam is then focused by an aspheric lens, secured in a 2 axis cage mount, onto the end of a 90° polished fibre. Image created by Dr. Euan McBrearty

focused onto the input facet of the waveguides. Fibres with smaller spot-sizes were often used for better power coupling and reduced scattering from the cladding but these are fragile and easily broken. To aid in alignment, each sample was designed to have very wide waveguides ($\sim 40\,\mu$m) and a triplet of 5 µm wide waveguides. The very wide waveguides are easy to align to and ensure approximate alignment of the system. The waveguide triplet indicated that the correct working distance had been set when light was well coupled into the centre waveguide and poorly coupled into the peripheral waveguides. Light exiting the chip is collimated using a microscope objective lens and can be detected using a silicon camera for alignment purposes or a silicon large area photo-detector connected to a Princeton 5210 lock-in amplifier for recording transmission spectra. The lock-in amplifier was configured with a time constant of 10 ms and typically the 1 mV scale was used.

The SolsTis laser is controlled using proprietary software that communicates with the laser using JSON (JavaScript Object Notation) via TCP (Transmission Control Protocol). It would have been desirable to begin data acquisition as the SolsTiS scan begins and end acquisition as the scan ends but the closed source software meant that communicating with the laser using 3rd party software proved to be a significant challenge. When the laser is configured to sweep across the same frequency range continuously, this results in rapid motion of the mirrors in the internal cavities of the SolsTiS between the start and end points of the sweep. The rapid mirror motion results in a sharp change in the power transmission which can be easily and precisely identified on the transmission spectrum. The lock-in amplifier is controlled using a modified LabVIEW file [118] which saves the data to a .txt file. The resulting raw data is shown in Figure 6.5.

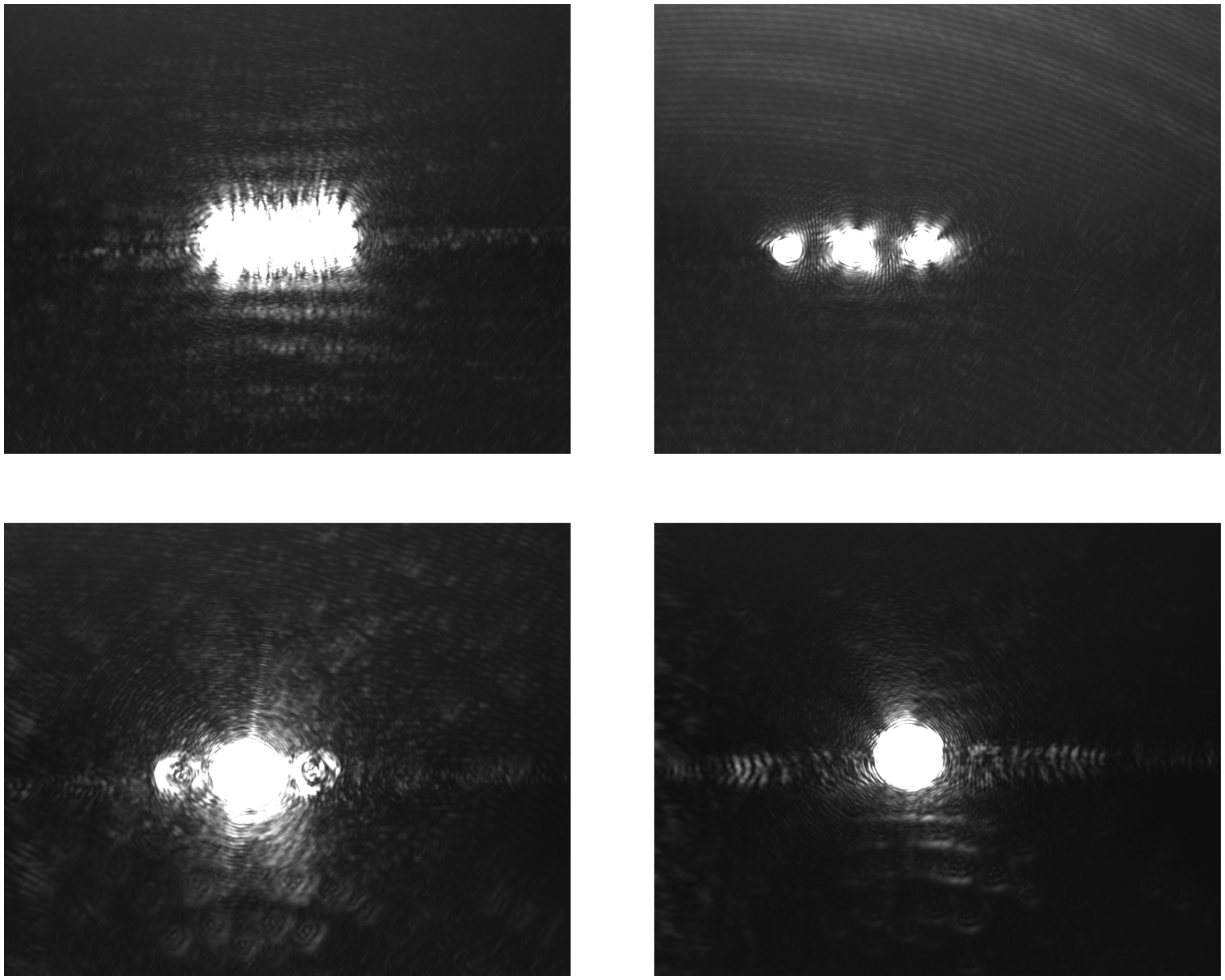

Figure 6.3: Top left: 40 µm slab mod waveguide for alignment of sample relative to lensed fibre input and objective lens at the output. Top right: Triplet of 5 µm waveguides used to find the lensed fibre working distance. Bottom left: Waveguide triplet with lensed fibre at the correct working distance. Bottom right: An aligned single mode waveguide with good power in coupling from lensed fibre. This is illustrated here with SU8 waveguides discussed in Chapter 8.

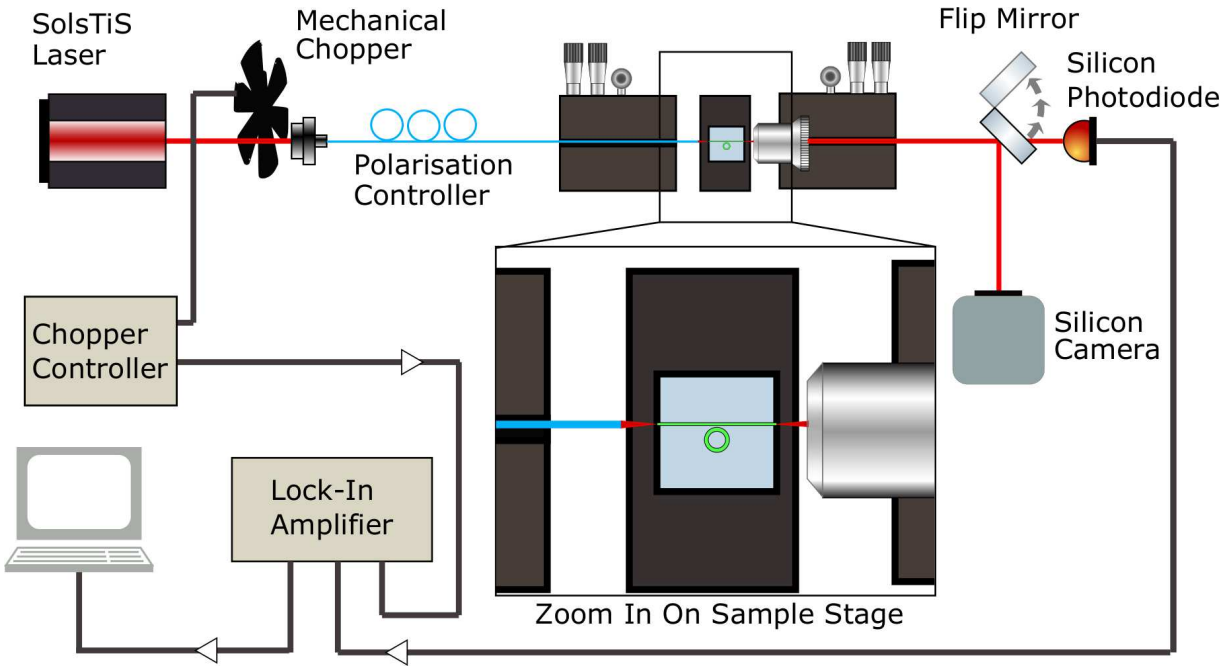

Figure 6.4: Schematic diagram of ring resonator optical transmission experimental setup.

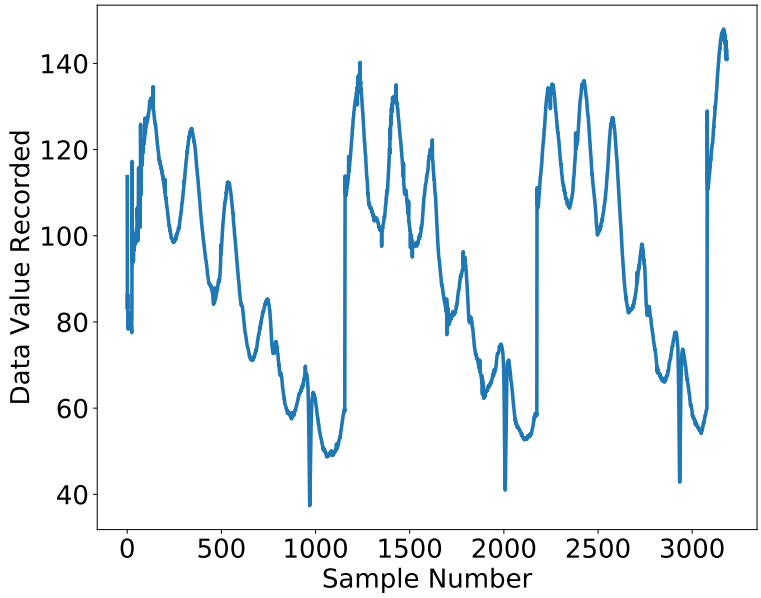

Figure 6.5: Raw data as recorded using LabVIEW directly from the Princeton 5210 lock-in amplifier. Data shows a few complete scans of the SolsTiS with data acquisition begins and ends at arbitrary times.

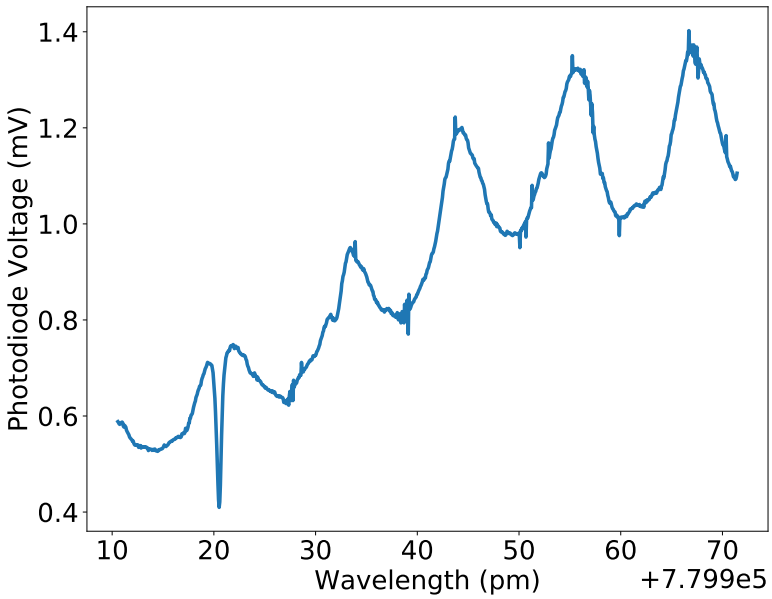

Figure 6.6: The data shown is cropped to include only one distinct sweep of the SolsTiS. The wavelength axis is determined by the centre wavelength and frequency span input to the SolsTis. The voltage axis is determined by scaling the recorded value by the scale setting on the lock-in amplifier at the time of acquisition.

6.2 Analysis

The data was loaded from the .txt file for analysis using a python script. The raw data is cut at the beginning and end of the wavelength sweep thereby creating y-data which is scaled by the voltage setting on the lock-in amplifier. A corresponding x-axis of the same length is created using the frequency span and centre wavelength input to the SolsTiS to create a linearly spaced variable. It is assumed here that the wavelength sweep is linear. The result is a calibrated plot of each SolsTiS sweep, see Figure 6.6 for a 30 GHz (60 pm) scan of the transmission spectra of a micro-ring resonator with 1100 nm wide 200 nm thick waveguide core, a 1 µm thick top cladding, and a radius of 300 µm. Sample spectra typically show a Fabry Pérot artefact resulting from reflections from the chip facets. The nature of these artefacts can be verified by considering Equation 6.1 [119, 120] in which the waveguide length is given by

$$L = \frac{\lambda^2}{2n_{\text{eff}} FSR_\lambda} \tag{6.1}$$

where $n_{\text{eff}} = 1.71$ and $FSR_\lambda \approx 12\,\text{pm}$ which gives a waveguide length of 15 mm as expected.

For each sweep, the peaks are found by first low pass filtering the calibrated signal data to avoid false peak detection and then differentiating the result and returning the indices of the zero crossings between adjacent maximum and minimum values (see Figure 6.7). The zero crossing

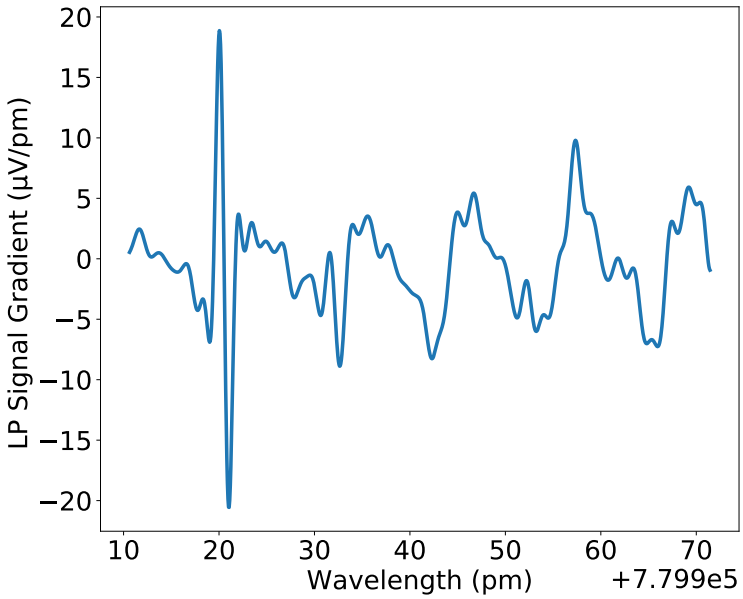

Figure 6.7: The derivative of the low pass filtered data shown in Figure 6.6. This clearly shows the position of the resonance peak between the maximum and minimum values shown in this plot.

index found in this method provides the peak location in Figure 6.6 and a symmetric window around the peak is selected for curve fitting, the window size is ideally set to be wide enough such that the tails of the probability distribution are adequately fitted to and the resulting Q factor values converge. A pre-defined curve such as a Gaussian or Lorentzian distribution can be fitted to the resonance peaks using the curve_fit function in the scipy package to perform a non-linear least squares fit [121]. The y error of the raw data is required to obtain errors on the fitting parameters. To obtain suitable y errors for the raw data, a transmission spectra of the same centre and span was recorded with no sample in place. This allows for total effect of the laser amplitude noise and the photodiode noise sources to be characterised. However, with the sample no longer in place there is much more power incident on the photodiode. To turn the laser power down to account for this would misrepresent the amplitude noise of the laser and so the noise was recorded for much greater incident power. The photodiode voltage is approximated by a straight line fit which is subtracted from this data to remove the effect of longer term drift (that is accounted for in the polynomial for the resonance curve fitting) and the standard deviation of the result provides an estimate of the noise, see Figure 6.8. This uncertainty is then propagated to y data in the measured resonance spectra and shown by the y error bars (an example of this can be seen in Figure 6.14).

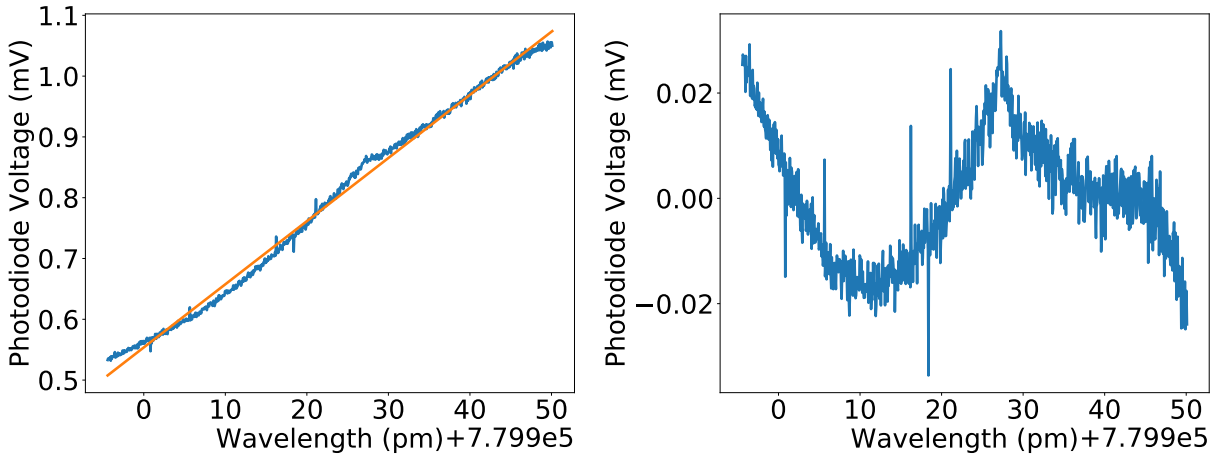

Figure 6.8: Left: The photodiode voltage against laser wavelength recorded with no sample in place with straight line fit through the data approximating the long term drift in laser power. Right: The data subtracted from the straight line fit. The standard deviation of this is found and taken to be an estimate of the noise. This noise is due to laser amplitude noise and the photodiode noise sources, it is scaled appropriately as it is propagated to the resonance transmission spectra as shown in Figure 6.14.

The power transmission of light through an all-pass micro-ring resonator is described by

$$P_{\text{tran}}(\nu) = A\frac{t^2 - 2t\tau\cos\left[2\pi(\nu-\nu_{\text{res}})t_{RT}\right]+\tau^2}{1-2t\tau\cos\left[2\pi(\nu-\nu_{\text{res}})t_{RT}\right]+t^2\tau^2} + B(\nu) \tag{6.2}$$

where A is the amplitude of the power transmission peak, t is coefficient for the field amplitude transmitted through the bus waveguide (rather than coupled into the resonator), τ is the field amplitude loss of the ring resonator, ν is the free space frequency, ν_{res} is the resonance frequency of the resonator, t_{RT} is the round trip time for the micro-ring resonator (see Equation 4.5), and B is a background function describing the data in the absence of the resonance peak [90,92]. This is equivalent to Equation 4.19 but expressed as a function of frequency instead of phase using $\theta = 2\pi(\nu-\nu_{\text{res}})t_{RT}$. It has been shown that it is possible to determine both the loss and coupling coefficients of a ring resonator by fitting Equation 6.2 to the recorded power transmission spectra but that these values are irrevocably entangled for a single resonance measurement such as this. They could, however, be distinguished by performing measurements of a series of resonance peaks and determining which fitted parameter shows the (co)sinusoidal behaviour with wavelength expected for the coupling coefficient [46]. Using the coupling coefficient values found in Chapter 2, the resonator loss and in turn the waveguide propagation loss can be determined by fitting Equation 6.2. This equation is relatively complex to fit because the input variable (frequency) is an argument in a cosine function in both the numerator and the denominator.

Micro-ring resonators are more routinely characterised by fitting a Lorentzian distribution to

the resonance peak [40, 41, 122],

$$f(\nu) = -A\frac{1}{1+\left[\frac{\nu-\nu_{\text{res}}}{\gamma}\right]^2} + B(\nu), \tag{6.3}$$

where ν_{res} is the mean frequency of the distribution corresponding to the resonance frequency and γ is the half width at half maximum (HWHM). By fitting Equation 6.3, via a non-linear least squares method, the essential attributes of the resonance peak can be found. The Q factor is defined in Equation 4.27 as the ratio of the resonance peak mean position and the full width at half maximum (FWHM)

$$Q = \frac{\nu_{\text{res}}}{2\gamma} \tag{6.4}$$

and the amplitude is given by A which is also used to find the extinction ratio of the resonance peak. The peak slope gradient is determined by taking the derivative of the Lorenztian distribution and finding its maximum value which corresponds to the side of the resonance peak. The background function, $B(\nu)$, used in Equations 6.2 and 6.3 is the second degree polynomial,

$$B(\nu) = b_0 + b_1(\nu - \nu_{\text{res}}) + b_2(\nu - \nu_{\text{res}})^2 \tag{6.5}$$

where $b_{0,1,2}$ are coefficients of the polynomial. This accounts for long term power drift of the laser and the Fabry-Pérot resonance that occurs due to the reflections for the end facets of the sample chip. The result of the noise estimation, background fitting, and Lorentzian curve fitting is shown in Figure 6.14. The photodiode voltage V is converted into optical power P by considering the PDA100A detector responsivity of 0.580 A W^{-1} [123], load resistance R of 50 Ω, and finding the light power using Equation 6.6.

$$P = \frac{V}{R \cdot \text{Resposivity}} \tag{6.6}$$

6.3 Results

Initial experiments with 500 nm wide, 200 nm thick waveguides with and without top cladding illustrate that higher Q factor values can be achieved with an SiO_2 top cladding layer. The Q factor was measured at least 3 times for each gap spacing for both the air clad ridge waveguide and SiO_2 clad buried waveguide samples (see Figure 6.9). The samples with the top SiO_2 cladding are shown to exhibit a Q factor about twice as great as the samples with no top cladding. It is expected that the sidewall roughness of the waveguide core is a critical loss mechanism [66, 72] and it has been shown in other work that low propagation losses can be achieved either by designing high aspect ratio waveguides such that the modal interaction with the sidewalls is minimised [77, 78, 94]. For this reason, the width of the waveguides was increased in subse-

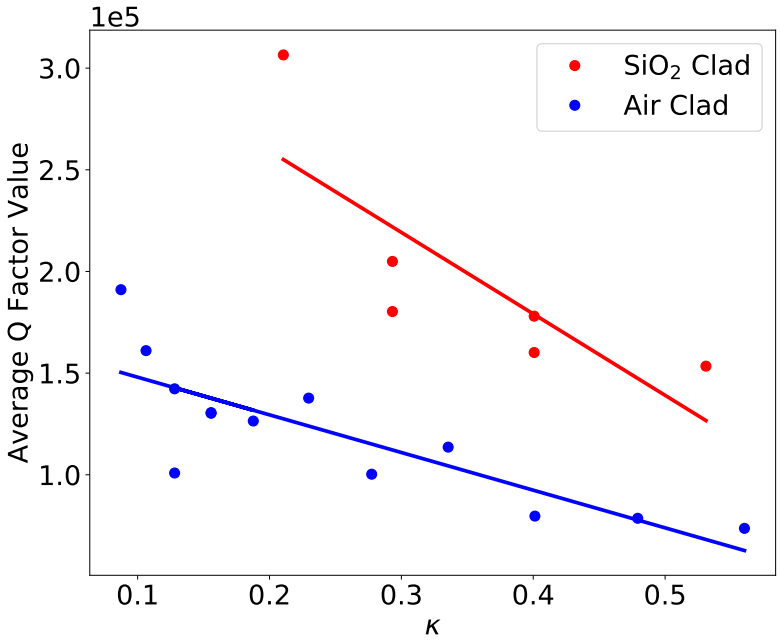

Figure 6.9: Average measured Q factor values against the coupling coefficient κ for micro-rings comprised of 200 nm LPCVD Si_3N_4 waveguide core on a 4 µm SiO_2 bottom cladding. The waveguide width is 500 nm, micro-ring radius is 250 µm, and the SiO_2 top cladding is 1 µm. A linear fit is provided as a guide for the eye, this trend should not be assumed to be linear. Errors bars were found to be too small to be seen and so have been omitted. This sample was designed and fabricated by Dr. Kevin Gallacher.

quent devices. Chapter 4 suggests that the Q factor can be optimised by reducing the coupling coefficient and so for each waveguide width that was tested, micro-rings with a range of gap spacings were characterised. At higher Q factor values, the effect of under sampling became more pronounced when using the 250 GHz scan. This presents most noticeably as a difference between the resonance peak amplitudes observed within a recorded transmission spectrum of a single micro-ring resonator. The tips of the peaks are not adequately sampled resulting in the FWHM being taken at closer to the base the resonance peak, artificially reducing the Q factor. For this reason the maximum Q factor values are recorded in Figure 6.10 as this is deemed to be more representative of the true Q factor value. The resonance peaks in the transmission spectra of micro-ring resonators with 1100 nm wide waveguides could not be adequately resolved using the 250 GHz scan and so had to be recorded using the higher resolution cavity with 30 GHz scanning range. The trend shown in Figure 6.10 of Q factor increasing with waveguide width suggests that the limiting loss mechanism was the sidewall scattering and that higher Q factor values are achievable for wider waveguides. Results from Figure 6.10 are for samples with no top cladding; considering also Figure 6.9, it is clear that higher Q values can be obtained for wider waveguides with a SiO_2 top cladding but it is essential to characterise these micro-rings using the high resolution scanning cavity with a range of 30 GHz.

The sidewall interaction can also be reduced by either making the waveguides very thin

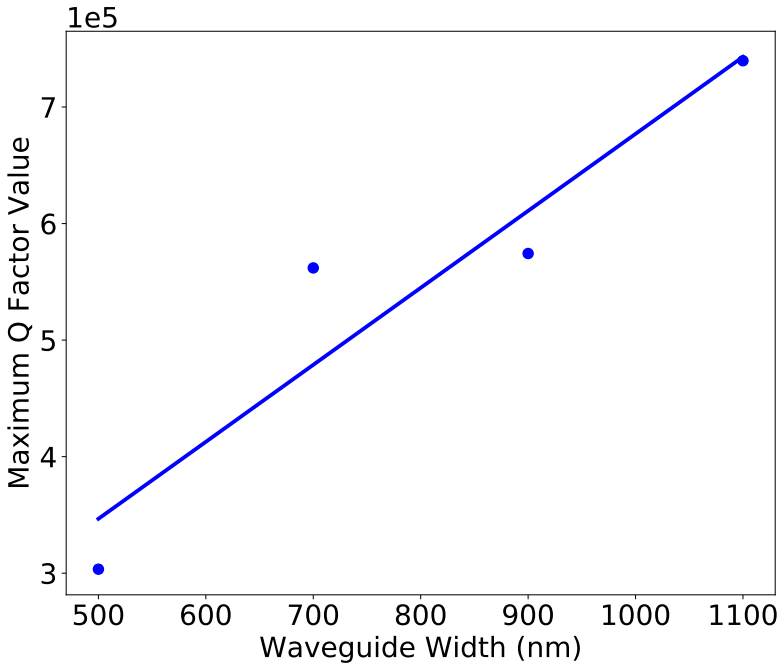

Figure 6.10: The maximum measured Q values against waveguide widths for micro-rings with 200 nm LPCVD Si_3N_4 waveguide core on a 4 µm SiO_2 bottom cladding with no top cladding. Micro-ring radius is 300 µm except for the 250 µm radius micro-ring resonator with 500 nm wide waveguides, this is expected to have no significant effect.

[77, 78, 94], i.e. weakly confined, or by making the waveguides quite thick [12, 41, 122], i.e. highly confined. The aim of the weakly confined approach is simply to minimise the surface area of the sidewalls and make the waveguides wide enough such that the intensity of the field interacting with these small sidewalls is low enough to yield low losses. The highly confined approach relies upon reducing the intensity of light interacting with sidewalls by confining the mode to the waveguide core. This approach is predicated upon the ability to deposit thick films of Si_3N_4 without cracks which would normally be prohibited by the high tensile stress of LPCVD Si_3N_4. This has been overcome utilising temperature cycling and annealing to fabricate crack-free films up to 744 nm [32]. Thick Si_3N_4 waveguides have also been fabricated using the photonic Damascene process whereby Si_3N_4 is deposited into trenches etched into SiO_2 allowing for waveguides up to 1.35 µm thick [33]. Both of these options would be expected to require a great deal of process development before crack free waveguides could be fabricated and so the high confinement approach was ruled out for this work.

Here an attempt was made to produce weakly confined waveguides in order to reduce loss due to sidewall scattering and achieve high Q factor micro-ring resonators by using a Si_3N_4 core layer only 100 nm thick, with a 1 µm thick top cladding. The decreased core thickness and additional top cladding affects the modal distribution and so a fair comparison cannot be made to waveguides of the same width in Figure 6.10. Q values were measured for micro-ring resonators with 100 nm thick Si_3N_4 waveguides 900 nm and 1300 nm wide for a range of gap spacing

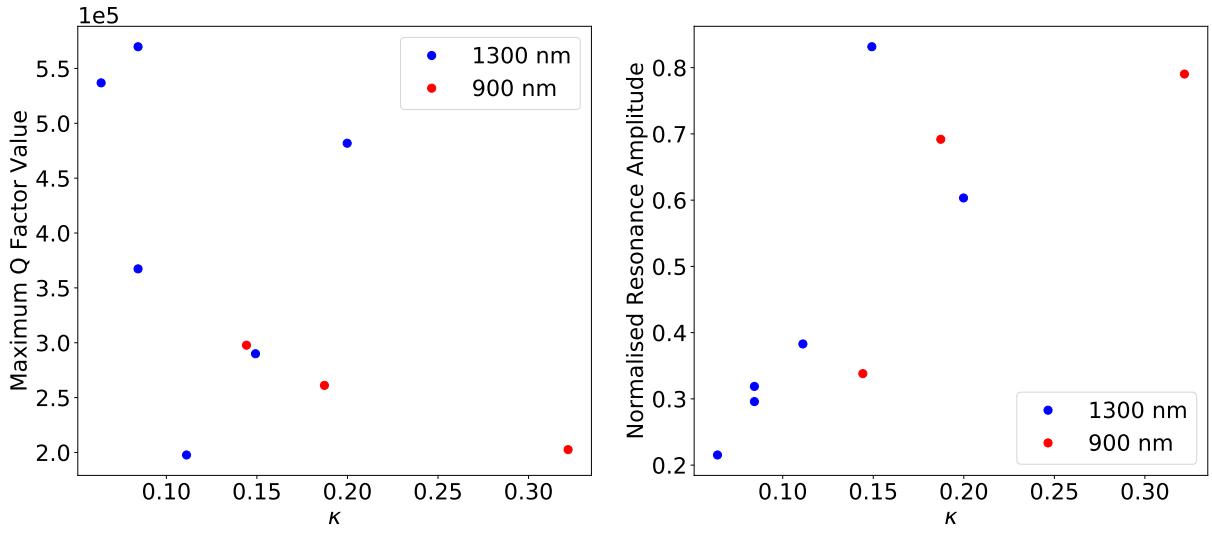

Figure 6.11: Left: Maximum Q factor values against coupling for micro-ring resonators with 100 nm thick Si_3N_4 waveguide cores, 1 µm thick SiO_2 top cladding, and waveguide widths indicated by the legend. Right: Normalised resonance peak amplitude against coupling coefficient for micro-ring resonators with 100 nm thick Si_3N_4 waveguide cores, 1 µm thick SiO_2 top cladding, and waveguide widths indicated by the legend.

values. This resulted in Q values which were lower than anticipated, see Figure 6.11. The data would seem to suggest that higher Q factors could be measured for slightly larger gap spacing, lower κ, in the case of the 900 nm wide waveguides but these structures were present and characterised and no resonance peaks could be detected. The resonance peak amplitude is shown, in Figure 6.11, to decrease as coupling is decreased for larger gap spacing. It is therefore reasonable to assume that these resonance peaks could not be resolved against the noise floor of the transmission spectra. To better understand these results, the electric field intensity halfway up the sidewall of the waveguides was simulated using the 2D FDE solver for 100 nm thick waveguides with the top cladding and 200 nm thick waveguides without a top cladding, both with 4 µm bottom cladding, see Figure 6.12. Based upon these results, the electric field intensity at the sidewall of 100 nm thick waveguides 900 nm and 1300 nm wide is equivalent to that of 200 nm thick unclad waveguides which are 650 nm and 850 nm wide respectively. If the reduction in sidewall surface area caused a significant reduction in loss then this would result in a higher Q factor for the equivalent 100 nm thick waveguides. By comparing the Q factors in Figures 6.10 and 6.11, it is clear that using 100 nm thick waveguides with a top cladding has not resulted in an improvement in Q factor. This could be because the thinner Si_3N_4 waveguide core resulted in reduced modal confinement and therefore increased interaction with the silicon substrate (see the 1D FDE simulation shown in Figure 3.1) which resulted in substrate leakage loss that proved detrimental for building up a resonance peak even at high laser powers.

In order to achieve the highest Q possible with the available material and processes, a series of micro-ring resonators 300 µm in radius with a 4 µm thick SiO_2 bottom cladding, a 200 nm

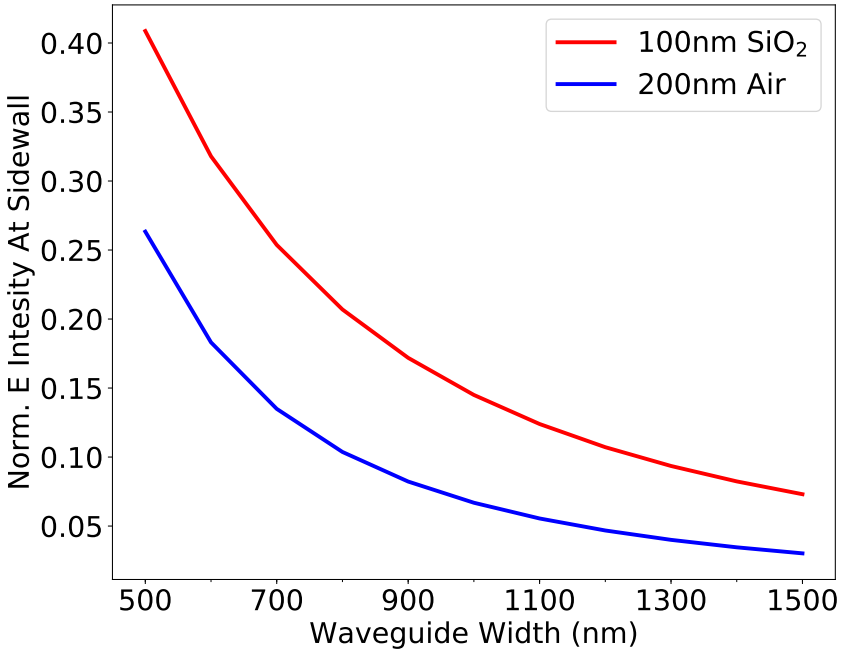

Figure 6.12: The electric field intensity of the TE_0 mode at the sidewall of waveguides 100 nm and 200 nm thick plotted against waveguide width. The 100 nm thick waveguide has 1 µm thick top cladding and the 200 nm thick waveguide has no top cladding. In both cases there was a 4 µm thick bottom cladding.

thick 1100 nm wide Si_3N_4 core, and 1 µm SiO_2 top cladding were made with a variety of gap spacings. The effect of HSQ mask removal was also under consideration at this time and so samples were prepared which did not have lift-off performed, leaving the HSQ etch mask on during top cladding deposition, which were otherwise identical to samples which did have lift-off performed. The resulting Q factor measurements are the corresponding normalised resonance peak amplitude of each measurement are plotted in Figure 6.13. The highest Q found in these measurements was $(1.38 \pm 0.04) \times 10^6$ and spectrum from which this was found is shown in Figure 6.14. This values represents a record high Q factor for buried silicon nitride waveguides at such short wavelengths, this is discussed further in Section 6.4. Higher Q factor values are found for micro-rings with the HSQ etch mask than are found for the micro-rings for which lift-off is performed. An explanation for this is that the increased resist thickness of the HSQ-PMMA bi-layer with respect to a single layer of HSQ resulted in increased roughness during pattern transfer but it could also simply be a result of too coarse stepping in the coupling gap spacing. This warrants further investigation than could be done in the course of this work.

A Q factor value of 3.6×10^6 has been demonstrated for strip-loaded waveguide micro-rings at 780 nm [124] wherein a thin film of Si_3N_4 acts as the waveguide core but the mode is localised instead by a strip of SiO_2 on top of the core layer (see Figure 1.1 for an illustration of the differences between the common waveguide types). This strip-loaded waveguide does not require etching of the waveguide core and so avoids the sidewall scattering losses typically found to

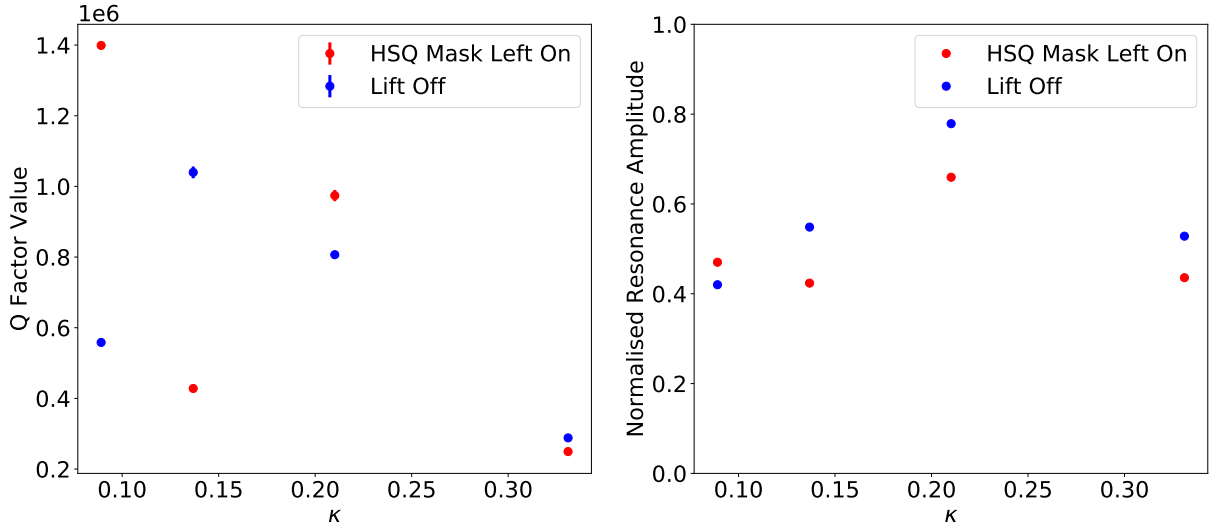

Figure 6.13: Left: The Q factor against the coupling coefficient values for micro-rings with 200 nm thick Si_3N_4 waveguide cores, 1 µm thick SiO_2 top cladding, and waveguide widths of 1100 nm. The legend indicates whether lift-off of the HSQ etch match was or was not performed. Right: Normalised resonance peak amplitude against the coupling coefficient values for micro-rings with 200 nm thick Si_3N_4 waveguide cores, 1 µm thick SiO_2 top cladding, and waveguide widths of 1100 nm. The legend indicates whether lift-off of the HSQ etch match was or was not performed.

be the dominant loss mechanism in buried/ridge waveguides, thereby potentially demonstrating an upper limit of Q factor for micro-ring resonators with a similar size and wavelength. However, the strip-loaded waveguides fabricated using this process [124] offer limited possibilities for integration because the addition of top cladding or any other material to the surface of the completed micro-ring resonator (e.g. for metallisation or packaging) would interact with the mode which could cause optical loss. Additional waveguide cladding deposited on the surface would need to have a refractive index lower than that of SiO_2 to ensure that the waveguide mode persists which would present a significant challenge for integration. By contrast, the foundry compatible process detailed in this work results in a buried waveguide with a top cladding surface that ensures that any material deposited on the surface cannot interact with the waveguide mode. This facilities metallisation, packaging, and prevents any surface contamination.

The transmission spectra shown in Figure 6.14 is the same spectrum used to illustrate the measurement method in Figures 6.5, 6.6, and 6.7. The transmission spectra shown in these figures corresponds to a laser sweep of 30 GHz (60 pm) bandwidth around a centre wavelength of 780 nm. The micro-ring resonator characteristics found by fitting Equations 6.2 and 6.3 are shown in Table 6.2. The propagation loss was calculated to be 0.261 ± 0.009 dB cm^{-1} from the ring resonator length and the loss parameter τ found in Equation 6.2. The FWHM$_\lambda$ of 570 fm equates to a FWHM$_\nu$ of 280 MHz. A high resolution scan of 60 fm (30 GHz) is required to adequately resolve this resonance peak; it cannot be detected using the scanning cavity with a range of 500 pm (250 GHz) which is required to measure the free spectral range (FSR) of the

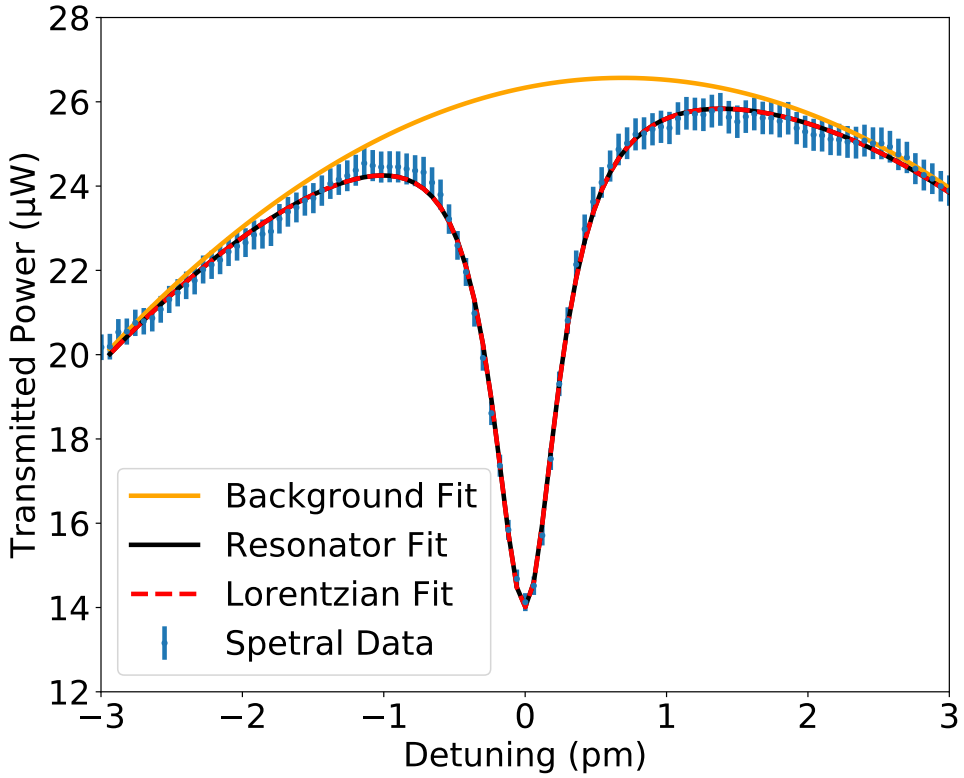

Figure 6.14: A resonance peak with y error bars found by noise estimation based upon spectra recorded with no sample in place, a background curve accounting for long term laser drift and Fabry-Pérot resonance due to the sample chip facets, and a Lorentzian distribution fitted to the resonance peak and used for parameter estimation. The Q factor found from this spectrum was $(1.38 \pm 0.04) \times 10^6$, this represents a record high Q factor for buried waveguides operating at $\sim 780\,\text{nm}$. The other micro-ring resonator characteristics determined from the fit parameters of the Lorentzian distribution are shown in Table 6.2.

Table 6.1: A comparison of micro-ring resonators at or close to 780 nm operational wavelength.

Material platform	Wavelength (nm)	Waveguide loss (dB/cm)	Micro-ring diameter (μm)	Micro-ring loaded Q	Ref.
Si_3N_4	668.38		25	$(1.52 \pm 0.02) \times 10^5$	[125]
AlN	774.24	40	20	3.0×10^4	[126]
Si_3N_4	780		20	1.5×10^4	[127]
polymer	780	1.1	60	1×10^5	[128]
TiO_2	780		150	1.6×10^5	[129]
Si_3N_4	**780**	**0.261**	**600**	**$(1.38 \pm 0.04) \times 10^6$**	**This work** [1]
strip-loaded Si_3N_4	784	0.2	700	3.6×10^6	[124]
SiO_xN_y	850	0.8	200	1.3×10^5	[130]
Si_3N_4	933.62		25	$(1.04 \pm 0.02) \times 10^6$	[125]

Table 6.2: The micro-ring resonator characteristics are determined from the parameters used to fit a Lorentzian distribution and Equation 6.2 to the resonance peak in the power transmission spectra.

Q (10^6)	FWHM$_\lambda$ (fm)	Mean λ (nm)	Amplitude (μW)	Extinction Ratio %	Propagation Loss (dB cm^{-1})
1.38±0.04	570± 20	779.9±0.8	12.3±0.2	46.8±0.6	0.261±0.009

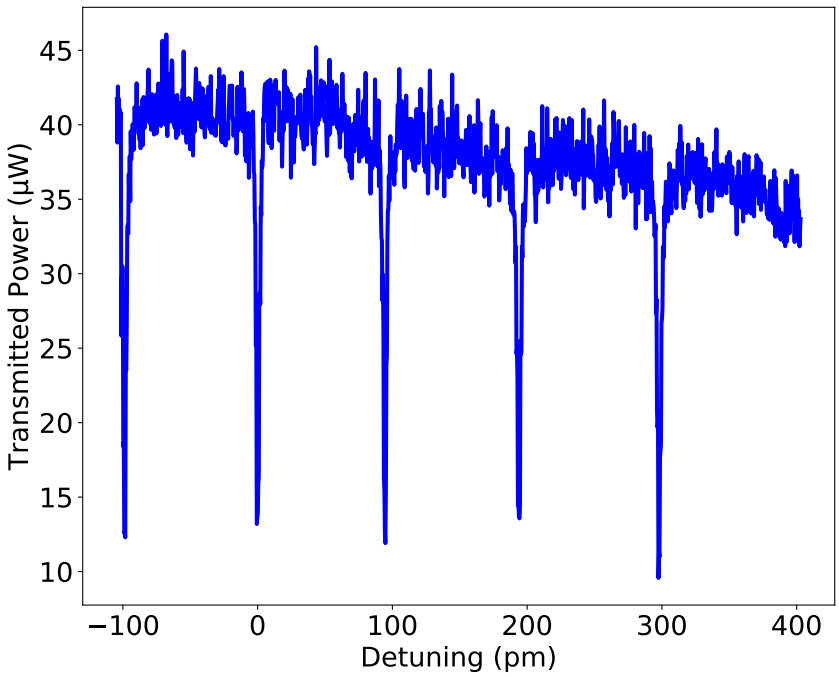

Figure 6.15: The transmission spectra of a low Q factor micro-ring resonator of equivalent path length to the 1.4 million Q factor micro-ring resonator. The free spectral range is shown to be (99 ± 3) pm.

micro-ring resonator.

This scan was performed on lower Q factor micro-rings with the same path length and an FSR of (99 ± 3) pm or (49 ± 1) GHz was found (see Figure 6.15). This disagrees with the FSR values found using Equation 4.7 and 4.8. The particular waveguide cross-section has Si_3N_4 waveguide core 700 nm wide and 200 nm thick on top of a 4 μm SiO_2 bottom cladding with a no top cladding. The effective index is found to be 1.63 and so for a ring resonator with a radius 300 μm, the FSR is found to be 60 GHz or 120 pm which is about 20 pm greater than the result found experimentally as shown in Figure 6.15. This difference could be due to the wavelength dependence of the effective index. This is regularly accounted for by using the group refractive index in place of the effective index [40, 91] but in this case the group index found using the FDE solver is 2.11 resulting in an FSR of 72 pm, about 30 pm less than the experimental value. This can be attributed to inaccuracy in the dispersion modelling used to determine the group refractive index.

Waveguide propagation loss was determined for micro-ring resonators with a 200 nm thick

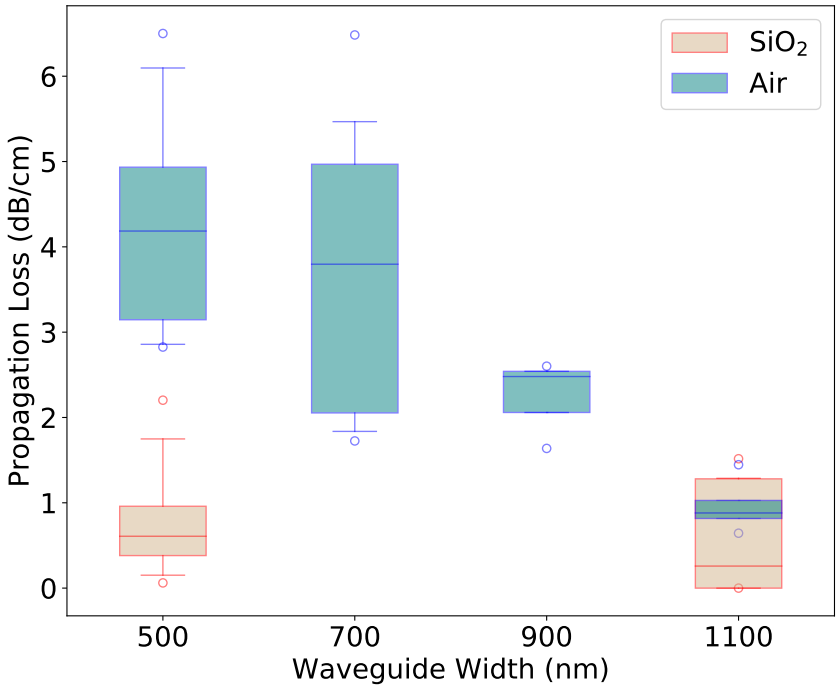

Figure 6.16: The propagation loss of waveguides with a 200 nm thick Si_3N_4 core is found by fitting Equation 6.2 to all of the available micro-ring resonator transmission spectra. Samples have either a 1 µm thick SiO_2 top cladding or only air as a top cladding as indicated in the legend. The box extends from the lower to upper quartile values of the data and the line in between shows the median. The whiskers extend to the 5th and 95th percentile of data and outlier points beyond the whiskers are plotted.

core by fitting Equation 6.2 to all of the available transmission spectra, see Figure 6.16. The relatively large errors associated with these propagation loss values could be due to the complexity of Equation 6.2 but it could also be representative of the a wide variation in propagation loss due to inconsistencies in sample fabrication. The dependence of the propagation loss on waveguide width does however broadly agree with results of Lacey-Payne scattering model as shown in Figure 3.11.

6.4 Discussion

In this work, a Q factor value of $(1.38 \pm 0.04) \times 10^6$ has been reported, this constitutes a record high value for a buried waveguide micro-ring resonators operating at $\sim 780\,\text{nm}$ wavelength, see Table 6.1 for a comparison to the literature. Higher Q factors than this have been recorded for the strip-load waveguide platform [124] but that platform is not suitable for an integrated photonic device for the reasons mentioned in Section 6.3. If the micro-ring resonator demonstrated in this work were to be used as a frequency reference for stabilising a diode laser using the simple side locking method [131, 132], then the transmission spectra provides an error response of $30\,\text{nW fm}^{-1}$ corresponding to an error signal of $800\,\text{nV fm}^{-1}$ produced by the amplified photodetector. The total actuation range is $\sim$400 fm with a maximum deviation from a set point of $\pm$ 200 fm. The resonance frequency of the micro-ring resonator would however be susceptible to temperature fluctuations and so some form of active or passive temperature stabilisation would be required in order to utilise this micro-ring as a frequency reference for laser stabilisation, this is discussed in Chapter 7. The implementation of Pound-Drever-Hall laser frequency stabilisation in particular is discussed within the context of future work in Chapter 9.

This high Q factor has been made possible by reducing the sidewall scattering loss and operating in the under-coupled regime. The sidewalls scattering has been reduced in two ways: the first is by increasing the width of the waveguides and thereby reducing the modal interaction with the sidewalls, the second is by developing a PECVD SiO_2 top cladding resulting in a reduced index contrast (and therefore reduced scattering loss) compared to an air clad ridge waveguide. The reduction in sidewall scattering follows from the Lacey-Payne model discussed in Chapters 2 and 3. The decision to operate in the under-coupled regime in order to achieve higher Q factor values is based upon the analytical modelling in Chapter 4. The experimentation with waveguide width and thickness presented in this chapter was facilitated by first verifying that the desired TE_0 mode would be supported by the given waveguide cross-section using the simulation procedure given in Chapter 3 and the fabrication of the micro-rings has of course required the development of the fabrication processes as detailed in Chapter 5.

Chapter 7

Athermalisation Of Micro-ring Resonators

The theoretical temperature dependence of a waveguides effective index and the resulting temperature dependence of a micro-ring resonators resonant wavelength are discussed. A scheme is introduced whereby the extent of this dependence is reduced by using a top cladding material with a temperature dependence that opposes that of the waveguide core and bottom cladding. The thermo-optic properties of these potential top cladding materials are determined experimentally, the resulting temperature dependence of the micro-ring resonators resonant wavelengths are determined by simulation and compared directly with that of a micro-ring resonator with the typical silicon dioxide top cladding.

7.1 Thermo-optic Coefficient And Temperature Dependent Wavelength Shift

Light propagating in a medium is susceptible to the thermo-optic effect whereby a change in the temperature of that medium results in a change in its refractive index. For a waveguide comprised a bottom cladding layer, a top cladding layer, and a core. The total thermo-optic coefficient (TOC) of the waveguide is determined by the bulk TOCs of the materials that form the waveguide weighted by the modal confinement factor corresponding to each of those materials [133],

$$\frac{dn_{\mathrm{eff}(\lambda)}}{dT} = \Gamma_c(\lambda)\frac{dn_{\mathrm{c}(\lambda)}}{dT} + \Gamma_{tcl}(\lambda)\frac{dn_{\mathrm{tcl}(\lambda)}}{dT} + \Gamma_{bcl}(\lambda)\frac{dn_{\mathrm{bcl}(\lambda)}}{dT}, \tag{7.1}$$

where T is the temperature and Γ is the modal confinement factor which describes the fraction of the total light power confined to the waveguide core, top cladding, and bottom cladding. The group refractive index of the mode is found using Lumerical's FDE solver and used in Equation 7.2 to find temperature dependent wavelength shift (TDWS) of a micro-ring resonance peak [133].

$$\frac{d\lambda}{dT}(\lambda) = \frac{\lambda}{n_g}\frac{dn_{\mathrm{eff}}}{dT}(\lambda) \tag{7.2}$$

The condition for an athermal waveguide is that $\frac{dn_{\text{eff}(\lambda)}}{dT} = 0$ which can only be achieved if the materials used have an appropriate mix of positive and negative TOCs. The TOCs of SiO_2, Si_3N_4, and air are $1.0 \times 10^{-5}\,K^{-1}$ [133, 134], $2.5 \times 10^{-5}\,K^{-1}$ [133, 135], and -0.698×10^{-6} K^{-1} [136] respectively, so a top cladding layer must have a negative TOC and be greater in magnitude than $\sim 10^{-5}$ in order to overcome the thermo-optic effect of the core and bottom cladding layers. From literature, PMMA is found to have a TOC of $-1.28 \times 10^{-4}\,K^{-1}$ at 656 nm [137]. Another polymer of interest is the commonly used epoxy based resist SU8, it is often used in micro-machining applications due its robust mechanical properties [138] and as a polymer waveguide material for spot-size converters [139, 140] (see Chapter 8). SU8 has been found to have a TOC of $-1.1 \times 10^{-4}\,K^{-1}$ at 1300 nm [141]. These polymers were characterised in order to determine their suitability as top cladding layer which could satisfy the athermal condition. SU8 is of particular interest because it is a negative tone electron beam lithography resist and so can be patterned precisely to be only where it is required to achieve athermalisation, this would be of great benefit for realising an integrated photonic device. Polyurethane acrylate (PUA) has been shown to have a TOC of $-4.2 \times 10^{-4}\,K^{-1}$ [142] but attempts to develop a spin coating process were not successful as ellipsometer results were not repeatable within the span of a few days and so TOC characterisation was ruled out.

7.2 Measurements Of Thermo-optic Coefficients

To characterise the thermo-optic coefficients of PMMA and SU8, each polymer was spin coated on a silicon chip, and samples were prepared with 150 nm and 300 nm thick films of PMMA and SU8 respectively. The refractive indices of these films were characterised (as in Chapter 5) by fitting a Cauchy model to ellipsometer data. The refractive indices were found to be $n_{\text{PMMA}} = 1.50$ at 22 °C and $n_{\text{SU8}} = 1.57$ at 22 °C. In order to determine the TOC, the temperature of the sample must be varied and the refractive index recorded. To achieve this, a thin film heater was secured by tape and by vacuum to the eillipsometer stage (see Figure 7.1) and the voltage varied from 0-20 V. The resulting temperature change was recorded using a Thorlabs negative-temperature-coefficient thermistor and calibrated temperature logger [143] attached to the heater, immediately next to the sample. The refractive index change with temperature is shown in Figure 7.2. The TOCs of PMMA and SU8 were found to be $\frac{dn_{\text{PMMA}}}{dT} = (-1.01 \pm 0.08) \times 10^{-4}\ K^{-1}$ and $\frac{dn_{\text{SU8}}}{dT} = (-1.7 \pm 0.1) \times 10^{-4}\ K^{-1}$ by performing a straight line fit to the experimental data and taking the gradient of the straight line to be the TOC.

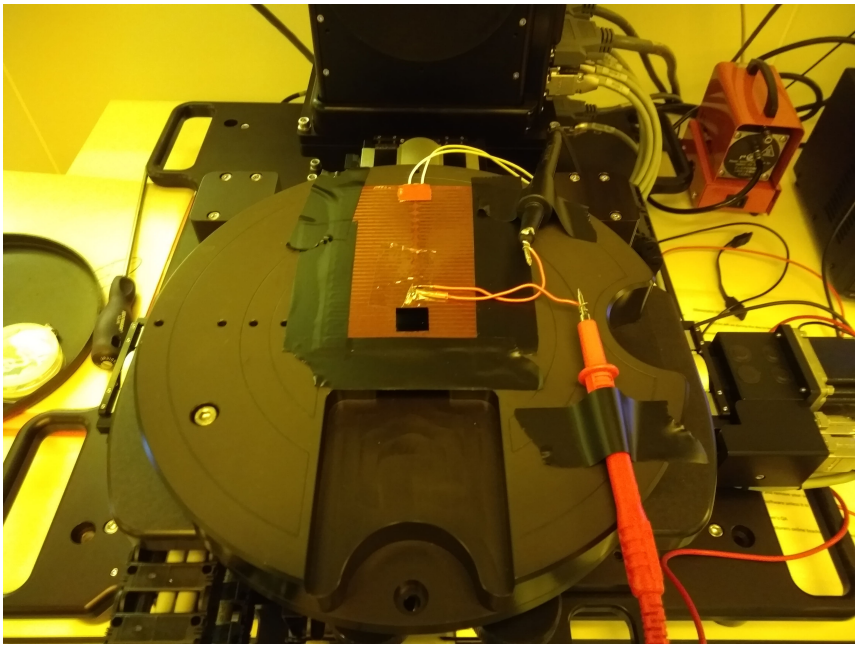

Figure 7.1: Experimental setup used to characterise the thermo-optic coefficients of PMMA and SU8. The thin film heater raises the temperature of the sample and a thermometer taped down next to the sample records the temperature. Shown, is a pt100 resistance thermometer, a Thorlabs negative temperature coefficient thermistor and calibrated temperature logger were used to record the data presented in this work.

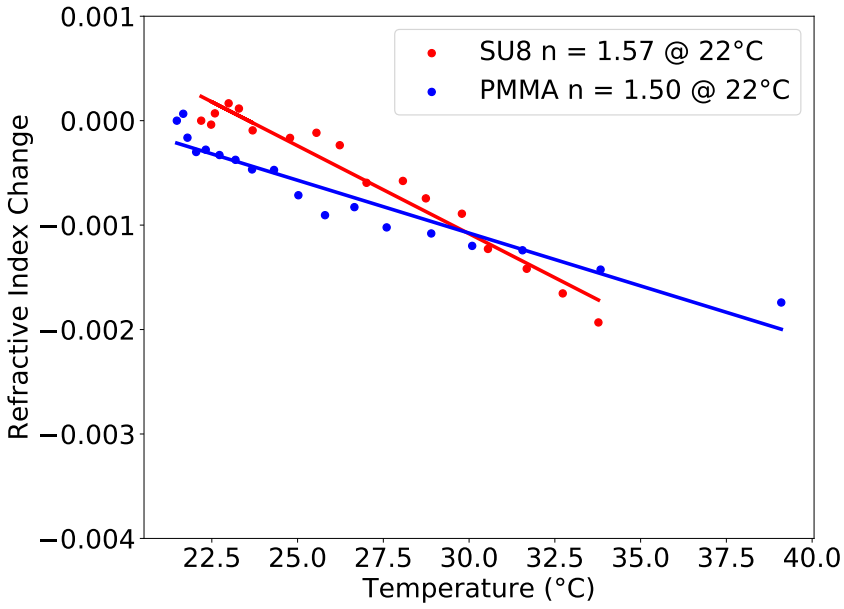

Figure 7.2: The change in refractive index as a function of temperature is shown for PMMA and SU8. The TOCs are found by straight line fit to be $\frac{dn_{\text{PMMA}}}{dT} = (-1.01 \pm 0.08) \times 10^{-4}$ K^{-1} and $\frac{dn_{\text{SU8}}}{dT} = (-1.7 \pm 0.1) \times 10^{-4}$ K^{-1}.

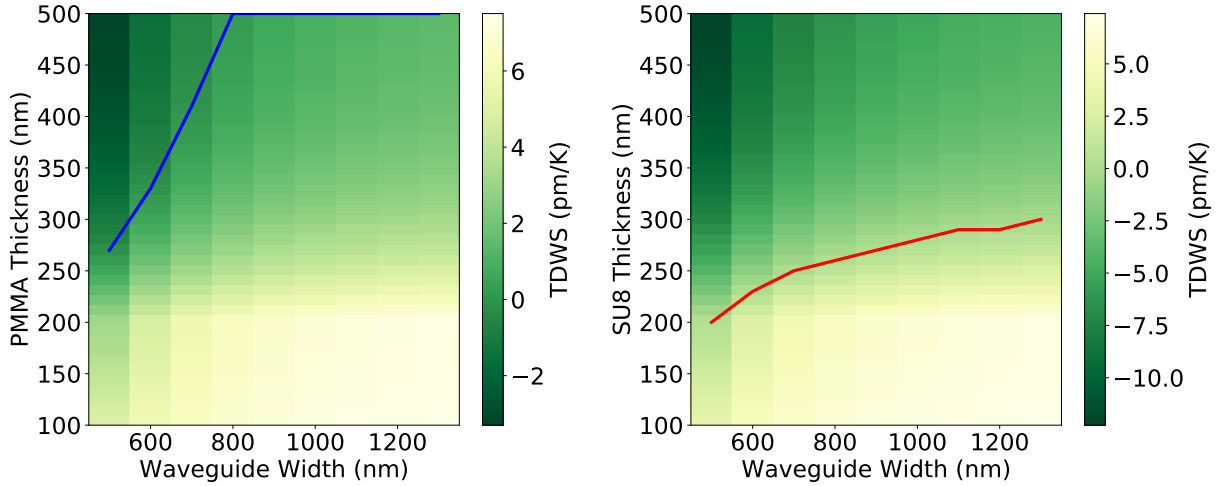

Figure 7.3: The temperature dependent wavelength shift of a micro-ring resonance peak is shown as a function of the waveguide core width and the top cladding thickness for both a PMMA and an SU8 top cladding. The waveguide core is 200 nm thick Si_3N_4 and the bottom cladding is 4 µm thick SiO_2. A temperature dependent wavelength shift of zero is indicated by the blue and red traces for PMMA and HSQ respectively.

7.3 Simulation Of Temperature Dependent Wavelength Shift

The confinement factors given in Equation 7.1 can be found by simulating the waveguide geometry using the Lumerical 2D FDE solver, integrating the electric field intensity in each material over its cross-sectional area to find the total power confined to that material and dividing this by the integral of the total input power over the complete simulation area. By iterating over a range of waveguide widths and polymer top cladding thicknesses, the waveguide TOC can be optimised. In this simulation it assumed that the spin coated polymer is planar rather than conformal but this would need to be investigated further in the course of developing this process in future work.

Top cladding thickness is capped at 500 nm to ensure that it cannot support a slab mode, thereby avoiding any potential of the waveguide mode being obscured due to slab mode formation in the top cladding such as was encountered while characterising the micro-ring resonators with a 1 µm silicon dioxide top cladding. Increasing the top cladding thickness any further was found to have little effect on the TOC in the examples presented here due to the evanescent decay of the light field in the cladding. Figure 7.3 shows the TDWS of the resonance peak of a micro-ring resonator with a 200 nm Si_3N_4 core, a 4 µm bottom cladding and a top cladding comprised of either PMMA or SU8 for an array of waveguide core widths and top cladding thicknesses. The PMMA top cladding is shown to be able to approximately satisfy the athermal condition for the waveguide widths $\leq$ 800 nm while SU8 is shown to satisfy the athermal condition for all waveguide widths. The TDWS for these optimised top cladding layers is compared with the TDWS found for a top cladding comprised of 1 µm of SiO_2 (see Figure 7.4).

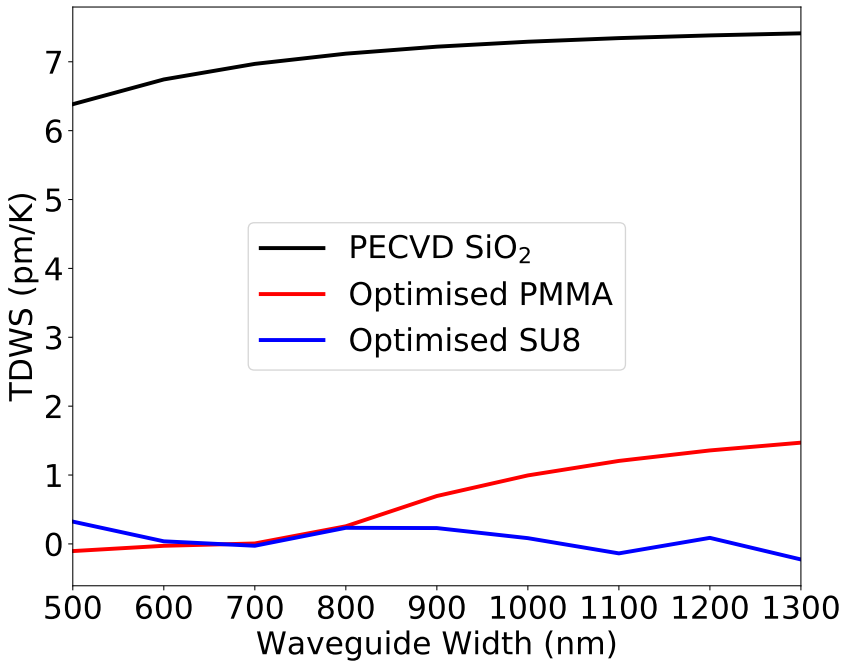

Figure 7.4: The optimised TDWS of the micro-ring resonance peak is shown for PMMA and SU8 top cladding layers and compared with the TDWS found for an SiO_2 top cladding.

7.4 Summary

The TDWS of the resonance peak of the 1.4 million Q factor micro-ring demonstrated in Chapter 6 is found here to be 7.34 pm K^{-1} which for an actuation range of $\pm$200 fm corresponds to a temperature stability requirement of less than $\pm$27 mK for wavelength locking applications. For the same waveguide width and thickness, the corresponding TDWS of the resonance peak is 1.20 pm K^{-1} for 500 nm thick PMMA and 0.14 pm K^{-1} for an optimised SU8 thickness of 290 nm. This would result in a temperature stability requirement of $\pm$167 mK with the 500 nm thick PMMA top cladding and $\pm$1.43 K with the 290 nm thick SU8 top cladding. A step size of 10 nm was used while simulating different top cladding thicknesses. PMMA and SU8 are commonly used lithography resists and spin coating process have been well developed for these and so a film thickness tolerance of $\pm$5 nm is achievable.

Chapter 8

Free-space Coupled Interferometer Development

Efficient coupling of light from a silicon nitride waveguide to free-space is a requirement for many potential applications. The application considered in this chapter is an interferometer to be used to measure the displacement of a micro electro-mechanical system (MEMS) accelerometer, specifically the MEMS gravimeter developed at the University Of Glasgow [144–146]. This application requires that the light couples from the waveguide to free space, reflects from the MEMS proof mass, and returns to the waveguide it originated from. An inverse taper spot-size converter with an SU8 waveguide is to be used to expand the mode diameter thereby reducing the beam divergence in free space. The development of a spot-size converter has wide-reaching applications because this allows for a silicon nitride waveguide to interface more effectively with laser sources, photodetectors, and other waveguide platforms thereby facilitating hybrid photonic devices. Eigenmode expansion simulation is used to optimise the inverse taper spot-size converter design. A micro optical bench approach is considered using a micro-ball lens to collimate the beam and the effect of misaligning this lens is examined by simulation. The use of a lens allows for light to be focused onto the spot-size converter allowing for effective coupling of light into the waveguide from greater distances and even greater modal mismatch than could be achieved with the spot-size converter alone. Processes have been developed for fabricating prototype devices including SU8 waveguides, registration blocks, and micro-ball lens receptacles. A process for aligning a waveguide with a spot-size converter to the micro-ball lens is discussed but completing the development of this process was not within the scope of this work.

8.1 MEMS Gravimeter: Principle Of Operation

The MEMS gravimeter is at a basic level of abstraction, a mass on a spring. When oriented vertically, the force due to the spring constant k acts in opposition to gravity, this relationship is

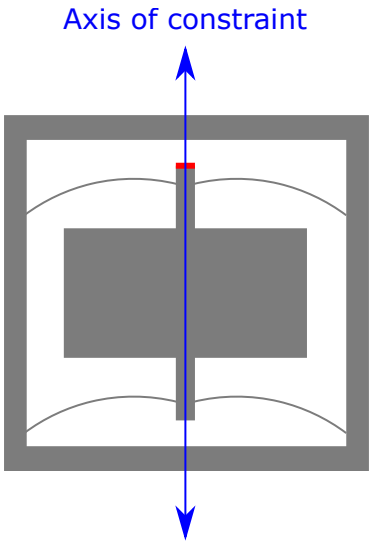

Figure 8.1: The 4-flexture variant of the MEMS gravimeter. The proof-mass oscillates in the axes of constraint. The red line indicates the edge taken to be point of reflection which is characterised in Figure 8.5.

governed by the equation

$$\Delta g = \frac{k}{m}\Delta x = \omega_0^2 \delta x \tag{8.1}$$

where g is the gravitational acceleration $\left(\mathrm{m\,s^{-2}}\right)$, m is the proof-mass (kg), x is the displacement of the proof-mass (m), and ω_0 is the fundamental resonant frequency of the proof-mass oscillation (rad $\mathrm{s^{-1}}$) [147]. Therefore the sensitivity of the MEMS gravimeter can be improved by either lowering the resonant frequency or by improving the displacement sensitivity. A geometric anti-spring system has been development and thoroughly optimised to reduce the resonant frequency to $< 10\,\mathrm{Hz}$ (the resulting geometry is illustrated in Figure 8.1) and so means of improving the displacement sensitivity are sought after. The displacement sensitivity could be improved using with interferometric methods to the measure the displacement of the proof-mass. An integrated interferometer may also allow for significant miniaturisation, this is important because one of the main advantages of this gravimeter is its small size (and low cost) which allow for it to used in a gravitational imaging array or as a payload on a drone [144, 146, 147].

8.2 Waveguide To Free-space Mode Coupling

To measure the displacement of the proof-mass, light must couple from the waveguides to free-space. Upon coupling to free-space, light behaves as a Gaussian beam propagating in the x direction. Taking the waveguide facet as the origin of the beam, the Gaussian beam is described

by the wave equation [148]

$$E(x,y,z,t) = E_0 \overbrace{\frac{w_0}{w(x)} \exp\left(-\frac{y^2+z^2}{w(x)^2}\right)}^{\text{Spatial}} \overbrace{\exp\left[-i\left((kx-\omega t)+k\frac{(y^2+z^2)}{2R(x)}-\psi(x)\right)\right]}^{\text{Phase}} \tag{8.2}$$

where E_0 is the electric field distribution, w_0 is the radius of the Gaussian beam at its origin (or waist), and $w(x)$, $R(x)$, and $\psi(x)$ are the beam radius, wave-front radius of curvature, and Gouy phase each as a function of x. The phase related terms will mostly be neglected in this analysis. Instead attention will be focused on the spatial terms describing the beam divergence. The transverse radius of the beam is given by [148]

$$w(x) = w_0\sqrt{1+\frac{x^2}{x_R^2}} \tag{8.3}$$

where the parameter x_R is the Rayleigh range given by

$$x_R = \frac{\pi w_0^2 n}{\lambda} \tag{8.4}$$

and the wave-front radius of curvature is given by

$$R = x\left[1+\frac{x^2}{x_R^2}\right]. \tag{8.5}$$

Therefore, the divergence of the beam is determined by the beam radius at its origin, the refractive index of the propagation medium, and the wavelength of the light. To minimise the divergence of the Gaussian beam, a spot-size converter can be used to expand the mode and increase w_0 but this must be optimised in order to reduce modal loss. Using the shortest suitable wavelength would also reduce the beam divergence. The other factors determining the return power are the reflectance of the waveguide (or spot-size converter) facet and the reflectance of the silicon proof mass.

8.2.1 Simulation Of Spot-size Converters

Spot-size converters of various designs have been demonstrated to increase mode diameter [3, 35]. These designs include relatively simple lateral tapers where the waveguide width is reduced to expand the mode [149, 150], an inverse taper within a much larger and lower index waveguide core (typically a polymer) [139, 140, 151, 152], a segmented taper (which allows control over vertical confinement by varying the spacing of the segments) [153, 154], and three dimensional tapers where the core thickness is varied [155]. A design consisting of an inverse taper within a SU8 waveguide core was decided upon because SU8 processing is routinely carried out in the

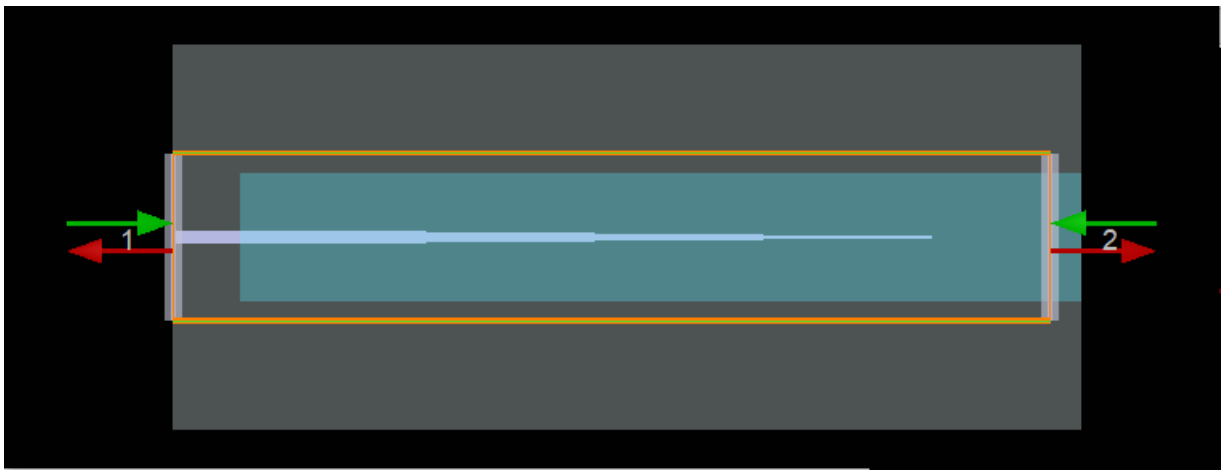

Figure 8.2: Top down view of eignemode expansion simulation of a inverse taper spot-size converter. The 1100 nm wide Si_3N_4 waveguide core tapers to a 100 nm wide point within the SU8 waveguide core. Ports 1 and 2 are labelled, port 1 is on the left in the Si_3N_4 waveguide and port 2 is on the right in the SU8 waveguide.

Table 8.1: The S-matrix represents the field transmission and reflection coefficients for ports 1 and 2 illustrated in Figure 8.2. S_{11} is the reflection coefficient for output port 1 from input port1. S_{12} is the transmission coefficient for output port 1 from input port 2. S_{21} is the transmission coefficient for output port 2 from input port 1. S_{22} is the reflection coefficient for output port 2 from input port 2.

		Input	
		1	**2**
Output	**1**	S_{11}	S_{12}
	2	S_{21}	S_{22}

JWNC and the resolution afforded by electron beam lithography negates some of the benefits of a segmented taper. A segmented taper and a three dimensional taper would both require much process development. This is true for the segmented taper because the segments would be more sensitive to electron beam dosage and the etched facets of the segments could potentially cause catastrophic losses due to the resulting edge roughness. The three dimensional taper would require at least one more lithography step and potentially one more deposition step depending on the process.

The inverse taper spot-size converter was simulated for a wavelength of 780 nm using Lumerical's Eigenmode Expansion (EME) solver as explained in Section 3.3 and illustrated in Figure 8.2. The refractive index of the SU8 waveguide was found experimentally (this result is discussed further in Section 8.4.1). The EME solver is used to find the scattering matrix, **S**, which represents the amplitude transmission and reflection coefficients of the entire structure. The elements of the scattering matrix are explained in Table 8.1.

The power transmission from a 1 µm by 200 nm Si_3N_4 waveguide core to a square SU8 waveguide is determined by taking the square of the absolute value of the scattering matrix

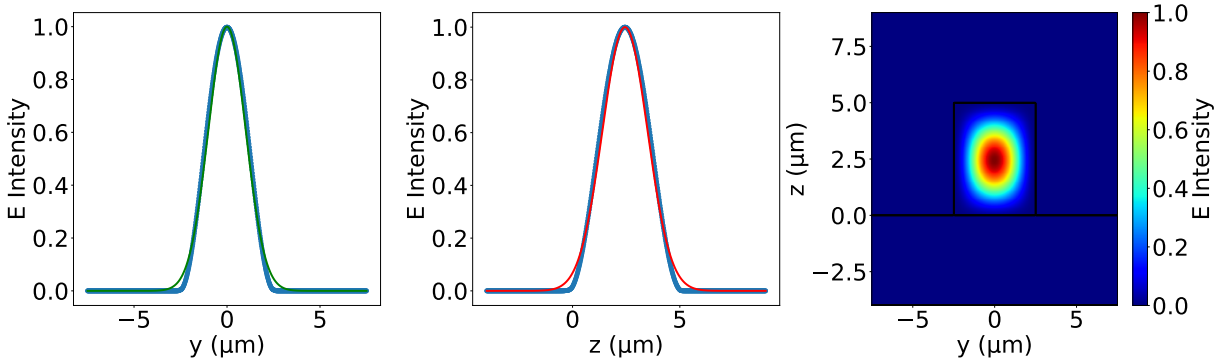

Figure 8.3: The y, z, and y-z electric field intensity profiles are shown. A Gaussian distribution is fit to each 1D profile to illustrate that they are approximate Gaussian modes. The discontinuous refractive index results in non-Gaussian behaviour near the material boundary.

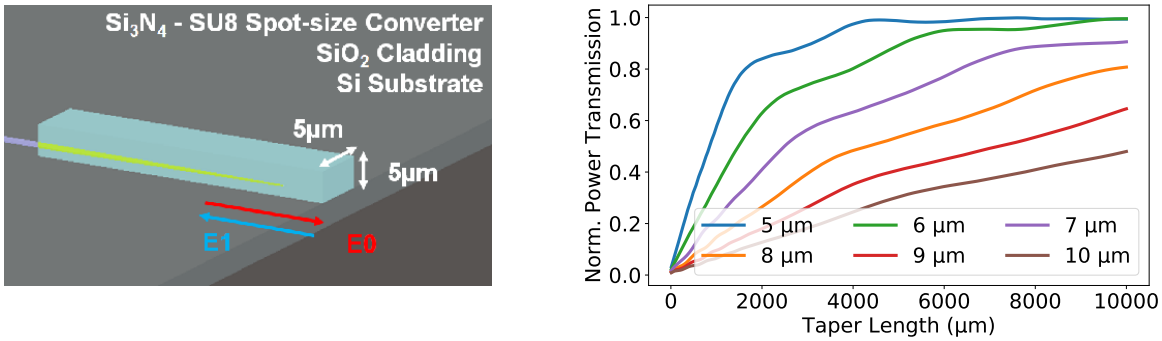

Figure 8.4: Left: A perspective view of a inverse taper spot-size converter with a 5×5 μm SU8 cross-section is shown. The output electric filed amplitude in the SU8 is labelled E_0 while the return amplitude is labelled E_1. Right: The spot-size converter power transmission for each SU8 waveguide cross-section as a function of taper length.

parameter S_{21}. The transmission from the Si_3N_4 taper to SU8 waveguide can be improved by increasing taper length. The power transmission as a function of taper length is shown in Figure 8.4 for SU8 waveguides of different cross section, where each cross section is a square with side length from 5-10 μm. Normalised transmission reaches ~ 1 for both the 5 μm and 6 μm SU8 waveguides for a 10 mm taper length. This is quite long for an integrated device and so a side length of 5 μm is assumed from here on to allow for a shortened taper length and transmission is taken to be 1. The mode profile found in this simulation was used to find the diameter of that mode, defined as the width of the beam at the points where the intensity of the beam is equal to $\frac{1}{e^2}$ (see Figure 8.3). The mode profile is slightly elliptical because the waveguide has a SiO_2 bottom cladding and no top cladding. The mode diameters in the y and z directions are found to be $d^y = 4.16\,\mu m$ and $d^z = 3.88\,\mu m$. These diameters are used in Section 8.2.3.

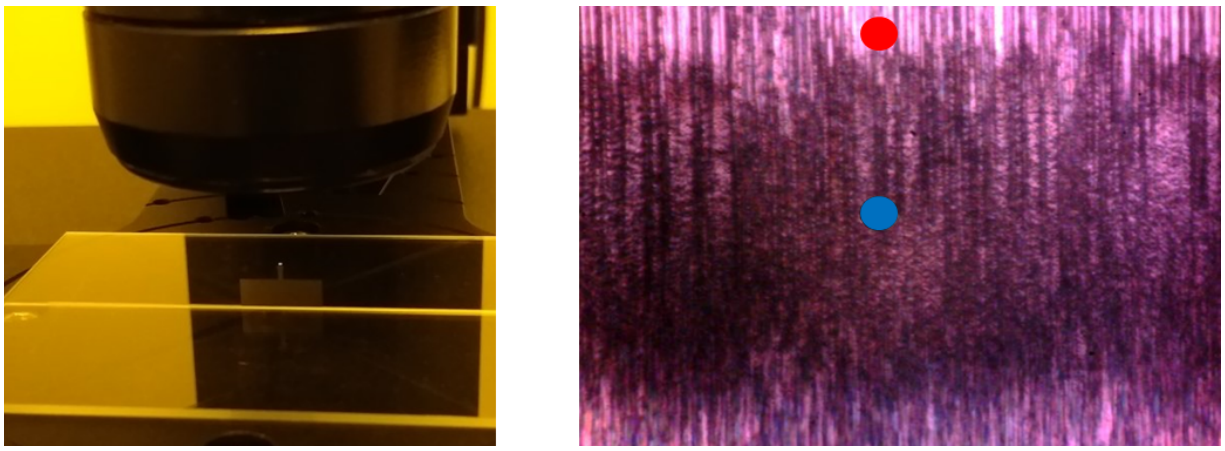

Figure 8.5: Left: The MEMS proof mass is held vertically under the 50× objective lens of the Filmetrics thin film mapping tool to measure the edge indicated in red in Figure 8.1. Right: The captured microscope image with red and blue spots to indicate the high and low refletance areas respectively. The diameter of these spots is approximately the diameter of the beam used to perform the reflectance measurement.

8.2.2 Measuring Silicon Proof Mass Reflectivity

The intended optical path of the MEMS interferometer would have the light coupling from the tapered Si_3N_4 waveguide to the SU8 waveguide and into free-space, reflecting from the edge of the MEMS proof mass and coupling back into the waveguide through the inverse taper spot-size converter. The reflectively of the proof mass cannot simply be taken to be the Fresnel reflectivity of a silicon surface because the edge has been etched using a physical reactive ion process resulting in a rough surface, assuming that no surface conditioning or reflective coating is used. The roughness of this surface will introduce a lot of scattering and reduce the reflectivity of the surface. The power reflected from the surface was measured directly using the Filmetrics thin film mapping tool discussed in Section 5.3.3. It is the edge of the proof mass that would act as a mirror for the interferometer and so it is the edge that needed to be measured. Delicate handling is required because the proof mass is only 200 µm thick and therefore quite fragile.

The proof mass was removed from its frame and sandwiched between two microscope slides such that one of its axial posts is directed towards the Filmetrics tools objective lens. This setup is shown in Figure 8.5 and so is the resulting microscope image captured by the Filmetrics tool. The micropscope image illustrates the beam spot-size used for the reflectance measurement (in red and and in blue) which for the 50× objective lens used in this instance is 10 µm in diameter. This measurement clearly shows areas of high reflectance at the top and bottom edges of the proof mass and a large area in between which has lower reflectance. The data from the reflectance measurements performed at these areas of high and low reflectance is shown in Figure 8.6. At 780 nm wavelength the reflectance is between 3 % in the low reflectance area and 14 % in the high reflectance area.

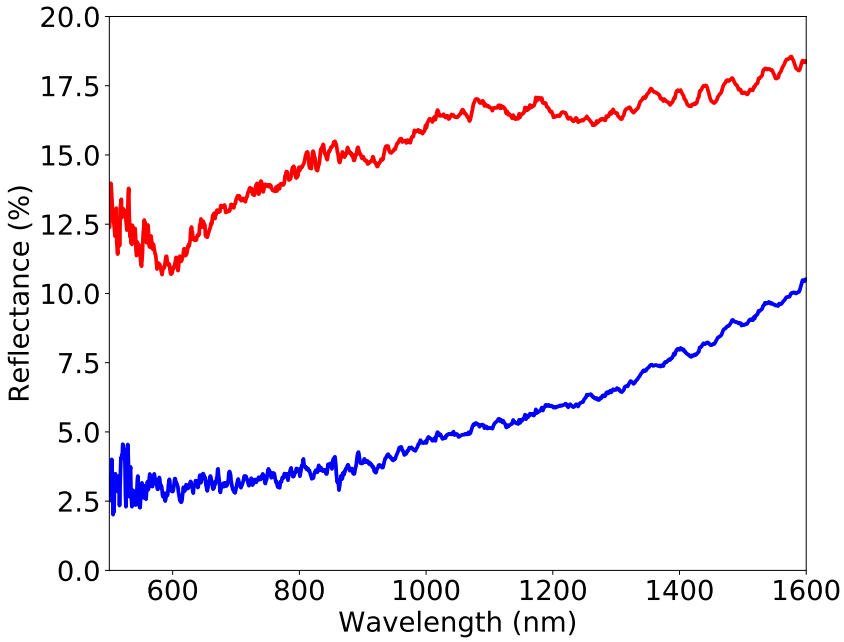

Figure 8.6: The percentage of reflectance is shown against the wavelength of light for both the high and low reflectance regions indicated in red and blue respectively as in Figure 8.5. Reflectance is lower at shorter wavelengths as expected due to increase scattering.

8.2.3 Mode Overlap Of The Diverging Return Beam

The power return coupling into the Si_3N_4 waveguide can be found by modelling the divergence of a 780 nm wavelength Gaussian beam and taking into account the following considerations; the spot-size converter transmission (from Si_3N_4 to SU8) is taken to be lossless, the SU8 waveguide cross-section of $5\times5\,\mu$m is chosen, the reflectivity from the SU8 waveguide is assumed to be the Fresnel reflectivity, and the reflectivity of the proof mass is taken from the data presented in Section 8.2.2. The Fresnel power reflection coefficient corresponding to the SU8-air interface is given by [156]

$$R = \left|\frac{n_{\mathrm{SU8}} - n_{\mathrm{air}}}{n_{\mathrm{SU8}} + n_{\mathrm{air}}}\right|^2 = 0.049. \tag{8.6}$$

Using the notation convention introduced in Figure 8.4, where E_0 is the outgoing field amplitude in the SU8 and E_1 is the returning field amplitude, the mode overlap integral is given by [84]

$$S = \frac{|\int E_0 E_1 dA|^2}{\int |E_0|^2 dA \int |E_1|^2 dA}. \tag{8.7}$$

Decomposing the Gaussian form given in Equation 8.2 into the spatial terms for the y and z component, and normalising the amplitude gives

$$E(x,y,z) = \frac{w_0^y}{w^y(x)} \exp\left(-\frac{y^2}{w^y(x)^2}\right) \frac{w_0^z}{w^z(x)} \exp\left(-\frac{z^2}{w^z(x)^2}\right) \tag{8.8}$$

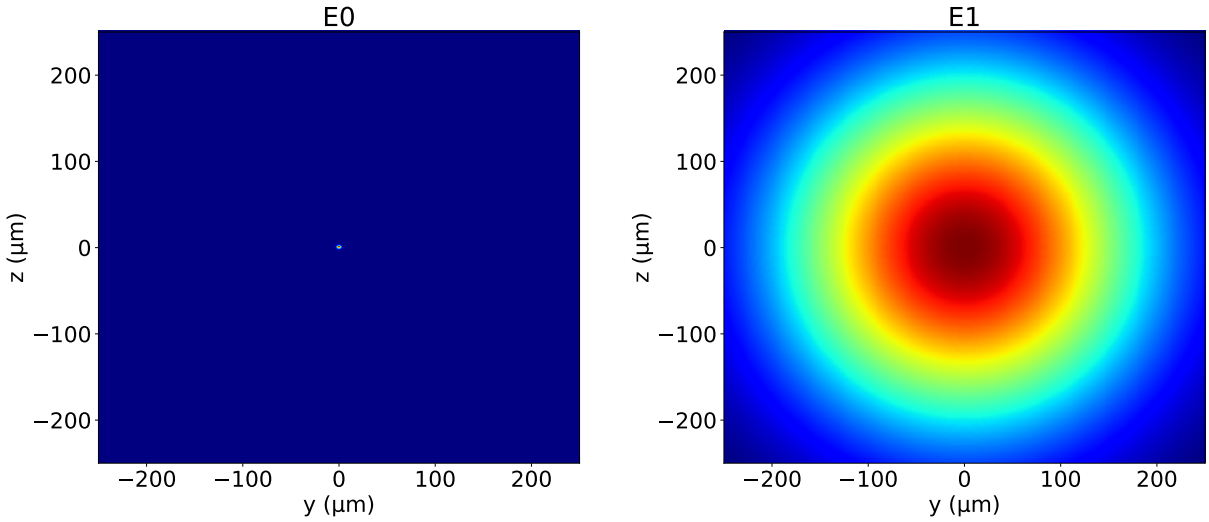

Figure 8.7: The electric field amplitude distributions for the output 780 nm beam E_0 and the returning beam E_1 after propagating a total distance of 1600 µm. The beam is shown to diverge significantly while propagating in free-space.

where w_0^y and w_0^z take the values found in Section 8.2.1 and $w^{y,z}(x)$ is found using Equation 8.3. The MEMS gravimeter has an actuation range of $\sim 800\,\mu m$ [144] and so if the facet of the spot-size converter were as close as it could possibly be to the MEMS proof mass then it would still have to be able to measure it's displacement when it is up to 800 µm away. For the light to travel from the spot-size converter to the proof mass and back would be a distance of 1600 µm. The Gaussian field amplitude distributions for an outgoing field E_0 and a returning field E_1 having propagated a total distance of 1600 µm are shown in Figure 8.7. By combining the effects of the beam divergence, the SU8 Fresnel reflectance, and the silicon proof mass reflectance, the total return power can be calculated as a function of propagation distance (see Figure 8.8). This demonstrates that the beam divergence is the dominant loss mechanism for any realisable propagation distance. In order to increase the return power, it is desirable to have some way of focusing the beam. A micro-ball lens was considered for this application.

8.3 Micro-ball Lens Alignment Tolerance

The micro-ball lens to be used to collimate the diverging light emanating from the waveguide facet can characterised by five main parameters (the spatial parameters are illustrated in Figure 8.9). The main parameters are the diameter of the ball lens D, the effective focal length EFL, the back focal length BFL, the refractive index of the lens material n, and the diameter of the resulting collimated beam d. The effective focal length is given by

$$EFL = \frac{nD}{4(n-1)} \tag{8.9}$$

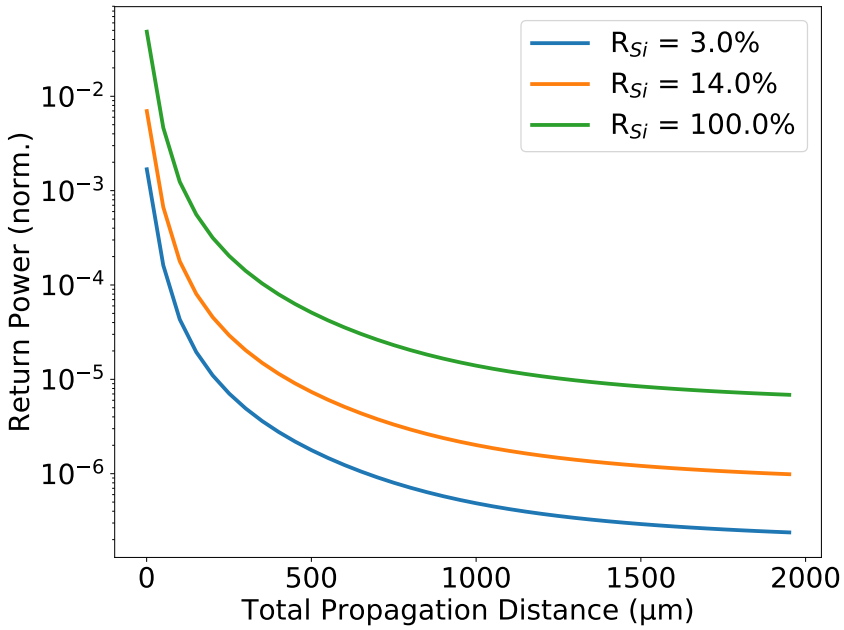

Figure 8.8: The return power of a 780 nm Gaussian beam as a function of the total propagation distance is shown for silicon reflectance values of 3 %, 14 %, and 100 %. The beam divergence is shown to be the dominant loss mechanism.

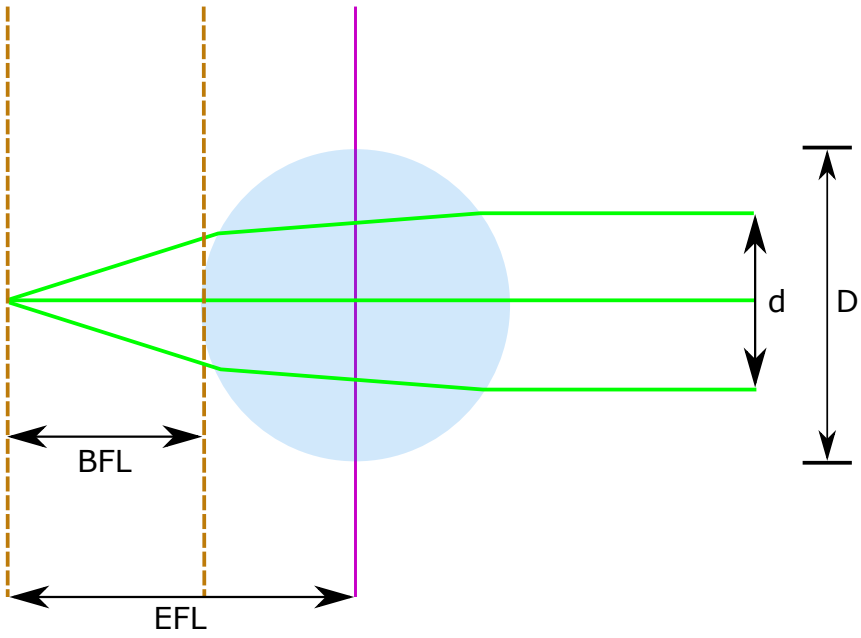

Figure 8.9: Key parameters of a micro-ball lens; the diameter of the ball lens D, the effective focal length EFL, the back focal length BFL, and the diameter of the resulting collimated beam d.

and the back focal length is given by

$$BFL = EFL - \frac{D}{2}. \tag{8.10}$$

For a fused silica micro-ball lens the refractive index is 1.458 and a diameter of 1 mm was chosen resulting in an effective focal length of 296.0 µm. In the case of collimated incident light, the numerical aperture of the lens is given by

$$NA = n_{\text{air}} \sin\theta = \frac{1}{\sqrt{1+4\left(\frac{n_{\text{lens}}D}{4d(n-1)}\right)^2}} \tag{8.11}$$

but in this application θ is the divergence angle of the Gaussian beam, in the paraxial case this is given by

$$\theta = \frac{\lambda}{\pi n w_0} \tag{8.12}$$

where w_0 is the beam waist. This is taken to be half of the corresponding mode diameter value found in Section 8.2.1. The inherent assumption made here is that the light field is continuous at the waveguide facet. The divergence angles in the y and z axes are $\theta_y = 0.1279\,\text{rad}$ and $\theta_y = 0.1193\,\text{rad}$. The resulting collimated beam diameters are $d_y = 204.8\,\mu\text{m}$ and $d_z = 190.9\,\mu\text{m}$. Heretofore, perfect alignment of the micro-ball lens has been assumed. The effect of micro-ball lens misalignment upon the Gaussian beam profile was investigated using a combination of ray transfer matrix analysis, numerical modelling, and the Lumerical FDE solver.

8.3.1 Ray transfer matrix analysis

The tolerance of the micro-ball lens alignment could be simulated using a finite difference or finite element approach but this would have been computationally expensive and time consuming. Instead, a ray transfer (or ABCD) matrix analysis approach was implemented using the python library raytracing 1.1.11 [157]. This technique is based upon the paraxial approximation, that is the assumption that rays form a small enough angle θ with the optical axis such that $\sin\theta \approx \theta$. Each element in the optical path is described by a 2×2 ray transfer matrix operating on a vector which describes the incident light ray (see Figure 8.10). The transfer matrix representing any component in the optical path is given by an "ABCD" matrix such that [158]

$$\begin{pmatrix} z_2 \\ \theta_2 \end{pmatrix} = \begin{pmatrix} A & B \\ C & D \end{pmatrix} \begin{pmatrix} z_1 \\ \theta_1 \end{pmatrix}. \tag{8.13}$$

Therefore, propagation in a region of space of length s with constant refractive index is

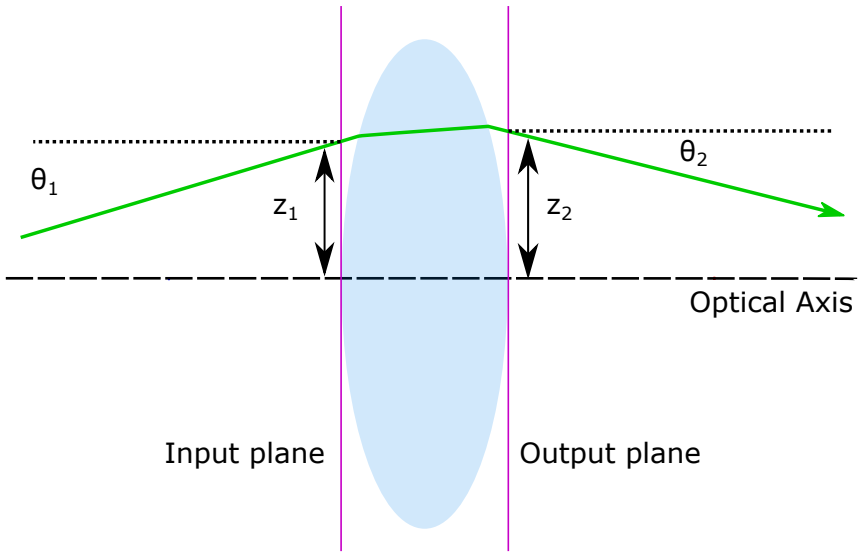

Figure 8.10: A light right passing through a thick lens. The ray transfer matrix gives the transformation of the light ray position and angle on the input plane to its position and angle on the output plane.

therefore represented by the transfer matrix [157, 158]

$$M = \begin{pmatrix} 1 & s \\ 0 & 1 \end{pmatrix} \tag{8.14}$$

and refraction at a curved dielectric interface with radius R is represented by the transfer matrix [157, 159]

$$M = \begin{pmatrix} 1 & 0 \\ \frac{n_1 - n_2}{n_2 R} & \frac{n_1}{n_2} \end{pmatrix} \tag{8.15}$$

where n_1 is the refractive index at the input plane, n_2 is the refractive index at the output plane, $R < 0$ represents a concave radius, and $R > 0$ represents a convex radius. Generally, a lens can be considered as an interface with radius R_1 followed by propagation of a length equal to the lens thickness t followed by an interface of radius R_2. This is given by

$$M = \begin{pmatrix} 1 & 0 \\ \frac{n_1 - n_2}{n_2 R_1} & \frac{n_1}{n_1} \end{pmatrix} \begin{pmatrix} 1 & t \\ 0 & 1 \end{pmatrix} \begin{pmatrix} 1 & 0 \\ \frac{n_2 - n_1}{n_1 R_2} & \frac{n_2}{n_1} \end{pmatrix} \tag{8.16}$$

where n_1 is the refractive index at the input plane and at the output plane and $n_2 = n_L$ is now the refractive index of the lens material. If the lens is in air then $n_1 = 1$ and so the transfer matrix for this lens becomes

$$M = \begin{pmatrix} \frac{t(1-n_L)}{n_L R_1} + 1 & \frac{t}{n_L} \\ -(n-1)\left(\frac{1}{R_1} - \frac{1}{R_2} + \frac{t(n_L-1)}{n_L R_1 R_2}\right) & t\frac{n-1}{n_L R_2} + 1 \end{pmatrix}. \tag{8.17}$$

This ray transfer matrix is used for the micro-ball lens considered in this work because the micro-ball lenses do not satisfy the thin lens approximation which would allow using the much simpler ray transfer matrix

$$M = \begin{pmatrix} 1 & 0 \\ -\frac{1}{f} & 1 \end{pmatrix}. \tag{8.18}$$

where f is the focal distance.

One of the advantages of the ray transfer matrix approach is that it can be used to consider Gaussian beam propagation as well as optical rays. This is done by propagating the complex beam parameter q defined by [158, 160, 161]

$$\frac{1}{q} = \frac{1}{R(x)} - i\frac{\lambda}{\pi n w(x)^2} = \frac{x}{x^2 + x_R^2} - i\frac{\lambda}{\pi n w(x)^2} \tag{8.19}$$

such that for any optical element, or sequence of elements, the complex beam parameter at the output plane is given by the following transformation,

$$q_2 = \frac{Aq_1 + B}{Cq_1 + D}, \tag{8.20}$$

where q_1 is the complex beam parameter at the input plane and q_2 is the complex beam parameter at the output plane. The power of this approach is that a Gaussian beam can be tracked through a complicated optical path by simple matrix linear algebra.

The required arguments for optical ray propagation using the python library raytracing 1.1.11 [157] are the height of the object, the object position ($x = 0$), the ray number indicating number of points on the object that are to be tracked, the fan number indicating number of individual rays in each set (or fan) of rays, and the total fan angle encompassed by a set of individual rays. These rays can be propagated through the optical system to form what is referred to as the "imaging path". The Gaussian beam can be generated using the variables of the complex beam parameter. In this instance the waist, refractive index of air ($n = 1$), and wavelength ($\lambda = 780\,\text{nm}$) were used to generate the beam. Considering equations 8.3, 8.4, and 8.19, this is all the information required. This beam is propagated through the system to form what is referred to as the "laser path". The rays in the laser path representation indicate the beam radius w at that point. The diffraction of the Gaussian beam in free space is accounted for by subdividing each space element into smaller space elements and calculating the beam radius at the interface of each of these [157].

8.3.2 Alignment Tolerance Simulation

In Section 8.2.3 it was stated that the proof mass could have an actuation range of 800 µm. In this analysis the space between the lens and the proof mass mirror is set to 1 mm, this assumes that the proof mass is at its maximum displacement with respect to the lens while leaving a

200 µm gap when the proof mass at its minimum displacement. The optical path of the MEMS interferometer is considered by unfolding it around the point of reflection (the proof mass) and creating a duplicate of the micro-ball lens. The mirror is assumed to be perfect here, as the focus of this treatment is to determine the affect on lens misalignment upon the return power coupling of the beam. The ray matrix imaging path illustrated in Figure 8.12 was used to determine the effect of transverse misalignment from 0-1.5 µm while the ray transfer matrix laser path in Figure 8.11 was used to find the effect of misalignment in the optical axis for an array of test focal lengths from 276-316 µm.

The ray transfer matrix analysis was validated for the imaging path by varying the position of the first lens using the array of test focal lengths. The difference between the object height and the image height is found for each test focal length and the lens position which minimised this difference is returned, the spacing between lenses was kept constant. Using this method, a focal length of 295.9 µm was found in accordance with the expected value of 296.0 µm. Similarly for the laser path, the lens position was varied and the difference between the input and output waists was minimised. For the small distance between the lens required for this application, the focal length is found to be 296.2 µm using this method, again agreeing with the expected value. For much larger propagation distances, the diffraction of the Gaussian beam in free space becomes more significant and the value found for focal length using this method differs from the expected value increasingly as the propagation distance is increased.

To determine the effect of defocus (misplacement of the lens along the optical axis) upon the returning beam radius (the output of the ray transfer analysis), the difference in radii between outgoing and returning beam in the plane of the SU8 waveguide facet must be found. For each test focal length, the return beam radius is found at a distance after the second lens equal to the test focal length. This is not always equal to the position of the beam waist and to use the radius value of the waist would break the symmetry of the system. The outgoing beam radius (the radius used to initialise the Gaussian beam) is divided by the return radius to provide a single value which characterises this change in radius.

The transverse misalignment of the lens is considered only for lens displacements of the same order of magnitude as the mode diameter in the SU8 waveguide, for lens displacement values greater than this, the resulting modal overlap is assumed to be negligible. In this regime the paraxial approximation holds true. The ray transfer imaging path is used to consider the resulting beam steering due to object heights representing the extremes of the SU8 mode diameter, $w_z = 2.08\,\mu\text{m}$, plus the maximum lens displacement of interest, $\Delta z_{max} = 1.5\,\mu\text{m}$, and so the resulting object height maximum is 3.58 µm. The increase in propagation length (and therefore the Gaussian beam diffraction) is found to be negligible ($\sim 10^{-8}$ m). The distance from the lens at which the image formed was found, for each test lens position on the optical axis, for the maximum transverse misalignment. This distance was found to deviate from the lenses focal length by less than $\pm 1\,\mu\text{m}$ of the focal length and so this effect will be neglected, that is the

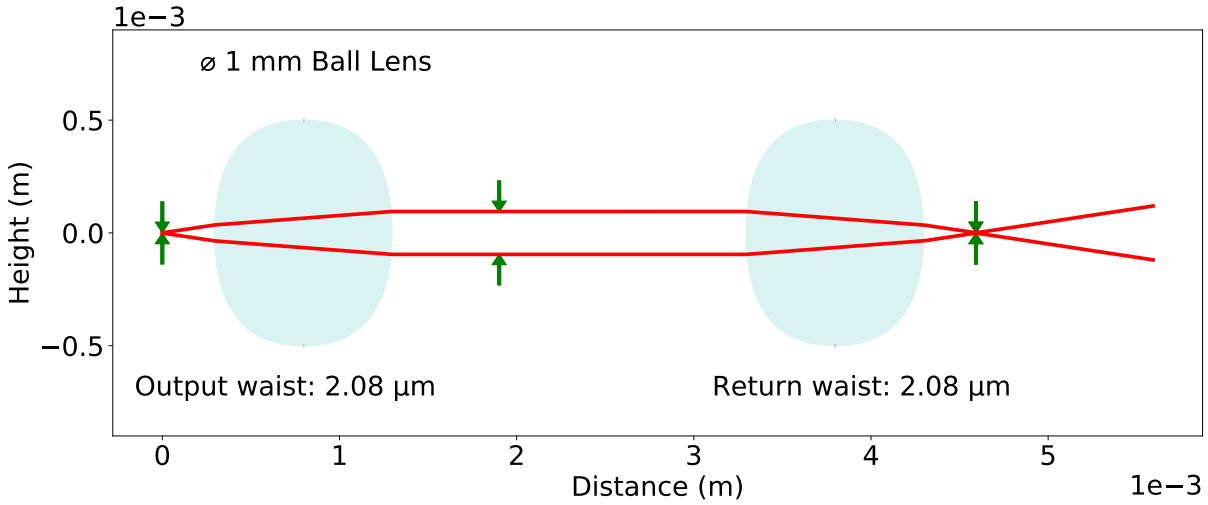

Figure 8.11: The red rays represent the beam radius of an optimally aligned Gaussian beam. The green arrows indicate the waist positions.

image height will be directly compared to the object height. The final result of this analysis was that the image height was always found to be equal in magnitude but opposite in sign to the object height and so the relative displacement of the outgoing and returning Gaussian modes is effectively double the lens displacement.

The modal overlap of the outgoing and returning Gaussian beams was found using the same approach outlined in Section 8.2.3. For each value of the transverse lens misalignment the returning Gaussian profile was displaced by twice that value. For each test focal length, the returning Gaussian beam was scaled corresponding to the value found previously to characterise the change in radius for the given test focal length. The FDE solver uses a similar approach to find the mode overlap and determines the total power coupling by accounting for any reflection resulting from the mismatch of the effective indices of the modes. By using the FDE solver to find the power coupling from the SU8 mode profile to the outgoing Gaussian beam (this is a fixed value), squaring this value to represent the return trip and multiplying this by the mode overlap of the outgoing and returning Gaussian beam profiles, the total power coupling between the outgoing mode and the returning mode in the SU8 waveguide can be found. Instead of using an analytical method to determine the overlap integral of the outgoing and returning Gaussian beams, the power coupling between the returning Gaussian beam and the SU8 waveguide mode can be found directly using the FDE solver. This is multiplied by the power coupling between the SU8 waveguide mode and the outgoing Gaussian beam to find the total return power coupling. The resulting power coupling found using both of these methods is shown in Figure 8.13.

The alignment tolerance in the transverse plane poses a much more stringent requirement than the alignment in the optical axis. The lens placement accuracy in the plane of the device would be determined by electron beam lithography and therefore the lens alignment in the optical axes and in the y component in the transverse plane should not pose an issue. The alignment

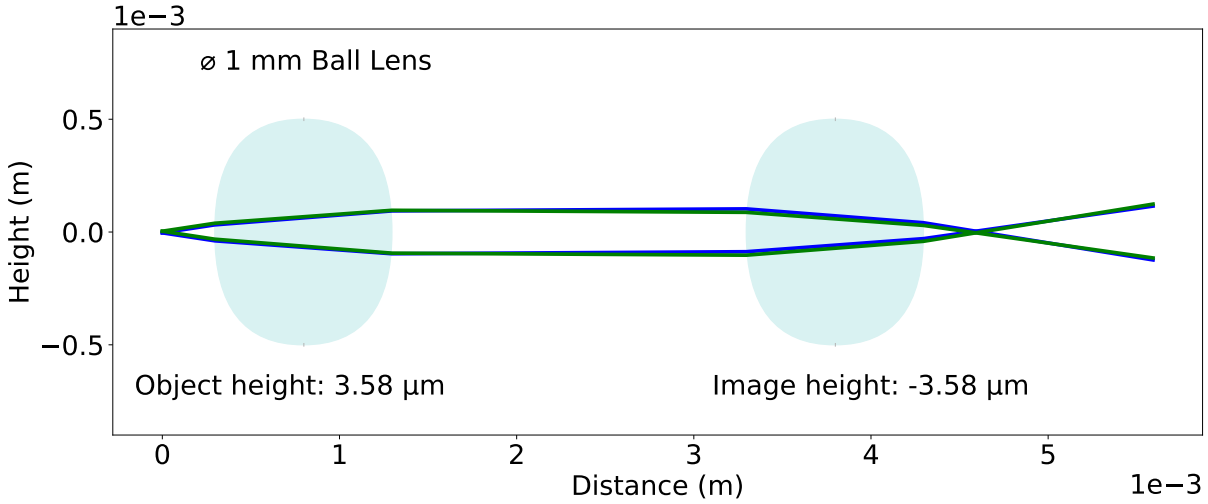

Figure 8.12: The object height is set equal to the beam radius in the z axes plus the maximum transverse misalignment value, $w_z + \Delta z = 2.08 + 1.5 = 3.58\,\mu\text{m}$. The green rays represent a positive valued object height while the blue rays represent a negative valued object height.

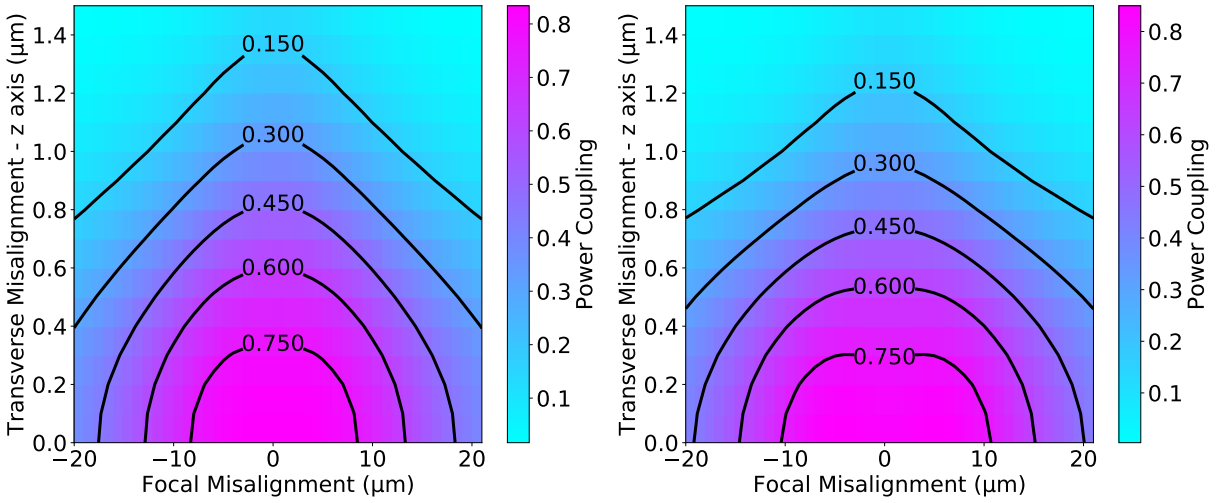

Figure 8.13: The return power coupling at the SU8-air interface of the beam which has propagated a total distance of 2 mm in free-space is found using the analytical method (left), where the overlap integral of the outgoing and returning Gaussian beam is found numerically, and using the FDE solver (right) to determine the power coupling between the returning Gaussian beam and the SU8 waveguide directly.

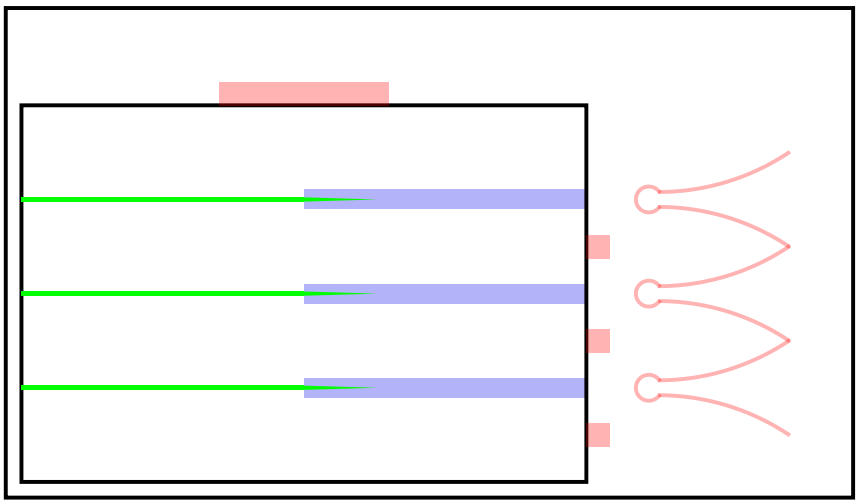

Figure 8.14: Concept design for the spot-size converter lens alignment. The top photonics chip has Si_3N_4 waveguide inverse taper (green) within $5 \times 5\,\mu m$ SU8 waveguide cores (blue). The SU8 features on the bottom carrier chip (red) include the registration blocks against which the photonics chip is aligned and the micro-ball lens receptacle. Waveguide widths are exaggerated for purposes of illustration. The alignment waveguides discussed in Sections 5.1, 6.1, and 8.4.1 are not shown here.

in the z axis in the transverse plane, of the waveguide spot-size converter to the micro-ball lens, is expected to require much more process development and this is discussed further in Section 8.4.2.

8.4 Process Development

A prototype design for coupling light from a Si_3N_4 waveguide to a collimated Gaussian beam in free-space via an SU8 spot-size converter and micro-ball lens is shown in Figure 8.14. This design consists of two sample chips. The photonics chip has the Si_3N_4 waveguides and SU8 spot-size converters, the second chip acts as a carrier for the first with registration blocks to align the photonics chip and act as lens receptacles. An SU8 spin-coating processes that can provide a thickness of $5\,\mu m$ is required for the spot-size converter. A second process is required that can provide a sufficiently thick film to fulfil the dual purpose of supporting the micro-ball lens at a suitable height and serve as registration blocks for the photonics chip. The registration block and lens receptacle are written in one stage of electron beam lithography to ensure alignment. SU8 is developed using propylene glycol methyl ether acetate (PGMEA) or the commercially available developer Microposit EC solvent.

8.4.1 SU8 Waveguide

A spot-size converter is to be used to expand the mode diameter from the Si_3N_4 waveguide in order to reduce the diffraction of the beam in free space. The underlying principle of the

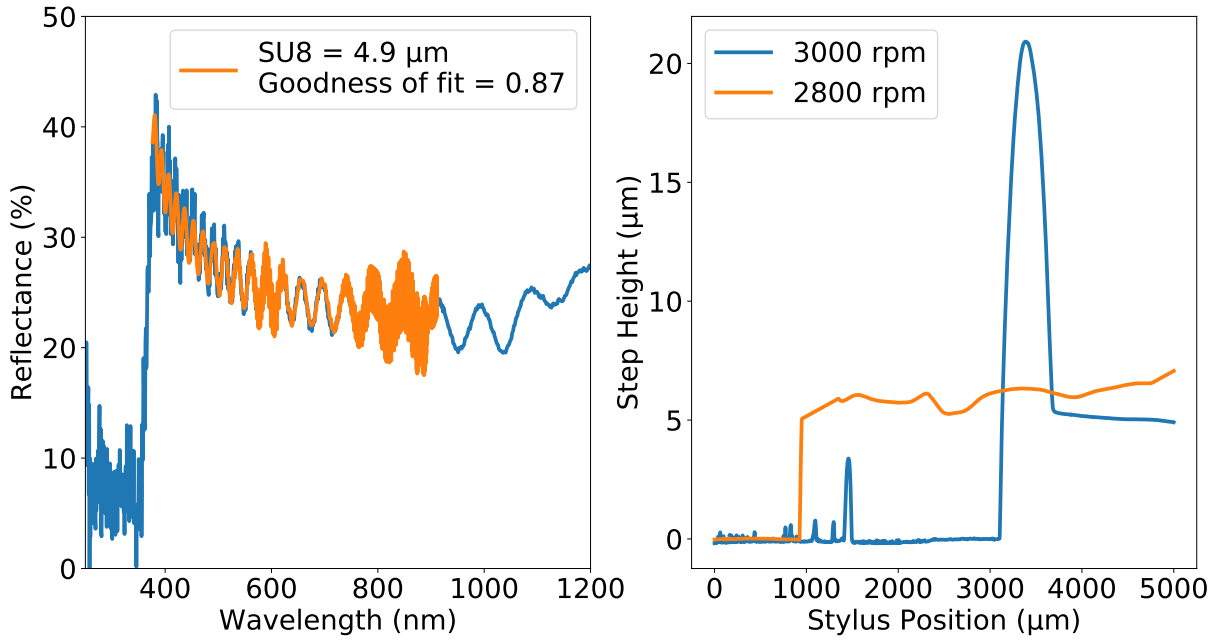

Figure 8.15: Measurements of SU8 film thickness using a Filmetrics thin film mapping tool (left) and a Dektak stylus profilometer (right). The filmetrics measurement was conducted up a a SU8 film deposited by spin coating at 3000 rpm. A "goodness of fit" of 1 would be a perfect fit. Right: The Detak measurement was conducted on the sample film that were deposited using spin coating speeds of 2800 rpm and 3000 rpm; the film corresponding to a spin speed of 3000 rpm exhibits edge-beading due to the solvent cleaning method used to expose some of the substrate.

spot-size converter is that the high index waveguide forms a taper within a larger, lower index waveguide core. The tapering of the high index waveguide allows for the effective index of the waveguide to be gradually reduced in the axis of propagation until the effective index matches the that of the larger, lower index waveguide. SU8 was chosen as the material for this larger, lower index waveguide because it has an index between those of Si_3N_4 and SiO_2, it is routinely deposited in layers from 2-200 µm in a single spin-coating process, and it is a negative tone electron beam lithography resist already available in the JWNC.

A SU8 thickness of 5 µm is desired for the SU8 waveguide. According to the data-sheet for SU8 3000 series [138], the target thickness can be realised by spin coating SU8 3005 with a spin speed of 3000 rpm. Test samples were prepared using spin speeds of 2800 rpm and 3000 rpm. These two film thicknesses were characterised using the Dektak stylus profilometer and film spun at 3000 rpm was also characterised using the Filmetrics thin film mapping tool, this measurement data is shown in Figure 8.15. This sample was characterised by ellipsometry to find the refractive index as a function of wavelength. The SU8 film was found to have a refractive of 1.57 at a wavelength of 780 nm, this data was used in the simulations in Section 8.2.1. To test the SU8 waveguide process, samples were designed and fabricated using many of the same process steps detailed in Chapter 5. The key differences are that the waveguide core layer is the resist in this case, so no etching or lift-off is required, and the electron beam dosage is much

lower for SU8 than it is for HSQ. The required dosage for SU8 waveguide was 4, much lower than the dose of 1300 used for written waveguide patterns in HSQ. This means that the highest resolution electron beam can be used without violating the maximum clock frequency of the VB6 pattern generator and still result in relatively short job times. For this reason, the 1 nA (4 nm) beam was used to write the SU8 waveguide pattern.

The exposed SU8 was developed using PGMEA for about 5 min resulting in clear waveguide features. For the first set of test SU8 waveguide samples, only the 5 µm wide waveguides were included in the design despite the design principles outlined Sections 5.1 and 6.1. This resulted in test samples that made it very difficult to perform the optical alignment required for testing. Another set of samples were fabricated following the previously established design principles and it is the images captured during testing of these samples that were used to illustrate the alignment technique in Figure 6.3. A microscope image of one of these test samples is shown in Figure 8.16.

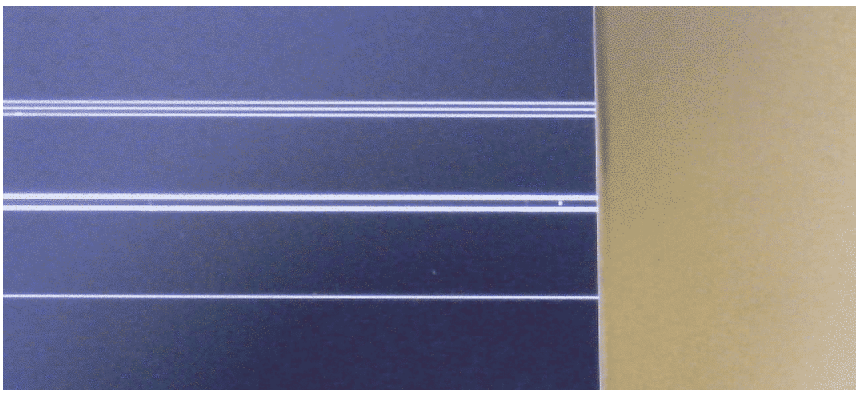

Figure 8.16: Microscope image of a triplet of $5 \times 5\,\mu m$ waveguides, a $40\,\mu m$ wide slab waveguide, and a single $5 \times 5\,\mu m$ waveguide

8.4.2 Registration Blocks And Micro-ball Lens Receptacle

The registration blocks on the carrier chip are to be used to determine the alignment of the photonics chip in the plane of the two chips. In this case the distance between the waveguide facet on the photonics chip and the micro-ball lens receptacle is determined by the lithography of the carrier chip. The benefit of writing the registration blocks and micro-ball lens receptacle in one pattern is that these features are automatically aligned. The transverse alignment in the plane of the chip is now determined by the distance between the waveguides and the parallel chip edge in contact with the registration blocks. The chip edge is to be cut parallel to the waveguide using a diamond blade dicing saw. Distance markers can be patterned in the SU8 to provide a visual cue of the desired edge position. The edge can be then be polished back to the desired position using the same polishing technique used to establish the waveguide facets. The same polishing tool can be used to perform bulk material removal on the underside of the photonics chip to lower the SU8 spot-size converter to the desired height. There is no way to use lithography markers to assist in this process and so the precision of the sample thinning is limited to $10\,\mu m$ by the polishing tools micrometer. The diameter of the micro-ball lens has a tolerance of $\pm 2.5\,\mu m$ [162] which further compounds this issue, this does not however effect the transverse alignment in the plane of the chip or the alignment in the optical axis. An attempt was made to measure the micro-ball lens diameter by microscopy using image analysis techniques (see Figure 8.17) but with this method the micro-ball lens diameter could only be measured with a precision of around $20\,\mu m$. These limitations could potentially be overcome using optical characterisation of the collimated beam to determine the quality of waveguide-lens alignment and thinning the sample further if required in an iterative fashion. An alternative method of achieving vertical alignment would be to etch a recess in the carrier chip that the photonics chip would rest within, this method could eliminate the need for the SU8 registration blocks and could potentially be used to form some sort of micro-ball lens receptacle. This method would require the development of an etch process which is why it was not pursued, however it would

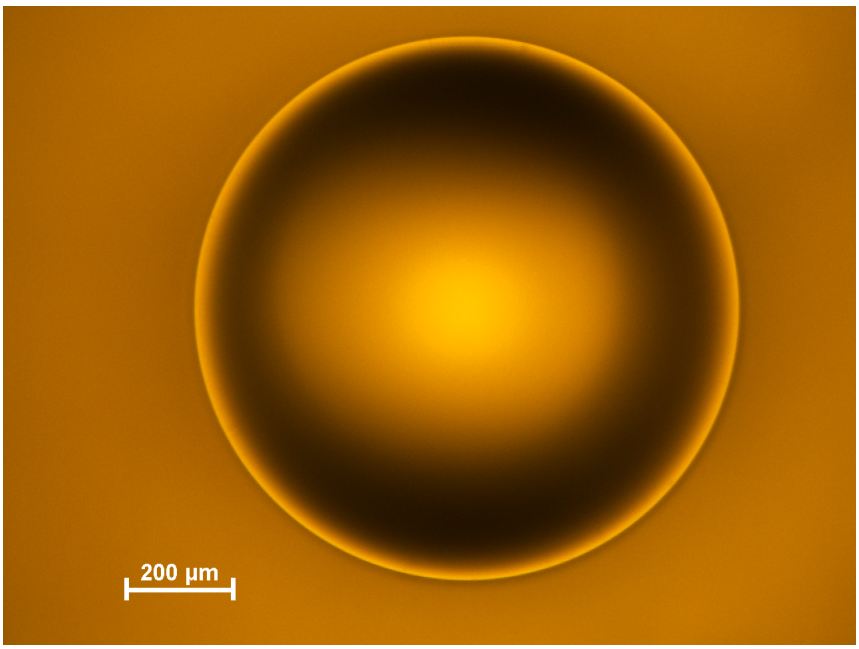

Figure 8.17: A microscope image of the micro-ball lens taken using a $\times 20$ objective lens.

mean that the etch depth could be measured with great accuracy using an interferometer such as in Figure 5.10.

No specific requirement for the height of the registration blocks has been determined but the micro-ball lens receptacle must be tall enough to raise the ball from the sample in order to locate it precisely. The functionality of the registration blocks was verified simply by preparing a square silicon test chip and pushing that test chip against the registration blocks. The blocks remained intact and the test chip remained in place once pushed against the blocks. Adhesive could be used to fix the photonics chip in place once aligned to the registration blocks. The initial design of the micro-ball receptacle consisted of a ring with an inner diameter of 280 µm and an outer diameter of 380 µm. Using the Pythagorean theorem, the centre of the 1 mm micro-ball lens would be found at 480 µm above the receptacle if the inner diameter of the receptacle were in contact with the lens. To ensure that the lens is properly seated in the receptacle and not simply rolling within it on the silicon substrate, the SU8 must be > 20 µm thick. The data-sheet [138] was once more consulted and ultimately a spin coating process was found to deposit ~ 23 µm of SU8 using SU8 3050 and a spin speed of 1000 rpm. This characterisation was performed using the Dektak stylus profilometer (see Figure 8.18). The first batch of samples produced received a soft bake (prior to lithography) of only 3 h at 90 °C which resulted in delamination of the SU8 during the development phase. Following samples received a soft bake of ~ 18 h at 90 °C resulting in mechanically stable SU8 registration blocks. The exposed SU8 was developed using PGMEA for about 20 min resulting in clear features.

The initial design was entirely dependent upon the lens being placed in the correct position in order for it to seat correctly within the receptacle, this proved to be very difficult to do by hand

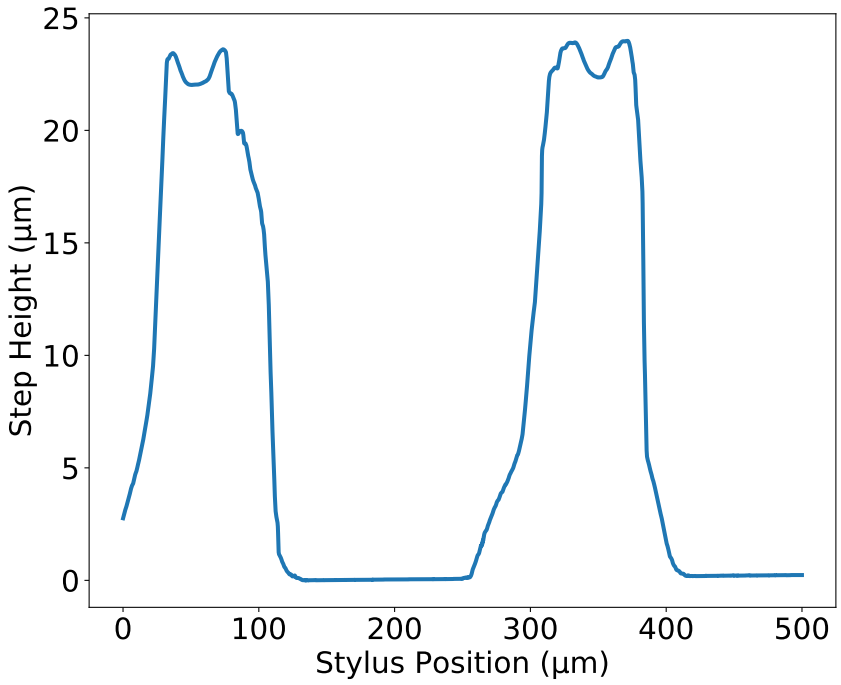

Figure 8.18: The step height of the SU8 film is measured by Dektak stylus profilometer. The film thickness is greater than 20 µm as required.

given the small size of the lens and the receptacle. The second iteration of the micro-ball lens receptacle design invoked the principle of self-assembly to assist in placement of the micro-ball lens. The basic principle is that the ball lens is to be pushed down a two dimensional "funnel" until it is longer resting on the substrate but instead on the guide rails of the funnel, the lens is raised to it's highest point at the bottom of the funnel and then falls into the circular receptacle of the same inner and outer diameter as before. It was a test sample with this design that was characterised using the Dektak stylus profilometer to provide the surface profile in Figure 8.18. Lens placement using this structure was tested and found to successfully guide the lens toward and subsequently contain it within the circular receptacle (see Figure 8.19). This design could be further improved by employing some sort of mechanism to apply downward pressure to the lens and hold it in position or using an adhesive to fix the lens position. This design iteration can only be transported with extreme caution without resulting in dislocation of the lens.

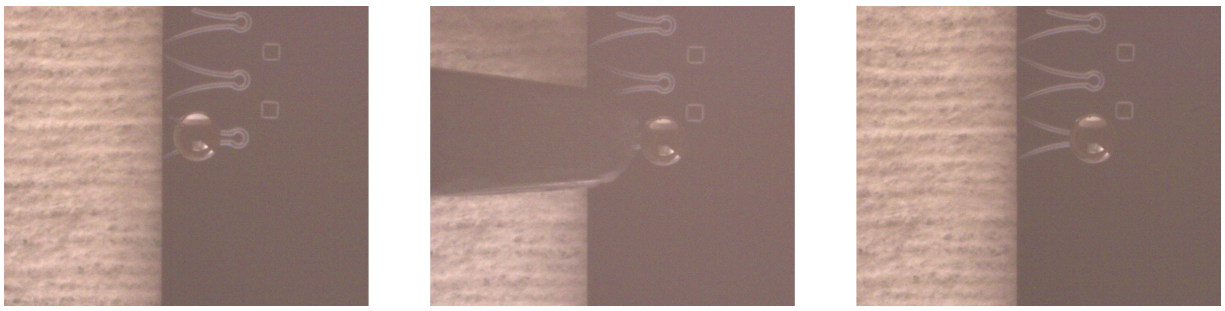

Figure 8.19: The micro-ball lens is placed in the mouth of the "funnel" and pushed with tweezers towards the lens receptacle. It raises up at the funnel mouth and falls into place within the receptacle.

8.5 Discussion

Progress has been made towards realising efficient coupling of 780 nm light from a Si_3N_4 waveguide to a collimated free-space Gaussian beam within the context of a developing an on-chip interferometer for measuring the displacement of the MEMS gravimeter. The transmission through an SU8 spot-size converter was simulated and found to approach a normalised transmission value of 1 within a taper length of 10 mm for SU8 cross-sections of $5 \times 5\,\mu m$ and $6 \times 6\,\mu m$. Choosing the $5 \times 5\,\mu m$ cross-section allows for a reduction in taper length by about a factor of 2 compared to the $6 \times 6\,\mu m$ cross-section while still realising total power transmission. The return power for the waveguide interferometer was determined analytically taking into account the reflectance of the SU8 waveguide facet and silicon proof mass. The free-space divergence of the Gaussian beam was found to be the dominant loss mechanism for the propagation distances required and so a scheme has been conceived to collimate the Gaussian beam by a micro optical bench approach. A 1 mm micro-ball lens was chosen to collimate the beam and the misalignment of this lens is considered by a combination of ray transfer matrix analysis, numerical modelling, and the Lumerical FDE solver. The alignment in the vertical axis z was found to pose the most stringent alignment tolerance. Processes have been developed to produce prototype SU8 waveguides, registration blocks, and micro-ball lens receptacles. Further development of these processes is required but this will be pursued in future work.

There are however a number of issues that still need to be resolved. The proof mass reflectivity is still low and non uniform throughout its cross-section. This could be improved upon with the addition of a mirror-like surface. This could be achieved by angled metal deposition to produce a metal surface on the edge of the proof mass or more simply by fixing a mirror on top of the proof mass such that the optical plane is raised above the plane of motion of the proof mass. The effect of these proposals on MEMS gravimeter performance has not been considered. Imperfect beam collimation would result in return power coupling which is a function of proof mass position. This is undesirable because the intended application is to determine the position of the proof-mass by interpreting the interferogram resulting from the outgoing and returning

beams. If this effect proved significant, then the interferogram signal would be significantly weaker for greater proof mass displacement and result in reduced sensitivity.

Chapter 9

Conclusions And Future Work

9.1 Conclusions

The goal of this work has been to further the development of a chip-scale atomic system based upon the D2 transition of ^{87}Rb atoms by developing a waveguide platform, consisting of a silicon dioxide bottom cladding, a silicon nitride waveguide core, and a silicon dioxide top cladding, that is compatible with a wavelength of 780.241 nm. Micro-ring resonators have been the focus of this development because they are a useful tool for characterising the performance of a waveguide platform and could proof to be a useful as a frequency reference for stabilisation of a diode laser in an integrated chip-scale atomic system. A record high Q factor value of $(1.38 \pm 0.04) \times 10^6$ has been demonstrated for buried waveguide micro-ring resonators operating around 780 nm corresponding to a propagation loss of 0.261 ± 0.009 dB cm^{-1}. The Q factor has been optimised by reducing the sidewall scattering loss and operating in the under-coupled regime of the micro-ring resonator. Utilisation of the micro-ring resonator as a frequency reference for laser frequency stabilisation has been explored by investigating the thermal dependence of the micro-ring resonance peak position. Negative thermo-optic polymers PMMA and SU8 have been characterised and considered as potential top cladding layers which could reduce the temperature dependent shift of the resonant wavelength. Further development of the waveguide platform has included work towards a free-space coupled interferometer for measuring the displacement of a MEMS gravimeter proof-mass. This included the process development for SU8 waveguide spot-size converters, registration blocks, and micro-ball lens receptacles.

The ray optic and electromagnetic theory pertaining to planar optical waveguides is discussed in Chapter 2. This forms the basis of coupled mode theory and provides context for subsequent simulations of waveguide properties. From coupled mode theory, an analytical solution is found for the coupling coefficient of the micro-ring resonators characterised in this work. This is based upon the coupling between two parallel similar waveguides but is adapted to the particular geometry presented by a straight bus waveguide coupled to a circular micro-ring resonator. The Lacey-Payne model of scattering loss is introduced, this model suggests that

scattering loss can be reduced by increasing waveguide width and by reducing the index contrast between the waveguide core and cladding.

The simulation tools used to determine the essential design parameters for silicon nitride waveguides and micro-ring resonators are introduced in Chapter 3. The predominant simulation tool used in this work was the finite difference eigenmode (FDE) solver. One dimensional FDE simulations wre used to decide upon appropriate thickness for the bottom and top cladding layers and the core layer. A 4 µm thick SiO_2 bottom cladding was found to be sufficient to reduce loss due to substrate leakage for a TE_0 mode in a 200 nm thick Si_3N_4 core. A top cladding layer of 1 µm thick SiO_2 was found to adequately suppress slab mode formation in the top cladding, an experimental issue caused by imperfect in-coupling. Two dimensional FDE simulations were used to find the effective index of the first few TE and TM modes supported by a 200 nm thick waveguide core as a function of the waveguide width. The overlap integral of curved and straight waveguides was determined for a series of widths and bend radii leading to the conclusion that a radius of 300 µm (the radius of all the micro-rings discussed in this work) can be considered to be equivalent to a straight waveguide and therefore does not introduce additional radiative loss due to the bend. The even and odd effective indices of a coupled pair of similar and parallel waveguides was found and used to determine the coupling coefficient of the rings tested in this work from the analytical solution derived in Chapter 2. The Lacey-Payne model has been used to estimate the sidewall scattering induced loss of 200 nm thick Si_3N_4 waveguide with and without SiO_2 top cladding layers. This informed the design decision to increase the waveguide width in order to optimise the micro-ring Q factor and provided further motivation for the development of an index matched SiO_2 top cladding layer which did not result in the slab mode formation that prevented characterisation of the micro-ring resonators. The eigenmode expansion solver used in Chapter 8 to simulate the inverse taper spot-size converter was also explained in Chapter 3 for the sake of completeness.

The performance of a micro-ring resonator was modelled analytically, the results of this modelling are reported in Chapter 4. The normalised power transmission of an all-pass micro-ring resonator was derived and this equation was used in Chapter 6 to determine the micro-ring resonator field amplitude loss coefficient by parameter estimation, the waveguide propagation loss can be determined from this value of the length of the micro-ring resonator. The behaviour of the Q factor, resonance peak amplitude, and slope gradient of a micro-ring resonance peak is determined a function of the coupling parameter κ. This lead to the conclusion that Q factor can be optimised by increasing the gap spacing of the evanescent coupling section in order to operate in the under-coupled regime and so this informed the design of the micro-ring resonators.

The fabrication processes developed in order to realise the silicon nitride waveguide platform are explained in Chapter 5. Silicon wafers 6 ” in diameter are used as the substrate for deposition of the bottom cladding and core layers. The bottom cladding is formed by wet thermal oxidation and the core layer is deposited by low pressure chemical vapour deposition. Hydrogen

silsequioxane was used as an electron beam lithography resist and as an etch mask for trifluoromethane reactive ion etching. Sulphur hexafluoride reactive ion etching may result in smoother sidewalls and presents a potential avenue of further process development in future work. Waveguide facets were prepared either by cleaving the sample or by dicing the sample using a diamond saw and polishing the exposed waveguide facets prior to device characterisation. Lithography patterns were designed using the Python-3 based tool Nazca Design™ and prepared for electron beam lithography using a combination of commercial and custom software.

The micro-ring resonators were characterised using the method presented in Chapter 6. Transmission spectra were recorded by sweeping the frequency of a tunable 780 nm Ti:sapphire laser and detecting the transmitted power using a silicon photodetector. The recorded spectra were analysed using regression analysis to fit a Lorentzian distribution and the normalised power transmission equation to the raw data by the method of least squares in order to perform parameter estimation. This allows for the Q factor and waveguide propagation loss to be determined along with other key attributes of micro-ring resonators. The potential of the 1.4 million Q factor micro-ring resonator to be used as a frequency discriminator for laser stabilisation was also briefly discussed.

Utilisation of the 1.4 million Q factor micro-ring resonator as a frequency reference is expanded upon further in Chapter 7 by considering the temperature dependence of the resonance peak position for micro-rings with the same core dimensions and a series of top cladding materials. The resonance peak position of this micro-ring with the SiO_2 top cladding was found by simulation to have a temperature dependent wavelength shift of $7.34\,\mathrm{pm\,K^{-1}}$. From this, is determined that active temperature stabilisation of $\pm 27\,\mathrm{mK}$ would be required to use this micro-ring as a frequency reference. The finite difference eigenmode solver is used to optimise the thickness of negative thermo-optic top cladding materials PMMA and SU8 in order to reduce the temperature dependent wavelength shift of the resonance peak position. A required temperature stability of $\pm 167\,\mathrm{mK}$ is found for 500 nm thick PMMA and $\pm 1.43\,\mathrm{K}$ for 290 nm thick SU8. A fabrication tolerance of $\pm 5\,\mathrm{nm}$ is assumed for the thickness of these potential top cladding layers because they are familiar resist materials.

Coupling from a silicon nitride waveguide to a free-space Gaussian beam has been investigated within the context of developing an interferometer for measuring the displacement of a MEMS gravimeter proof-mass as reported in Chapter 8. An inverse taper spot-size converter with an SU8 waveguide has been designed in order to expand the mode diameter and thereby reduce the beam diffraction. The reflectivity of the SU8 waveguide and silicon proof-mass have been considered and the diffraction of Gaussian beam still proved to be the dominant loss mechanism for the return beam and so a collimation lens would be required. A 1 mm diameter micro-ball lens has been chosen for this purpose and the alignment tolerance has been simulated using a combination of ray tracing matrix analysis, numerical modelling, and the finite difference eigenmode solver. SU8 waveguides, registration blocks, and micro-ball lens receptacles

have been successfully demonstrated. The alignment in the z axes will proof to be the most significant fabrication challenge and although means to address this have been discussed, the alignment procedure will require further development in future work.

9.2 Future Work

There is still some development required to improve upon the silicon nitride waveguide platform demonstrated in this work. To perform a direct measurement of waveguide propagation loss would help in designing photonic components in the future. This could be done by fabricating waveguide of different lengths and measuring the resulting loss of each waveguide which is known as the cut-back method [102]. This would require consistent power coupling throughout the rest of the system optical path and so could not be realised with cleaved waveguide facets which are inherently inconsistent. The dicing and polishing process facilitates this type of experiment but this process became available late into this research. The obfuscation of the waveguide mode due to slab mode formation in the cladding is believed to be caused by scattering light at the point of in-coupling from the lensed fibre to Si_3N_4 waveguide via free-space. This could be reduced by improving the in-coupling and could be achieved using an SU8 spot-size converter, possibly in conjunction with micro-ball lens as outlined in Chapter 8. Metalisation of the top cladding surface could lead to the development of components such as thermally tuned micro-ring resonators, phase modulators, and optical switches. Further integration is possible by including diode lasers and photodetectors on-chip.

There are many potential avenues for expanding upon applications of the Si_3N_4 waveguide platform. Some of these were considered in detail but could not fit within the scope of this work. Primary among these are frequency stabilisation of a diode laser by the Pound-Drever-Hall method using a micro-ring resonator as a frequency discriminator, atomic systems requiring atom trapping and laser stabilisation, and resonant micro-optic gyroscopes utilising the Sagnac effect in large area micro-ring resonators to sense rotation. Research areas which have not received the same level of attention include but are not limited to filters, delay lines and switches [40], a source of frequency comb generation [48], a source of entangled photon pairs [49], and light detection and ranging (LIDAR) [163].

9.2.1 Pound-Drever-Hall Laser Frequency Stabilisation

Pound-Drever-Hall (PDH) is a laser frequency stabilisation scheme developed for interferometric gravitational wave detectors [132, 164] based upon previous work on the stabilisation of microwave oscillators [165]. The transmitted power of an all-pass micro ring resonator is equivalent to the reflected power from a free-space Fabry Pérot cavity. One of the benefits of PDH is that the laser intensity fluctuations are decoupled from laser frequency fluctuations. In the side-of-peak locking method, a change in laser frequency is detected as a change in power transmitted

through a resonator and so is indistinguishable from a change in laser power. If the fluctuations in transmitted power were to be minimised (held at zero in the case of critical coupling) by actuating upon the laser frequency then this would be independent of the laser intensity. However, the spectral response is symmetric around the resonance peak and so there would be no way to determine in which direction the frequency has shifted. The derivative is anti-symmetric around the resonance peak, approximately linear close to the peak centre frequency, and crosses through zero on resonance (see Figure 4.4). It is therefore the ideal signal for controlling the tuning of the laser to achieve frequency stabilisation [132, 164], this is called the error signal.

The error signal can be found by modulating the frequency of the input laser light and demodulating the detected signal. This is fundamentally a derivative of the transmission spectrum as the frequency is changed slightly (modulation) and the resulting change in transmitted power is measured. The local oscillator signal used to drive the modulator is also passed into a mixer along with the detected power signal, effectively multiplying these signals together, resulting in an output signal with a low frequency component and a frequency component about twice the modulation frequency. This can be understood by considering the trigonometric identity

$$\cos(\omega_m t)\cos(\omega_{LO} t) = \frac{1}{2}\cos(\omega_m t - \omega_{LO} t) + \frac{1}{2}\cos(\omega_m t + \omega_{LO} t)$$

where ω_{LO} is the local oscillator frequency and ω_m is the modulation frequency, ideally $\omega_m = \omega_{LO}$. A low pass filter is used to remove the high frequency component leaving only the low frequency component which is the desired error signal. The amplitude of this signal is linear and proportional to the frequency offset from the desired set-point. An ideal layout is shown in Figure 9.1. In practise a phase shifter may be required to ensure the oscillator signal used for demodulation is in phase with the modulated signal and an optical isolator maybe required to prevent reflection from entering the laser and causing instability.

9.2.2 Sagnac Gyroscope

Sagnac interferometry measures a phase change in light caused by rotation. Light from a laser is split into two paths which counter-propagate in a closed loop before they are detected at the interferometer output using a photodetector. At rest these light waves will have the same phase but if the interferometer is rotating then this will cause an equal and opposite phase change for the counter-propagating waves. Mathematical derivations pertaining to the Sagnac effect can be found in Appendix B. The phase shift is given by Equation B.7. If instead of passing only once through the interferometer, light resonates within an optical resonator such as a micro-ring resonator, then this phase shift will occur for each round trip through the resonator. This results in counter-propagating light waves experiencing different resonant frequencies within the same resonator. The difference between these resonant frequencies is considered for multiple different reference frames in Appendix B. An integrated resonant micro-optic gyroscope (RMOG) with

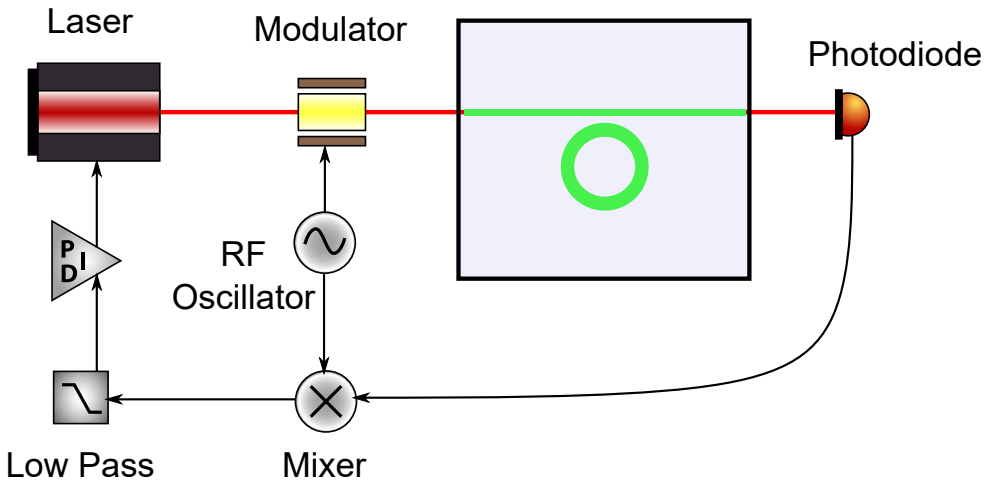

Figure 9.1: Layout for locking a laser to a micro-ring resonator frequency reference using Pound-Drever-Hall frequency stabilisation. The radio frequency oscillator provides the signal for the frequency modulator and the demodulation signal used in the mixer. The output is low-pass filtered to produce the desired error signal.

micro-ring resonator, source, and detectors on chip corresponds to co-rotating interferometer and propagation medium, the frequency difference in this reference frame is given by Equation B.48.

The shift in resonance could be tracked by methods analogous to those used for laser frequency stabilisation. There is the side-of-peak method in which there is a set operating point corresponding to the transmitted power half way up the resonance peak. The power transmitted from one of the two co-rotating paths used as an error signal for a feedback loop which controls the frequency of the input laser. In the open loop configuration, the second optical path is unaltered and so the dynamic range of the gyroscope is limited to the corresponding frequency shift enveloped by one side of a resonance peak. In a closed loop configuration, a frequency shifter is introduced in the second optical path, the transmitted power of this optical path is used as an error signal for a feedback loop controlling the frequency shifter, this configuration is illustrated in Figure 9.2. In this configuration, the error signal from either the laser stabilisation or frequency shifting control loops provides the rotation signal. The Pound-Drever-Hall method could be used instead of the a side-of-peak method. This would require that two light paths are frequency modulated before entering the resonator, the transmitted signals would be demodulated and low-pass filtered to provide PDH error signals used to control the laser stabilisation or frequency shifting control loops. A double-closed resonant micro-optic gyroscope with a phase modulator operating as a frequency shifter by applying a stair-like digital serrodyne waveform has been demonstrated experimentally with a silica (glass) waveguide micro-ring resonator [166].

The gyroscope output signal is proportional to the area enclosed by the micro-ring resonator. Fabricating a large area micro-ring resonator using electron beam lithography could result in

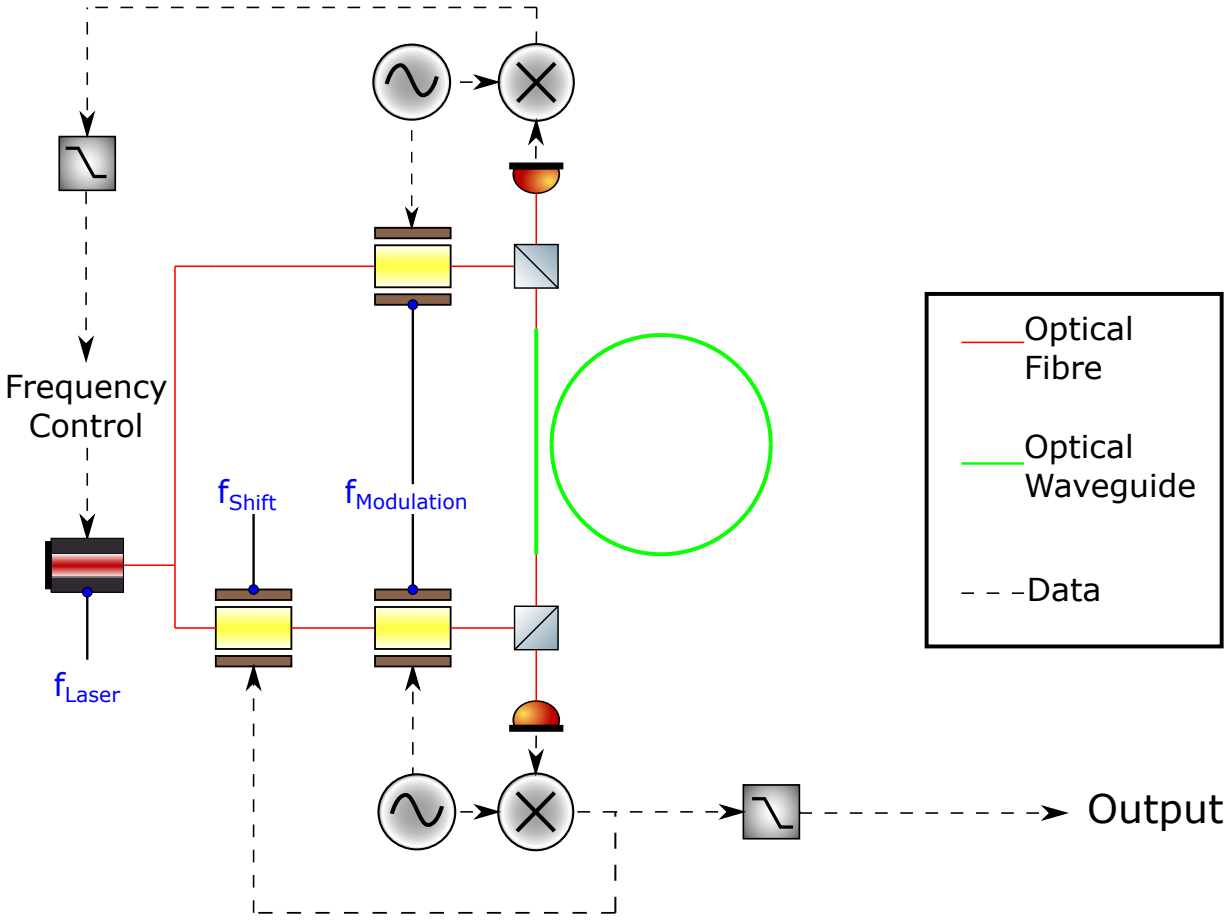

Figure 9.2: The laser beam is split and each path is frequency modulated prior to coupling into the micro-ring resonator and the transmitted beam is detected and demodulated. The demodulated signal from one path provides the error signal for stabilising the laser while the error signal from the other path provides the output signal and is used to control the frequency shift driver.

stitching errors within the resonator. Heretofore all micro-ring resonators in this work have been smaller than one main field of the VB6 electron beam lithography tools and so the micro-rings did not exhibit any stitching errors because samples were designed such that the rings were within the main fields. Stitching errors can be avoided by using photolithography instead of electron beam lithography, this would require further process development to find a suitable photoresist and exposure time to produce the waveguide features without introducing roughness or over-exposing the coupling region. The critical dimension (minimum feature size) for the photolithography tools in the JWNC is of the order 1 µm and so the size of the coupling gap would need to be much larger than it typically has been in this work, typically a few hundred nanometers. It may be necessary to design racetrack type micro-ring resonators to ensure adequate power coupling into the resonator. A racetrack micro-ring resonator is more simple to design that a circular micro-ring resonator because the coupling region could be treated as two parallel waveguides simplifying the coupling coefficient calculation.

Equation B.72 can be used to find the minimum resolution expected for a given setup. Assuming the setup shown in Figure 9.2 is used with a 1 mW DFB laser, with a relative intensity noise of 140 $\mathrm{dB/Hz^{-1/2}}$ [167], a silicon diode with a responsivity of 0.58 $\mathrm{A\,W^{-1}}$ [123], load resistance of 50 Ω [123], bandwidth of 0.05 Hz (10 s integration time) [168]. For this setup the minimum detectable rotation rate can be calculated as a function of resonator path length for a series of potential waveguide propagation losses, the result is shown in Figure 9.3. The simulation results are compared with the shot noise limited sensitivity stated in literature for a few resonant micro optic gyroscopes with the same laser power and integration time [168–173]. These RMOGs consist of micro-ring resonators with high Q factor values of 1.5-7 million. Therefore very low loss silicon nitride waveguides (lower than have been reported here) would be required to realise similar shot noise limited resolution for similar laser power and integration time. Fortunately this application can take advantage of the low losses achievable for longer wavelengths such as 1550 nm where propagation losses as low as 0.045 $\mathrm{dB\,m^{-1}}$ have been demonstrated for the low confinement waveguides (films < 100 nm) at 1580 nm and (0.13 $\mathrm{dB\,m^{-1}}$) for high confinement waveguides (films > 400 nm). Design techniques such as a spiral ring resonator [173] allow for a dramatic increase in the effective area of the of the micro-ring resonator leading to increased sensitivity without having to increase the footprint of the end device. There have also been many proposed designs [168, 174, 175] consisting of multiple coupled resonators.

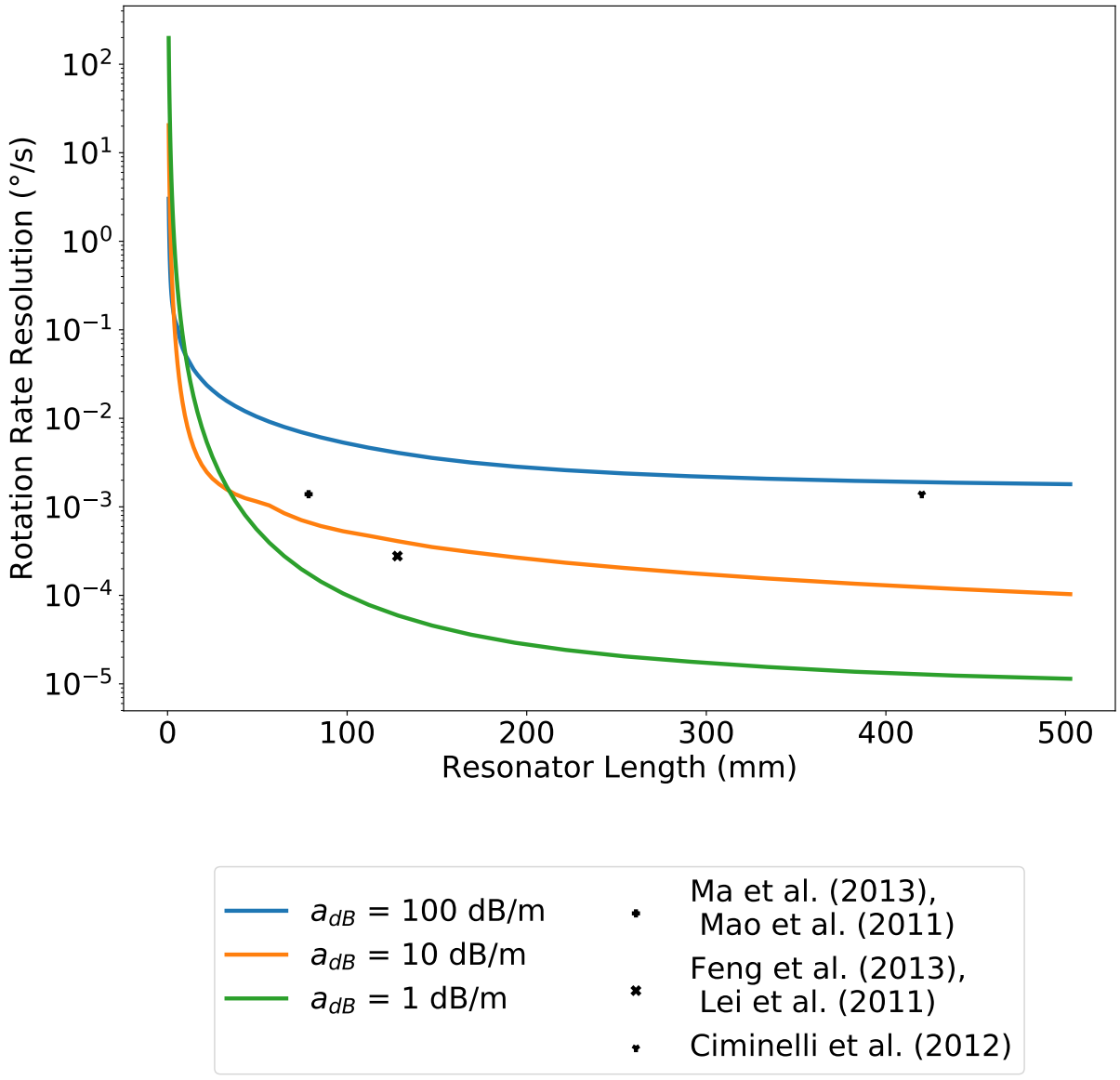

Figure 9.3: Rotation rate resolution is predicted for resonant micro optic gyroscopes as a function of resonator path length for a range of possible waveguide propagation loss values. Values for shot noise limited sensitivity found in literature are plotted for comparison.

Appendix A

Scattering Model Derivations

A.1 Integral Of Spectral Density Function

Equation 2.88 is now solved by first substituting in equation 2.84 to express this integral in terms of auto-correlation function rather than the spectral density function. This gives

$$S = \int_0^{\pi} \int_{-\infty}^{\infty} R(u) e^{i\Omega u} du \, d\theta \tag{A.1}$$

where $\Omega = \beta - n_2 k_0 \cos\theta$. Upon substitution of the exponential form of the auto-correlation function from equation 2.87, this gives

$$S = \int_0^{\pi} \int_{-\infty}^{\infty} \sigma^2 e^{-\frac{|u|}{L_c}} e^{i\Omega u} du \, d\theta. \tag{A.2}$$

The integral with respect to u can be solved independently first. This is given by [176]

$$
\begin{aligned}
A &= \sigma^2 \int_{-\infty}^{\infty} e^{\left(\frac{|u|}{L_c} + i\Omega u\right)} du \\
&= \sigma^2 \left[\frac{L_c e^{-\frac{u}{L_c}} \left(\operatorname{sgn}(u)+1\right) \left(2e^{\frac{u}{L_c}} - [1 + iL_c\Omega] e^{i\Omega u}\right)}{2\left(1+L_c^2\Omega^2\right)} + \frac{L(\operatorname{sgn}(u)-1) e^{u\left(\frac{1}{L_c}+i\Omega\right)}}{-2(1+iL_c\Omega)} + \mathcal{C} \right]_{-\infty}^{\infty} \\
&= \sigma^2 L_c e^{\frac{-u}{L_c}} \left[\frac{[\operatorname{sgn}(u)+1] 2e^{\frac{u}{L_c}} - [\operatorname{sgn}(u)+1] e^{i\Omega u} - [\operatorname{sgn}(u)+1] iL_c\Omega e^{i\Omega u}}{2\left(1+L_c^2\Omega^2\right)} \right]_{-\infty}^{\infty} \\
&= \frac{\sigma^2 L_c}{2\left(1+L_c^2\Omega^2\right)} \left[2(\operatorname{sgn}(u)+1)\right]_{-\infty}^{\infty} \\
&= \frac{\sigma^2 L_c}{2\left(1+L_c^2\Omega^2\right)} [4-0] \\
&= \frac{2\sigma^2 L_c}{1+L_c^2\Omega^2}
\end{aligned}
\tag{A.3}
$$

where $\operatorname{sgn}(u)$ is the sign function such that for positive values of u, $\operatorname{sgn}(u) = 1$ and for negative values of u, $\operatorname{sgn}(u) = -1$. Substituting this back into equation A.2 and remembering that $\Omega = \beta - n_2 k_0 \cos\theta$ gives a new form of equation 2.88.

$$
S = 2\sigma^2 L_c \int_0^{\pi} \frac{d\theta}{1 + L_c^2(\beta - n_2 k_0 \cos\theta)^2}. \tag{A.4}
$$

Appendix B

Sagnac Effect Theory

B.1 Relativity

Consider the general case of the Sagnac effect in a ring interferometer. The counter-propagating waves have a round trip propagation length (in the stationary frame), $l^{\pm}$, and a phase velocity, $v_{\text{ph}}^{\pm}$.

Where

$$l^{\pm} = 2\pi R \pm R\Omega t^{\pm} \tag{B.1}$$

given by combing the stationary round length and the distance given by multiplying the tangential velocity ($R\Omega$) by the change in round trip propagation time due to rotation (which will be solved for later), and

$$v_{\text{ph}}^{\pm} = \frac{v_{\text{ph}} \pm R\Omega}{1 \pm \frac{v_{\text{ph}} R\Omega}{c^2}} \tag{B.2}$$

uses Einstein velocity addition from special relativity to combine the phase velocity of the light and the tangential velocity due to rotation [177, 178].

Then $t^{\pm}$ is found from the velocity and propagation lengths,

$$\begin{aligned}
t^{\pm} &= \frac{l^{\pm}}{v_{\text{ph}}^{\pm}} \\
t^{\pm} &= \frac{2\pi R \pm R\Omega t^{\pm}}{v_{\text{ph}} \pm R\Omega}\left(1 \pm \frac{v_{\text{ph}} R\Omega}{c^2}\right) \\
t^{\pm} &= \frac{2\pi R \pm R\Omega t^{\pm}}{v_{\text{ph}} \pm R\Omega} \pm \frac{2\pi R v_{\text{ph}} R\Omega c^{-2} \pm R\Omega t^{\pm} v_{\text{ph}} R\Omega c^{-2}}{v_{\text{ph}} \pm R\Omega} \\
t^{\pm} v_{\text{ph}} \pm t^{\pm} R\Omega \mp t^{\pm} R\Omega \mp \frac{t^{\pm} R\Omega v_{\text{ph}} R\Omega}{c^2} &= 2\pi R\left(1 \pm \frac{v_{\text{ph}} R\Omega}{c^2}\right) \\
t^{\pm} v_{\text{ph}}\left(1 - \frac{R^2\Omega^2}{c^2}\right) &= 2\pi R\left(1 \pm \frac{v_{\text{ph}} R\Omega}{c^2}\right) \\
t^{\pm} &= \frac{2\pi R\left(1 \pm \frac{v_{\text{ph}} R\Omega}{c^2}\right)}{v_{\text{ph}}\left(1 - \frac{R^2\Omega^2}{c^2}\right)} \\
\Delta t = t^{+} - t^{-} &= \frac{4\pi R^2 \Omega}{c^2\left(1 - \frac{R^2\Omega^2}{c^2}\right)}.
\end{aligned} \tag{B.3}$$

To find the difference in propagation times for the counter-propagating in the co-rotating reference frame the Lorentz transformation is used [177, 178]

$$\begin{aligned}
\Delta t' = \Delta t \gamma &= \Delta t \sqrt{\left(1 - \frac{v_{\text{tangential}}^2}{c^2}\right)} \\
&= \Delta t \sqrt{\left(1 - \frac{R^2\Omega^2}{c^2}\right)} \\
&= \frac{4\pi R^2 \Omega}{c^2 \sqrt{\left(1 - \frac{R^2\Omega^2}{c^2}\right)}} \\
&= \frac{4A\Omega}{c^2 \sqrt{\left(1 - \frac{R^2\Omega^2}{c^2}\right)}}.
\end{aligned} \tag{B.4}$$

Multiply this change in propagation time by the angular laser frequency to find the phase difference due to the Sagnac effect [177],

$$\begin{aligned}
\Phi_S' = \Delta\phi' &= \omega \Delta t' \\
&= \frac{4A\omega\Omega}{c^2 \sqrt{\left(1 - \frac{R^2\Omega^2}{c^2}\right)}}.
\end{aligned} \tag{B.5}$$

In the limit such that

$$R\Omega \ll c \tag{B.6}$$

the Sagnac phase difference is given by

$$\Phi'_S = \frac{4A\omega\Omega}{c^2}. \tag{B.7}$$

B.2 Geometric optical theory

The phase of light after one circulation of a closed loop

$$\phi = \frac{1}{2\pi}\oint \vec{k}\cdot d\vec{r} - \frac{1}{2\pi}\int_0^\tau \omega dt \tag{B.8}$$

is separated into its spatial component, a closed line integral of the wave vector $\vec{k}$, and its temporal component, an integral of the lights frequency between $t = 0$ and $t = \tau$ where τ is the circulation time for the light for stationary loop. By multiplying this by Planck's constant this can be converted into a Hamilton action integral

$$S = \int L dt = \oint \vec{p}\cdot d\vec{r} - \int H dt \tag{B.9}$$

Therefore action, S, and phase, ϕ are related invariants for general space-time transformations.

If light circulating in a closed loop interferometer is subjected to a displacement, $\vec{q}$, due to a velocity, $\vec{v}$, the phase is a general invariant and should be unaffected if the change in boundary conditions are accounted for.

$$\delta\phi = \delta Z - \delta T = 0 \tag{B.10}$$

Where

$$\begin{aligned} 2\pi\delta Z &= \delta\oint \vec{k}\cdot d\vec{r} \\ 2\pi\delta Z &= \oint \left[\delta\vec{k} - \vec{q}\times\nabla\times\vec{k} + \nabla(\vec{k}\cdot\vec{q})\right] d\vec{r} \end{aligned} \tag{B.11}$$

The Sommerfeld-Runge law gives

$$\nabla\times\vec{k} = 0 \tag{B.12}$$

and by integrating the final term in the above integral

$$2\pi\delta Z = \oint \delta\vec{k}d\vec{r} + \left(\vec{k}\cdot\vec{q}\right)_2 - \left(\vec{k}\cdot\vec{q}\right)_1 \tag{B.13}$$

and

$$2\pi\delta T = \delta\int_0^\tau \omega dt = \int_0^\tau \delta\omega dt + \omega\delta\tau \tag{B.14}$$

If a coherent light source is co-moving with the interferometer and its propagation medium,

we can be sure that

$$\delta\omega = 0. \tag{B.15}$$

In a linear medium

$$\omega = ku \tag{B.16}$$

where u is the phase velocity of light in that medium.

$$\begin{aligned} \delta\omega = 0 &= u\delta k + k\delta u \\ &\Rightarrow u\delta k = -k\delta u \\ &\Rightarrow \frac{\delta k}{k} = -\frac{\delta u}{u} \end{aligned} \tag{B.17}$$

Here, δu is the change in phase / effective propagation velocity in the moving medium as seen by a station observer. As an approximation, it is assumed that

$$\delta u = \alpha\vec{v}\cdot\frac{d\vec{r}}{ds} \tag{B.18}$$

where

$$\alpha = \left(1 - \frac{1}{n^2}\right) \tag{B.19}$$

is the Fresnel-Fizeau drag coefficient in the co-rotating reference frame, $\vec{v}$ is the tangential velocity vector, $\frac{d\vec{r}}{ds}$ is the unit vector tangent to the beam direction where $d\vec{r}$ is a vector line element and ds is a scalar line element such that

$$ds^2 = d\vec{r}\cdot d\vec{r}.$$

Therefore we can write the infinitesimal change in wave number as

$$\delta k = -\frac{k}{u}\alpha\vec{v}\cdot\frac{d\vec{r}}{ds} \tag{B.20}$$

and substitute this into (B.13)

$$\delta Z = \frac{1}{2\pi}\oint -\frac{k}{u}\alpha\vec{v}\cdot d\vec{r} + \frac{1}{2\pi}\left[\left(\vec{k}\cdot\vec{q}\right)_2 - \left(\vec{k}\cdot\vec{q}\right)_1\right] \tag{B.21}$$

using

$$\frac{d\vec{r}}{ds}\cdot d\vec{r} = \frac{d\vec{r}\cdot d\vec{r}}{\sqrt{d\vec{r}\cdot d\vec{r}}} = d\vec{r}.$$

By expressing $\left(\vec{k}\cdot\vec{q}\right)$ in terms of the integrated velocity field

$$\left(\vec{k}\cdot\vec{q}\right)_2 - \left(\vec{k}\cdot\vec{q}\right)_1 = \int_0^\tau \vec{k}\cdot\vec{v}dt, \tag{B.22}$$

this change in time is a scalar value found using

$$dt = \frac{ds}{u}$$

and so

$$\left(\vec{k}\cdot\vec{q}\right)_2 - \left(\vec{k}\cdot\vec{q}\right)_1 = \oint \vec{k}\cdot\vec{v}\frac{ds}{u} = \oint \frac{k}{u}\vec{v}\cdot d\vec{r} \tag{B.23}$$

using

$$\frac{\vec{k}}{d\vec{r}} = \frac{k}{ds}.$$

So now

$$\begin{aligned} \delta Z &= \frac{1}{2\pi}\left[\oint -\frac{k}{u}\alpha\vec{v}\cdot d\vec{r} + \oint \frac{k}{u}\vec{v}\cdot d\vec{r}\right] \\ \delta Z &= \frac{1}{2\pi}\oint \frac{k}{u}(1-\alpha)\vec{v}\cdot d\vec{r} \end{aligned} \tag{B.24}$$

Due to phase invariance, (B.10),

$$2\pi\delta T = 2\pi\delta Z \tag{B.25}$$

so using the (B.15), (B.14), and (B.24)

$$\omega\delta\tau = \oint \frac{k}{u}(1-\alpha)\vec{v}\cdot d\vec{r} \tag{B.26}$$

But this one for one path only. When considering two paths the difference in circulation time is simply double the change in the circulation time of each path.

$$\omega\Delta\tau = 2\oint \frac{k}{u}(1-\alpha)\vec{v}\cdot d\vec{r} \tag{B.27}$$

Substituting in

$$k = k_0 n = \frac{2\pi n}{\lambda_0} \tag{B.28}$$

and

$$u = \frac{c}{n} \tag{B.29}$$

Allow for the expression

$$\Delta Z = 2\delta Z = \frac{2}{c\lambda_0}\oint n^2(1-\alpha)\vec{v}\cdot d\vec{r} \tag{B.30}$$

and

$$\Delta\tau = \frac{2}{c^2}\oint n^2(1-\alpha)\vec{v}\cdot d\vec{r}. \tag{B.31}$$

Applying Stokes theorem

$$\oint \vec{v}\cdot d\vec{r} = \oint \nabla\times\vec{v}\cdot d\vec{A} = 2\Omega\cdot A \tag{B.32}$$

therefore

$$\Delta\tau = \frac{4\Omega \cdot A}{c^2} n^2 (1-\alpha) \tag{B.33}$$

and

$$\Delta\Phi_{\text{Sagnac}} = \omega\Delta\tau = \frac{4\omega\Omega \cdot A}{c^2} n^2 (1-\alpha) \tag{B.34}$$

B.2.1 Co-rotating reference frame: Interferometeric phase difference

In the co-rotating reference frame where the Fresnel-Fizeau drag coefficient is

$$\alpha = \left(1 - \frac{1}{n^2}\right) \tag{B.35}$$

The phase difference between two counter-propagating completing a revolution as given by (B.34) now becomes

$$\Delta\Phi_{\text{Sagnac}} = \omega\Delta\tau = \frac{4\omega\Omega \cdot A}{c^2} \tag{B.36}$$

This is true for a moving ring interferometer (source, mirrors, detectors) with passive co-moving medium as is the case of interest. The crucial assumption here is that $\delta\omega = 0$.

B.2.2 Co-rotating reference frame: Resonant frequency difference

For an resonant cavity, active or passive, the phase must not change in order to satify the resonance condition. There must be no fringe shift. There is now a difference in frequency between the counter propagating waves.

$$\delta\phi = \delta Z - \delta T = 0 \tag{B.37}$$

because

$$\delta Z = 0 \tag{B.38}$$

and

$$\delta T = 0. \tag{B.39}$$

This leads to

$$2\pi\delta T = \delta \int_0^\tau \omega dt = \int_0^\tau \delta\omega dt + \omega\delta\tau = 0 \tag{B.40}$$

concluding that

$$\int_0^\tau \delta\omega dt + \omega\delta\tau = 0. \tag{B.41}$$

It follows that

$$\frac{\delta\omega}{\omega} = -\frac{\delta\tau}{\tau} \tag{B.42}$$

this effect is simply doubled when comparing the co-rotating and counter co-rotating paths

$$\left|\frac{\Delta\omega}{\omega}\right| = \frac{\Delta\tau}{\tau} \tag{B.43}$$

Using (B.43), (B.33), and the Fermat integral to find the time for a complete round trip

$$\tau = \oint \frac{n}{c} ds = \frac{nL}{c} \tag{B.44}$$

Where L is the total path length. Now (B.43) becomes

$$\left|\frac{\Delta\omega}{\omega}\right| = \frac{4\Omega \cdot A}{c^2} n^2 (1-\alpha) \cdot \frac{c}{nL} = \frac{4\Omega \cdot A}{cnL} n^2 (1-\alpha). \tag{B.45}$$

If

$$\alpha = 1 - \frac{1}{n^2} \tag{B.46}$$

is taken as the Fresnel drag coefficient then the change in resonant frequency can be expressed as

$$\Delta\omega = \frac{4\omega\Omega \cdot A}{cnL} \tag{B.47}$$

or

$$\Delta\nu = \frac{4A\Omega}{\lambda_0 Ln}. \tag{B.48}$$

B.2.3 Rotating interferometer, stationary medium: Interferometric phase difference

The propagation velocity is being observed in a frame of reference in which the medium is at rest, therefore

$$\delta u = 0. \tag{B.49}$$

Using (B.17) and (B.49)

$$\delta k = 0, \tag{B.50}$$

this is then substituted into (B.13)

$$\delta Z = \frac{1}{2\pi}\left(\vec{k}\cdot\vec{q}\right)_2 - \left(\vec{k}\cdot\vec{q}\right)_1 = \frac{1}{2\pi}\oint \frac{k}{u}\vec{v}\cdot d\vec{r} \tag{B.51}$$

Then similarly as before $\Delta\tau$ is found from ΔZ and Stokes theorem is used to perform the integrals resulting in

$$\Delta\tau = \frac{4\Omega \cdot A}{c^2} n^2 \tag{B.52}$$

and

$$\Delta\Phi_{\text{Sagnac}} = \omega\Delta\tau = \frac{4\omega\Omega \cdot A}{c^2} n^2 \tag{B.53}$$

B.2.4 Rotating interferometer, stationary medium: Resonant frequency difference

For a medium that appears stationary to the observer, the Fresnel drag coefficient is

$$\alpha = 0 \tag{B.54}$$

and so (B.33) becomes

$$\Delta\tau = \frac{4\Omega \cdot A}{c^2} n^2 \tag{B.55}$$

Using (B.43), (B.44), and (B.55)

$$\left|\frac{\Delta\omega}{\omega}\right| = \frac{4\Omega \cdot A}{c^2} n^2 \cdot \frac{c}{nL} = \frac{4\Omega \cdot A}{cnL} n^2 \tag{B.56}$$

yielding

$$|\Delta\omega| = \frac{4\omega\Omega \cdot An}{cL} \tag{B.57}$$

or

$$\Delta\nu = \frac{4A\Omega n}{\lambda L}. \tag{B.58}$$

B.2.5 Stationary interferometer, rotating medium: Interferometric phase shift

The interferometer is now stationary and so

$$\left(\vec{k}\cdot\vec{q}\right)_2 - \left(\vec{k}\cdot\vec{q}\right)_1 \to 0 \tag{B.59}$$

which means that (B.21) becomes

$$\delta Z = \frac{1}{2\pi} \oint \frac{k}{u} \alpha \vec{v} \cdot d\vec{r} \tag{B.60}$$

and substituting (B.28) and (B.29) gives

$$\delta Z = \frac{2}{c\lambda} \oint n^2 \alpha \vec{v} \cdot d\vec{r}. \tag{B.61}$$

Then similarly as before $\Delta\tau$ is found from ΔZ and Stokes theorem is used to perform the integrals resulting in

$$\Delta\tau = \frac{4\Omega \cdot A}{c^2} n^2 \alpha \tag{B.62}$$

and

$$\Delta\Phi_{\text{Sagnac}} = \omega\Delta\tau = \frac{4\omega\Omega \cdot A}{c^2} n^2 \alpha \tag{B.63}$$

B.2.6 Stationary interferometer, rotating medium: Resonant

Using (B.43), (B.44) and (B.62)

$$\left|\frac{\Delta\omega}{\omega}\right| = \frac{4\Omega\cdot A\alpha}{c^2}n^2\cdot\frac{c}{nL} = \frac{4\Omega\cdot A\alpha}{cnL}n^2 \tag{B.64}$$

yielding

$$|\Delta\omega| = \frac{4\omega\Omega\cdot An\alpha}{cL} \tag{B.65}$$

or

$$\Delta\nu = \frac{4A\Omega n\alpha}{\lambda L}. \tag{B.66}$$

For medium rotating within fixed boundaries the Fresnel drag coefficient with the Lorentz correction is used

$$\alpha = 1-\frac{1}{n^2}\frac{\lambda}{n}\frac{dn}{d\lambda}. \tag{B.67}$$

For medium rotating within movable boundaries the Laub drag coefficient is used

$$\alpha = 1-\frac{1}{n^2}\frac{\lambda}{n^2}\frac{dn}{d\lambda}. \tag{B.68}$$

B.3 Deriving minimum resolution

Minimum detectable angular rate can be estimated by translating uncertainty in light intensity to uncertainty in phase shift

$$\delta\phi = \frac{\delta i}{m} \tag{B.69}$$

where δi is the noise rms current due to amplitude noise (shot noise, thermal noise, and laser noise), and m is the gradient of current Vs. phase,

$$m = R\frac{\partial|E|^2}{\partial\phi} = \frac{q\eta}{\hbar\omega_0}\frac{\partial|E|^2}{\partial\phi} \tag{B.70}$$

where $R=\frac{q\eta}{h\nu}$, in units of $\mathrm{A\,W^{-1}}$, is the responsivity of the photodiode, $h = 6.626\times10^{-34}\mathrm{J\,s}$ is Planck's constant, ν is the optical wave frequency in Hz, η is the quantum efficiency [90]. For real results it is important that real input power is used to find $|E|^2$ and not the normalised form shown above, this can be achieved simply by multiplying the normalised $|E|^2$ by the input laser power. The nose rms current is found by combing the shot, thermal, and laser power noise sources,

$$\delta i = \sqrt{\left(2qi_D+\frac{4k_BT}{R_L}+i_D^2\mathrm{RIN}\right)B} \tag{B.71}$$

where $i_D = R|E|^2$ is the maximum photodiode current $q = 1.6 \times 10^{-19}$C is the fundamental electric charge, $k_B = 1.38 \times 10^{-23}$ J K^{-1} is Boltzmann's constant, R_L denotes the photodetector load resistance, RIN is the relative intensity noise of the laser, usually expressed in dB Hz^{-1}, and B is the photodiode bandwidth in Hz, with $B = \frac{1}{\tau_{PD}}$ where τ_{PD} is the integration time of the photodiode [90].

The rotation rate resolution for a suitable configuration is given by

$$\Omega = \frac{c^2}{2\omega_0 A}\delta\phi = \frac{c^2}{2\omega_0 A}\frac{\delta i}{m} = \frac{c^2}{2\omega_0 A}\frac{\delta i}{\frac{q\eta}{\hbar\omega_0}\frac{\partial|E|^2}{\partial\phi}}. \tag{B.72}$$

In order to model this, equations for δi and $\frac{\partial|E|^2}{\partial\phi}$ are required and the variables contained therein. The max value is taken for $\frac{\partial|E|^2}{\partial\phi}$ and used to find the minimum rotation rate resolution for varying resonator circumference. Equation B.72 can be considered as a scale factor,

$$\frac{c^2}{2\omega_0 A}$$

divided by a SNR,

$$\frac{\frac{q\eta}{\hbar\omega_0}\frac{\partial|E|^2}{\partial\phi}}{\delta i}.$$

Bibliography

[1] Martin Sinclair, Kevin Gallacher, Marc Sorel, Joseph C. Bayley, Euan McBrearty, Ross W. Millar, Stefan Hild, and Douglas J. Paul. 1.4 million Q factor Si_3N_4 micro-ring resonator at 780 nm wavelength for chip-scale atomic systems. *Opt. Express*, 28(3):4010–4020, Feb 2020.

[2] Robert Blum. Silicon photonics - The key to data center connectivity. https://www.intel.co.uk/content/dam/www/public/us/en/documents/product-briefs/silicon-photonics-the-key-to-data-centre-connectivity-robert-blum.pdf. (Accessed on 06/09/2020).

[3] G.T. Reed and A.P. Knights. *Silicon Photonics: An Introduction*. Wiley, 2004.

[4] Roel Baets, Ananth Z. Subramanian, Stéphane Clemmen, Bart Kuyken, Peter Bienstman, Nicolas Le Thomas, Günther Roelkens, Dries Van Thourhout, Philippe Helin, and Simone Severi. Silicon photonics: silicon nitride versus silicon-on-insulator. In *Optical Fiber Communication Conference*, page Th3J.1. Optical Society of America, 2016.

[5] Rüdiger Paschotta. RP photonics encyclopedia - optical fiber communications, data transmission, capacity, telecom windows, C band, L band, WDM. https://www.rp-photonics.com/optical_fiber_communications.html. (Accessed on 06/10/2020).

[6] Enxiao Luan, Hossam Shoman, Daniel M Ratner, Karen C Cheung, and Lukas Chrostowski. Silicon photonic biosensors using label-free detection. *Sensors*, 18(10):3519, 2018.

[7] Nicholas C Harris, Jacques Carolan, Darius Bunandar, Mihika Prabhu, Michael Hochberg, Tom Baehr-Jones, Michael L Fanto, A Matthew Smith, Christopher C Tison, Paul M Alsing, et al. Linear programmable nanophotonic processors. *Optica*, 5(12):1623–1631, 2018.

[8] Miguel Ángel Guillén-Torres, Edmond Cretu, Nicolas A F Jaeger, and Lukas Chrostowski. Ring resonator optical gyroscopes-parameter optimization and robustness analysis. *Journal of Lightwave Technology*, 30(12):1802–1817, 2012.

[9] Shiyun Lin, Stevan S Djordjevic, John E Cunningham, Ivan Shubin, Ying Luo, Jin Yao, Guoliang Li, Hiren Thacker, Jin-Hyoung Lee, Kannan Raj, et al. Vertical-coupled high-efficiency tunable III-V-CMOS SOI hybrid external-cavity laser. *Optics express*, 21(26):32425–32431, 2013.

[10] John Kitching. Chip-scale atomic devices. *Applied Physics Reviews*, 5(3):031302, 2018.

[11] Adam Densmore, D-X Xu, Philip Waldron, Siegfried Janz, Pavel Cheben, J Lapointe, A Delge, Boris Lamontagne, JH Schmid, and Edith Post. A silicon-on-insulator photonic wire based evanescent field sensor. *IEEE Photonics Technology Letters*, 18(23):2520–2522, 2006.

[12] Xingchen Ji, Felippe A. S. Barbosa, Samantha P. Roberts, Avik Dutt, Jaime Cardenas, Yoshitomo Okawachi, Alex Bryant, Alexander L. Gaeta, and Michal Lipson. Ultra-low-loss on-chip resonators with sub-milliwatt parametric oscillation threshold. *Optica*, 4(6):619–624, Jun 2017.

[13] Long Chen, Christopher R Doerr, Po Dong, and Young-kai Chen. Monolithic silicon chip with 10 modulator channels at 25 Gbps and 100-GHz spacing. *Optics express*, 19(26):B946–B951, 2011.

[14] Long Chen, Christopher R Doerr, Larry Buhl, Yves Baeyens, and Ricardo A Aroca. Monolithically integrated 40-wavelength demultiplexer and photodetector array on silicon. *IEEE Photonics Technology Letters*, 23(13):869–871, 2011.

[15] Wesley D Sacher, Ying Huang, Guo-Qiang Lo, and Joyce KS Poon. Multilayer silicon nitride-on-silicon integrated photonic platforms and devices. *Journal of Lightwave Technology*, 33(4):901–910, 2015.

[16] Quentin Wilmart, Houssein El Dirani, Nicola Tyler, Daivid Fowler, Stéphane Malhouitre, Stéphanie Garcia, Marco Casale, Sébastien Kerdiles, Karim Hassan, Christelle Monat, et al. A versatile silicon-silicon nitride photonics platform for enhanced functionalities and applications. *Applied Sciences*, 9(2):255, 2019.

[17] Siegfried Janz, Pavel Cheben, Dan Dalacu, Andr Delge, Adam Densmore, Boris Lamontagne, Marie-Josee Picard, Edith Post, JH Schmid, Philip Waldron, et al. Microphotonic elements for integration on the silicon-on-insulator waveguide platform. *IEEE Journal of selected topics in quantum electronics*, 12(6):1402–1415, 2006.

[18] Dirk Taillaert, Peter Bienstman, and Roel Baets. Compact efficient broadband grating coupler for silicon-on-insulator waveguides. *Optics letters*, 29(23):2749–2751, 2004.

[19] W. P. Maszara, G. Goetz, A. Caviglia, and J. B. McKitterick. Bonding of silicon wafers for silicon-on-insulator. *Journal of Applied Physics*, 64(10):4943–4950, 1988.

[20] J. S. Penadés, A. Z. Khokhar, M. Nedeljkovic, and G. Z. Mashanovich. Low-loss mid-infrared SOI slot waveguides. *IEEE Photonics Technology Letters*, 27(11):1197–1199, 2015.

[21] M. Rouifed, C. G. Littlejohns, G. X. Tina, Q. Haodong, T. Hu, Z. Zhang, C. Liu, G. T. Reed, and H. Wang. Low loss SOI waveguides and MMIs at the MIR wavelength of 2 μm. *IEEE Photonics Technology Letters*, 28(24):2827–2829, 2016.

[22] Pieter Dumon, Wim Bogaerts, Vincent Wiaux, Johan Wouters, Stephan Beckx, Joris Van Campenhout, Dirk Taillaert, Bert Luyssaert, Peter Bienstman, Dries Van Thourhout, et al. Low-loss SOI photonic wires and ring resonators fabricated with deep UV lithography. *IEEE Photonics Technology Letters*, 16(5):1328–1330, 2004.

[23] Giancarlo C Righini and Andrea Chiappini. Glass optical waveguides: A review of fabrication techniques. *Optical Engineering*, 53(7):071819, 2014.

[24] Ray DeCorby and Mehrdad Irannejad. *Glasses for Photonic Integration*, pages 1–1. Springer International Publishing, Cham, 2017.

[25] Jun Guan, Xiang Liu, Patrick S Salter, and Martin J Booth. Hybrid laser written waveguides in fused silica for low loss and polarization independence. *Optics express*, 25(5):4845–4859, 2017.

[26] David Duchesne, Marcello Ferrera, Luca Razzari, Roberto Morandotti, Brent E. Little, Sai T. Chu, and David J. Moss. Efficient self-phase modulation in low loss, high index doped silica glass integrated waveguides. *Opt. Express*, 17(3):1865–1870, Feb 2009.

[27] Daniel J Blumenthal, Rene Heideman, Douwe Geuzebroek, Arne Leinse, and Chris Roeloffzen. Silicon nitride in silicon photonics. *Proceedings of the IEEE*, 106(12):2209–2231, 2018.

[28] R.G. Heideman, R.P.H. Kooyman, and J. Greve. Performance of a highly sensitive optical waveguide Mach-Zehnder interferometer immunosensor. *Sensors and Actuators B: Chemical*, 10(3):209 – 217, 1993.

[29] Michael J Shaw, Junpeng Guo, Gregory Allen Vawter, Scott Habermehl, and Charles T Sullivan. Fabrication techniques for low-loss silicon nitride waveguides. In *Micromachining Technology for Micro-Optics and Nano-Optics III*, volume 5720, pages 109–118. International Society for Optics and Photonics, 2005.

[30] Pascual Muñoz, Gloria Micó, Luis A Bru, Daniel Pastor, Daniel Pérez, José David Doménech, Juan Fernández, Rocío Baños, Bernardo Gargallo, Rubén Alemany, et al. Silicon nitride photonic integration platforms for visible, near-infrared and mid-infrared applications. *Sensors*, 17(9):2088, 2017.

[31] Yoshitomo Okawachi, Kasturi Saha, Jacob S Levy, Y Henry Wen, Michal Lipson, and Alexander L Gaeta. Octave-spanning frequency comb generation in a silicon nitride chip. *Optics letters*, 36(17):3398–3400, 2011.

[32] Alexander Gondarenko, Jacob S. Levy, and Michal Lipson. High confinement micron-scale silicon nitride high Q ring resonator. *Opt. Express*, 17(14):11366–11370, Jul 2009.

[33] Martin Hubert Peter Pfeiffer, Clemens Herkommer, Junqiu Liu, Tiago Morais, Michael Zervas, Michael Geiselmann, and Tobias J Kippenberg. Photonic damascene process for low-loss, high-confinement silicon nitride waveguides. *IEEE Journal of Selected Topics in Quantum Electronics*, 24(4):1–11, 2018.

[34] Shankar Kumar Selvaraja and Purnima Sethi. Review on optical waveguides. *Emerging Waveguide Technol*, 95, 2018.

[35] L. Chrostowski and M. Hochberg. *Silicon Photonics Design: From Devices to Systems*. Cambridge University Press, 2015.

[36] Luceda Photonics. Multi mode interferometers - IPKISS 3.3 documentation. http://docs.lucedaphotonics.com/picazzo/filters/mmi/index.html. (Accessed on 06/11/2020).

[37] Mac Watanabe Bernard Lee, Ryo Konno. Arrayed waveguide grating. https://www.senko.com/technical/pdf/Arrayed%20Waveguide%20Grating.pdf. (Accessed on 06/11/2020).

[38] Kevin Gallacher, Ross W. Millar, Ugne Griškevičiūtė, Martin Sinclair, Marc Sorel, Leonetta Baldassarre, Michele Ortolani, Richard Soref, and Douglas J. Paul. Ultra-broadband mid-infrared Ge-on-Si waveguide polarization rotator. *APL Photonics*, 5(2):026102, 2020.

[39] Hsing Chien Cheng and Ramu V Ramaswamy. Symmetrical directional coupler as a wavelength multiplexer-demultiplexer: theory and experiment. *IEEE journal of quantum electronics*, 27(3):567–574, 1991.

[40] W. Bogaerts, P. De Heyn, T. Van Vaerenbergh, K. De Vos, S. Kumar Selvaraja, T. Claes, P. Dumon, P. Bienstman, D. Van Thourhout, and R. Baets. Silicon microring resonators. *Laser & Photon. Rev.*, 6(1):47–73, 2012.

[41] Brian Stern, Xingchen Ji, Yoshitomo Okawachi, Alexander L Gaeta, and Michal Lipson. Battery-operated integrated frequency comb generator. *Nature*, 562(7727):401, 2018.

[42] Daryl T. Spencer, Michael L. Davenport, Tin Komljenovic, Sudharsanan Srinivasan, and John E. Bowers. Stabilization of heterogeneous silicon lasers using Pound-Drever-Hall locking to Si_3N_4 ring resonators. *Opt. Express*, 24(12):13511–13517, Jun 2016.

[43] Yuguang Zhang, Xiao Hu, Daigao Chen, Lei Wang, Miaofeng Li, Peng Feng, Xi Xiao, and Shaohua Yu. Design and demonstration of ultra-high-Q silicon microring resonator based on a multi-mode ridge waveguide. *Opt. Lett.*, 43(7):1586–1589, Apr 2018.

[44] Daryl T. Spencer, Jared F. Bauters, Martijn J. R. Heck, and John E. Bowers. Integrated waveguide coupled Si_3N_4 resonators in the ultrahigh-Q regime. *Optica*, 1(3):153–157, Sep 2014.

[45] R. Adar, Y. Shani, C. H. Henry, R. C. Kistler, G. E. Blonder, and N. A. Olsson. Measurement of very low-loss silica on silicon waveguides with a ring resonator. *Applied Physics Letters*, 58(5):444–445, 1991.

[46] WR McKinnon, D-X Xu, C Storey, E Post, A Densmore, A Delâge, P Waldron, JH Schmid, and S Janz. Extracting coupling and loss coefficients from a ring resonator. *Opt. Express*, 17(21):18971–18982, 2009.

[47] Tomoya Taniguchi, Anna Hirowatari, Takeshi Ikeda, Masataka Fukuyama, Yoshiteru Amemiya, Akio Kuroda, and Shin Yokoyama. Detection of antibody-antigen reaction by silicon nitride slot-ring biosensors using protein G. *Optics Communications*, 365:16 – 23, 2016.

[48] Pascal Del'Haye, Albert Schliesser, Olivier Arcizet, Tom Wilken, Ronald Holzwarth, and Tobias J Kippenberg. Optical frequency comb generation from a monolithic microresonator. *Nature*, 450(7173):1214, 2007.

[49] Davide Grassani, Stefano Azzini, Marco Liscidini, Matteo Galli, Michael J. Strain, Marc Sorel, J. E. Sipe, and Daniele Bajoni. Micrometer-scale integrated silicon source of time-energy entangled photons. *Optica*, 2(2):88–94, Feb 2015.

[50] S. Knappe, P. Schwindt, V. Shah, L. Hollberg, J. Kitching, L. Liew, and J. Moreland. A chip-scale atomic clock based on ^{87}Rb with improved frequency stability. *Opt. Express*, 13(4):1249–1253, Feb 2005.

[51] Liang Liu, De-Sheng Lü, Wei-Biao Chen, Tang Li, Qiu-Zhi Qu, Bin Wang, Lin Li, Wei Ren, Zuo-Ren Dong, Jian-Bo Zhao, Wen-Bing Xia, Xin Zhao, Jing-Wei Ji, Mei-Feng Ye, Yan-Guang Sun, Yuan-Yuan Yao, Dan Song, Zhao-Gang Liang, Shan-Jiang Hu, Dun-He Yu, Xia Hou, Wei Shi, Hua-Guo Zang, Jing-Feng Xiang, Xiang-Kai Peng, and Yu-Zhu Wang. In-orbit operation of an atomic clock based on laser-cooled ^{87}Rb atoms. *Nature Communications*, 9(1):2760, 2018.

[52] J Kitching, E A Donley, S Knappe, M Hummon, A T Dellis, J Sherman, K Srinivasan, V A Aksyuk, Q Li, D Westly, B Roxworthy, and A Lal. NIST on a chip: Realizing SI

units with microfabricated alkali vapour cells. *Journal of Physics: Conference Series*, 723:012056, jun 2016.

[53] Daniel A Steck. Rubidium 87 D line data. http://steck.us/alkalidata, 2001.

[54] Haifeng Dong, Jiancheng Fang, Binquan Zhou, Jie Qin, and Shuangai Wan. Review of atomic mems: Driving technologies and challenges. *Microsystem technologies*, 16(10):1683–1689, 2010.

[55] Kevin Gallacher, Ross W Millar, Douglas J Paul, Francesco Mirando, Gary Ternent, Gordon Mills, and Brenden Casey. Distributed feedback lasers operating at 780 nm wavelength integrated on Si substrates for chip-scale atomic systems. In *2018 IEEE 15th International Conference on Group IV Photonics (GFP)*, pages 1–2. IEEE, 2018.

[56] H.D. Young, R.A. Freedman, A.L. Ford, M.W. Zemansky, and F.W. Sears. *University Physics*. Pearson Education, Limited, 2009.

[57] William Arnott. Atms 749 radiation transfer. http://www.patarnott.com/atms749/pdf/FresnelEquations.pdf, 2014. (Accessed on 01/24/2020).

[58] Katsunari Okamoto. *Fundamentals of Optical Waveguides*. Elsevier Science, 2010.

[59] Ye Liu, TieJun Chang, and Alan E Craig. Coupled mode theory for modeling microring resonators. *Optical Engineering*, 44(8):084601, 2005.

[60] R.G. Hunsperger. *Integrated Optics: Theory and Technology*. Advanced texts in physics. Springer New York, 2009.

[61] M. Kuznetsov. Expressions for the coupling coefficient of a rectangular-waveguide directional coupler. *Opt. Lett.*, 8(9):499–501, Sep 1983.

[62] E. A. J. Marcatili. Dielectric rectangular waveguide and directional coupler for integrated optics. *The Bell System Technical Journal*, 48(7):2071–2102, 1969.

[63] Dietrich Marcuse. Directional couplers made of nonidentical asymmetric slabs. Part I: Synchronous couplers. *Journal of lightwave technology*, 5(1):113–118, 1987.

[64] Brent E Little, Sai T Chu, Hermann A Haus, J Foresi, and J-P Laine. Microring resonator channel dropping filters. *Journal of lightwave technology*, 15(6):998–1005, 1997.

[65] Shiao-Min Tseng, Jing-Hong Zhan, and Ding-Yuan Chen. Derivation of coupling coefficients of modes in slab couplers: Ray theory. *Japanese journal of applied physics*, 38(4R):1989, 1999.

[66] F. P. Payne and J. P. R. Lacey. A theoretical analysis of scattering loss from planar optical waveguides. *Optical Quantum Electron.*, 26(10):977–986, Oct 1994.

[67] JPR Lacey and FP Payne. Radiation loss from planar waveguides with random wall imperfections. *IEE Proceedings J-Optoelectronics*, 137(4):282–288, 1990.

[68] F Ladouceur, JD Love, and TJ Senden. Effect of side wall roughness in buried channel waveguides. *IEE Proceedings-Optoelectronics*, 141(4):242–248, 1994.

[69] Dietrich Marcuse. Mode conversion caused by surface imperfections of a dielectric slab waveguide. *Bell System Technical Journal*, 48(10):3187–3215, 1969.

[70] F Ladouceur, JD Love, and TJ Senden. Measurement of surface roughness in buried channel waveguides. *Electronics Letters*, 28(14):1321–1322, 1992.

[71] Norbert Wiener. Generalized harmonic analysis. *Acta Math.*, 55:117–258, 1930.

[72] F Grillot, L Vivien, S Laval, D Pascal, and E Cassan. Size influence on the propagation loss induced by sidewall roughness in ultrasmall SOI waveguides. *IEEE Photonics Technology Letters*, 16(7):1661–1663, 2004.

[73] M.J. Adams. *An Introduction to Optical Waveguides*. Wiley-Interscience Publication. John Wiley & Sons, 1981.

[74] Daniele Melati, Francesco Morichetti, and A Melloni. A unified approach for radiative losses and backscattering in optical waveguides. *Journal of Optics*, 16(5):055502, 2014.

[75] K.Y. Kim. *Advances in Optical and Photonic Devices*. IntechOpen, 2010.

[76] Kevin K Lee, Desmond R Lim, Hsin-Chiao Luan, Anuradha Agarwal, James Foresi, and Lionel C Kimerling. Effect of size and roughness on light transmission in a Si/SiO2 waveguide: Experiments and model. *Applied Physics Letters*, 77(11):1617–1619, 2000.

[77] Jared F. Bauters, Martijn J. R. Heck, Demis John, Daoxin Dai, Ming-Chun Tien, Jonathon S. Barton, Arne Leinse, René G. Heideman, Daniel J. Blumenthal, and John E. Bowers. Ultra-low-loss high-aspect-ratio Si_3N_4 waveguides. *Opt. Express*, 19(4):3163–3174, Feb 2011.

[78] Jared F. Bauters, Martijn J. R. Heck, Demis D. John, Jonathon S. Barton, Christiaan M. Bruinink, Arne Leinse, René G. Heideman, Daniel J. Blumenthal, and John E. Bowers. Planar waveguides with less than 0.1 dB/m propagation loss fabricated with wafer bonding. *Opt. Express*, 19(24):24090–24101, Nov 2011.

[79] E.D. Palik. *Handbook of Optical Constants of Solids*. Academic Press handbook series. Elsevier Science, 1998.

[80] Zhaoming Zhu and Thomas G Brown. Full-vectorial finite-difference analysis of microstructured optical fibers. *Optics Express*, 10(17):853–864, 2002.

[81] MS Stern. Semivectorial polarised finite difference method for optical waveguides with arbitrary index profiles. *IEE Proceedings J (Optoelectronics)*, 135(1):56–63, 1988.

[82] Ming-Chun Tien, Jared F. Bauters, Martijn J. R. Heck, Daryl T. Spencer, Daniel J. Blumenthal, and John E. Bowers. Ultra-high quality factor planar Si3N4 ring resonators on Si substrates. *Opt. Express*, 19(14):13551–13556, Jul 2011.

[83] Working with lossy modes and dB/m to k conversion - Lumerical support. https://support.lumerical.com/hc/en-us/articles/360034917493. (Accessed on 02/10/2020).

[84] Rüdiger Paschotta. Encyclopedia of laser physics and technology - mode matching, cavity, resonator. https://www.rp-photonics.com/mode_matching.html. (Accessed on 12/15/2020).

[85] U. Griskeviciute, K. Gallacher, R. W. Millar, D. J. Paul, and I. MacGilp. Understanding the sidewall dependence of loss for Ge-on-Si waveguides in the mid-infrared. In *2019 IEEE 16th International Conference on Group IV Photonics (GFP)*, pages 1–2, 2019.

[86] Peter Bienstman and Roel Baets. Advanced boundary conditions for eigenmode expansion models. *Optical and Quantum Electronics*, 34(5-6):523, 2002.

[87] Dominic F. G. Gallagher and Thomas P. Felici. Eigenmode expansion methods for simulation of optical propagation in photonics: Pros and cons. In Yakov S. Sidorin and Ari Tervonen, editors, *Integrated Optics: Devices, Materials, and Technologies VII*, volume 4987, pages 69 – 82. International Society for Optics and Photonics, SPIE, 2003.

[88] Peter Bienstman. *Rigorous and efficient modelling of wavelenght scale photonic components*. PhD thesis, Ghent University, 2001.

[89] Mode - Eigenmode expansion (EME) solver introduction - Lumerical support. https://support.lumerical.com/hc/en-us/articles/360034396614-MODE-EigenMode-Expansion-EME-solver-introduction. (Accessed on 04/17/2020).

[90] Miguel Ángel Guillén-Torres. *Feasibility of optical gyroscopic sensors in silicon-on-insulator technology*. PhD thesis, University of British Columbia, 2015.

[91] D.G. Rabus. *Integrated Ring Resonators: The Compendium*. Springer Series in Optical Sciences. Springer Berlin Heidelberg, 2007.

[92] Andreas Freise and Kenneth Strain. Interferometer Techniques for Gravitational-Wave Detection. *Living Reviews in Relativity*, 13(1):1, Feb 2010.

[93] Rüdiger Paschotta. RP photonics encyclopedia - bandwidth, optical spectrum, telecom fiber. https://www.rp-photonics.com/bandwidth.html. (Accessed on 06/16/2020).

[94] Ming-Chun Tien, Jared F. Bauters, Martijn J. R. Heck, Daryl T. Spencer, Daniel J. Blumenthal, and John E. Bowers. Ultra-high quality factor planar Si3N4 ring resonators on Si substrates. *Opt. Express*, 19(14):13551–13556, Jul 2011.

[95] Rüdiger Paschotta. Encyclopedia of laser physics and technology - group index, group refractive index. https://www.rp-photonics.com/group_index.html. (Accessed on 08/02/2016).

[96] Homepage - Nazca Design. https://nazca-design.org/. (Accessed on 05/24/2019).

[97] Marcus Rommel, Bengt Nilsson, Piotr Jedrasik, Valentina Bonanni, Alexandre Dmitriev, and Jürgen Weis. Sub-10nm resolution after lift-off using HSQ/PMMA double layer resist. *Microelectronic Engineering*, 110:123 – 125, 2013.

[98] Bruce E Deal and AS Grove. General relationship for the thermal oxidation of silicon. *Journal of Applied Physics*, 36(12):3770–3778, 1965.

[99] Oxide growth time calculator - BYU cleanroom. https://cleanroom.byu.edu/OxideTimeCalc. (Accessed on 06/01/2020).

[100] BM Azizur Rahman, Vesel Haxha, Shyqyri Haxha, and Kenneth TV Grattan. Design optimization of polymer electrooptic modulators. *Journal of lightwave technology*, 24(9):3506, 2006.

[101] Sofia Tönnberg. Optimisation and characterisation of LPCVD silicon nitride thin film growth. Master's thesis, Chalmers University of Technology, 2006.

[102] Jacob Levy. *Integrated Nonlinear Optics In Silicon Nitride Waveguides And Resonators*. PhD thesis, Cornell University, Ithica, USA, August 2011.

[103] Kirill O Bugaev, Anastasia A Zelenina, and Vladimir A Volodin. Vibrational spectroscopy of chemical species in silicon and silicon-rich nitride thin films. *International Journal of Spectroscopy*, 2012, 2011.

[104] F Ay and A Aydinli. Comparative investigation of hydrogen bonding in silicon based PECVD grown dielectrics for optical waveguides. *Optical materials*, 26(1):33–46, 2004.

[105] Jared Bauters, Martijn Heck, Demis D. John, Ming-Chun Tien, Wenzao Li, Jon S. Barton, Daniel J. Blumenthal, John Bowers, Arne Leinse, and Rene G. Heideman. Ultra-low-loss single-mode silicon nitride waveguides with 0.7 dB/m propagation loss. In *37th European Conference and Exposition on Optical Communications*, page Th.12.LeSaleve.3. Optical Society of America, 2011.

[106] J. Viard, E. Beche, D. Perarnau, R. Berjoan, and J. Durand. XPS and FTIR study of silicon oxynitride thin films. *Journal of the European Ceramic Society*, 17(15):2025 – 2028, 1997. International Symposium on Nitrides Journees d'Etudes sur les Nitures.

[107] Wojciech Kijaszek, Waldemar Oleszkiewicz, Adrian Zakrzewski, Sergiusz Patela, and Marek Tłaczała. Investigation of optical properties of silicon oxynitride films deposited by rf pecvd method. *Materials Science-Poland*, 34(4):868–871, 2016.

[108] Kevin Gallacher. *Germanium on silicon photonic devices*. PhD thesis, University of Glasgow, 2013.

[109] Frank D Egitto and Luis J Matienzo. Plasma modification of polymer surfaces for adhesion improvement. *IBM Journal of Research and Development*, 38(4):423–439, 1994.

[110] Muhammad M. Mirza. *Nanofabrication of silicon nanowires and nanoelectronic transistors*. PhD thesis, University of Glasgow, 2015.

[111] Hideo Namatsu, Yasuo Takahashi, Kenji Yamazaki, Toru Yamaguchi, Masao Nagase, and Kenji Kurihara. Three-dimensional siloxane resist for the formation of nanopatterns with minimum linewidth fluctuations. *Journal of Vacuum Science and Technology B: Microelectronics and Nanometer Structures*, 16(1):69–76, jan 1998.

[112] Yi Xuan, Yang Liu, Leo T Varghese, Andrew J Metcalf, Xiaoxiao Xue, Pei-Hsun Wang, Kyunghun Han, Jose A Jaramillo-Villegas, Abdullah Al Noman, Cong Wang, et al. High-Q silicon nitride microresonators exhibiting low-power frequency comb initiation. *Optica*, 3(11):1171–1180, 2016.

[113] Tetramethylammonium hydroxide (25%) tmah.pdf. https://wcam.engr.wisc.edu/Public/Safety/MSDS/Tetramethylammonium%20hydroxide%20(25%25)%20TMAH.pdf. (Accessed on 07/28/2017).

[114] TC Mele, J Nulman, and JP Krusius. Selective and anisotropic reactive ion etch of LPCVD silicon nitride with CHF3 based gases. *Journal of Vacuum Science & Technology B: Microelectronics Processing and Phenomena*, 2(4):684–687, 1984.

[115] J Dulak, BJ Howard, and Ch Steinbrüchel. Etch mechanism in the reactive ion etching of silicon nitride. *Journal of Vacuum Science & Technology A: Vacuum, Surfaces, and Films*, 9(3):775–778, 1991.

[116] X Li, RJW Hill, H Zhou, CDW Wilkinson, and IG Thayne. A low damage Si3N4 sidewall spacer process for self-aligned sub-100 nm III-V mosfets. *Microelectronic Engineering*, 85(5-6):996–999, 2008.

[117] Richard J Bojko, Jing Li, Li He, Tom Baehr-Jones, Michael Hochberg, and Yukinori Aida. Electron beam lithography writing strategies for low loss, high confinement silicon optical waveguides. *Journal of Vacuum Science & Technology B, Nanotechnology and Microelectronics: Materials, Processing, Measurement, and Phenomena*, 29(6):06F309, 2011.

[118] Princeton applied research egg5210 amplifier - IEEE 488.2 (GPIB) driver for LabVIEW - National Instruments. http://sine.ni.com/apps/utf8/niid_web_display.download_page?p_id_guid=E3B19B3E9510659CE034080020E74861. (Accessed on 03/30/2020).

[119] Yiming He, Zhaosong Li, and Dan Lu. A waveguide loss measurement method based on the reflected interferometric pattern of a Fabry-Pérot cavity. In *Integrated Optics: Devices, Materials, and Technologies XXII*, volume 10535, pages 250 – 255. International Society for Optics and Photonics, SPIE, 2018.

[120] Atsushi Sakai, Go Hara, and Toshihiko Baba. Propagation characteristics of ultrahigh-δ optical waveguide on silicon-on-insulator substrate. *Japanese Journal of Applied Physics*, 40(Part 2, No. 4B):L383–L385, apr 2001.

[121] Peyton Murray. scipy.optimize.curve_fit - SciPy v1.4.1 reference guide. https://docs.scipy.org/doc/scipy/reference/generated/scipy.optimize.curve_fit.html. (Accessed on 02/16/2020).

[122] Brian Stern, Xingchen Ji, Avik Dutt, and Michal Lipson. Compact narrow-linewidth integrated laser based on a low-loss silicon nitride ring resonator. *Opt. Lett.*, 42(21):4541–4544, Nov 2017.

[123] Si free-space amplified photodetectors. https://www.thorlabs.com/newgrouppage9.cfm?objectgroup_id=3257. (Accessed on 02/26/2020).

[124] L. Stefan, M. Bernard, R. Guider, G. Pucker, L. Pavesi, and M. Ghulinyan. Ultra-high-Q thin-silicon nitride strip-loaded ring resonators. *Opt. Lett.*, 40(14):3316–3319, Jul 2015.

[125] Xiyuan Lu, Qing Li, Daron A. Westly, Gregory Moille, Anshuman Singh, Vikas Anant, and Kartik Srinivasan. Chip-integrated visible–telecom entangled photon pair source for quantum communication. *Nature Physics*, 15(4):373–381, 2019.

[126] Wolfram H.P. Pernice, Chi Xiong, and Hong X. Tang. High Q micro-ring resonators fabricated from polycrystalline aluminum nitride films for near infrared and visible photonics. *Opt. Express*, 20(11):12261–12269, May 2012.

[127] C. Doolin, P. Doolin, B. C. Lewis, and J. P. Davis. Refractometric sensing of Li salt with visible-light Si_3N_4 microdisk resonators. *Appl. Phys. Lett.*, 106(8):081104, 2015.

[128] Tao Ling, Sung-Liang Chen, and L. Jay Guo. High-sensitivity and wide-directivity ultrasound detection using high Q polymer microring resonators. *Applied Physics Letters*, 98(20):204103, 2011.

[129] Christopher C. Evans, Chengyu Liu, and Jin Suntivich. Low-loss titanium dioxide waveguides and resonators using a dielectric lift-off fabrication process. *Opt. Express*, 23(9):11160–11169, May 2015.

[130] Alina Samusenko, Davide Gandolfi, Georg Pucker, Tatevik Chalyan, Romain Guider, Mher Ghulinyan, and Lorenzo Pavesi. A SiON microring resonator-based platform for biosensing at 850 nm. *J. Lightwave Technol.*, 34(3):969–977, Feb 2016.

[131] R. L. Barger, M.S. Sorem, and J.L. Hall. Frequency stabilization of a cw dye laser. *Applied Physics Letters*, 22(11):573–575, 1973.

[132] R. W. P. Drever, J. L. Hall, F. V. Kowalski, J. Hough, G. M. Ford, A. J. Munley, and H. Ward. Laser phase and frequency stabilization using an optical resonator. *Applied Physics B*, 31(2):97–105, 1983.

[133] Vivek Raghunathan, Winnie N. Ye, Juejun Hu, Tomoyuki Izuhara, Jurgen Michel, and Lionel Kimerling. Athermal operation of silicon waveguides: spectral, second order and footprint dependencies. *Opt. Express*, 18(17):17631–17639, Aug 2010.

[134] Jie Teng, Pieter Dumon, Wim Bogaerts, Hongbo Zhang, Xigao Jian, Xiuyou Han, Mingshan Zhao, Geert Morthier, and Roel Baets. Athermal silicon-on-insulator ring resonators by overlaying a polymer cladding on narrowed waveguides. *Opt. Express*, 17(17):14627–14633, Aug 2009.

[135] Ali W Elshaari, Iman Esmaeil Zadeh, Klaus D Jöns, and Val Zwiller. Thermo-optic characterization of silicon nitride resonators for cryogenic photonic circuits. *IEEE Photonics Journal*, 8(3):1–9, 2016.

[136] Arlee V Smith, Jesse J Smith, and Binh T Do. Thermo-optic and thermal expansion coefficients of RTP and KTP crystals over 300-350 K. *arXiv preprint arXiv:1607.03964*, 2016.

[137] NG Sultanova, SN Kasarova, and ID Nikolov. Characterization of optical properties of optical polymers. *Optical and Quantum Electronics*, 45(3):221–232, 2013.

[138] SU-8 3000 Data sheet ver 4.2. https://kayakuam.com/wp-content/uploads/2019/09/SU-8-3000-Data-Sheet.pdf. (Accessed on 05/08/2020).

[139] Kumar Saurav, Sulakshna Kumari, and Nicolas Le Thomas. CMOS fabricated large array of free standing substrate-less photonic crystal cavities for biosensing applications. *IEEE Photonics Journal*, 9(2):1–8, 2017.

[140] Thorsten Wahlbrink, Wan Shao Tsai, Michael Waldow, Michael Först, Jens Bolten, Thomas Mollenhauer, and Heinrich Kurz. Fabrication of high efficiency SOI taper structures. *Microelectronic engineering*, 86(4-6):1117–1119, 2009.

[141] Payam Rabiei, William H Steier, Cheng Zhang, and Larry R Dalton. Polymer micro-ring filters and modulators. *Journal of lightwave technology*, 20(11):1968, 2002.

[142] Zhiyi Zhang, Ping Zhao, Peng Lin, and Fengguo Sun. Thermo-optic coefficients of polymers for optical waveguide applications. *Polymer*, 47(14):4893 – 4896, 2006.

[143] Thorlabs. 2-channel compact usb temperature and humidity logger. https://www.thorlabs.com/newgrouppage9.cfm?objectgroup_id=5884. (Accessed on 04/09/2020).

[144] Richard Paul Middlemiss. *A practical MEMS gravimeter*. PhD thesis, University of Glasgow, 2016.

[145] Richard P Middlemiss, Steven G Bramsiepe, Rebecca Douglas, James Hough, Douglas J Paul, Sheila Rowan, and Giles D Hammond. Field tests of a portable mems gravimeter. *Sensors*, 17(11):2571, 2017.

[146] Richard P Middlemiss, Steven G Bramsiepe, Rebecca Douglas, Stefan Hild, James Hough, Douglas J Paul, Antonio Samarelli, Sheila Rowan, and Giles D Hammond. Microelectromechanical system gravimeters as a new tool for gravity imaging. *Philosophical Transactions of the Royal Society A: Mathematical, Physical and Engineering Sciences*, 376(2120):20170291, 2018.

[147] Andreas Noack, Richard Middlemiss, Abhinav Prasad, and Giles Hammond. MEMS gravity sensors for imaging density anomalies. In Kishan Dholakia and Gabriel C. Spalding, editors, *Optical Trapping and Optical Micromanipulation XV*, volume 10723, pages 48 – 54. International Society for Optics and Photonics, SPIE, 2018.

[148] Enrique J Galvez. Gaussian beams in the optics course. *American journal of physics*, 74(4):355–361, 2006.

[149] Vilson R Almeida, Roberto R Panepucci, and Michal Lipson. Nanotaper for compact mode conversion. *Optics letters*, 28(15):1302–1304, 2003.

[150] B. Ben Bakir, A. V. de Gyves, R. Orobtchouk, P. Lyan, C. Porzier, A. Roman, and J. . Fedeli. Low-loss ($<$ 1 dB) and polarization-insensitive edge fiber couplers fabricated on

200-mm silicon-on-insulator wafers. *IEEE Photonics Technology Letters*, 22(11):739–741, 2010.

[151] T. Tsuchizawa, K. Yamada, H. Fukuda, T. Watanabe, Jun-ichi Takahashi, M. Takahashi, T. Shoji, E. Tamechika, S. Itabashi, and H. Morita. Microphotonics devices based on silicon microfabrication technology. *IEEE Journal of Selected Topics in Quantum Electronics*, 11(1):232–240, 2005.

[152] Gunther Roelkens, Pieter Dumon, Wim Bogaerts, Dries Van Thourhout, and Roel Baets. Efficient silicon-on-insulator fiber coupler fabricated using 248-nm-deep UV lithography. *IEEE Photonics Technology Letters*, 17(12):2613–2615, 2005.

[153] Z Weissman and A Hardy. 2-D mode tapering via tapered channel waveguide segmentation. *Electronics letters*, 28(16):1514–1516, 1992.

[154] MH Chou, MA Arbore, and Martin M Fejer. Adiabatically tapered periodic segmentation of channel waveguides for mode-size transformation and fundamental mode excitation. *Optics letters*, 21(11):794–796, 1996.

[155] I Day, Ivan Evans, Andrew Knights, Fred Hopper, Stephen Roberts, Jeff Johnston, Stephen Day, Jonathan Luff, H Tsang, and Mehdi Asghari. Tapered silicon waveguides for low insertion loss highly-efficient high-speed electronic variable optical attenuators. In *Optical Fiber Communication Conference*, page TuM5. Optical Society of America, 2003.

[156] Rüdiger Paschotta. RP photonics encyclopedia - fresnel reflections, impedance matching, suppression, anti-reflection coatings. https://www.rp-photonics.com/fresnel_reflections.html. (Accessed on 06/17/2020).

[157] Daniel Côté. GitHub - DCC-LabRayTracing. https://github.com/DCC-Lab/RayTracing, 2019. (Accessed on 05/04/2020).

[158] Rüdiger Paschotta. RP photonics encyclopedia - ABCD matrix, ray transfer matrix. https://www.rp-photonics.com/abcd_matrix.html. (Accessed on 05/04/2020).

[159] Philbert Tsai David Kleinfeld. An introduction to basic optical design: Matrix techniques through scanning microscopy. https://neurophysics.ucsd.edu/courses/physics_173_273/Phys_173_optics.pdf, April 2004. (Accessed on 05/04/2020).

[160] Amnon Yariv. *Quantum electronics*. Wiley, 1989.

[161] Christopher L Mueller. *Techniques for Resonant Optical Interferometry with Applications to the Advanced LIGO Gravitaional Wave Detectors*. PhD thesis, University of Florida, 2014.

[162] Edmund Optics. Fused silica ball lenses - fused silica half-ball lenses. https://www.edmundoptics.co.uk/f/used-ilica-all-and-alf-all-enses/14111/. (Accessed on 05/19/2020).

[163] S Malhouitre, D Fowler, S Garcia, O Lemonnier, N Tyler, and W Rabaud. Silicon nitride photonic platform for lidar applications. In *2018 IEEE 15th International Conference on Group IV Photonics (GFP)*, pages 1–2. IEEE, 2018.

[164] Eric D Black. An introduction to Pound-Drever-Hall laser frequency stabilization. *American journal of physics*, 69(1):79–87, 2001.

[165] Robert V Pound. Electronic frequency stabilization of microwave oscillators. *Review of Scientific Instruments*, 17(11):490–505, 1946.

[166] Huilian Ma, Jianjie Zhang, Linglan Wang, and Zhonghe Jin. Double closed-loop resonant micro optic gyro using hybrid digital phase modulation. *Optics express*, 23(12):15088–15097, 2015.

[167] Fang Wei, Fei Yang, Xi Zhang, Dan Xu, Meng Ding, Li Zhang, Dijun Chen, Haiwen Cai, Zujie Fang, and Gu Xijia. Subkilohertz linewidth reduction of a DFB diode laser using self-injection locking with a fiber Bragg grating Fabry-Pérot cavity. *Optics express*, 24(15):17406–17415, 2016.

[168] F Dell'Olio, T Tatoli, C Ciminelli, and MN Armenise. Recent advances in miniaturized optical gyroscopes. *J. European Optical Society: Rapid Publications*, 9:14013, 2014.

[169] Huilian Ma, Wenyi Wang, Yang Ren, and Zhonghe Jin. Low-noise low-delay digital signal processor for resonant micro optic gyro. *IEEE Photonics Technology Letters*, 25(2):198–201, 2012.

[170] Hui Mao, Huilian Ma, and Zhonghe Jin. Polarization maintaining silica waveguide resonator optic gyro using double phase modulation technique. *Opt. Express*, 19(5):4632–4643, Feb 2011.

[171] Lishuang Feng, Ming Lei, Huilan Liu, Yinzhou Zhi, and Junjie Wang. Suppression of backreflection noise in a resonator integrated optic gyro by hybrid phase-modulation technology. *Applied optics*, 52(8):1668–1675, 2013.

[172] Ming Lei, Lishuang Feng, and Yinzhou Zhi. Sensitivity improvement of resonator integrated optic gyroscope by double-electrode phase modulation. *Applied optics*, 52(30):7214–7219, 2013.

[173] Caterina Ciminelli, Clarissa Martina Campanella, Francesco Dell'Olio, Carlo Edoardo Campanella, and Mario Nicola Armenise. Label-free optical resonant sensors for biochemical applications. *Progress in Quantum Electronics*, 37(2):51–107, 2013.

[174] Christopher Sorrentino, John RE Toland, et al. Ultra-sensitive chip scale sagnac gyroscope based on periodically modulated coupling of a coupled resonator optical waveguide. *Optics express*, 20(1):354–363, 2012.

[175] C Ciminelli, CE Campanella, F Dell'Olio, CM Campanella, and MN Armenise. Theoretical investigation on the scale factor of a triple ring cavity to be used in frequency sensitive resonant gyroscopes. *Journal of the European Optical Society-Rapid publications*, 8, 2013.

[176] WolframAlpha. https://www.wolframalpha.com/input/?i=int+exp%28-abs%28u%29%2FL+%2B+i+m+u%29+du. (Accessed on 03/03/2020).

[177] Grigorii B Malykin. The Sagnac effect: correct and incorrect explanations. *Physics-Uspekhi*, 43(12):1229–1252, 2000.

[178] Grigorii B Malykin. Sagnac effect in ring lasers and ring resonators. How does the refraction index of the optical medium influence the sensitivity to rotation? *Uspekhi Fizicheskih Nauk*, 184(7):775–781, jul 2014.